# Electrochemical Characterization of Solid Acid Fuel Cell Electrodes.

Thesis by

Kenji Alexander Sasaki

In Partial Fulfillment of the Requirements

for the Degree of

Doctor of Philosophy

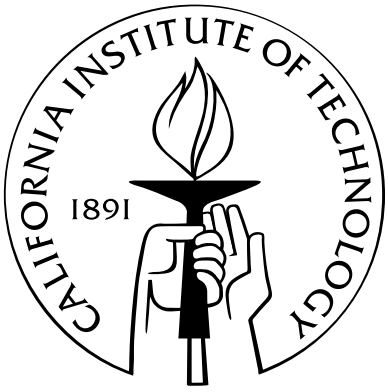


California Institute of Technology

Pasadena, California

2010

(Defended 26 August 2009)

This thesis is dedicated to...the Love of my Life.

*Parvis imbutus tentabis grandia tutus.*

In truth, I'm thankful for it all. The moments frozen in crystal and the songs scribed in the sand on life's windy beach. The heartbreak, the joy, the lessons learned. *Per Ardua ad Astra* and all that. But most of all, I'm thankful for the people.

To my grandfather, Vincent, who I assisted in my first ever experiment - qualitative differential analysis of Lucky Charms$^{TM}$marshmallows by microwave. [*under preparation*]
To Papa, stronger than I'll know, I miss you still.
To Grandma and Grandma, who taught me about Family.
My best friend Mo, who snuck warm frivolity into my heart where it nested
- like a tiny pig.
To those that came before: to Tetsuya, to Calum, to Dane - young giants all.
To the C-boys: Sprout, Gordo, and El Chupacabra - bombing structures the safe way.
To ML. Never was a destructive weather pattern such a good friend.
To Jesse and Ryan - when I run, I'm chasing you.
To Peter and Lisa - better officemates than I ever was.
To my aunts, uncles, and cousins. There's not space enough. Expect letters.
To the countless friends who have shared their food, their homes, their adventures, and their lives with me. A man counts himself lucky.

**To my mother**
whose love is a physical thing - solid and broad -
the sort of love you could build castles on.

**To my father**
whose love seems self-conscious,
so hides in the next room, but listens with warmth.

**To my sisters**
who've given me direction and perspective.
You were always there for me, whether I liked it or not.

To my advisor, Professor Haile, the best writer I know. And to her band of merry, nerdy researchers - there will always be space at my table for you.

And as I write this, I acknowledge those that have left. For whatever reason. The gravity of our decisions pulls us every which way; sometimes apart. Life, like research, is a learning experience. We never begin our adventures knowing the same things that we know by the end. We are, therefore, never the same people that we were when we started. This work, then, I acknowledge as a record of who I was and an indicator of who I came to be. And taken together, all the souls that touched my life will guide my next steps. The steps though, are mine to take. And that may be the greatest lesson learned.

# Abstract

The quest for high-efficiency, high-power output fuel cells can be largely equated to the quest for high-performance components (anode, cathode, electrolyte). Solid Acid electrolytes, notably CsH2PO4, have been demonstrated to be affordable, stable, excellent ion conductors, and impermeable to parasitic fuel cross-over. Moreover, they operate at a temperature 'sweet-spot' high enough to promote electrode kinetics and low enough to enable low-cost infrastructure. Fuel cell devices based on these materials are known to be limited, however, by electrode losses - even with high platinum loading. Improving the performance and lowering the cost of these components is necessary if such devices are to be considered viable alternatives.

In this work, the primary focus was the development of electrochemical characterization approaches. In doing so, we investigated electrode losses through steady-state and time-dependent electrochemical characterization and identified the primary rate limiting process and mechanism as oxygen reduction at the cathode. To characterize anode kinetics, new testing approaches were implemented which employed robust, asymmetric electrode geometries to isolate electrode kinetics without the inclusion of a reference electrode. These geometries' isolation efficacy was assessed by numerical computation - the results of which were leveraged into an explicitly defined, material-agnostic tool to evaluate asymmetric electrode geometries.

While for platinum, the cathode mechanism was shown to be insensitive to the microstructures tested, the mechanism of hydrogen reduction/oxidation was seen to vary between nanoscale powder and microscale defined electrodes - reconfirming the importance of rigorous testing approaches. Asymmetric electrode geometries with defined microstructures allowed direct characterization and comparative evaluation of non-platinum candidates for both the anode and the cathode. On the anode, palladium was over an order of magnitude more active than platinum and nickel, which exhibited a comparable activity. Palladium

and silver were shown to be stable cathode materials, though less active than platinum. As a demonstration of the developed methodology's flexibility, a palladium-silver alloy was synthesized and tested.

The tools and methodologies developed in this work enable the rapid and flexible screening of electrodes for solid acid fuel cells.

# Contents

# List of Figures

# List of Tables

# Chapter 1

# Introduction

## 1.1 Chemical to Thermal conversion

While fire has key places in many belief systems of history, none are so poetic as the Greek myth of Prometheus. Most remember the story of Prometheus as the Titan who stole fire from Olympus for humanity - and was condemned to eternal torture by Zeus as a result. But Ovid's Metamorphoses credits the Titan with the very creation of humanity. Crafted from clay and imbued with life by Zeus, humanity was beloved by Prometheus. Then too, it was Prometheus who freed Athena from Zeus's skull by bashing the elder god's head open with a rock.

Thus did Greek mythology depict the bringer of fire as one who defied the gods to bring humanity the warmth of flame and the Goddess of craftsmen and artisans (among others). It is a fitting allegory as perhaps no other capability has empowered humanity so much as the ability to control fire - to exploit the energy stored in chemical bonds.

The first signs of domesticated fire predate Homo Sapiens, though controlled ignition is relatively recent - within the last 10,000 years. Early man, then, relied on lightning strikes to start fires, which were then tended and protected without means to rekindle them should they be extinguished. And a precious tool it was. Cooking food was perhaps early humanity's single greatest step forward in fighting disease. Fire was used to clear underbrush to aid in hunting, to produce crude fertilizers, to clear fields. Smoke signals were the first forms of telecommunication.

For as long as our species has walked this earth, fire has kept us warm, cooked our food, and lit the dark places. This is metaphorically true as well - alchemists used fire to probe chemical reactions and laid the foundations for modern chemistry. Metallurgists relied on

the fire to smelt ore and forge tools. The vein continues through history, and the flame which has lit human civilization since its cradle, burns still.

## 1.2 Chemical to Mechanical conversion

As useful as releasing the energy stored in chemical bonds was, for dozens of millenia the energy was used solely to heat and to illuminate. The next capability was to convert the chemical energy to mechanical energy through steam. Certain desktop demonstration devices existed, since 1500s, but it wasn't until Thomas Newcomen commercialized his atmospheric engine in the early 1700s. It was primarily used to move water - away from deep mines or to factory water wheels. With Watt's refinements by 1775, external combustion engines spread throughout factories and mills and railroads - propelling the industrial revolution in Britain and in America. External combustion engines using the Rankine cycle are even used to this day in fission reactors and solar-thermal turbines.

And the most recent development in the saga of human pyromania is the direct conversion of chemical energy to mechanical energy with the internal combustion engines and with rockets.

Thus we can chart the sophistication in which humanity employs the chemical bond over the entire history of our time on the planet. We have gone from burning hydrocarbons for cooking to . . burning hydrocarbons for cooking. The truth of the matter is that humanity left the stone age (with fire's help, no less) but we never really advanced beyond the "fire age". Currently over 90% of energy consumption in the world comes from reacting oxygen with fuels or from replacing combustion with a different heat source in the case of fission reactors. And the magnitude of that consumption increases every day.

Even ignoring the potential environmental effects of pouring unprecedented levels of carbon into our atmosphere (some estimates predict disaster if even a quarter of current proven energy reserves are burned), we are running out of energy. There's a great deal remaining, to be sure. Plants have been growing, dying and being compressed under sediment for hundreds of millions of years - so there are some reserves to work through. The fact of the matter is, though, we will run out of coal, natural gas, and oil - simply because we're using it faster than it's being made. Without leaving our atmosphere, and without fusion, the only energy input we have is from the sun.

The sun moves water to elevations so that it can be used to power hydroelectric generators. The sun heats the surface of the earth, causing wind patterns that can turn turbines or cause waves. The sun powers photosynthesis as plants store energy in chemical bonds. The sun pours 0.12 exawatts of energy onto our planet. Until we can travel the stars, mining asteroids for uranium, or create our own mini-suns with fusion, any long-term solution to powering humanity must come from solar power.

For the entirety of our species' existence, we have coasted on the energy wealth accumulated by vegetation over hundreds of millions of years, on what chemical energy plants could store on shorter time-scales, (Dr. Hansen recently suggested a return to wood-burning to control atmosphere carbon dioxide levels (1)) and on what mechanical energy was accessible.

It's a course that we can choose to continue. We have centuries of energy under our feet, ready for the fire. By the time we run out, perhaps we'll have developed fusion, but the consequences of inaction are weighed against the opportunities of discovery. I believe the next chapter in our relationship with the chemical bond should be opened - the efficient conversion, storage, and utility of chemical energy.

## 1.3 Chemical to Electrical

In the last several decades, devices have been developed which convert chemical energy directly into electrical energy. Known as fuel cells, they gained considerable attention for their potentially high efficiencies, scalability, and fuel flexibility. Fundamentally, they operate by selectively conducting charge carriers across an electrolyte membrane. Fuel cells are categorized based on the nature of this electrolyte: the charge carriers, and the operating temperature. William Grove in 1839 is credited as demonstrating the first device of this kind, based on platinum electrodes in a sulfuric acid bath.

Hydrogen gas would dissociate into protons and electrons - and the protons were able to diffuse through the solution to the oxygen lead where it would react with oxygen and electrons to form water. With this approach, chemical potential was converted directly into electrical potential. Without a thermodynamic cycle, the efficiency can exceed the carnot efficiency which limits thermal engines. Most attractively to many, the product of the reaction is pure water.

Since then, and in recent years especially, two fuel cell electrolytes have emerged as

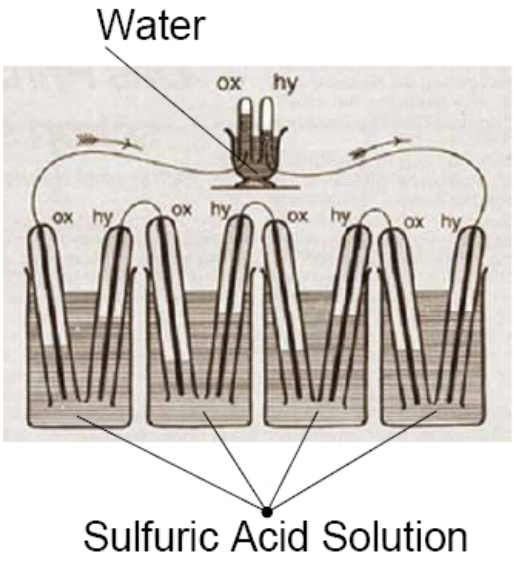


Figure 1.1: Schematic of William Grove's fuel cell.

viable energy conversion devices. The first uses a polymer electrolyte to conduct hydronium ions ($H_3O^+$) near room temperature as it relies on liquid water for conduction. These are termed Polymer Electrolyte Membrane Fuel Cells (PEMFCs). The second uses a ceramic electrolyte to conduct oxygen ions ($O^{2-}$ at high temperatures ($> 500$ °C ) as oxygen ion conduction is sluggish at low temperatures.

Each has their own advantages and disadvantages, based primarily on operating temperature. For example, PEMFCs generally require noble catalysts, such as platinum, to operate, due to the low temperature. In their favor, they have extremely high conductivities and device construction can be achieved with low-cost materials. Conversely, SOFCs are at such high temperatures that electrode kinetics are facile, but require expensive processing and infrastructure.

In 2001, a new type of fuel cell electrolyte was introduced (2). The materials, termed "Solid Acids" possessed properties of both acids and salts - that is, they are ionically-conducting and electrically-insulating. Mechanically, these materials are brittle at room temperature (though superplastic at high temperature (3) and soluble in water. The mechanism by which they achieve high ionic conductivity (on the order of 0.01 S/cm), was the subject of a some controversy. The solid acid, $CsH_2PO_4$ specifically, was seen to undergo a phase change at approximately 230 °C from the monoclinic crystal structure shown in

figure 1.2(a) to the cubic structure in figure 1.2(b), at which point, the measured conductivity sharply increased but the material dehydrated - causing some to conclude that the dehydration event caused the spurious spike.(4) A number of approaches were attempted in order to discern the identify the cause and effects of this transition, but the one that was ultimately successful was simply to suppress the dehydration with a high ambient water partial pressure. Thus stabilized, the $CsH_2PO_4$ electrolyte was able to be studied and the nature of its phase transition described as a shift from monoclinic to cubic crystal structure, and the rapid reorientation of oxyanion groups provided a Grotthuss mechanism by which protons could reorient on the oxyanion tetrahedra and hop to receptive neighbors. Solid Acid electrolytes, then, are distinct in that the conducting species is stoichiometric, rather than induced by vacancies or associated with otherwise neutral permeating species.

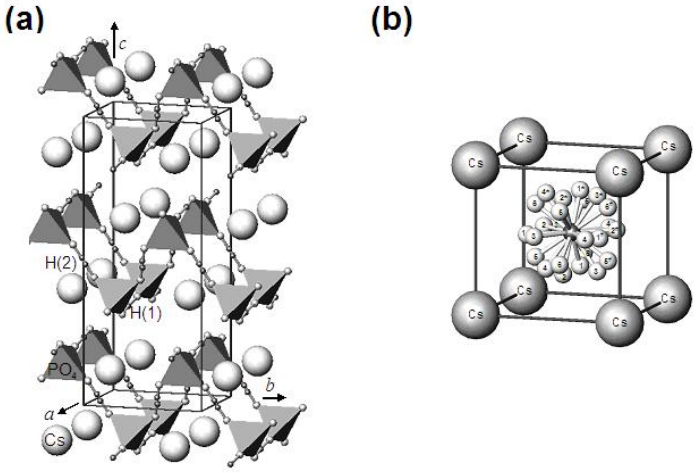


Figure 1.2: Room temperature (a) and high temperature (b) crystal structures of $CsH_2PO_4$ . Also shown in (b) are possible oxyanion orientations within the cubic Cs lattice. The entropic contribution of these multiple states drives the phase transition.

As a solid, stoichiometric proton-conductor, operating at 240 °C , $CsH_2PO_4$ electrolyte fuel cells are unlike any major fuel cell system, occupying a regime where the slightly elevated temperature could increase electrode activity without being so high as to incur the drawbacks of SOFCs. The lower temperature electrolytes are universally liquid and mechanisms occur through solvated reactants. With few exceptions, the high-temperature ceramic fuel cells conduct oxygen.

In spite of the obstacles necessarily faced in implementing truly novel materials, re-

searchers in Professor Haile's lab fabricated MEA assemblies (diagramed in figure 1.3) which demonstrated relatively high performance with platinum-based composite electrodes. With preliminary optimization of electrodes and fabricating thinner electrolytes, high power densities (400 mW/cm$^2$) were demonstrated and shown in figure 1.4 (5).

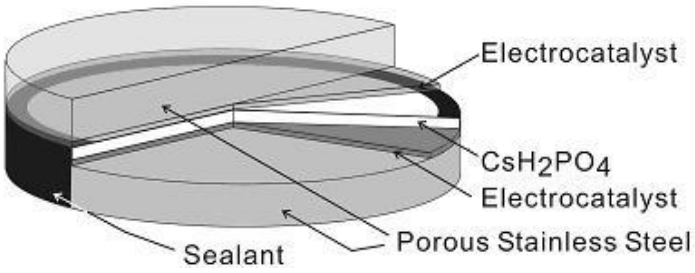


Figure 1.3: Diagram of a complete fuel cell Membrane-Electrolyte Assembly, including gas diffusion layers and seals

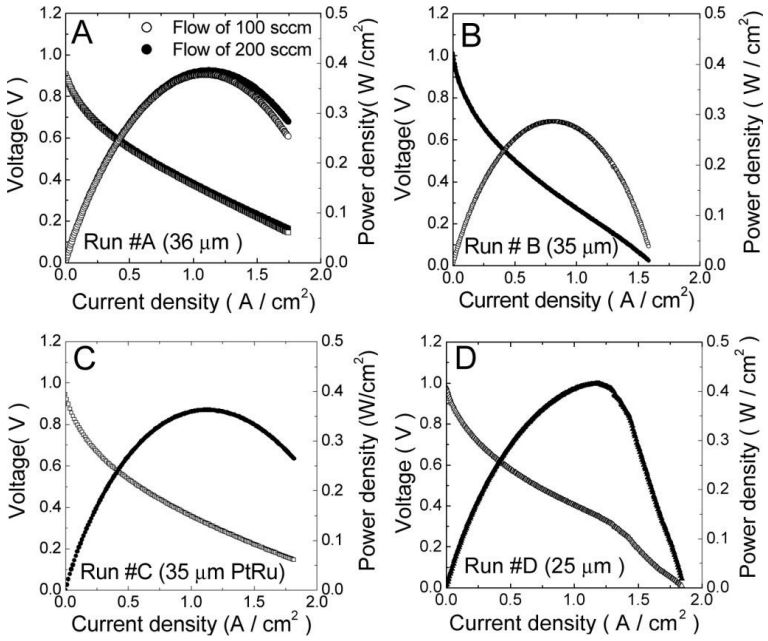


Figure 1.4: High performance polarization curves of SAFCs diagrammed in figure 1.3 measured in humid (0.33 atm $p\mathrm{H_2O}$)$\mathrm{H_2}$ and $\mathrm{O_2}$ at 240 °C

In fabricating high-conductivity electrolytes on the order of 25 microns thick, the ohmic loss through the electrolyte has only a minor effect on the operating performance. Electrocatalysis then, is the key limitation to $CsH_2PO_4$ fuel cell performance. Developing and applying the analytical approaches necessary to characterize the electroactivity of this system is the focus of this thesis.

# Chapter 2

# Fuel Cell Electrochemistry and Theory of Experimental Methods

Fuel cells are energy conversion devices. They take advantage of an electrochemical potential gradient to convert energy from chemical bonds into electrical energy in the form of potential and current. As such, they do not operate on a thermal cycle, as internal combustion engines do, and their efficiencies are therefore not limited by carnot efficiencies. Which is not to say that fuel cells are inherently more efficient than internal combustion counterparts - just that efficiencies are calculated differently. Conventionally, theoretical limits on fuel cell efficiencies are related to combustion efficiencies by comparing the maximum amount of electricity extractable from a fuel cell to the maximum energy released simply by burning the reactants.

These thermodynamically determined efficiencies, however, are seldom realized as kinetic losses further decrease the electrical energy extracted. Such losses, also termed overpotentials, increase monotonically with drawn current. The consequence of this behavior is a decrease in fuel cell energy conversion with increased operating load; thus, there exists an inescapable trade-off between operating efficiency and utility. A fuel cell producing infinitesimal current is near its thermodynamic efficiency, but is also effectively useless. In order to maintain high efficiencies, then, kinetic losses in fuel cells must be minimized. First though, they should be understood.[(6)]

## 2.1 EMF across a fuel cell

The maximum electrical energy extractable from a redox reaction is given by the nernst equation, which calculates the EMF, $E$, of a cell from the change in Gibbs free energy under given operating conditions:

$$E = \frac{\Delta G}{nF} = \frac{\Delta G_0}{nF} + \frac{RT}{nF} ln \left( \frac{[\prod a_{reactants}}{\prod a_{products}} \right), \tag{2.1}$$

where a is the activity of each species given by an activity coefficient times species concentration, n is the number of participating electrons, and F is Faraday's constant. Because activity coefficients are unity at low concentrations (as in the case of a gas), activities may be replaced by concentrations. For the balanced fuel cell reaction of hydrogen and oxygen to form water, then, Eq. 2.1 becomes

$$E = \frac{\Delta G_0}{nF} + \frac{RT}{nF} ln \left( \frac{[O_2]^{1/2}[H_2]}{[H_2O]} \right) \tag{2.2}$$

For the $CsH_2PO_4$ system, operating at 230 °C in humid (0.33 atm $pH_2O$)hydrogen and oxygen, the theoretical open-circuit potential is approximately 1.123 V.

## 2.2 Definition of Overpotentials

At equilibrium, the theoretical external potential of the electrochemical cell is defined by the chemical potential gradient across the electrolyte. The internal potential of the electrolyte, however, is not single-valued and in liquid electrolyte systems, is described by the local concentrations of ions through the electrolyte. As fuel cell electrolytes generally only carry a single charge (considered protons for this discussion), at equilibrium under an external chemical potential gradient, the protons will migrate from the anode to the cathode. As electrons cannot pass through the electrolyte, charge accumulates at the interface, forming an electrical double layer (often termed the Gouy-Chapman double layer) at the interface. This junction potential of electrons on the metal surface and protons in the electrolyte near the metal increases as more protons enter the electrolyte from the anode, which decreases the driving force for incorporation, until the electrical potential of the junction equals the chemical driving force and the interface equilibrates. Conversely, at the cathode of this

example, protons are depleted from the electrolyte layer near the metal, and electrons within the cathode are depleted, creating a charged double-layer of opposite sign. The potential difference between electrode and electrolyte is known as the equilibrium potential difference and is, simply put, unknowable as a reference electrode cannot be introduced into the electrolyte without developing its own junction potential. As a consequence, electrode potentials are generally considered as relative to a reference electrode with a known, albeit arbitrary, potential. Conveniently, the equilibrium potential of the standard (or normal) hydrogen electrode is defined as zero at any temperature.

$$H \rightarrow e^- + H^+ \qquad \equiv 0V \tag{2.3}$$

Thus, each electrode has a defined equilibrium potential ($\epsilon_0$, under defined environmental conditions, which is a consequence solely of thermodynamics. When current flows (from driving or drawing), however, the electrode potential is necessarily modified in order to drive the electrode reaction at the rate dictated by the current density. As a consequence, the operating potential of the anode is always more positive than its equilibrium value and the operating potential of the cathode is always more negative than its equilibrium value. This difference is termed the reaction overpotential $\eta = \epsilon - \epsilon_0$(7); and as fuel cell efficiency varies directly with cell voltage, $\eta$ is a direct measure of fuel cell inefficiencies.

While any and all deviations from the half-cell's thermodynamically predicted voltage are lumped together as overpotentials, there are three functionally distinct types of overpotentials governing electrodes:

- Activation Overpotential
- Concentration Overpotential
- Resistance Overpotential

Activation Overpotential, $\eta_{CT}$ is the deviation from equilibrium needed to produce a current. Also termed the polarization overpotential, it is derived in the appendix and is described by the Butler-Volmer equation. In the symmetric expression

$$j = j_0 \left( e^{\frac{nF\alpha}{RT}\eta} - e^{-\frac{nF(1-\alpha)}{RT}\eta} \right) \tag{2.4}$$

Though termed a symmetric expression based on putative reversibility, it should be noted that for $\alpha \neq 0.5$, this expression can result in asymmetric $j - \eta$ characteristics. In the most general, asymmetric reaction case, the Butler-Volmer equation can be modified to treat each current direction distinctly.

$$j = j_{0,a} e^{\frac{nF\alpha_a}{RT}\eta} - j_{0,c} e^{-\frac{nF\alpha_c}{R_c T}\eta} \tag{2.5}$$

Where $j_0$ is the exchange current density, $n$ is the number of electrons involved in a process, $\alpha$ is the exchange coefficient, $T$ is the temperature in Kelvin, R is the Rydberg gas constant, and $F$ is Faraday's constant. The subscripts $a$ and $c$ represent the anodic and cathodic directions respectively.

At high polarizations, one of the two terms of the Butler-Volmer expression approaches zero, yielding the Tafel equation, an empirically derived anachronism still commonly used today

$$\eta = A \times ln\left(\frac{j}{j_0}\right) \qquad where\ A = \frac{RT}{nF\alpha_a} \tag{2.6}$$

At times, Tafel slopes, $A$, are described in terms of "mV/dec". This, of course, merely modifies $A$ by Napier's constant, $e$.

Concentration overpotential $\eta_{MT}$ is also known as mass-transport overpotential or diffusional overpotential. Nomenclature aside, it is the deviation from equilibrium potential caused by depletion of charge-carrying reactants and the accumulation of products. While the reactants are considered "charge-carrying", neutral, participating molecules are considered as well.

The mass transport overpotential includes migration and diffusion of charge-carrying species. $\eta_{MT}$ for 1-dimensional Fickian diffusion is derived as a function of current density

$$\eta = \frac{RT}{nF} ln\left(1 - \frac{j}{j_{lim}}\right) \tag{2.7}$$

where $j_{lim}$ is the limiting current density, corresponding to a maximum concentration gradient of reactants.

Lastly, Resistance overpotential is broadly defined and describes all ohmic drops within the cell - including ion diffusion and junction potentials. It is treated here simply as an ohmic loss $R_S$, primarily informed by ionic diffusion resistance within the electrolyte.

## 2.3 Two-probe d.c. under chemical potential gradient

Taken together, the observed cell potential under a chemical gradient is defined as

$$V = V_0 - jR_S - \eta_{CT}(j) - \eta_{MT}(j) \tag{2.8}$$

As a function of current, the cell voltage is shown in figure 2.1 showing (a) the theoretical potential, (b) including activation losses (from the Tafel expression), (c) also including ohmic resistance, and (d) showing contributions from all the components of equation 2.8.

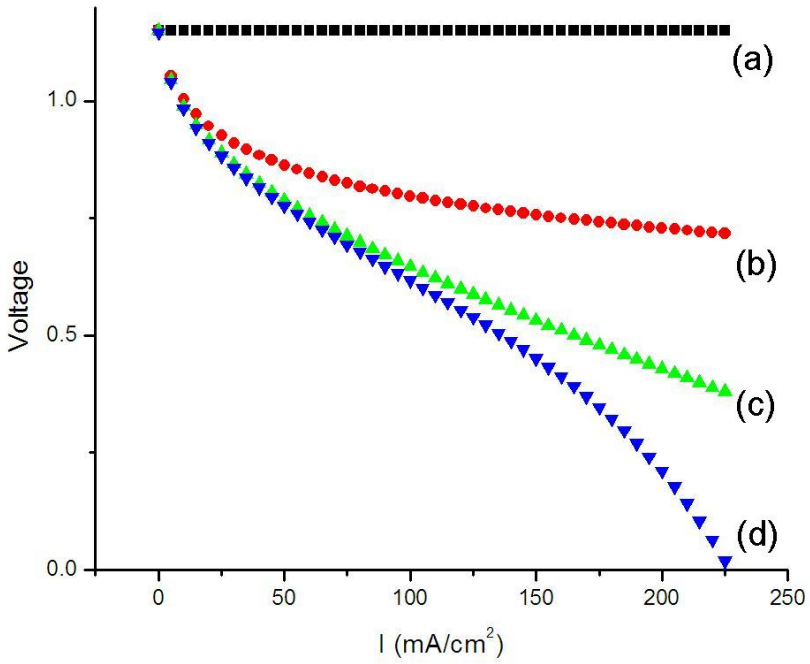


Figure 2.1: Three general forms of energy loss during fuel cell operation. Trace (d) represents a theoretical polarization curve of a thermodynamic voltage modified by ohmic, activation, and mass diffusion losses.

Every fuel cell is composed of two electrodes, however, therefore a more rigorous expression of the cell voltage separates contributions and directions from the anode and cathode. Using the convention that positive overpotentials are termed "anodic" while negative overpotentials are termed "cathodic" - regardless of which electrode is involved, we can also define "forward"(f) and "reverse"(r) reaction directions as those which are spontaneous. That is, the positive electrode (anode, a) experiences anodic current, while the negative

electrode (cathode, c) experience cathodic current. Under spontaneous current,

$$V = V_0 - j\sum R_S - \eta_{CT,af}(j) - \eta_{CT,cf}(j) - \eta_{MT,af}(j) - \eta_{MT,cf}(j) \tag{2.9}$$

Given the number of informing variables, d.c. measurements under potential gradient are valuable for assessing overall fuel cell performance (power density, P=jV, being directly calculable from the $j - V$ curves) but less useful for fundamental explication of individual overpotentials. The experimental exigencies involved in obtaining "perfect" seals (necessary to avoid polluting the measured overpotentials with non-ideal equilibrium potentials), is near prohibitive. Experimentally, "perfect" seals are defined functionally: attained when the measured cell potential equals the theoretical open circuit potential derived from the change in Gibbs free energy.

## 2.4 Two-probe d.c. under no chemical potential gradient

An excellent approach to exactly controlling the chemical potential gradient across a cell's electrodes is to eliminate it. By removing the chemical potential gradient, the cell potential is defined only by the sums of overpotentials, though there is now no defined anode or cathode, so the electrodes, 1 and 2, each may experience forward (f) and reverse (r) reactions. Equation 2.9 then becomes

$$V = j\sum R_S \quad +\eta_{CT,1f}(j) + \eta_{CT,1r}(j) + \eta_{CT,2f}(j) + \eta_{CT,2r}(j) \tag{2.10}$$

$$+\eta_{MT,1f}(j) + \eta_{MT,1r}(j) + \eta_{MT,2f}(j) + \eta_{MT,2r}(j) \tag{2.11}$$

While the sealing issues have been eliminated, analysis does not intrinsically become any simpler. If the cell electrodes are identical however, eq 2.11 reduces to

$$V = j\sum R_S + \eta_{CT,1f}(j) + \eta_{CT,1r}(j) + \eta_{MT,1f}(j) + \eta_{MT,1r}(j) \tag{2.12}$$

While charge transfer overpotential and mass transport overpotentials have very different current density dependencies and the $j - V$ curves could be potentially be fit to

separate them, the difficulty that presents itself, even in this simplified form, is that the forward and backwards reactions of a given electrode are inextricably summed. Given the potential asymmetry of the Butler-Volmer equation, for example, accurate description of electrode overpotentials requires isolating its directional kinetics.

$$H_2 \underset{rev}{\overset{for}{\rightleftarrows}} 2H^+ + 2e^- \tag{2.13}$$

For example, fuel cell investigations are concerned primarily with the forward reaction of Eq 4.4, as hydrogen is oxidized under fuel cell operating conditions. In two-probe conditions under a symmetric environment, when hydrogen oxidation is occurring at one electrode, reduction is necessarily occurring at the other one.

Fortunately, more sophisticated methods of electrochemical analysis have been developed prior to this work. By introducing time as a variable, all electrode processes with distinct characteristic frequencies can be clearly distinguished. Separating the forward and reverse reactions of a given electrode is more experimentally complicated, however, and is often attempted by including a third electrode as a reference.

## 2.5 Reference electrodes

At this juncture is may be helpful to introduce the perspective of the equivalent circuit. Due to the capacitative nature of chemical interfaces, it is common to conceptualize a standard cell as an equivalent circuit in order to discern the sources of voltage loss at a given current. A schematic of a three-element circuit representing two electrodes separated by an electrolyte is shown in figure 2.2a. Including chemical capacitance of electrode-electrolyte interfaces yields 2.2b and demonstrates a challenge of two-point measurements - namely that a current that passes through both electrodes will develop overpotentials at each. Measuring voltage from the same electrodes will always combine the contributions of both.

By introducing a reference electrode, however, current can pass through one electrode and as long as the equilibrium electrode potential of the reference electrode is undisturbed, it can theoretically measure the relative change in potential from equilibrium - that is to say, it can measure the overpotential of a single electrode.

Details being comfortable homes for devils, the conditional regarding the undisturbed

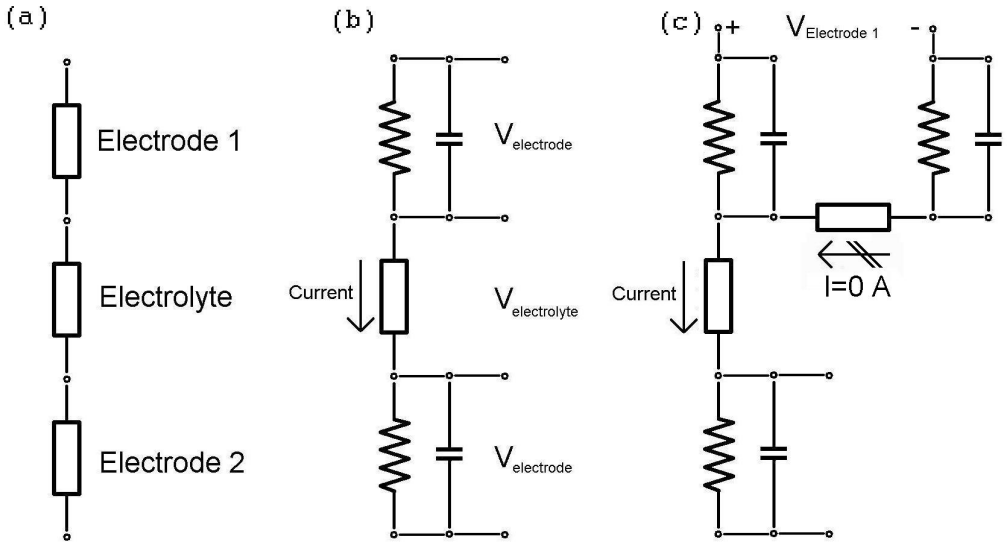


Figure 2.2: Electrode-electrolyte assembly schematically represented as an equivalent circuit. (a) basic three elements in series, (b) including chemical capacitance, and (c) with the inclusion of a reference electrode.

equilibrium electrode potential is often complicated to achieve - particularly for solid electrolytes which have limited options in terms of reference electrode placement. The ideal geometry was calculated to be the geometry shown in figure 2.3. (8)

This cell is so complex because for an accurate reference electrode measurement,the potential within the electrolyte must be single-valued at the reference electrode (hence its small size), equipotential lines must be near-parallel (hence the radial placement), and the ohmic resistance must be as low as possible (hence the proximity to the working electrode). The external ridges shown in figure 2.3 are a consequence of shaping the potential within the electrolyte. Naturally, such geometries are prohibitive to implement, so less accurate geometries are commonly employed, despite a significant body of literature describing why they shouldn't be. [ (9)(10)]

However, if reference electrodes can be accurately implemented, Eq. 2.11 becomes much more tractable

$$V = j \sum R_S + \eta_{CT,1}(j) + \eta_{MT,1}(j) \tag{2.14}$$

The additional ohmic resistance is folded into the summed $R_S$ terms and while modeling, combined with multiple reference electrodes can provide insight into the equipotential distribution, and therefore the ohmic resistance, a more approachable method is to introduce

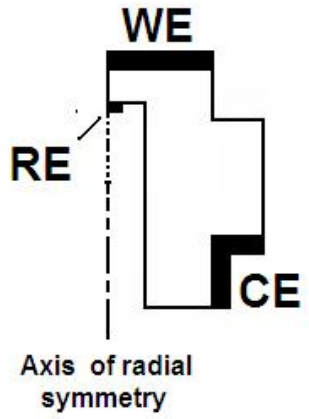


Figure 2.3: Mathematically determined ideal reference electrode geometry is similar to the shape of a cup with the working electrode on the bottom, the reference electrode as small as possible on the radial axis directly opposite to the working electrode and the counter electrode on the rim.

time as a variable as mentioned earlier.

This is suitable in any case, as DC methods are still not very sensitive to discerning different processes - especially if qualitatively similar or if only weakly non-linear.

## 2.6 Electrochemical Testing Methods

This work investigated electrodes with three primary electrochemical characterization methods: cyclic voltammetry, galvanostatic current interrupt, alternating current impedance spectroscopy. All three provide different routes to probe the relationship between current and voltage - and to separate the contributions of each process to the total overpotential.

### 2.6.1 Cyclic Voltammetry (CV)

Cyclic voltammetry is a well-utilized technique for characterizing electrodes for polymer electrolyte membrane fuel cells. Careful control of scan speed and experimental construction enable the acquisition of invaluable information regarding electroactive species in solution or on the electrode surface. Given the solid-solid-gas interface of investigated systems, however, there is often little in the way of identifiable peaks, save only the reduction and oxidation of the catalyst material in oxygen. Cyclic voltammetry at varying scan rates does provide insight into capacitive voltage relaxations, but such characteristics are more facilely

investigated with other methods.

For that reason, cyclic voltammetry was most often conducted in the low scan-rate limit (less than 10 mV/s) in order to reduce the capacitive hysteresis seen at higher scan rates. When cycling in the slow scan-rate limit between the thermodynamic equilibrium values of a fuel cell's half-cells (between the Nernst Voltage and zero volts), each leg of the cyclic voltammogram yields the same steady state current as a function of voltage and is also known as a polarization curve. The most basic electrochemical characterization tool, a polarization curve simply begins at zero current, then draws current with increasing magnitude until the voltage between electrodes equals zero. With sufficiently slow scan speeds, polarization curves depict the steady-state I-V characteristics seen in figure 2.1(d). As such, it is difficult to separate polarization curves into its distinct component contributions, but polarization curves give the most accurate picture of actual fuel cell capabilities, including peak power density and short-circuit current. Fitting the result to the various losses is not impossible, of course, but higher accuracy methods exist.

### 2.6.2 Galvanostatic Current Interrupt (GCI)

One such method attempts to exploit the vastly different characteristic frequencies of each process. Ohmic losses are considered to have essentially infinite characteristic frequencies (and therefore relaxation times of zero), while electrode processes are much slower . A time dependent method, such as GCI, attempts to identify the voltage associated with each process at a given current by instantaneously interrupting the current (hence the name) and measure the subsequent voltage evolution with time [(11)(12)]. For the theoretical cell, figure 2.4(a) shows a sample graph of measured voltage vs time after interrupting a 100 $mA/cm^2$ current. The initial voltage is a constant and is informed by ohmic and kinetic overpotentials. These two overpotentials, indistinguishable at steady-state, can be resolved as the voltage contribution from an ohmic resistance relaxes instantaneously. The remaining voltage relaxation may be attributed to the remaining overpotentials. The initial current can be varied, and the measurements depicted in figure 2.4(a) repeated and the results compiled into a graph of the form presented in figure 2.4(b). In this manner, GCI may distinguish between ohmic losses and electrode losses. It should be noted, additionally, that a number of processes may be co-limiting. In this case, GCI may still be used, but the exponential decay following the initial drop will be multiple-order. If the characteristic

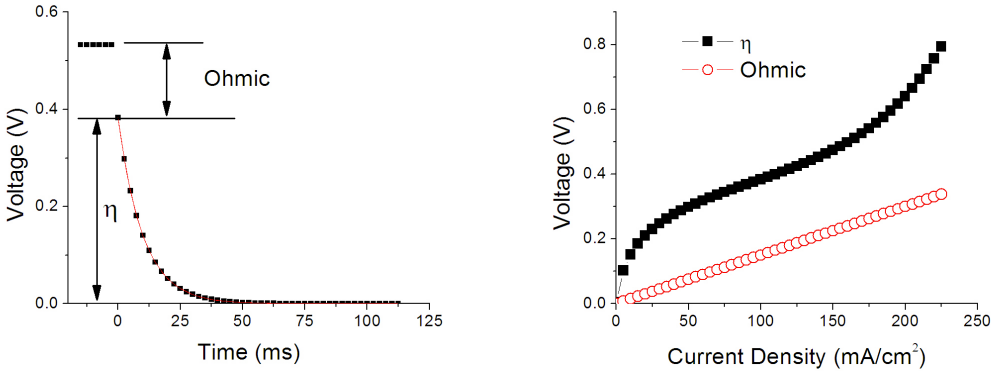


(a) Sample GCI scan showing a steady state voltage at 100 mA/cm$^2$, followed by the interruption of current at t=0 s. The immediate drop corresponds to ohmic losses at this current while the exponential decay corresponds to losses in the electrode.

(b) Compiled results for the theoretical cell's ohmic and overpotential losses through the tested current range.

Figure 2.4: Example of how GCI might be used to separate the theoretical cell's ohmic losses from its electrode overpotentials.

frequencies of each process in the co-limiting regime are similar, it may be difficult to fit a multiple-order exponential decay to the measured data in an accurate manner.

### 2.6.3 Alternating Current Impedance Spectroscopy (ACIS)

For the highest resolution of individual processes, ACIS may be employed [(13)]. ACIS also depends on the differing characteristic frequencies of different processes in order to identify the contribution of each to the total impedances - and therefore losses. However, instead of being resolved in the time domain like GCI, ACIS is resolved in the frequency domain. By inputting an oscillating frequency of small amplitude and measuring both the gain and phase shift of the response signal, ACIS measures the complex impedance for any given input frequency. By scanning a wide range of frequencies, parametric plots of imaginary impedance (Z") vs real impedance (Z') can be obtained. These parametric plots are known as Nyquist plots and are a powerful way of visualizing a system's impedance. Figure 2.5 depicts how ACIS might be used to probe our theoretical cell (eq 2.8), whose $j$-$V$ behavior is depicted in figure 2.5(a). A small amplitude voltage oscillation is introduced around a given bias and the resulting current amplitude and phase shift are recorded. By changing the bias, we probe a different linear regime of the overall $j - \eta$ behavior of the cell. Nyquist plots for the zero-bias (zero-current) and for the biased impedance plots are shown in figure

2.5(b).

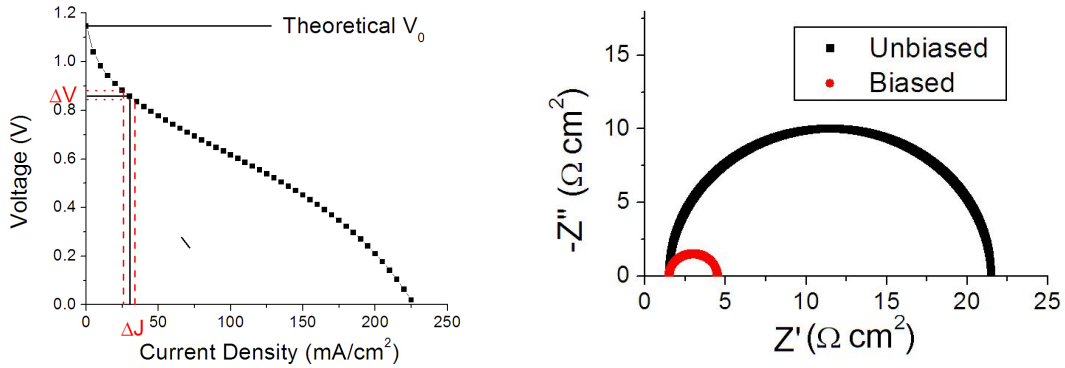


(a) Polarization curve after figure 2.2d, showing linear excursions in voltage and current density at a -240 mV bias, corresponding to 30 mA/cm$^2$.

(b) Nyquist representation of ACIS measurements at at open circuit, and at the -240 mV bias.

Figure 2.5: Example of how ACIS might be implemented with bias to probe the linear regime of the theoretical cell's $j - V$ relation with sample Nyquist plots for unbiased and biased impedance measurements.

The biased scan shows a decrease in total resistance, corresponding to the decrease in electrode $\frac{\Delta\eta}{\Delta j}$ at bias while ohmic resistance remains constant. In this manner, ACIS may identify the impedances of each process at a given bias.

While a plot of a particular process's impedance at different biases can be integrated to describe the sort of $j - \eta$ characteristics that may be more familiar, it is more prudent and simpler to differentiate the response of a likely mechanism to obtain the steady-state resistance as a function of bias. A detailed derivation may be found in Appendix A, but the resulting resistance vs bias curves are presented here in figure 2.6.

### 2.6.4 Equivalent circuits

While the approaches of each testing method have been presented, the explanation behind each method's time (or frequency) dependent measurements has yet to be discussed. An empirical approach to fitting a cell's electrochemical response is to postulate an equivalent circuit element for each process. Solutions obtained in this manner, however, are non-unique - which can create complications when trying to obtain mechanisms from equivalent circuits. A more accurate approach is to begin with a postulated mechanism, then rigorously obtain the complex response of each element, and attempt to fit the data with the model.

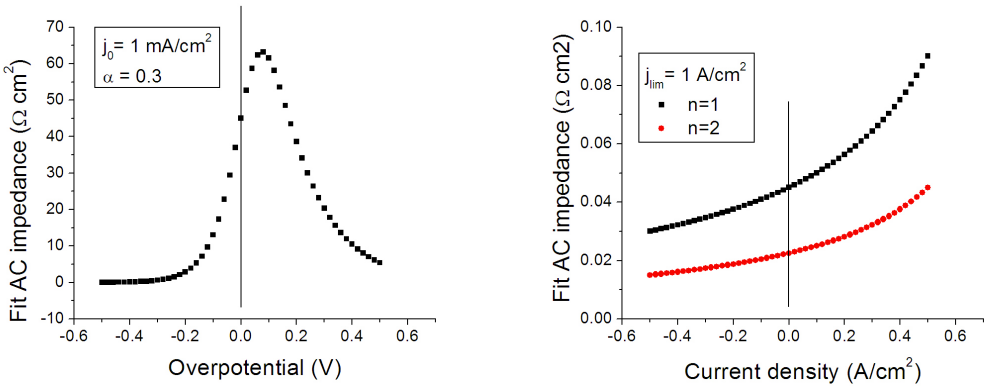


(a) Impedance vs $h$ for a charge transfer step that obeys Butler-Volmer behavior with an $\alpha = 0.3$. Note that near equilibrium, impedance briefly increases with positive bias.

(b) Impedance vs $j$ for a mass-diffusion step that obeys 1-dimensional Fickian diffusion for n values of 1 and 2. Note that while both increase, the two cases cannot be mapped to one another, allowing a probe of electrons per diffusing species.

Figure 2.6: Theoretical resistance vs bias curves for a charge transfer step and for a mass-diffusion step as derived in Appendix A.

An excellent investigation into the complexities and insight of this approach was described by Maier (14)(15) and implemeted by Lai (16) for mixed ionic-electronic conductors. For a purely ionic conductor, the treatment becomes significantly simpler, often reducing to equivalent circuits on the order of the one depicted in figure 2.7.

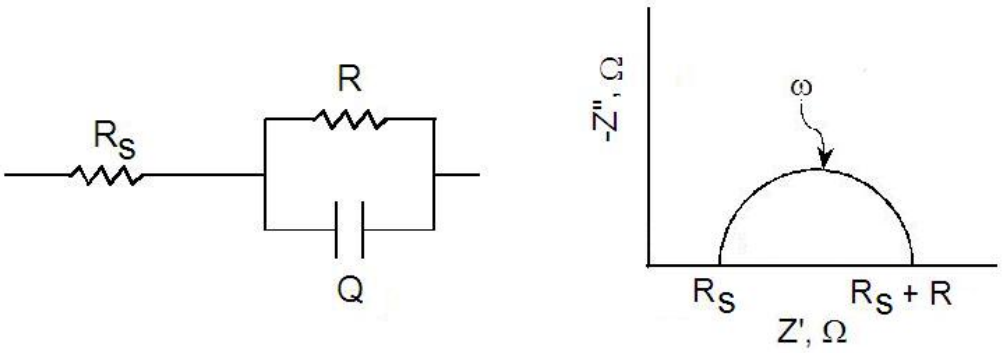


Figure 2.7: Electrolyte-Electrode equivalent circuit of form R(RQ) (left) with corresponding Nyquist plot (right).

Shown also is the Nyquist representation of the equivalent circuit. As expected, at high frequencies, the total impedance approaches that of the series resistor, $R_s$, while at low frequency, the total impedance approaches the sum of $R_s$ and R. The element Q is a constant phase-element, similar to a capacitor, but with a degree of resistive character with

impedance $Z_Q = A(i \cdot \omega^{-n})$. The shorthand notation for an equivalent circuit of the form in figure 2.7(a) would be R(RQ). The parenthetical notation denotes parallel elements.

Mathematically, the equivalent circuit elements can be treated in either the time-domain or the frequency-domain. By using the Laplace transform to represent circuit elements in frequency-space, however, modelling the equivalent circuits becomes significantly more facile. The time-dependent and frequency-dependent responses of basic circuit elements are stated in table 2.1.

| Element | Time-domain | Frequency domain |
|---|---|---|
| Resistor (R) | $\Delta V(t) = R\Delta I(t)$ | $Z(i\omega) = R$ |
| Capacitor (C) | $\Delta I(t) = C\frac{d\Delta V(t)}{dt}$ | $Z(i\omega) = \frac{1}{i\omega C}$ |
| Inductor (L) | $\Delta V(t) = L\frac{d\Delta I(t)}{dt}$ | $Z(i\omega) = i\omega L$ |

Table 2.1: Table summarizing the time and frequency response of simple circuit elements.

Impedances in frequency space can then be combined to describe complicated circuits in a straightforward manner. In this work, an empirical fitting approach was used to determine process resistances, which were then analyzed to investigate the nature of each identified step. Impedance data was fit to equivalent circuits with either the program ZView, by Scribner and Associates, or with proprietary Autolab GPES software.

### 2.6.5 Interchangeability

Because the analysis of both GCI and ACIS data is based on the equivalent circuit model - whose frequency-dependent responses are simply the laplace transform of their time-dependent responses - both methods can theoretically obtain the same information from a given system. [(17)] To confirm, the Autolab was used to probe a test circuit $R_1(R_2C)$ with values defined in table 2.2, the ACIS and GCI results are shown in figure 2.8.

| Element | Nom. value | ACIS fitting | ACIS error % | GCI Fitting | GCI error % |
|---|---|---|---|---|---|
| $R_S$ ($k\Omega$) | 10.1 | 10.05 | 0.5 | 12.792 | 26.7 |
| R ($M\Omega$) | 1.0 | 1.001 | 0.1 | 0.987 | 1.3 |
| C (nF) | 1000 | 1017 | 1.7 | 1015 | 1.5 |

Table 2.2: Table summarizing the results of test circuit of the form $R_S$(RQ), analyzed by zero-bias ACIS and by GCI. Listed errors are internally calculated measurement uncertainty.

As can be seen, both methods are able to correctly apportion the impedance contributions of $R_S$ and $R_P$, as well as determine the capacitance of the element in parallel with

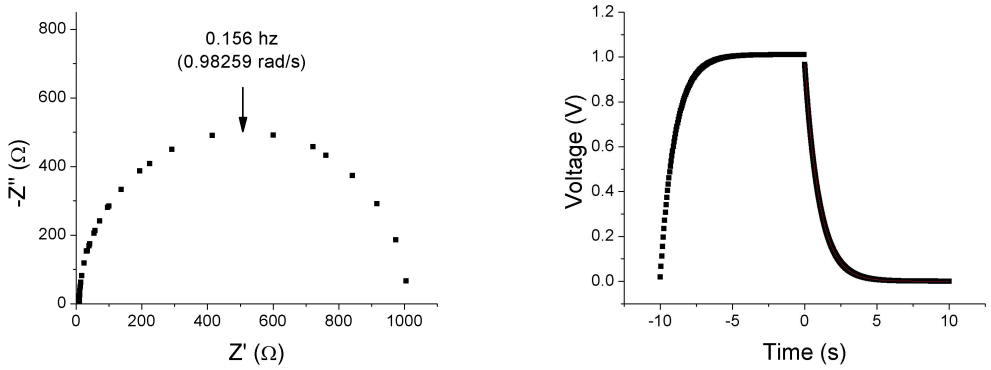


(a) Test Circuit measured by ACIS.

(b) Test Circuit measured by GCI at 1 $\mu$A.

Figure 2.8: Results of measuring a test circuit with both ACIS and GCI to identify circuit resistances.

$R_P$. The fit from ACIS is more accurate, however; particularly in quantifying the ohmic resistance, $R_S$.

### 2.6.6 Overview of methods

Fuel cells are often viewed as a monolithic subject of inquiry, but the two major systems, PEMFCs and SOFCs are exceptionally disparate. While PEMFCs tend to have simpler interfaces, being composed of pure ionic conductors, the rate limiting mechanisms are highly non-linear and require kinetic studies to elucidate. These kinetic studies are strongly enabled by liquid electrolytes which ease requirements for reference electrode placement. On the other hand, SOFCs rate limiting processes are highly linear, resulting in kinetic studies having less utility.

Studying solid acid fuel cells, however, is challenged by both restrictions - non-linear rate limiting mechanisms as well as a solid electrolyte to complicate the application of reference electrodes. Standard approaches, then, of each area of inquiry are utilized - as well as methods which are nonstandard for either.

Cyclic Voltammetry, Alternating Current Impedance Spectroscopy (with a bias), and Galvanostatic Current Interrupt each contain a steady state DC-limit which is necessarily uniform across each. Which method is optimal, however, will depend on experimental exigencies.(7)(18)(19)

## 2.7 New approach: referenceless geometry

As stated earlier, two-point measurements of a cell will invariably measure the response of both electrodes. The difficulties in implementing the reference electrode, however, motivated the development of an alternate geometry. As described in greater detail in chapter 5, by constricting one electrode to a very small area, the overpotential at the other electrode becomes vanishingly small. This asymmetric geometry requires careful treatment, but has been developed to allow similar kinetic isolation to reference electrode studies - but with significantly less demanding fabrication constraints.

# Chapter 3

# Experimental Methods

## 3.1 General Fuel Cell Design

To satisfy fuel cell requirements (transport of ions, electrons, and gas to each side, mechanical stability, and well-separated electrodes), while attempting to optimize performance, a multi-layer assembly was adopted wherein a porous, electrically conductive gas-diffusion layer provides electron and gas access to a composite electrode mixture pressed against the electrolyte layer. This three-component half-cell is mirrored, creating a membrane electrode assembly that satisfies all of the above requirements. If the electrolyte layer is thick, the cell can be considered to be "electrolyte-supported" and the other components need not be selected for their mechanical strength. A thick electrolyte results in high ohmic resistance, however, and an "electrode-supported" design requires thick electrodes which increases catalyst loading and reduce gas access to and from the electrode-electrolyte interface. A third option is to support the electrode layer with a porous and electrically conductive gas diffusion layer with high mechanical strength. The cells tested in this work were either electrolyte-supported with toray paper electrode supports, or were supported by porous stainless steel gas diffusion layers.

### 3.1.1 Cell Fabrication

While a number of different fabrication sequences are employed, based on the individual exigencies of the experiment and membrane design, the general approach is outlined here:

1. Prepare electrodes by dispersing catalyst mixture on gas diffusion layer

2. Inside the die, disperse powdered electrolyte material over an electrode

3. Lightly tamp down electrolyte

4. OPTIONAL: if sealing for dual chamber application, press this half-cell, remove from die, seal the rim, then reinsert into same die, or one a few microns larger in diameter

5. Invert other electrode and insert into die, pressing against electrolyte

6. Densify the cell within the die through uniaxial cold-pressing

The assembly design is presented in figure 1.1. This assembly was developed by Dr. Uda in 2005 and shows the stacked layer structure present in all symmetric cells tested in this work.

## 3.2 Material synthesis

### 3.2.1 $CsH_2PO_4$ overview

While a wide variety of chemistries exist within the solid acid family, the scope of this research focused almost exclusively on electrode studies with $CsH_2PO_4$ -based electrolytes. A more detailed discussion of investigation into $CsH_2PO_4$ mechanical properties will be presented in chapter 9, but earlier fundamental studies defined a great deal of what is known about $CsH_2PO_4$ . The synthesis approach, the phase transition leading to high conductivity (1E-2 S/cm) at 228 °C , the solubility in water (and insolubility in common organics like ethanol and toluene), as well as reactivity with common oxides such as alumina, were all determined prior to my research, and laid the foundation for my studies of the electrodes of the $CsH_2PO_4$ system. My periodic investigations of a similar solid-acid compound, $CsHSO_4$, were conducted only to provide additional perspectives on method of testing $CsH_2PO_4$ -based systems and are, as such, not included.

### 3.2.2 Coarse $CsH_2PO_4$

Generating the electrolyte material, $CsH_2PO_4$ , was done entirely in-house. Commercial $CsH_2PO_4$ became available, but was not utilized due to the robustness and convenience of in-house synthesis. $CsH_2PO_4$ was generated by reacting phosphoric acid with cesium carbonate, dissolving the resulting $CsH_2PO_4$ in water, then precipitating the $CsH_2PO_4$ with methanol.

This synthesis method gains a great deal of robustness from the fact that both reactants are soluble in methanol. In precipitating the $CsH_2PO_4$ , excess reactants are also, therefore, removed. To remove residual phosphoric acid fully, Ryan Lanman (a Caltech SURF student), determined that after filtering the $CsH_2PO_4$ from the slurry, washing the powder with an additional liter of methanol normalized the pH of the subsequent effluent to the same as that of the DI water. The presence of excess $Cs_2CO_3$ was not investigated, but due to its high solubility in methanol (0.12 g/mL), it is believed that this procedure is effective for removing excess $Cs_2CO_3$ as well - an assumption that is supported by X-ray diffraction (XRD) detecting no impurity phases in synthesized $CsH_2PO_4$ (ICSD code 35-0746). A detailed description of synthesis methods and apparati can be found in Appendix B, while x-ray diffraction investigations are presented in Appendix G.

### 3.2.3 Fine $CsH_2PO_4$

Unlike many solid oxide fuel cell electrolytes, grain boundary resistance in the $CsH_2PO_4$ system is not a detectable contributor to electrolyte impedance. That the electrolyte conductivity is independent of particle size allows a degree of optimization. Specifically, in electrode composites with platinum particle sizes approximately 4 nm in diameter, micron-scale $CsH_2PO_4$ particles restrict the triple-phase density. It is therefore desirable to reduce the $CsH_2PO_4$ particle size. A brief attempt was made to reduce particle size of coarse $CsH_2PO_4$ by milling for 20 minutes with 0.5 cm zirconia balls in toluene. Unfortunately, the $CsH_2PO_4$ clumped around each ball, dissipating the force.

Instead, efforts focused on directly synthesizing sub-micron $CsH_2PO_4$ particles. One high-yield approach uses a solution of $CsH_2PO_4$ saturated in water, then energetically dispersed (and precipitated) into methanol. Synthesizing in this fashion obtains dispersed particle sizes, but barring agglomeration, particles are approximately 1 micron in diameter. Again, a detailed description of this approach is presented in appendix C.3

### 3.2.4 $CsH_2PO_4$ + silica. (AKA "on the rocks"

To synthesize composite electrolyte materials, specifically $CsH_2PO_4$ with silica, the silica, suspended in water, is added to the methanol and is incorporated into the precipitating $CsH_2PO_4$ .

## 3.3 Electrodes and Electrode composites

In order to satisfy the myriad requirements for a high-performance electrode, composite electrodes were characterized - particularly in initial studies so as to recreate losses measured from optimized cells. While the composite components often varied (with the "standard" composite being a quaternary mixture of platinum black (Alfa 12755), fine $CsH_2PO_4$ , 40 wt.% Pt on carbon (Alfa 42204), and naphthalene (Alfa 33347) in a 3:3:1:1 ratio by weight), the synthesis method was maintained for all composites. The procedure:

1. Clean an agate mortar with DI water, acetone, ethanol, and isopropanol with kimwipes.
2. Measure desired mass of fine $CsH_2PO_4$ and non-soluble electrode materials into the mortar.
3. Add an excess of toluene to the mortar and mechanically mix with agate pestle for at least 2 minutes.
4. Dry the composite in a vented oven at 130 °C .
5. OPTIONAL: if a soluble pore-former is used, grind in a clean mortar, then add composite and mechanically mix
6. Filter final particles through a 100 mesh sieve
7. Store in a sealed vial.

While this process is straight-forward, it should be noted that using high pressure on naphthalene in the final step will cause caking of the pore former and therefore only a moderate amount of pressure is recommended.

## 3.4 Cells

Membrane-Electrolyte assemblies are multi-layer constructions consisting of, at minimum, two electrocatalyst-layers contacting the electrolyte on either side. For additional mechanical strength, electrocatalysts are often supported by conducting, porous gas-diffusion layers. A representative cell is shown in figure 1.3.

## 3.5 Sealing

Densification and intrinsic material properties should ideally preclude the possibility of leakage through the cell (be it electrical leakage or gas leakage). To ensure complete isolation of each chamber, then, it is necessary to seal the cell to the test fixture, making good contact to the electrolyte. Additional requirements include stability under operating temperatures and environments, a degree of elasticity to maintain the seal through thermal expansion, and chemical compatibility with all cell components. Three sealing methods were identified: Viton, silicone, and PTFE.

**Viton**

Viton is an air-curing rubber epoxy, and as such, is applied as a viscous liquid before hardening to form a flexible seal with a nominal maximum operating temperature of 200 °C . Fuel cells with viton seals were occasionally capable of high open circuit voltages, approaching 1.05 V.

**Silicone**

Briefly, a silicone was tried as a replacement for viton. Affordable, highly viscous without need for curing and rated to 260 °C , the only drawback was that the tested seals were electrically conductive, making them unsuitable for this application. The potential for identification and application of candidate silicone-based sealants still exists, but was not investigated.

**Polytetrafluoroethylene (PTFE)**

Dr. Zongping, in Prof. Haile's lab identified PTFE as an excellent sealant. Though the nominal operating temperature is also below cell operating temperatures, cells sealed with simple teflon tape reliably achieve 1.05-1.1 volts at open circuit. The flexibility and robustness of PTFE tape as a sealant made it the sealant of choice for all stainless-steel gas diffusion layers. Toray paper proved mechanically too weak for this application - being fractured and delaminated due to shrinkage of the PTFE tape at operating temperatures.

## 3.6 Reference-Electrode Cell Geometries and Fabrication

### 3.6.1 Reference electrode geometries

While the inclusion of a reference electrode is fairly straightforward for systems with liquid electrolytes, reference electrode placement becomes problematic when investigating solid-electrolyte systems. The ideal geometry is diagrammed in figure 2.3.

As it is clearly prohibitive to fabricate cells with ideal 3-point geometries, a number of radially symmetric alternatives are commonly employed - several of which are diagrammed in figure 3.1

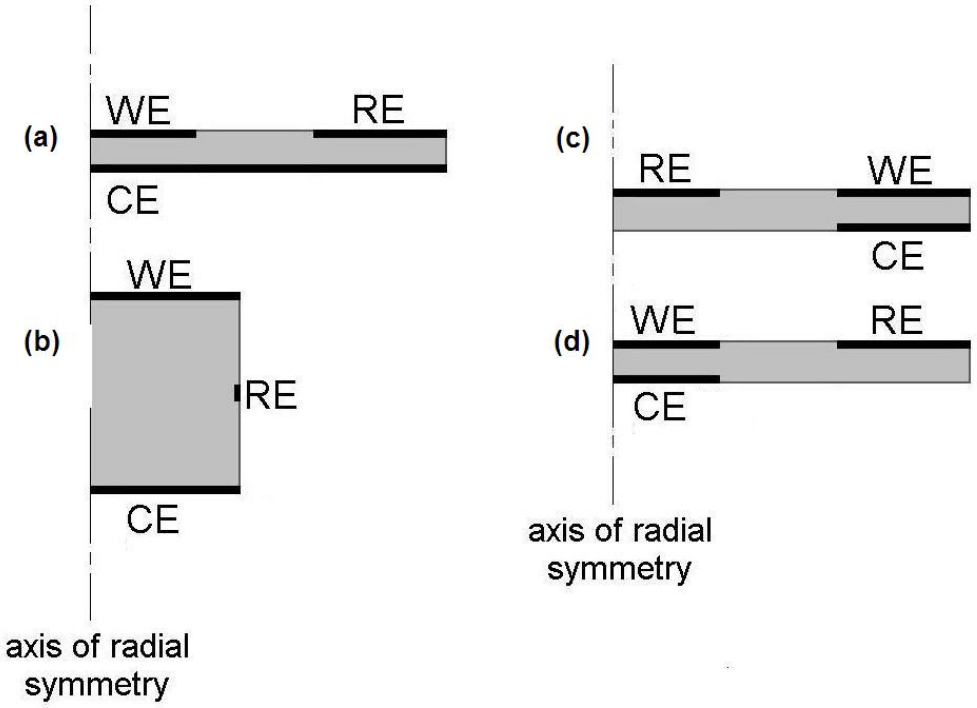


Figure 3.1: Radially symmetric reference electrode configurations potentially suitable for use with solid electrolytes.

It should be noted that while there are 4 distinct geometries presented, each is capable of at least one additional configuration. for instance, in figure 3.1(a), switching the counter and reference electrode designations allows the reference electrode to be close to the working electrode. Each of these configurations were tested, though only the geometries shown in figure 3.1(b) and (d) are presented. Geometries of this form are presented in figure 3.2.

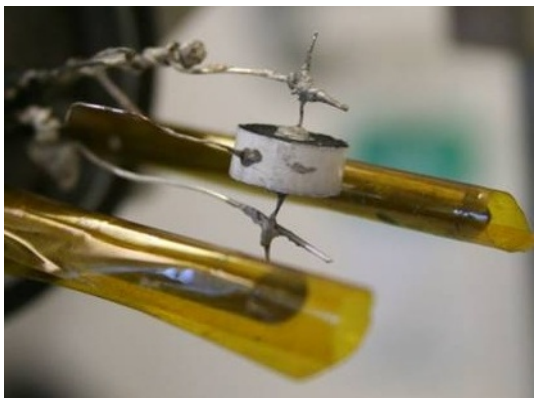

(a) Photograph of a thick referenced geometry cell after Fig. 3.1(b) with silver paint as a reference electrode.

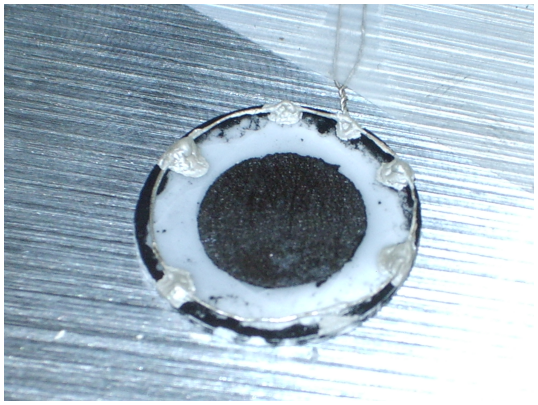

(b) Photograph of a thin referenced geometry cell after Fig. 3.1(d) with Pt mixture as a reference electrode, contacted with silver paint.

Figure 3.2: Sample three-point geometry cells.

## 3.7 Cell holders

Due to the wide variety of cell geometries and requirements, a number of test fixtures were fabricated in-house. For standard geometries, four functionally distinct fixtures were developed - three dual-chamber fixtures and one single-chamber fixture. Three dual-chamber fixtures were necessary to probe the three pressure regimes of interest, crudely categorized as high-pressure, low-pressure, and no-pressure. The single-chamber fixture was modified over time, but the base is flexible enough that it is able to accommodate a variety of cell-holding subassemblies.

### 3.7.1 Dual-chamber fixtures

Initially, low pressure test fixtures, schematically diagrammed in figure 3.3 were employed to acquire polarization curves of operating cells. The fixtures were made of stainless steel 316, though gas lines were stainless steel 304. the gas channels were radially symmetric and accessed with a single port each for gas inlet and exhaust. This allows uniform, radially-directed gas flow fields over the surface of the electrode. Small daubs of silver paint were used to create electrical contact between the cell and the fixture.

In order to investigate the extreme of low pressure, a fixture was designed and constructed that allowed pressurized sealing against an intermediate stress-member - itself a tri-layer structure of stainless steel 316 separated by a non-porous, insulating, machinable

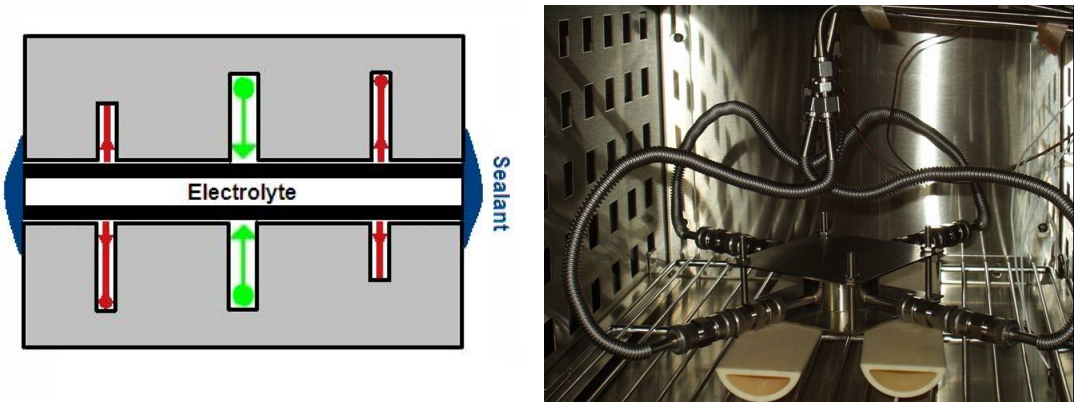


(a) Schematic showing gas inlet (green) and outlet (red), as well as how the cell is sealed (blue) into the test fixture.

(b) Photograph of low-pressure dual-chamber holder loaded into the testing oven.

Figure 3.3: Low-pressure dual-chamber fuel cell holder schematic and photograph.

ceramic called Macor - without pressing on the cell itself. This structure was bored out to create the gas chambers for the cell, then sealed together with viton. Tested cells were sealed into the Macor layer with viton, which was allowed to cure, then silver paint was used to contact each cell electrode to its corresponding steel current collector. The entire subassembly was then contacted with viton sheets on each side and compacted between the gas inlet/exhaust chambers - all within a stainless steel C-clamp.

In this manner, a cell could be tested in dual-chamber mode without being subject to any axial stress. Thermal expansion/contraction of the inner seal can, however, create in-plane stresses on the cell.

Superprotonic Inc. developed a high-pressure holder similar to the low-pressure cell in Fig. 3.3, but capable of higher force and built with tighter tolerances and integral bolts so that the axial force was evenly distributed over the cell. Polyamide layers separated the bolts from one of the holder halves, maintaining electrical isolation between electrodes.

### 3.7.2 Single-chamber holders

To prevent uncertainty in characterization due to imperfect seals, a commonly pursued alternative is to do away with seals entirely and maintain the electrodes in identical chemical environments. Thus, the symmetric chamber is simply a three-ported union with an internal diameter of 1.5 inches. Gas flows in one port, out the second, and the third is used to interpose the cell in the flow. Sealing the symmetric cell is done with metal collar in

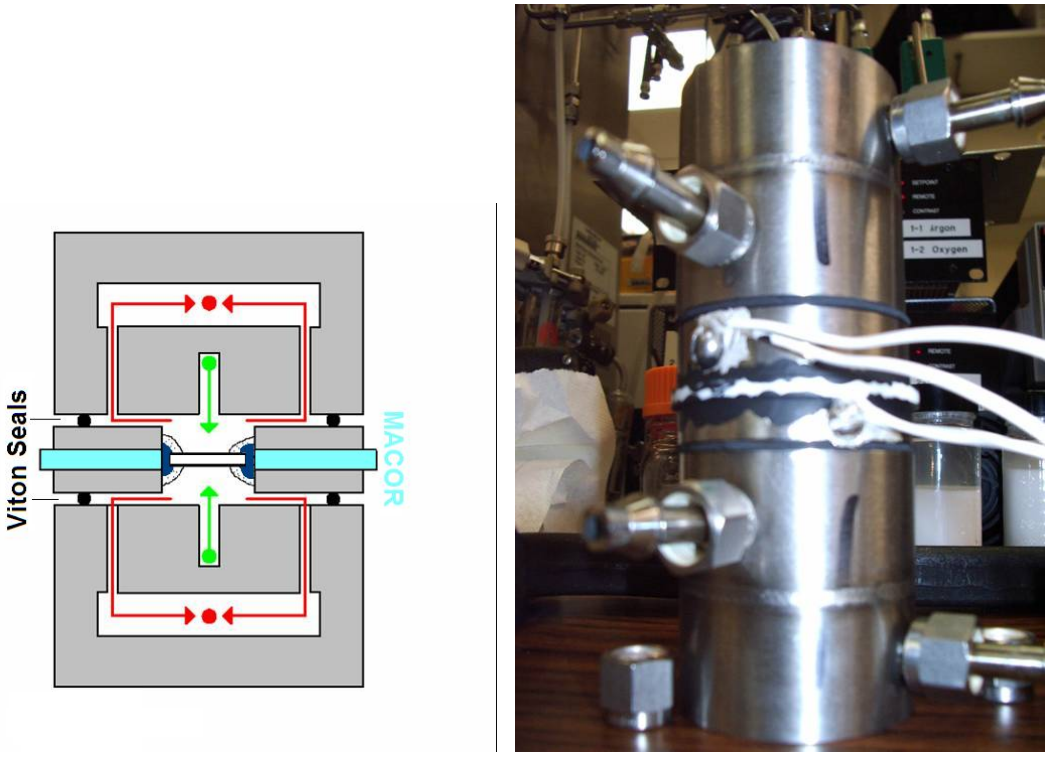


(a) Schematic showing how cell is sealed into a Macor separated subassembly, which is subsequently contacted with gas inlet/exhaust chambers.

(b) Photograph of full pressure-less assembly with seals, gas piping, and electrical contacts.

Figure 3.4: Pressure-less dual-chamber fuel cell holder showing inclusion of sandwiched stress-assembly electrically isolated from gas inlet/exhaust chambers. Pressure is provided via an external C-clamp.

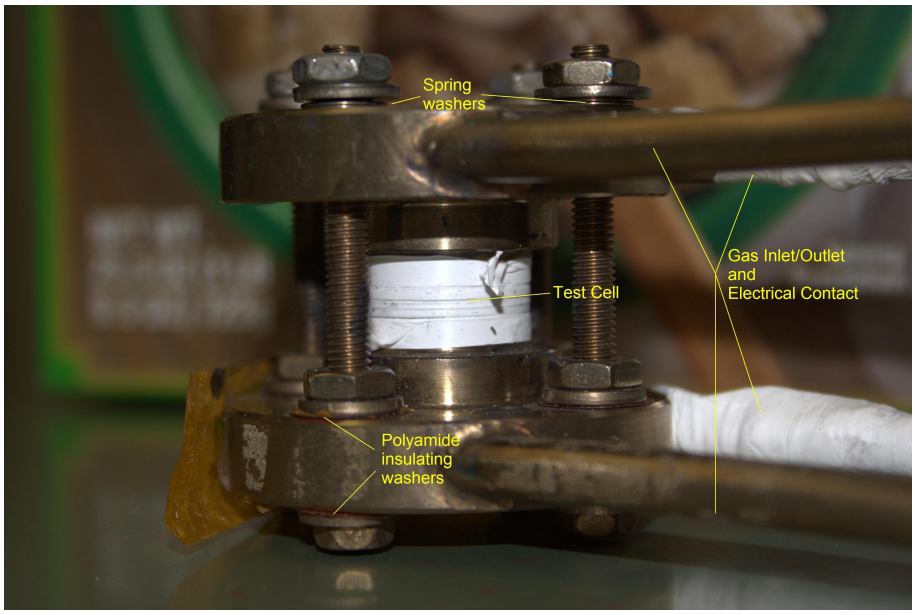


Figure 3.5: Photograph of the high-pressure dual-chamber fuel cell holder. Gas flow schematic is identical to that in figure 3.3(a)

conjunction with a teflon O-ring. While the teflon will deform over time, it can be easily re-wrapped with PTFE tape and maintain excellent seals. The cap itself requires access ports for electrical leads and a thermocouple. This was achieved by threading the desired lines through a quad-core 1/4 inch diameter alumina tube, then sealing with Ceramabond. To improve sealing, solid silver wire was used within the alumina, and contacted to flexible, braided wire on the outside. Because solid wire becomes fragile (and is not replaceable once sealed), especially after multiple temperature cycles, it's very important to include stress-relief lines when connecting the solid wire to an external line. After curing, the alumina tube is fed through a 1/4 inch inner diameter Swagelok ultratorr fitting that has been welded into the cap. This ensures a sealed chamber with temperature sensing and access of electrical leads. Because there are no internal seals, any number of subassemblies can be fitted to this general holder. One such assembly is depicted in figure 3.6 with a three-electrode geometry cell.

This assembly was later modified to allow the gas to have a more symmetric flow field by simply switching the exhaust port and the cell-holder port. A holder for two-electrode cells was developed with Mary Louie of Caltech, and is shown in figure 3.7.

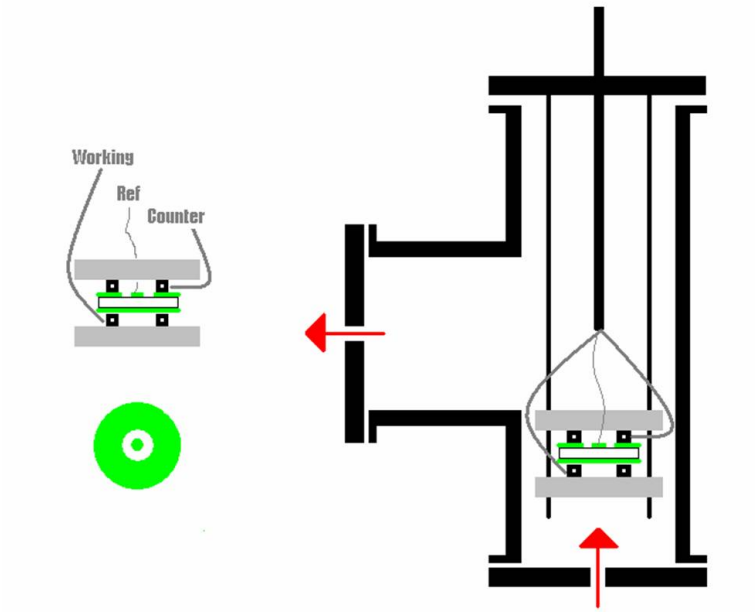


Figure 3.6: Schematic of single-chamber cell holder. This fixture was later modified to accommodate more flexible contacts. Also shown is the method for contacting a modified version of the three-electrode cell depicted in Fig. 3.1(a).

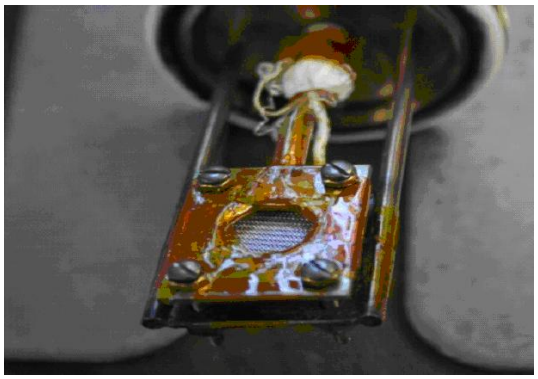

Figure 3.7: Alternate single-chamber cell holder for testing two-electrode cells. Test cell in the fixture is supported with porous stainless steel mesh.

## 3.8 Apparatus Kikue

### 3.8.1 Temperature control

| Component | Model | Quantity |
|---|---|---|
| Primary Oven | Lindberg Blue | 1 |
| Humidification Oven | Barnstead | 1 for Water, 1 for other |
| Temperature Controller | Omega 8200 | 5: 3 ovens, Inlet lines, Outlet Lines |
| Heat rope (silica sheath) | Omega | 1 inlet, 1 outlet |
| K-type Thermocouples | Omega | 2 in Primary Oven, 5 on gas lines |
| R-type Thermocouples | Omega | 2 in water Oven |

### 3.8.2 Gas control and delivery

| Component | Model | Quantity |
|---|---|---|
| Mass Flow Controller | PR4000 | 2 controller units |
| Mass Flow Valve | MKS21212 | 1 $H_2$, 3 Ar/$O_2$ |
| 1/4" SS304 pipe | physical plant | 5 meters |
| Flexible SS304 tubing | swagelok | 4 pieces |
| T Fitting | Swagelok | 4 pieces |
| High-temp valves | Swagelok | 4 pieces |
| Ball valves | Swagelok | 2 pieces |
| Union | Swagelok | 10 pieces |
| Pressure Relief Gauges | Swagelok | 2 pieces |

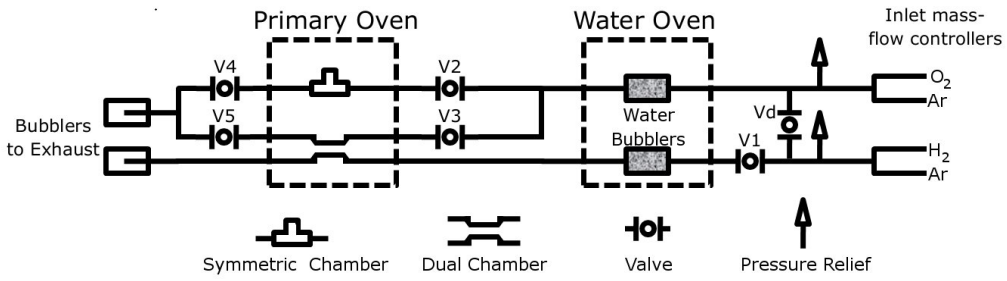


Figure 3.8: Mechanical diagram of fuel cell test station, Kikue

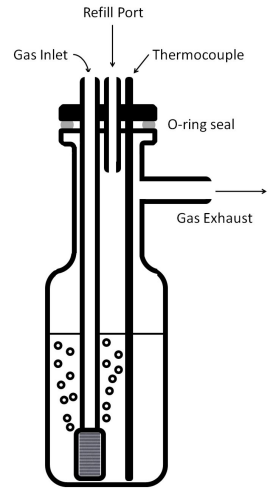


Figure 3.9: Diagram of gas partial-pressure equilibrator. Inlet gas is metered through a porous frit to create small bubbles with high surface area-to-volume in order to equilibrate the vapor-phase concentration of the liquid material in the gas stream.

## 3.9 Electrochemical testing equipment

### 3.9.1 Tektronix Oscilloscope

Data acquisition for GCI was achieved with a Tektronix 2012 oscilloscope. Sampling every 0.1 microseconds, it was suitable for the measuring of lower-frequency transients.

### 3.9.2 Keithley Sourcemeter

Early galvanostatic polarization curves were conducted with a Keithley 2420 sourcemeter capable of delivering up to 2 amperes of constant current at sub-milliampere resolution. Later, the Keithley was used to provide controlled current for GCI experiments, though the internal switch proved too sluggish to interrupt GCI in a clean manner, and the measurements proved somewhat sensitive to the voltage compliance setting - requiring care in implementation. Connection was made through a General Purpose Interface Bus (GPIB) to the primary control PC (Kikue)

### 3.9.3 HP Switching Unit

A Hewlett-Packard 3488A switching unit was also explored in the role of a switch for GCI. Like the Keithley's internal switch, however, it was also too slow. Both devices, in fact,

switched more slowly than interrupting the current by physically disconnecting the wires. The three methods were compared by interrupting a 300 mA current through a nominally 5 Ω resistor, and the resulting voltage measured and presented in figure 3.10.

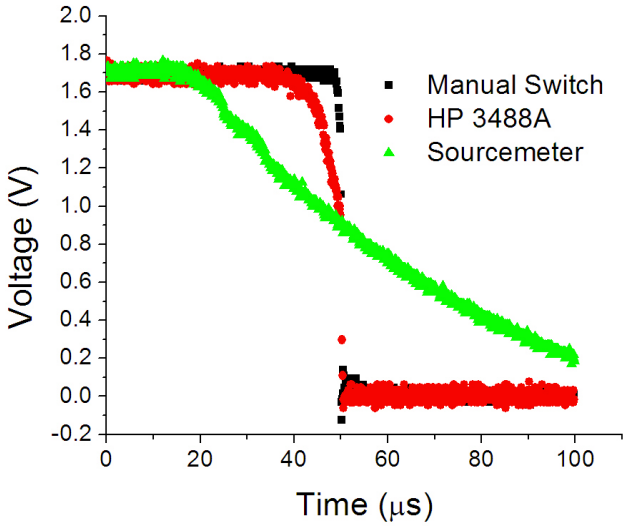


Figure 3.10: Comparison of switch speeds for three approaches shows manually interrupting the circuit is faster and cleaner than either the sourcemeter's internal switch and the HP switching unit.

Later, however, the HP switching unit was employed as a computer-controlled multiplexer, connecting an array of electrodes to the leads of a potentiostat.

### 3.9.4 Blinky

Due to the unsuitability of the three switches depicted in figure 3.10, it was seen as necessary to acquire a fast switching unit for the implementation of the GCI approach. Given the lack of commercial availability, one was designed and built in-house. Based on a simple asynchronous oscillating switch controlling the gate of a MOS-FET, it was named Blinky and while it could not interface with the computer, the on and off times could be tuned with appropriate circuit elements.

This homemade device shows ideal behavior for GCI - namely, stable current before the switch and clean switching on the microsecond scale without being overdamped or underdamped. As such, this device was used in all presented GCI tests.

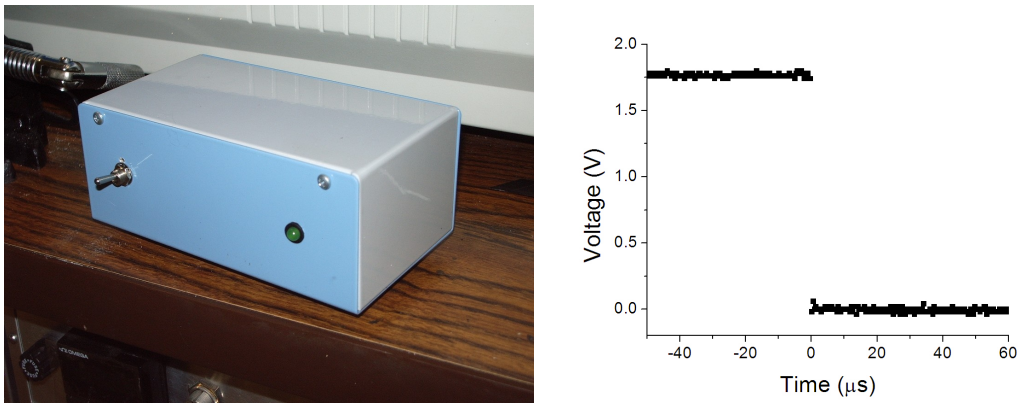


(a) Photograph of "Bimodal Line Interrupt Node (b) GCI tested with nom. 5 Ω resistor at 300 mA. by Kenji Y'all (B.L.I.N.K.Y.)."

Figure 3.11: Homemade GCI switch (left) with resulting test scan after compensating output.

### 3.9.5 Eco Chemie Autolab

In order to implement ACIS testing capability, an Eco Chemie Autolab PGSTAT302 was acquired by Superprotonic Inc. and loaned to the Haile lab pursuant to my research. An integrated electrochemical characterization tool, the Autolab is capable of cyclic voltammetry, impedance spectroscopy with and without bias, and, to a limited extent, Galvanostatic Current Interrupt - though the switching time is significantly slower than can be obtained with blinky. The frequency response analyzer (FRA - synonymous with ACIS) of the autolab is capable of measuring frequencies as high as 1 Mhz and as low as you'd like to wait. Both the amplitude and bias can be defined galvanostatically or potentiostatically. One additional capability of the Autolab, is the ability to test multiple sine-waves simultaneously, specifically the odd-multiples of the base frequency, up to 15 at a time, then using fourier analysis to separate the gain and phase shift of each frequency. This greatly speeds data acquisition - which in turn both saves time and obtains faster snapshots of unstable impedances. The only drawback is that because the frequencies are scaled linearly from the base frequency, the data-point spacing on Nyquist plots is not as uniform as if the frequencies were varied logarithmically. This does not adversely affect the fitting procedure, but may cause consternation in those accustomed to seeing Nyquist plots with evenly spaced points.

The autolab was connected to an independent control computer through a USB line.

Additionally, in order to record accurate temperature concurrently with the electrochemical testing, a K-type thermocouple was connected to one of the autolab's ADC ports and the voltage internally converted to a temperature. Temperature conversion calibrations were confirmed by testing with an independent thermocouple.

### 3.9.6 Autolab-Kikue interface

As it is desirable to automate and synchronize the test environment (controlled by Kikue) with the electrochemical tests (controlled by the autolab computer), a crude but effective connection was fabricated. Hand-splicing a serial cable, the autolab computer was able to send information to Kikue, which maintained an open port, listening for incoming communication. Those commands were then processed by Labview software and used to control temperature, gas flows, and the HP 3488A switching unit. Information flow was one-way, however, as the autolab proprietary software had limited output capability, but no effective ability to receive inputs. Clever use of programmed timing, however, mitigated most of the resulting obstacles.

# Chapter 4

# Characterizing platinum-based electrodes by standard methods.

With the demonstration of high conductivity and stability of the $CsH_2PO_4$ electrolyte, as well as proof of high power densities for platinum-based electrodes (platinum black, fine $CsH_2PO_4$ , 40 wt.% Pt on carbon, and naphthalene ), my research goals included elucidating the nature of electrode losses in this system - investigating both the anode and cathode for activity, longevity, and mechanism. Based on the specific nature of the electrode-electrolyte interface - namely the intermediate temperature between PEMFCs and SOFCs, the proton conductivity of the electrolyte, and the non-solvated gas phase reactants - a suite of standard characterization approaches were adapted from both PEMFCs and SOFCs. Cells were tested by AC methods (with and without bias), steady-state DC methods, and time-resolved DC methods in dual-chamber and single-chamber holders. Cell geometries were primarily symmetric, two-electrode construction, though reference-electrode cells were also tested in order to isolate reaction kinetics.

Early electrode characterization attempts focused on reproducing recent literature which employed platinum black, fine $CsH_2PO_4$ , 40 wt.% Pt on carbon, and naphthalene electrodes, and therefore 4 electrocatalyst mixes were investigated:

- the full quaternary electrode composite (platinum black, fine $CsH_2PO_4$ , 40 wt.% Pt on carbon, and naphthalene ) or 0.425 grams of platinum per gram of mixture
- 40 wt% Pt on C - a more uniform system that retained the same material components
- pure platinum
- a binary composite of platinum mixed with fine-powdered $CsH_2PO_4$ in a 3:7 ratio by

weight

## 4.1 Dual Chamber - two point

For the electrolyte, approximately 300 mg of $CsH_2PO_4$ was used in each case, corresponding to a thickness of 260 microns. Though the cells had a total area of 2.85 $cm^2$, sealing generally restricted the area to approximately 2.2-2.5 $cm^2$. 30 mg of quaternary powder composite comprised each electrode, or 5 milligrams of Pt per $cm^2$ of electrode. This high level of platinum loading was employed in an attempt to maximize electrode performance, mimic literature, and increase the number of data points obtained in a given measurement. Cells were analyzed galvanostatically with a Keithley 2420 sourcemeter measuring voltage as a function of current at current steps of 10 mA. Cell sealing was achieved with Viton for early tests, then PTFE tape later. While Viton-sealed cells were occasionally capable of high open-circuit voltages, PTFE-sealed cells yielded reliably higher OCVs, the record being 1.10 V. The impact of leakage, be it electrical or gas-phase, is such that cells with low open circuit voltages (below 0.9 V) were necessarily excluded from consideration, at a loss of both time and materials. Over 100 cells were tested, each requiring a minimum of 24 hours to fabricate, seal, heat, and cool, let alone test.

### 4.1.1 DC steady state

A typical polarization curve (with power density from $P = jV$ overlaid) is presented in figure 4.1. The shape of the voltage curve - with an upwardly concave curvature at low current densities, followed by a linear relation between voltage and current density - suggests that the primary electrode losses are related to a charge-transfer resistance, and therefore governed by the Butler-Volmer equation. Because there is no detectable inflection at high current densities, it is reasonable to assume that the maximum current density ($I_{sc}$=I(V=0)) is low enough to neglect mass-diffusion losses.

Based on these assumptions - that $CsH_2PO_4$ -electrolyte fuel cells with platinum-based composite electrode mixtures can be kinetically described by their open circuit voltage ($V_0$), charge-transfer electrode losses ($\eta_{CT}$), and ohmic electrolyte losses ($R_S$)- allows the reduction of Eq. 2.8 to Eq. 4.1

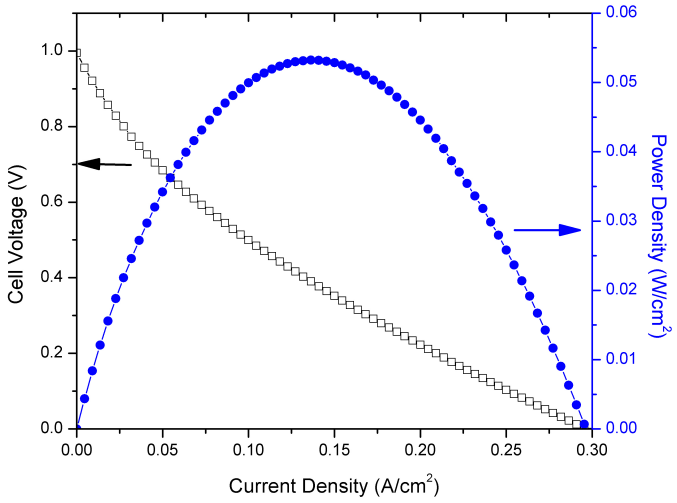


Figure 4.1: Polarization and power density curves of a representative dual-chamber fuel cell composed of Toray-supported quaternary composite electrodes with a $CsH_2PO_4$ electrolyte, operating under humidified (p[$H_2O$] = 0.33 atm) $H_2/O_2$ at 240 °C .

$$V = V_0 - jR_S - \eta_{CT}(j) \tag{4.1}$$

The standard approach of expressing the charge transfer overpotential, $\eta_{CT}$, as Tafel-losses of the form

$$\eta = \frac{RT}{\alpha nF} \times log(\frac{j}{j_0}) \tag{4.2}$$

is crude and anachronistic, but is undertaken here as an overall metric of fuel cell behavior for comparison with other cells in the literature. More mechanistic insights will require a more sophisticated approach, presented later in Chapter 8.

As seen in figure 4.2, fitting the data in this manner results in reasonably good fits when very low current densities are excluded. With this, the exchange current density ($j_0$) and the exchange coefficient ($\alpha$) can be extracted. While the exchange current density results from both intrinsic and extrinsic material properties - which are extremely difficult to quantifiably explicate, the exchange coefficient (and therefore the tafel slope) should result from fundamental material properties only. For this fitting, a relatively large number of cells were generated, but only those with open circuit voltages near theoretical are suitable for fitting, as leakage currents of either form dramatically influence the fit. Figures 4.3 and

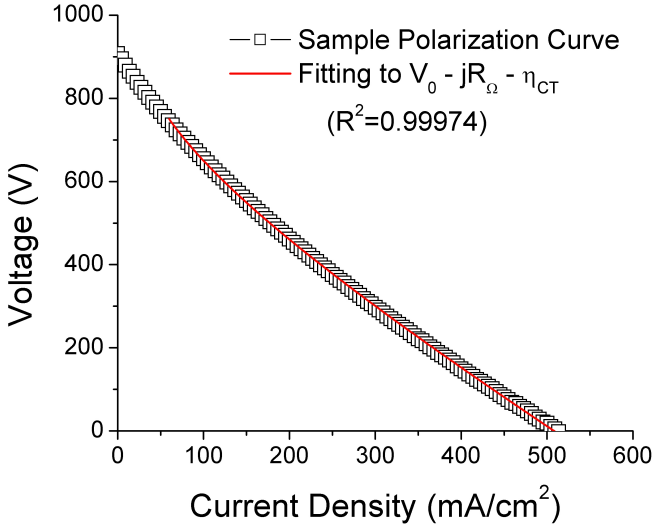


Figure 4.2: Polarization curve and fitting after Eq. 4.1 from a cell prepared and tested identically to the one presented in Fig. 4.1 .

4.4 summarize the fit values for cells with both open circuit voltages greater than 900 mV and ohmic resistances less than 5 ohms. The latter condition is necessitated by accurate fitting requiring a minimum number of data points. Though approximately 100 cells were prepared, only 25 met these criteria and were analyzed.

Given the quaternary powder electrode mixture, it is not unexpected (though still unfortunate) that figure 4.3 shows a wide variation in exchange current densities for the analyzed cells, statistical analysis yields a mean of 1.48 +/- 0.857 mA/cm$^2$.

While the data still contains a significant degree of scatter, it at least provides a range of values for the tafel slopes governing electrode losses during fuel cell operation. By assuming that at a fundamental level, all charge-transfer coefficients are likely one-electron processes (and therefore n=1), the tafel slope can be related back to the exchange coefficient to yield $\alpha$ = (0.417+/- 0.105).

It was considered that instead of simply assuming n=1, the slope of the polarization curve near zero bias could be treated as the low-bias resistance after Appendix B.5.1. By comparing the low-bias electrode resistance, $R_p$, to the fit exchange current density, $I_0$ obtained at high-bias, it might be possible to extract n, as with equation 4.3.

$$n = \frac{RT}{j_0 R_p F} \tag{4.3}$$

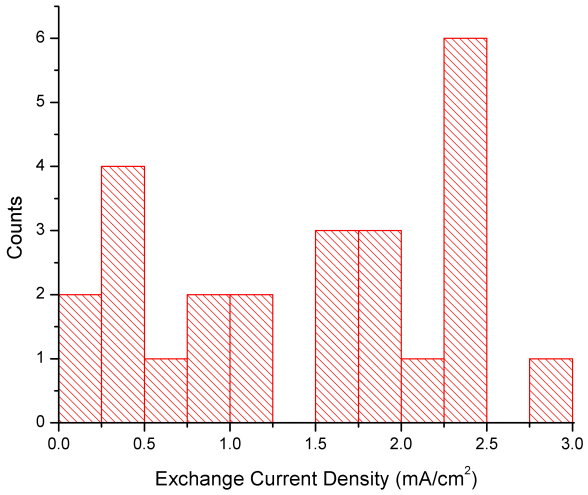


Figure 4.3: Histogram of quaternary platinum-based composite electrode fuel cell exchange current densities extracted from fitting $V(j)$ to Eq. 4.1.

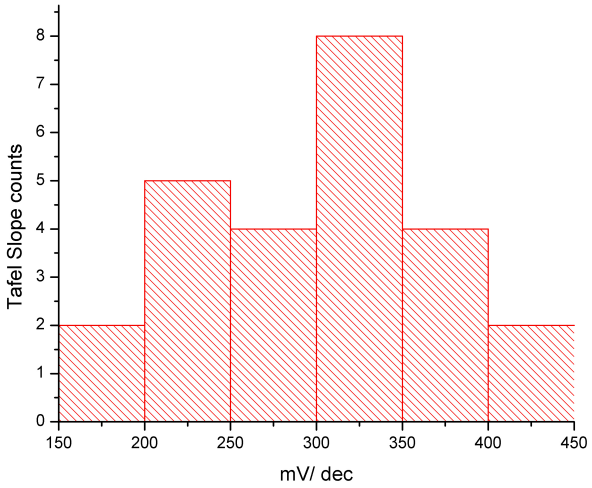


Figure 4.4: Histogram of quaternary platinum-based composite electrode fuel cell tafel slopes extracted from fitting $V(j)$ to Eq. 4.1.

Alternatively, $R_p$ could be more accurately determined by zero-bias ACIS. However, since platinum is thermodynamically unstable at zero bias, it is counter-intuitive that the standard Butler-Volmer expression is applicable. If the zero-bias resistance, $R_p$, is indeed informed by the forward and backward reactions of both platinum and platinum oxide - in proportions that evolve with time, the expression becomes considerably more complicated. Even if the zero-bias impedance of pure platinum were known, possibly by reducing the platinum oxide, then extrapolating an evolving impedance to t=0, it is not clear that the forward and reverse reactions on platinum are mechanistically symmetric. Indeed, by fitting both the high-current and low-current portions of the arc separately, and attempting to extract n for the reaction, as in figure 4.5. The compiled cell-measurements of figures 4.4 and 4.3 were analyzed in this manner and a histogram of calculated n values presented in figure 4.6.

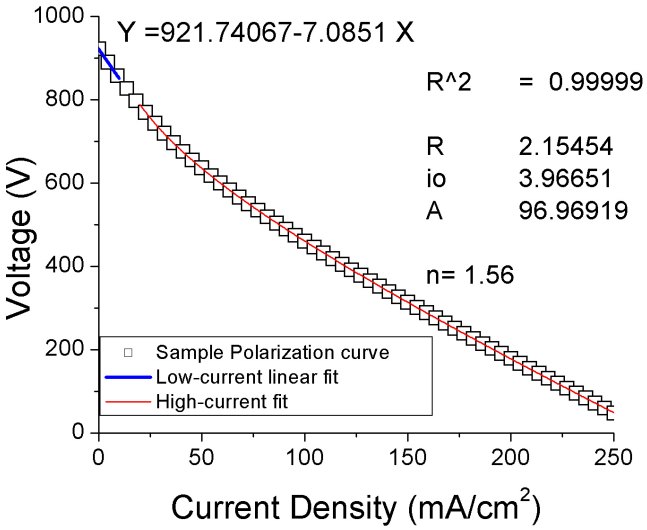


Figure 4.5: Sample polarization curve with distinct high-current and low-current fitting to extract n after Eq. 4.3. Current normalization is unnecessary for this application.

Due to the uncertainty involved in determining n in this manner, this line of inquiry was abandoned and while henceforth n is assumed to be equal to one for the ORR process, it is more rigorous to state that n is convolved with the exchange coefficient and all determined exchange coefficients, $\alpha$, are in fact $\alpha n$.

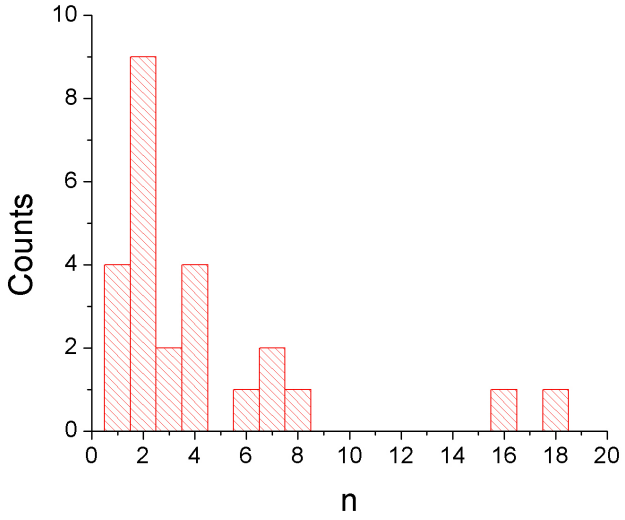


Figure 4.6: Histogram of compiled fit n values calculated as in figure 4.5.

### 4.1.2 Galvanostatic Current Interrupt

As fitting direct polarization curves can convolve ohmic losses, a common approach to isolating electrode kinetics is to separate involved processes by measuring the time-resolved capacitative discharges of each process through Galvanostatic Current Interrupt (GCI), the theory of which is discussed in chapter 4. Actual application of GCI for studying electrodes was tested on an operating fuel cell - with humid (0.33 atm $p\mathrm{H_2O}$)hydrogen on the anode and humid (0.33 atm $p\mathrm{H_2O}$)oxygen on the cathode. Both electrodes were composed of 40 mg of the quaternary electrode mixture supported by toray paper. The cell was fabricated and tested under identical conditions to those of the previous section. After the ohmic drop, the voltage relaxation fits better to a 2nd order exponential decay than a first order one as seen in figure 4.7. For comparison, a direct polarization curve was also measured as in section 5.1, to identify electrode contributions, the ohmic resistance, $R_S$, was determined by fitting the polarization curve to equation 4.1, and was used to obtain the IR-corrected polarization curve.

Figure 4.8 plots the activation losses obtained from both fitting approaches to the activation losses estimated from the IR-corrected polarization curve. The first order fitting yields the results that most closely agree with the IR-corrected curve. For the dataset in figure 4.7, the fit time constant to the 1st order exponential is 0.376 seconds - corresponding

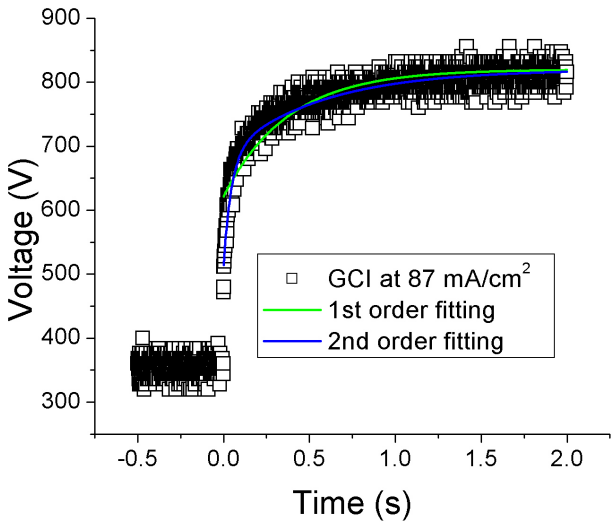


Figure 4.7: Sample GCI measurement at $j = 87$ mA/cm$^2$ showing exponential fits of 1st and 2nd order.

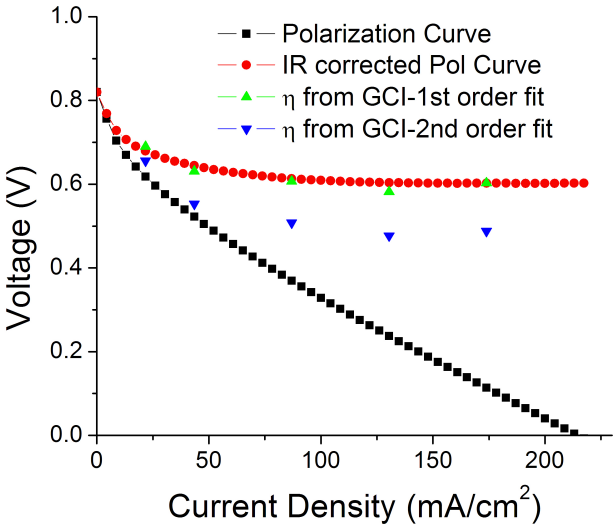


Figure 4.8: Comparison of activation losses measured by IR-corrected polarization curves and galvanostatic current interrupt measurement obtained from 1st or 2nd order exponential fittings.

to a characteristic frequency of 0.423 hz.

### 4.1.3 Longevity

An additional factor which has yet to be discussed, but has significant implications for both the study and application of $CsH_2PO_4$ electrolyte fuel cells is the performance stability. As an example, a fuel cell was fabricated with stainless-steel 304 mesh gas-diffusion layers supporting 30 mg of quaternary platinum composite mixture per electrode with a 260 micron $CsH_2PO_4$ electrolyte. The cell was sealed into a low-pressure test fixture with Viton and heated at 1 °C /min to 236 °C . After replacing the humid (0.33 atm $pH_2O$)Ar on the anode and cathode with humid (0.33 atm $pH_2O$)hydrogen and oxygen gas, respectively, the cell voltage was measured without current for an hour while the open circuit voltage equilibrated. An initial galvanostatic polarization curve was measured with a Keithley 2420 sourcemeter, followed by a constant current draw of 43.5 mA/cm$^2$ for 50 hours. A final polarization curve was then measured. The cell voltage vs time shown in figure 4.9(a) reveals a significant decrease in cell voltage with time, while the before and after polarization curves shown in figure 4.9(b) were fit to equation 4.1 to probe the mechanism of cell failure.

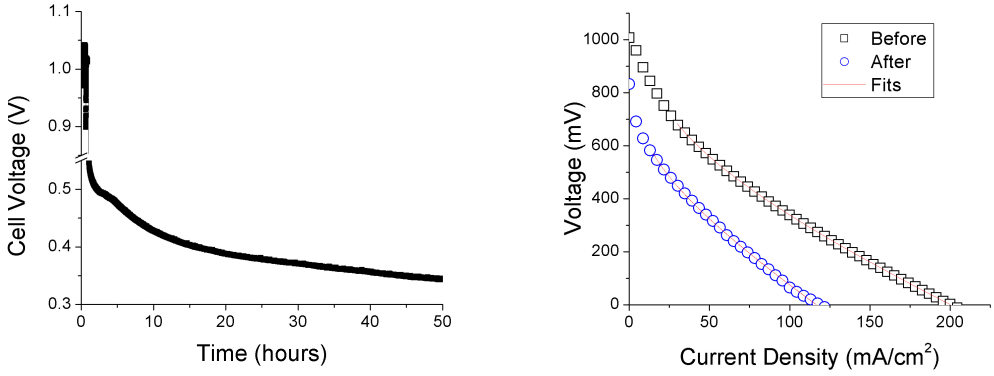


(a) Cell voltage as a function of time during a 43.5 mA/cm$^2$ current draw.

(b) Polarization curves taken before and after current draw.

Figure 4.9: Longevity test of a SS304 mesh-supported quaternary platinum composite electrode fuel cell operating at 236 °C in humid (0.33 atm $pH_2O$)dual-chamber $H_2/O_2$.

Table 4.1 shows the results from fitting the before and after polarization curves.

Over the course of the current draw, the cell degraded in nearly every manner possible. The open circuit voltage decreased 175 mV, the ohmic resistance increased by nearly 25%,

| | $V_0$ (mV) | $R_S^*$ ($\Omega$ cm$^2$) | $j_0$ (mA/cm$^2$) | Tafel slope (mV/dec) |
|---|---|---|---|---|
| Before | 1007 | 2.92 | 0.4215 | 318 |
| After | 832 | 3.61 | 0.287 | 268 |

Table 4.1: Before and after polarization curves fit to Eq. 4.1 in order to investigate the degradation shown in Fig 4.9.

and the exchange current density decreased to 68% of its initial value. The tafel slope is seen to improve, but the lowered open circuit voltage increases the error in quantification.

The decrease in open circuit voltage can be attributed to the seals and test fixture, while the decrease in exchange current density suggests a degradation in the electrode-electrolyte interfacial microstructure.

As the increase in ohmic resistance was unexpected, the role of the electrode support was investigated. Four cells were tested in humid (0.33 atm $p\mathrm{H_2O}$)oxygen at 240 °C with single-point zero-bias ACIS at 100 khz, corresponding to the high-frequency intercept. The four cells were two fuel cells supported by SS304 mesh or toray paper, respectively; and two constructions of a pair of stainless steel meshes separated by a toray-paper disk. The change in resistance from initial values is plotted in figure 4.10.

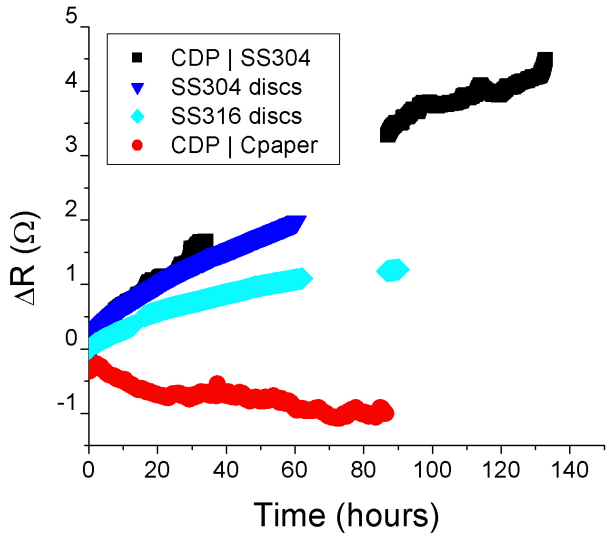


Figure 4.10: Change in ohmic resistance of different cells and supports in humid (0.38 atm $p\mathrm{H_2O}$) oxygen at 240 °C .

The ohmic resistance of a full cell ($\mathrm{CsH_2PO_4}$ electrolyte with standard quaternary platinum-based composite electrodes) supported by stainless steel 304 gas-diffusion lay-

ers is seen to increase by nearly 5 ohms over the tested range without stabilizing. Testing only two disks lightly pressed against each other reveals a similar increase in ohmic resistance, showing that surface oxidation of the stainless steel increases interfacial resistance, and explains the increase in ohmic resistance of the full SS304-supported fuel cell. Stainless steel 316 disks are considered more resistant to oxidation and can be seen to have 50% smaller increase in resistance compared to stainless steel 304 - though the resistance still does not stabilize over the tested time. Finally, a full cell as above, but with Toray paper supports instead of stainless steel, was seen to actually become less ohmically resistive with time.

With source of the changing ohmic resistance identified, as well as a method for stabilizing it, the impact of polarization losses can be then identified.

Though qualitative, an additional longevity measurement is worth mentioning: A cell with binary-composite electrodes (Pt:$CsH_2PO_4$ 3:7 by wt. 25 mg per side) was fabricated and sealed with PTFE tape into the high-pressure test fixture - though only at 1 in-lb of torque per bolt. After heating to 242 °C and introducing the humid (0.33 atm $pH_2O$)hydrogen and oxygen to the anode and cathode, respectively, the open circuit voltage was only 890 mV. As this potential is approximately 250 mV below the theoretical open circuit voltage, the combined electrode resistance was measured by ACIS without bias over 27 hours. An initial impedance scan is shown in figure 4.11(a). Similar scans were repeated and the dominant arc (at 27 mhz) was fit to a R(RQ) equivalent circuit. The fit resistance, as well as cell open circuit voltage, is recorded in figure 4.11(b).

Despite the unexplained event at 7 hours, figure 4.11 shows stability of the electrode-electrolyte interface for a carbon-free electrode composite at electrochemical potentials more than 250 mV lower than theoretical.

### 4.1.4 Conclusions

As fuel cells operate in dual-chamber mode, tests under these conditions are expected to be the most accurate predictors of genuine fuel cell kinetics. However, the great number of variables that inform a polarization curve under these conditions, coupled with the thermodynamic instability of both electrode materials and supports, makes a quantifiable investigation of electrode kinetics difficult. Certain qualitative information, however, is accessible - namely that for the quaternary platinum composite-$CsH_2PO_4$ interface, the

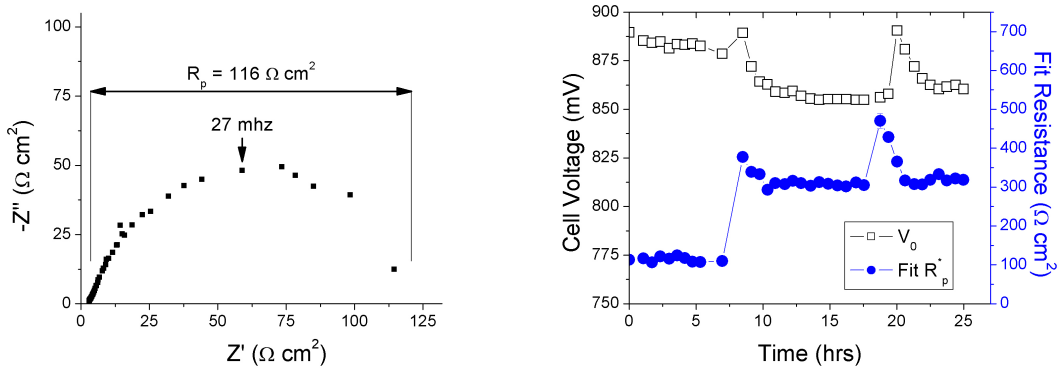


(a) Sample Nyquist plot measured without bias at 890 mV.

(b) Fit arc impedance and cell open circuit voltage plotted vs time.

Figure 4.11: Longevity test of a SS304 mesh-supported binary platinum composite electrode fuel cell operating at 242 °C in humid (0.33 atm $pH_2O$)dual-chamber $H_2/O_2$.

interfacial losses evince tafelian behavior, suggesting that the primary electrode losses are charge-transfer related. The tafel slopes, obtained by fitting polarization curves, exhibit a concerning level of scatter, but enough cells were fabricated and tested that the exchange coefficient for platinum-based catalysis is expected to be 0.417 +/- 0.105. Similarly, the exchange current density showed a great deal of scatter, but an estimate of 1.48 +/- 0.857 mA/cm$^2$.

Assuming that the anodic and cathodic exchange coefficients sum to 1 and that n=1 as well, this exchange current density corresponds to a polarization resistance, $R_p$ of 29.64 Ω cm$^2$, with the standard deviations suggesting a range from 18 to 70 Ω cm$^2$. Galvanostatic current interrupt also predicts that the limiting process will have a characteristic frequency on the order of 400 mhz. Again, this is for the quaternary electrode composite.

A binary composite electrode was shown to have a seemingly stable polarization resistance under less oxidizing conditions.

Further quantification of losses in $CsH_2PO_4$ fuel cells with platinum-based electrodes requires near-perfect control over the chemical potential at the electrodes of interest, either by improving seals between electrodes or by eliminating them entirely.

## 4.2 Single Chamber - two point

The advantage of single-chamber measurements, as discussed in chapter 2, is that firstly, the electrodes are at ideal conditions without concern for sealing; and secondly, that the zero-bias impedance of both anode and cathode can be identified by filling the chamber with hydrogen or oxygen, respectively. The disadvantage of this method is that with symmetric geometries, it is impossible to quantify electrode kinetics.

$$H_2 \underset{rev}{\overset{for}{\rightleftarrows}} 2H^+ + 2e^- \tag{4.4}$$

Combined with observations from dual-chamber, however, the fuel cell losses can begin to be identified.

### 4.2.1 ACIS measurements

Zero-bias Alternating Current Impedance Spectroscopy is the only effective electrochemical probe of single-chamber symmetric cells, but it is such a powerful tool, that even by itself, important insights may be gleaned. For instance, from the polarization curves taken of dual-chambered fuel cells in section 5.1, the electrode losses were treated as a single charge-transfer step. Based solely on these curves, we are unable to conclude if the measured losses were due to the cathode or the anode.

To represent the anode and cathode of cells tested under fuel cell conditions above, a quaternary electrode mixture was prepared composed of platinum black, 40 wt. % Pt on carbon, fine $CsH_2PO_4$ , and naphthalene. Both dry powder electrodes were densified with a $CsH_2PO_4$ electrolyte separating them, in a single, uniaxial cold press to over 95 % density. The cell was heated to 238 °C in a single chamber flowing humid (0.38 atm $pH_2O$) argon at approximately 30 sccm, then tested flowing pure hydrogen or pure oxygen as an inlet gas. Cells were tested with zero-bias AC Impedance spectroscopy (10 mV amplitude) and the Nyquist representation of the cell impedance in each environment is shown in figure 4.12.

Immediately, we observe that for the quaternary electrode composite, the impedance in oxygen is over two orders of magnitude greater than that in hydrogen, and is dominated by a single, low-frequency arc. As we know the primary electrode resistance under operating condition is due to a charge transfer mechanism, this low-frequency arc is representative

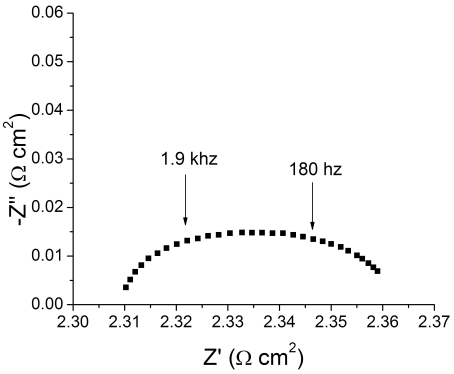


(a) Nyquist plot of electrode area-specific impedance in symmetric hydrogen.

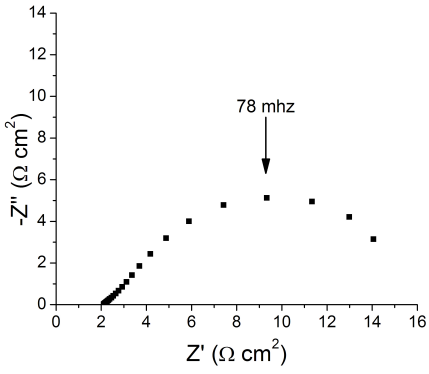


(b) Nyquist plot of electrode area-specific impedance in symmetric oxygen.

Figure 4.12: Symmetric cell, single chamber Pt:CDP:40 wt% Pt/C:N (3:3:1:1 by wt.) electrode resistances at 238 °C in humid (0.38 atm $p\mathrm{H_2O}$) hydrogen and oxygen.

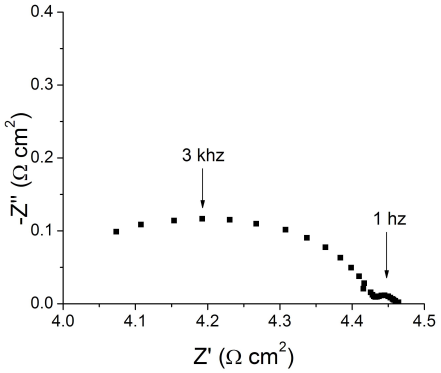


(a) Nyquist plot of platinum electrode impedance in symmetric hydrogen.

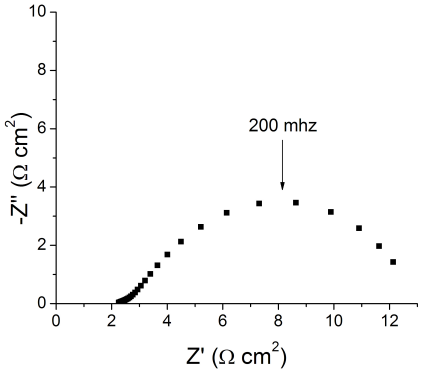


(b) Nyquist plot of platinum electrode impedance in symmetric oxygen.

Figure 4.13: Symmetric cell, single chamber 40 wt% Pt/C powder electrode resistances at 238 °C in humid (0.38 atm $p\mathrm{H_2O}$) hydrogen and oxygen.

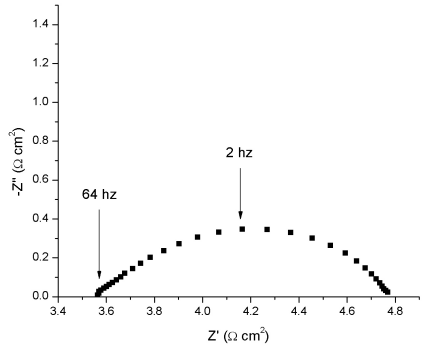


(a) Nyquist plot of electrode impedance in symmetric hydrogen.

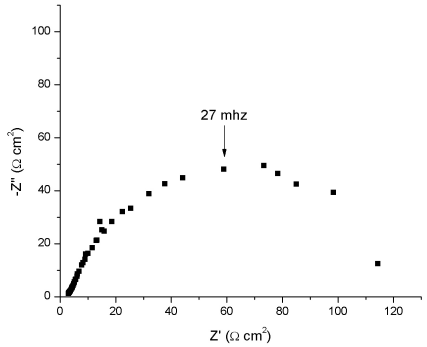


(b) Nyquist plot of electrode impedance in symmetric oxygen.

Figure 4.14: Symmetric cell, single chamber Pt:CDP (3:7 by wt.) powder electrode resistances at 238 °C in humid (0.38 atm $p\mathrm{H_2O}$) hydrogen and oxygen.

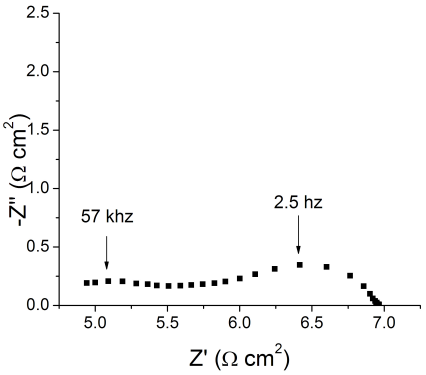


(a) Nyquist plot of electrode impedance in symmetric hydrogen.

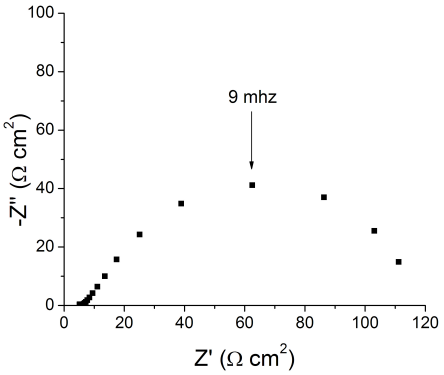


(b) Nyquist plot of electrode impedance in symmetric oxygen.

Figure 4.15: Symmetric cell, single chamber Pt powder electrode resistances at 238 °C in humid (0.38 atm $p\mathrm{H_2O}$) hydrogen and oxygen.

of that process. Because of their minor contribution to fuel cell operation, however, the smaller arc in oxygen and both arcs in hydrogen are unidentified.

The quaternary electrode composition, however, was developed to maximize electrode performance - and is therefore less suitable for detailed mechanistic analysis. To simplify the mixture, while still maintaining the material components, a cell with 40 wt.% platinum dispersed on carbon (Pt/C) electrodes was prepared and tested in an identical manner.

Interestingly, the impedance shape of this simplified composition in figure 4.13(a) is seen to differ from the quaternary composition in 4.12(a), with the high frequency process more resistive than the low-frequency one. This simplified composition seemingly shares the high-frequency arc with the quaternary mixture (based on characteristic frequency), but the overall impedance is slightly higher and the characteristic frequency of the low-frequency arcs do not match.

The impedance in oxygen shown in 4.13(b), however, has an identical shape to the nyquist plot for the quaternary mixture in figure 4.12(b) - though the characteristic frequency increases from 78 mhz to 200 mhz.

Further simplification of the electrode composition was achieved by directly mixing platinum powder with the electrolyte material, $CsH_2PO_4$ , in a 3:7 ratio by weight. Testing was performed in an identical manner as above and the data is presented in nyquist representation in figure 4.14.

Without carbon and in hydrogen, the low frequency arc in figure 4.14(a) is now the primary arc and evinces a characteristic frequency similar to that of the low-frequency arc of the Pt/c electrode in hydrogen. Again, the overall electrode resistance has increased.

In oxygen, the impedance shape differs only slightly, but the characteristic frequency is lower than that of both the quaternary composition and Pt/C electrodes.

Lastly, despite an expected higher interfacial resistance, pure platinum powder was dispersed and pressed directly into a pure $CsH_2PO_4$ electrolyte and measured identically as above.

The high frequency arc in figure 4.15(a) is unexpected and at such a high frequency (57 khz) that it is more likely attributable to an interfacial resistance, due to poor contact, than a genuine electrode process. The lower frequency arc, however, has a characteristic frequency almost identical to that of the Pt:$CsH_2PO_4$ electrode in figure 4.14(a), as expected. In oxygen, figure 4.15(b) shares a similar impedance shape with the previous three tested

electrode compositions in oxygen but with the lowest characteristic frequency thereof.

As can be seen for all platinum-based electrodes, the anode is generally co-limited by two processes of comparable resistance. The cathode, on the other hand, is dominated by a single low-frequency arc, but includes a smaller, high-frequency process as well. Moreover, the total electrode resistance in oxygen is approximately two, or more, orders of magnitude larger than that of the same cell in hydrogen. We can therefore safely consider cathodic losses to be the primary source of electrode overpotentials in the platinum - $CsH_2PO_4$ system.

This, combined with the observation that the primary electrode overpotentials appear to follow tafel behavior in figure 4.1, leads to the conclusion that the dominating process at the cathode is one involving charge transfer.

### 4.2.2 Anode longevity

True characterization of electrodes requires stability to probe intrinsic electrode properties accurately, such as activation energies and gas partial pressure dependencies, and also reproducibility to enable normalization of extrinsically measured properties. Operation under fuel cell operation has been shown to be rather unstable as in figure 4.9. Through investigating symmetric cells, we are able to identify the likely unstable electrode. First, we analyze the stability of the 4 platinum-based electrode compositions in hydrogen by running identical zero-bias impedance scans over time in humid (0.38 atm $pH_2O$) hydrogen at 240 °C .

Pt/C is initially stable over an hour seen in figure 4.16(b), so a parametric study - specifically varying temperature to obtain an activation energy for the primary arc was attempted. However, it showed degradation over the course of the test. Based on the two data points, the degradation was 0.77 % / hour. A linear correction of the degradation, however, does not result in a reproducible measurements. It is more likely, therefore, that the microstructure was mechanically changed during the heating and cooling cycle.

With this, we can summarize the resistances, characteristic frequencies, and total longevity behavior of the four platinum-based mixtures:

Table 4.2 shows the wide variety in both resistances and characteristic frequencies. The inclusion of carbon-supported platinum is shown to greatly reduce electrode impedance, and the shift to a higher characteristic frequency over the Pt:$CsH_2PO_4$ composite suggests

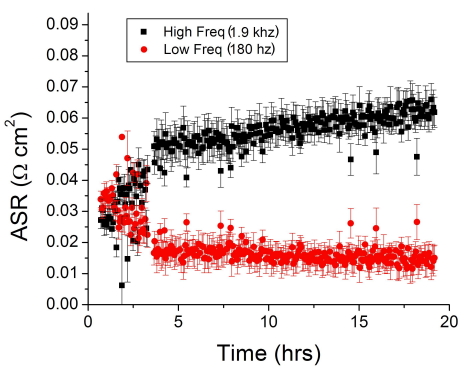


(a) Total Fit ASR of Pt:$CsH_2PO_4$ : 40 wt% Pt/C: Naphthalene (3:3:1:1 by wt.) anode vs time.

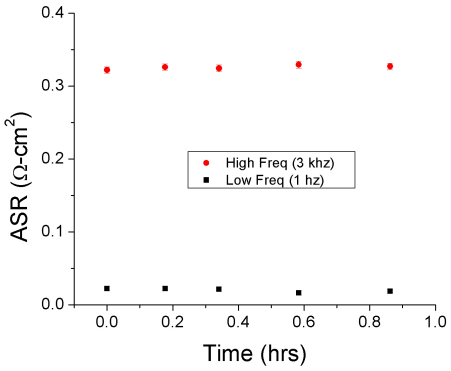


(b) Fit ASR of 40 wt% Pt/C anode vs time.

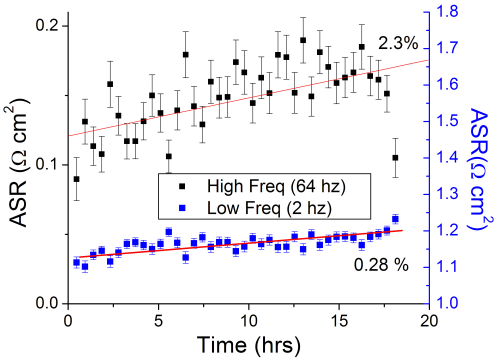


(c) Total Fit ASR of Pt:$CsH_2PO_4$ (3:7 by wt.) anode vs time.

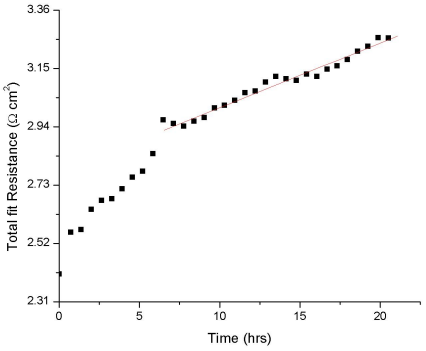


(d) Total Fit ASR of Pt anode vs time.

Figure 4.16: Symmetric cell, single chamber Pt-based powder electrode resistances at 240 °C in humid (0.38 atm $pH_2O$) hydrogen.

| Mixture | $ASR_1$ ($\Omega$ cm$^2$) | $f_0$ 1 (hz) | $ASR_2$ ($\Omega$ cm$^2$) | $f_0$ 2 (hz) | $ASR_{tot}$ ($\Omega$ cm$^2$) | Degradation (% /hr) |
|---|---|---|---|---|---|---|
| Pt:Pt/C:CDP:N | 0.0272 | 1900 | 0.0339 | 180 | 0.0611 | 0.9 |
| Pt/C | 0.249 | 3000 | 0.017 | 1 | 0.266 | 0.77 |
| Pt:CDP | 0.1125 | 64 | 1.491 | 2 | 1.603 | 0.33 |
| Pt | 1.844 | 57000 | 0.823 | 2.5 | 2.666 | 0.84 |

Table 4.2: Summary of Pt-based electrode mixtures' impedance in humid (0.38 atm $pH_2O$) hydrogen

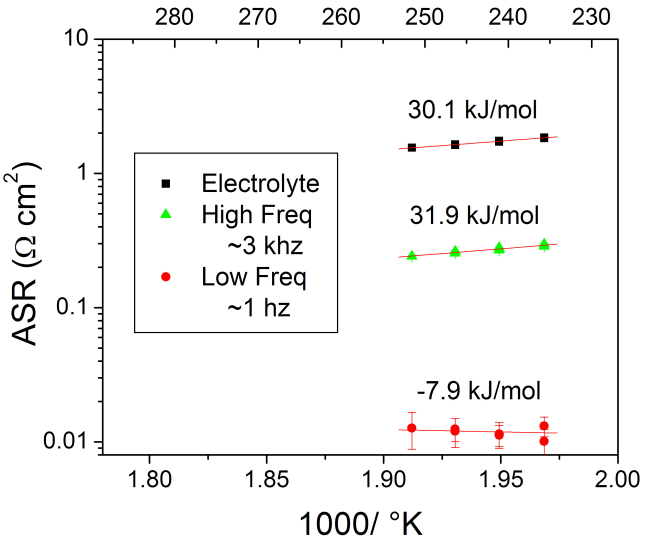


Figure 4.17: Arrhenius behavior of 40 wt% Pt/C anode at 240 °C in humid (0.38 atm $p\mathrm{H_2O}$) hydrogen. General activation energy is found to be approximately 32 kJ/mol, but 0.77% degradation per hour makes quantification less accurate.

that the carbon is genuinely catalytically active and therefore has a role beyond maintaining electrode porosity and electrical connectivity. That all mixtures increase in resistance almost 1% per hour supports the intuition that the degradation is not chemical in nature.

However, as the anode is shown to be approximately two orders of magnitude less resistive than the cathode, a several percent increase in anode resistance would not be noticeable in fuel cell operation over the time tested in figure 4.9.

### 4.2.3 Anode under bias

While biasing a symmetric cell in symmetric environment cannot give clear, quantitative information as it measures the average of the forward and reverse reaction rates far from equilibrium - qualitative information is nonetheless obtainable. For example, if a process is charge-transfer limited (and therefore obeys a Butler-Volmer relationship), the dV/dI impedance will reduce at both electrodes for a given current - so the total impedance will also be reduced. If a process is mass-diffusion limited, however, one electrode will develop a higher impedance while the other will develop a lower impedance - as this resistance varies exponentially with current, the total impedance would be expected to increase or stay the same (depending on the extent of current relative to internal parameters). Thus, biasing a

symmetric cell can provide a reasonable guess at a process mechanism. For simplicity, the two binary compounds were tested in this method and the results are shown in figure 4.19. At high bias, the Pt:$CsH_2PO_4$ (3:7 by wt.) electrode developed a third arc, and as it was not possible to resolve all three through the tested bias range (as seen in figure 4.18(a)), the resistances were simply summed and presented in figure 4.18(b).

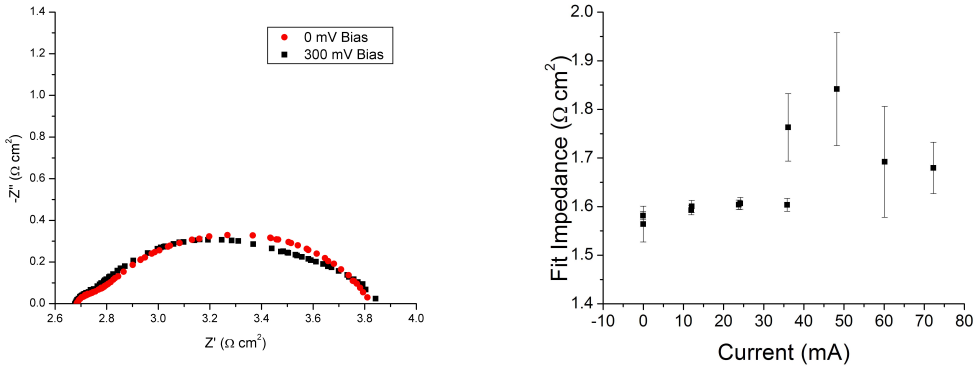


(a) Symmetric Pt:$CsH_2PO_4$ (3:7 by wt.) electrode (b) Total Fit ASR of Pt:$CsH_2PO_4$ (3:7 by wt.) cell tested under biases of 0 mV and 300 mV show with bias.
the development of a third arc.

Figure 4.18: Zero-bias ACIS measurements of $CsH_2PO_4$ electrolyte cells with symmetric binary composite electrodes tested in uniform humid (0.38 atm $pH_2O$) hydrogen at 238 °C
.

Because of the simplification of the fit for the Pt:$CsH_2PO_4$ electrodes in figure 4.18, the most that can be said is that mass-diffusion significantly contributes to the total resistance. That a third arc would develop while the total impedance remains constant suggests, however, that part of the low frequency arc becomes less resistive and is therefore related to charge-transfer - it should be noted that biased studies of symmetric electrodes in symmetric environments are not quantitative and the difference in nyquist plots in figure 4.18 is so small that strong conclusions cannot be made. The total fit resistance for the two-point Pt:$CsH_2PO_4$ electrode cell is graphed against current in figure 4.19(a) and is seen to vary little.

For the Pt/C electrode measurements shown in figure 4.19, however, the arcs are readily distinguishable and we can therefore observe a reduction in impedance for the smaller, low frequency arc, while the larger, high frequency arc becomes slightly more resistive. This observation implies that the large high-frequency arc is a mass-diffusion step, while the

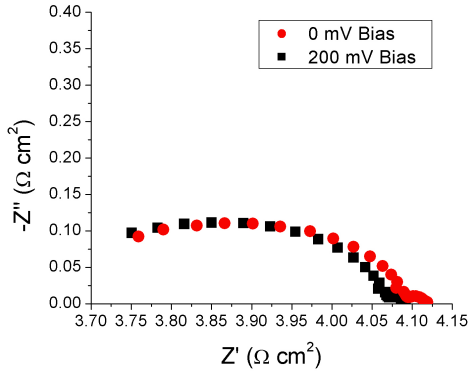


(a) Symmetric Pt/C (40 wt.%) electrode cell tested under biases of 0 mV and 200 mV.

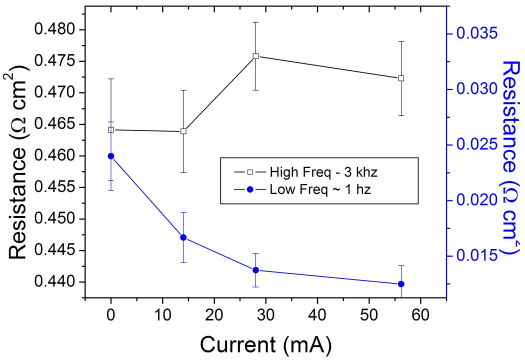


(b) Fit ASR of biased 40 wt% Pt/C.

Figure 4.19: Zero-bias ACIS measurements of $CsH_2PO_4$ electrolyte cells with symmetric Pt/C electrodes tested in uniform humid (0.38 atm $pH_2O$) hydrogen at 238 °C .

small low-frequency arc is a charge-transfer step. Interestingly, carbon, which was originally included simply as a porous electrically-conductive dispersant in the electrode composite, is seen to modify the anode mechanism and characteristic frequencies.

### 4.2.4 Cathode longevity

Degradation of the cell can, at the outset be anticipated to be more likely at the cathode than at the anode because both Pt and C are thermodynamically unstable under the temperatures and atmospheres of fuel cell operation. The reaction C + $O_2$(g) = $CO_2$ has a Gibbs free energy of approximately -395 kJ/mol (of C) at 240 °C and involves 4 electrons so the associated potential is simply $\frac{395000}{4\times96485} = 1.02V$. the reaction 2Pt + O2(g) = 2PtO has a Gibbs free energy of -26.5 kJ/mol (of pt) at the same temperature, or 0.137 V. Effectively, the carbon oxidation is so thermodynamically favored that it will occur at all operating voltages. The platinum oxide, however, is only favorable within 137 mV of the theoretical Nernstian Voltage. Furthermore, because the cathode is the source of much more significant overpotential than the anode, a slight degradation in this component will manifest itself more prominently in the overall fuel cell degradation than a moderate level of anode degradation. As in the anode case, two electrocatalyst mixes were evaluated for degradation: the quaternary composite, and pure Pt. The binary composite and Pt/C electrodes were tested for initial impedances, but not for longevity, given the known chemical instabil-

ity under these conditions. $CsH_2PO_4$ electrolyte cells were fabricated with these electrodes, then heated to 240 °C in symmetric, humid (0.38 atm $pH_2O$) oxygen. The results for the four electrocatalyst mixes are presented in figure 4.20.

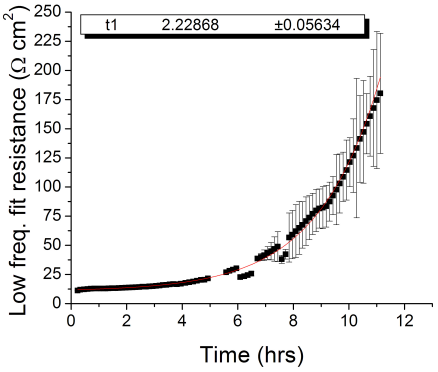


(a) Quaternary composite stability.

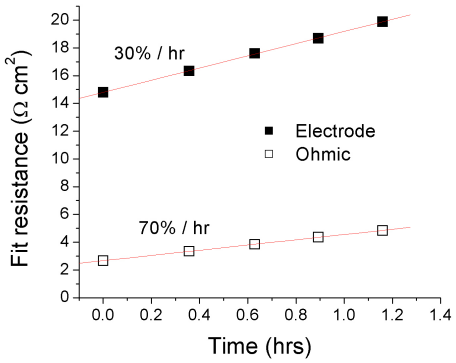


(b) Pt/C longevity

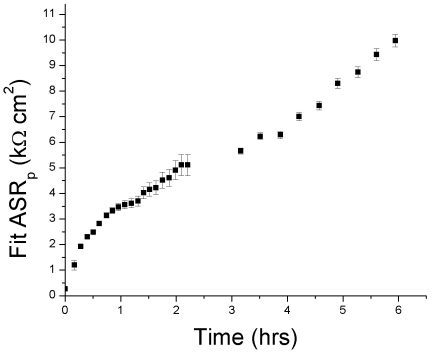


(c) Pt:$CsH_2PO_4$ longevity.

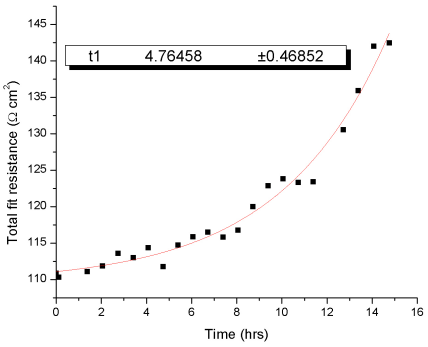


(d) Total Fit ASR of Pt cathode vs time.

Figure 4.20: Symmetric cell, single chamber ACIS measurements of four cells with differing electrode compositions in humid (0.38 atm $pH_2O$) oxygen at 240 °C . Impedances are fit and plotted against time - revealing instability in each.

The increased error in fitting for figure 4.20(a) is because the resistance increase, lowering the characteristic frequency so impedance scans to 1 mhz describe less and less of the total arc.

40 wt% Pt/C electrode were also tested in oxygen, but the ohmic resistance increased rapidly (70% per hour), suggesting increased interfacial resistance as carbon oxidized, and active catalysts became isolated through oxidation of the support.

The zero-bias impedance of electrode mixtures (both with and without carbon) increases exponentially with time - much more sharply than expected from the decrease in polarized

dual-chamber fuel cell performance shown in figure 4.9. This is therefore most likely due to the formation of oxide products.

As an additional check that oxide formation is the cause of the extreme increase in impedance measured by ACIS, a full quaternary electrode, was prepared and tested in a manner identical to the one in figure 4.20(a) for 14 hours, showing a similar exponential increase in measured impedance with a time constant of 2.07. The chamber was then purged with argon and hydrogen was flowed for 4 hours before purging again with argon and switching back to oxygen.

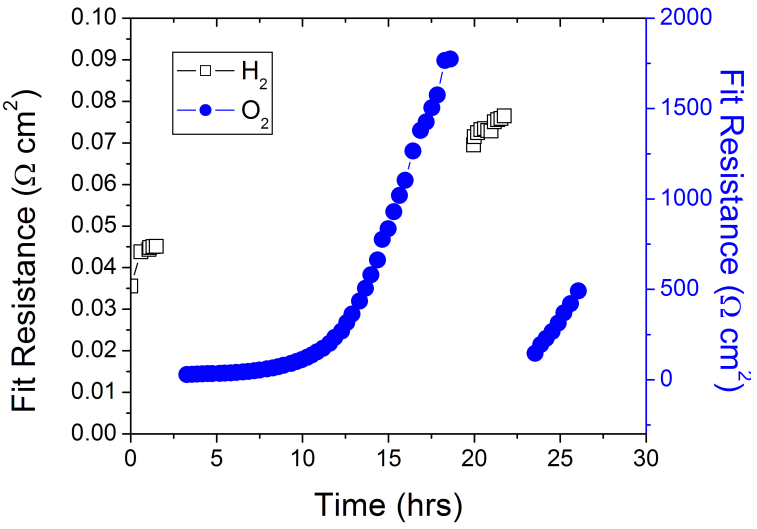


Figure 4.21: Total Fit ASR of Pt:$CsH_2PO_4$ : 40 wt% Pt/C: Naph (3:3:1:1 by wt.) electrode resistance in humid (0.38 atm $pH_2O$) hydrogen and oxygen with time and a repeated cycle.

The impedance lowered dramatically - though not back to initial values. Both observations support the hypothesis that oxide formation in humid oxygen causes the increase in measured impedance. Firstly, that the resistance can be lowered by dwelling the cell in reducing atmospheres confirms that the slow formation of platinum oxide is the primary cause of the exponential increase in resistance. Neither the impedance in hydrogen, nor the impedance in oxygen are fully recoverable after cycling, however, indicating lasting modification to the electrode microstructure.

Additionally, the surface oxide formation is observed to increase the ohmic resistance in a manner not reversible by subsequent reduction - suggesting that oxidized carbon supports

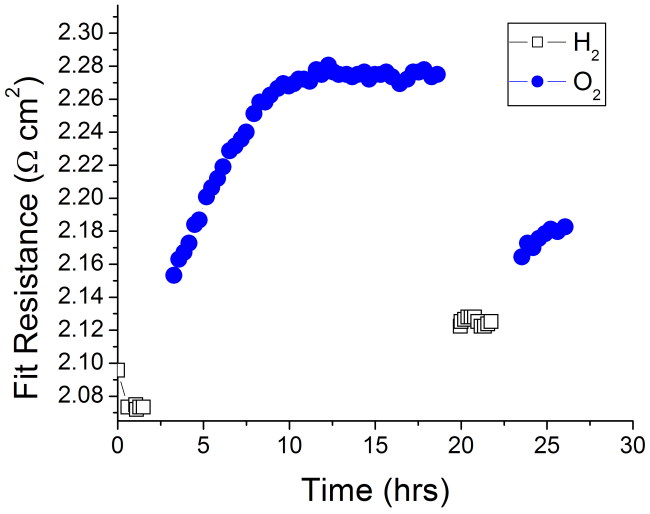


Figure 4.22: Area-specific ohmic resistance of Pt:$CsH_2PO_4$ : 40 wt% Pt/C: Naph (3:3:1:1 by wt.) in humid (0.38 atm $pH_2O$) hydrogen and oxygen with time and a repeated cycle.

have lost contact to electroactive interfaces.

As earlier, the primary resistances and longevity behavior of the tests can be summarized in table 4.3. Again, the inclusion of carbon is seen to significantly reduce the measured resistance, but is thermodynamically unstable.

| Mixture | ASR ($\Omega\ cm^2$) | $f_0$ (hz) | Degradation $\tau$ (hrs) |
|---|---|---|---|
| Pt:Pt/C:$CsH_2PO_4$ :N | 11.98 | 0.075 | 2.23 |
| Pt/C | 8.9 | 0.205 | linear |
| Pt | 110 | 0.009 | 4.76 |
| Pt:$CsH_2PO_4$ | 191 | 0.057 | N/A |

Table 4.3: Summary of Pt-based electrode mixtures' primary impedance in humid (0.38 atm $pH_2O$) oxygen at 240 °C

### 4.2.5 Cathode under bias

Biased AC impedance of symmetric cells, as mentioned above is purely qualitative. But in early investigation, even qualitative tests may provide insights or confirm other preliminary data. A symmetric platinum black, fine $CsH_2PO_4$ , 40 wt.% Pt on carbon, and naphthalene electrode composite was tested in symmetric oxygen and the impedance measured at bias. The impedance as a function of bias, shown in figure 4.23, clearly exhibits tafelian behavior,

with the instantaneous dV/dI decreasing dramatically with increased bias.

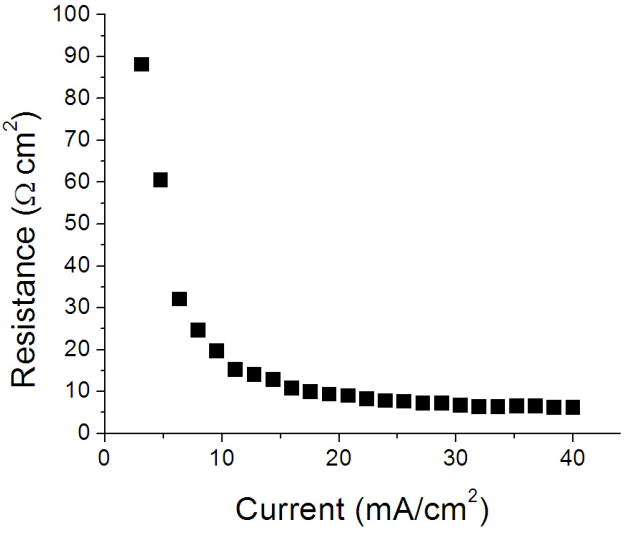


Figure 4.23: Impedance of platinum black, fine $CsH_2PO_4$ , 40 wt.% Pt on carbon, and naphthalene symmetric electrode measured under varying biases at 236 °C in humid (0.33 atm $pH_2O$)oxygen.

The high initial $R_p$ is due to one of the electrodes being oxidized by the bias and the environment. Again, two-probe biased impedance is nothing more than a qualitative tool as it averages the impedances of both electrodes under opposite reaction directions, but if the insights gleaned are small, so too is the fractional cost in time and effort of using it as an additional check on a cell already under examination.

### 4.2.6 Galvanostatic Current Interrupt

Lastly, we attempted to verify the suitability of the galvanostatic current interrupt method for analyzing electrodes in symmetric, humid (0.38 atm $pH_2O$) oxygen. A $CsH_2PO_4$ electrolyte cell with quaternary composite electrodes, supported on Toray-paper, was fabricated by uniaxial cold-pressing, contacted in two-point configuration with silver paint and heated to 240 °C at 1 °C /min in hydrogen. After purging with humid argon, the cell was tested by galvanostatic current interrupt in oxygen and by polarization (which was later modified by subtracting the ohmic contribution determined by ACIS). The resulting $j - \eta$ characteristics measured by the two methods are presented in figure 4.24. Because the forward and reverse reactions are simultaneously measured in both cases, this is not a suitable method

for determining electrode kinetics. It is, however, suitable as a check on the accuracy of GCI in identifying electrode losses.

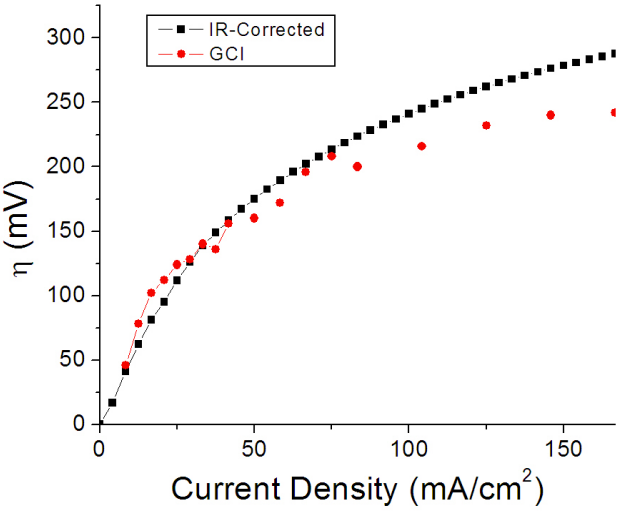


Figure 4.24: Comparison of electrode potentials measured by IR-corrected polarization and by GCI in a single chamber (humid (0.38 atm $pH_2O$) oxygen), two point configuration.

As in figure 4.8, overpotentials measured through GCI agree reasonably well with values obtained from the IR-corrected polarization curve, though values diverge at higher current densities.

### 4.2.7 Conclusions

In certain systems, a great deal of information can be potentially extracted from single-chamber symmetric cell tests. Quantitative use, however, requires both stable measurements and a detailed understanding of the mechanism being probed. In symmetric hydrogen, all tested platinum-based electrodes exhibited an increase in impedance of almost 1% per hour - as this is not due to a chemical reaction, it is necessarily due to mechanical degradation, the nature of which will be investigated further in chapter 8.

Mechanistically, we can conclude that the anode reaction is co-limited by two processes, at least one of which is mass-diffusion in nature. Carbon is seen to play a role in catalysis as well - lowering impedance and either increasing the characteristic frequency of the high-frequency process - or providing a different reaction mechanism entirely.

In oxygen, AC impedance measurements reveal that the cathode resistance is dominated by a single low-frequency process. As this process is far more resistive than the anode processes or the high frequency cathode process, it can be considered the primary source of electrode overpotentials in actual fuel-cell operation. Since the electrode behavior is clearly exhibits tafel behavior, we can identify this arc as being charge transfer-limited in nature.

AC measurements at zero-bias are extremely unstable, however. The instability is confirmed to be primarily due to the active catalyst, platinum, oxidizing over the course of several hours. The platinum oxide can be reduced, but for symmetric cells, only by changing the environment. After reducing the cell, however, a decrease in available active sites for catalysis due to the oxidation and subsequent corrosion of the carbon support explains why the initial resistance may not be fully recoverable. This test does not rule-out degradation due to mechanical deformation, and does not directly explain the operating degradation seen in figure 4.9. Rather, this highlights two significant obstacles for characterizing cathodes - firstly, that zero-bias ACIS is unsuitable due to platinum's chemical instability, and secondly that under the oxidizing conditions of open cell operation, the cathode microstructure degrades.

Additionally, GCI appears to be a promising method for resolving electrode overpotentials in both dual-chamber and single-chamber two-point configurations.

While dozens of cells were analyzed in section 5.1 to obtain estimates for the exchange current density and exchange coefficient of the limiting electrode process, only solitary representative measurements are presented for each system in this section. The reasoning behind this decision is based firstly on the extreme differences in magnitude of anode resistance and cathode resistance, secondly on a move towards mechanistic investigations, and lastly on the understanding that intrinsic, dimension-specific material properties are prohibitively difficult to ascertain with uncontrolled powder-based microstructures. With the goal of apples-to-apples comparisons between electrode material candidates, order-of-magnitude comparisons may suffice for uncontrolled microstructures.

## 4.3 Single-Chamber - three point

Qualitative mechanistic conclusions can be made by investigating the electrode impedance under different conditions, but true kinetic studies are necessary to identify which processes

are being probed. However, isolating the $j - \eta$ characteristics of a single electrode is a process rife with technical challenges. The nearly universal solution to electrode isolation is to include a reference electrode.

### 4.3.1 Using reference electrodes to isolate kinetics.

A number of reference electrode configurations were attempted to probe the mechanism of platinum catalysis with solid acid fuel cell. While most failed the necessary (but not sufficient) test for reference electrode placement: that the zero-bias ACIS measurement of an electrode in three-point configuration is half that of the same measurement done in two-point configuration. Or alternatively, that for a given current perturbation, $V_{WE-RE} = \frac{1}{2}V_{WE-CE}$. And if that is the case, then $V_{WE-CE} = V_{WE-RE} + V_{CE-RE}$. Figure 4.25 shows one such confirmation test.

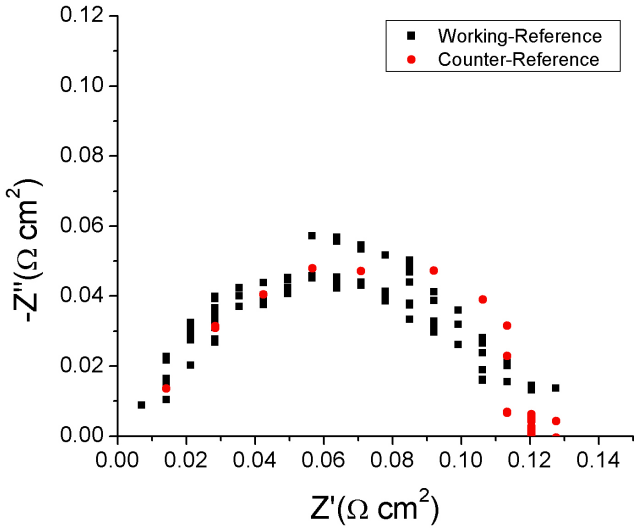


Figure 4.25: Sample reference electrode measurement showing equivalent resistance of the working electrode and of the counter electrode. Both nyquist plots have been shifted so that the high-frequency impedance intersects the origin.

It is worth noting, that even though the resistances are in excellent agreement, the characteristic frequencies differ by an order of magnitude (1.5khz for the working electrode, 15 khz for the counter electrode). It is expected that they be identical, since the working and counter electrodes are chemically and geometrically identical.

Those cells which fulfill this condition were tested by zero-bias ACIS and GCI. All three-

point cells were fabricated with the quaternary platinum-based composite material for the working, counter, and reference electrodes.

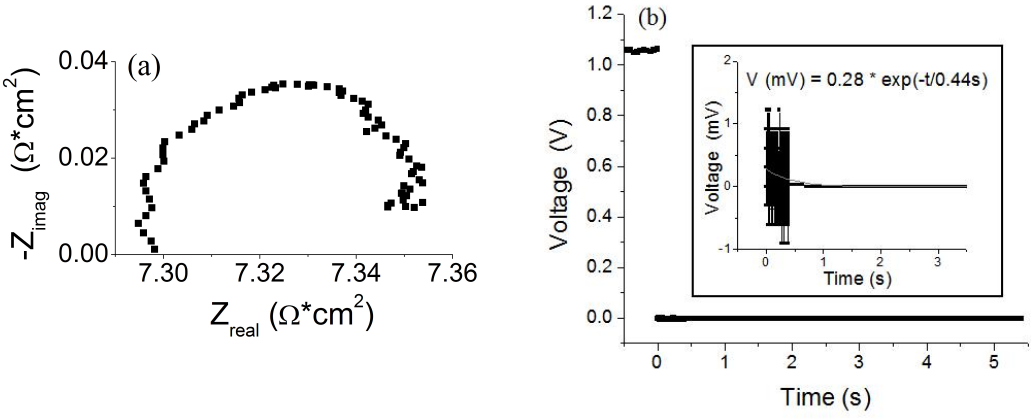


(a) Nyquist representation of ACIS measurement. (b) Sample GCI measurement. Inset: electrode relaxation with fit to 2nd order exponential decay.

Figure 4.26: Sample Measurements at 240 °C of Pt-based electrode mixture (platinum black, fine $CsH_2PO_4$ , 40 wt.% Pt on carbon, and naphthalene , 3:3:1:1 by wt) in humid (0.33 atm $pH_2O$)hydrogen.

Single-chamber tests in symmetric hydrogen confirmed the low resistance of platinum-based anodes - approximately 0.05 $\Omega cm^2$ Because the electrode resistance was so low, the electrode relaxation proved too small for GCI tests to measure accurately. Even at high currents, as in figure 4.26, the electrode response is within the noise of the switch.

In oxygen, however, the lower characteristic frequency translates to a larger time constant for the voltage relaxation and the much higher resistance makes GCI a viable tool for studying cathode kinetics. Figure 4.27 shows a representative nyquist plot and GCI voltage vs time chart.

The shape of the nyquist plot is similar to that obtained from the full symmetric cell, and the GCI measurement displays relatively clean behavior - *e.g.* a stable voltage for a given current, then a sharp drop as the current is shut off, followed by an exponential decay to the equilibrium voltage. Testing each cell at a number of initial currents, and fitting the exponential decay after the current is turned off, yields the working electrode overpotential as a function of current (which is only tested in the cathodic direction). A series of these overpotentials for a single cell are compiled in figure 4.28(a) and in tafel representation in figure 4.28(b).

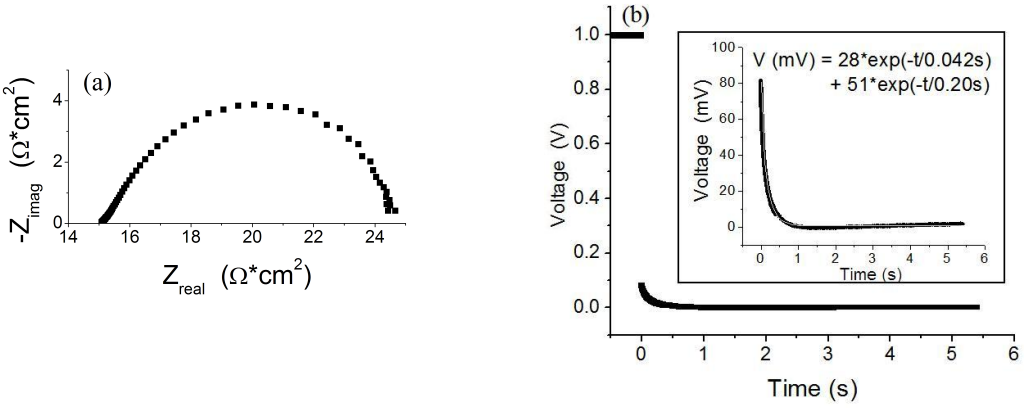


(a) Nyquist representation of ACIS measurement. (b) Sample GCI measurement. Inset: electrode relaxation with fit to 2nd order exponential decay.

Figure 4.27: Sample Measurements at 240 °C of platinum-based electrode mixture (platinum black, fine $CsH_2PO_4$ , 40 wt.% Pt on carbon, and naphthalene , 3:3:1:1 by wt) in humid (0.33 atm $pH_2O$)oxygen.

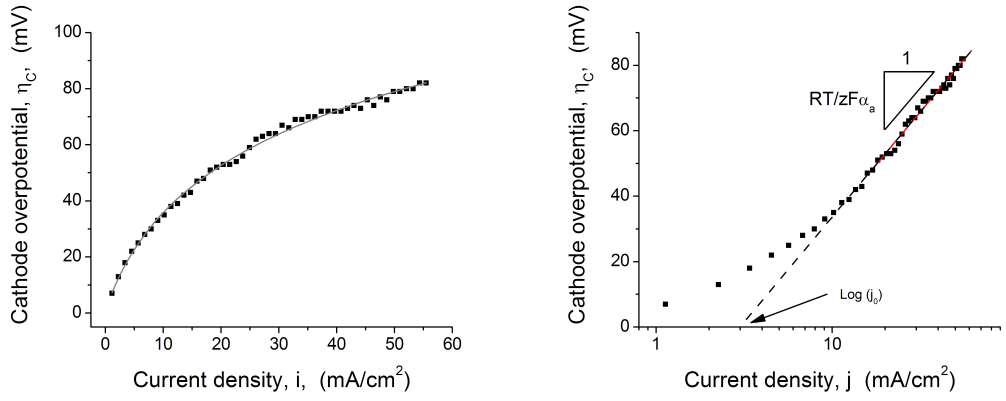


(a) Compiled $\eta$ vs current density.

(b) In Tafel represntation.

Figure 4.28: Compiled single-cell three-point GCI measurements at 240 °C of a single cell with platinum-based electrode mixture (platinum black, fine $CsH_2PO_4$ , 40 wt.% Pt on carbon, and naphthalene , 3:3:1:1 by wt) in humid (0.33 atm $pH_2O$)oxygen.

Three-point GCI measurements are seen to yield the expected qualitative behavior for platinum-based cathodes; namely, Tafel-behavior. Analyzing GCI measurements, however, allows separation of intrinsic properties (Tafel slope) from extrinsically influenced properties (exchange current density). Histograms of each for the 20 datasets are shown in figure 4.29.

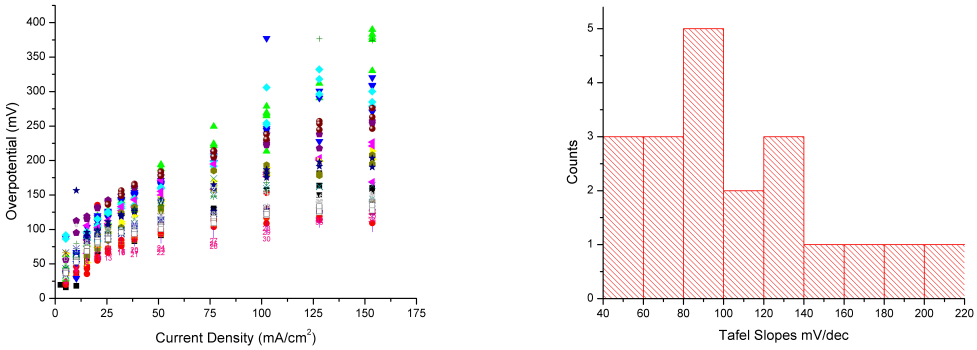


(a) Compiled Overpotential vs Current Density. (b) Histogram of Tafel slopes from fitting to $\eta$-j data.

Figure 4.29: Compiled single-cell three-point GCI measurements at 240 °C of platinum-based electrode mixture in humid (0.33 atm $p\mathrm{H_2O}$)oxygen.

The scatter in total electrode performance is evident from figure 4.29(a), but given the range of total performance seen from fuel cell operation in figure 4.3, this does not necessarily invalidate the method. The histogram in figure 4.29(b), however, shows that the measured Tafel slopes are significantly lower than expected from figure 4.4. In fact, the mean of 108 (+/- 45) mV/dec is less than the theoretical minimum for a one-electrode process, 120 mV/dec (corresponding to $\alpha$=1).

### 4.3.2 Conclusions

Unfortunately, it is evident that accurate reference electrode measurements are prohibitive to implement. Zero-bias AC impedance on such cells does not yield any information that could not be obtained more accurately with a symmetric cell. Kinetic properties, measured by galvanostatic current interrupt may initially appear to probe the electrode kinetics, but analysis shows that these measurements on this cell geometry are unable to predict the operating kinetics of platinum-based electrodes. On the whole, it is evident that kinetic studies on solid electrolyte cells would be facilitated by a more robust experimental approach.

## 4.4 Summary of standard experimental approaches for electrode characterization

The standard approaches are only somewhat useful in characterizing electrodes in the $CsH_2PO_4$ -electrolyte fuel cell system.

While the dual-chamber construction enables kinetic studies, it does not, in itself, determine losses at individual electrodes. Additionally, difficulty sealing between anode and cathode chambers introduces quantitative uncertainty by modifying the open circuit electrochemical potential. Qualitative information can be gleaned, however, as the mechanism of the primary rate determining step in the electrodes is identified as Tafelian. Though solid-state diffusion can result in similar $j - \eta$ behavior, charge-transfer is a more likely mechanism given the low conductivity of hydrogen through platinum.

In single chamber environments, we can apportion the zero-bias impedances of the anode and of the cathode by flowing hydrogen and oxygen, respectively. By doing so, we can determine the zero-bias impedance of the cathode is several orders of magnitude greater than that of the anode. High-quality quantitative understanding is, however, confounded by mechanical instability in the case of the platinum anode; and chemical instability in the case of the platinum cathode. Lastly, electrode kinetics, and therefore mechanisms, are inaccessible due to the two-point convolution of forward and backward reactions.

Though a significant amount of time and effort was devoted to implementing reference electrodes as a method of isolating electrode kinetics, the measurements remained irreproducible and inaccurate (when checked by comparison to operating fuel cell electrodes). Even recourse to investigating thick electrolytes (thus relaxing requirements for reference electrode placement) proved unfruitful. This methodology was therefore necessarily abandoned.

Lastly, there is little ability to compare different electrode materials in a meaningful manner in any of these approaches, as it is prohibitively difficult to control electrode material morphology and microstructure in porous structures with any degree of accuracy.

In summary, the standard approaches used for characterizing electrodes of polymer electrolyte fuel cells and of solid oxide fuel cells are, for this intermediate temperature application, ill-suited. Unlike most high-temperature systems, strong non-linearities necessitate kinetic studies. Then too, the solid electrolyte complicates the implementation of reference

electrodes. The development of an alternative approach, then, became a primary focus of my research efforts.

# Chapter 5

# Modelling Asymmetric Geometries

## 5.1 Introduction

Electrochemical studies of the interfacial reactions in solid electrolyte fuel cells have often taken the form of alternating current impedance spectroscopy at zero bias in a symmetric gas environment. As discussed in section 4.2, studies of symmetric- electrode cells in symmetric environment are unable to probe reaction kinetics effectively due to the convolution of the forward and reverse electrodes, as described in equation 4.4.

In order to study the forward and reverse reactions independently, it is typical to employ a reference electrode placed at an appropriate location. This strategy is furthermore often implemented in conjunction with an asymmetric gaseous environment in which one electrode is supplied with the reductant gas and the second with the oxidant, creating a voltage across the electrolyte. In such a case the impedance measurements are most often performed in the absence of any additional d.c. voltage bias. While this approach has provided important insight in many instances, the challenges inherent in obtaining sufficient seals and in properly placing the reference electrode are non-trivial and can generate results that are difficult to interpret.[(9), (10)]

An alternative to the reference-electrode method for the study of asymmetry in electrochemical reactions, specifically, reactions on solid oxygen ion conductors, was proposed by Fabry and Kleitz in 1974 [(20)]. These authors outlined a geometric approach in which the interfacial area of the working electrode is made very small relative to that of the counter electrode. It is then presumed that, as a consequence of this geometric asymmetry, the observed electrode response is dominated by the behavior of the working electrode. Thus, at non-zero current flow, with the reaction at the working electrode occurring in only one

direction, the polarization characteristics specific to this direction are revealed. The asymmetric geometry does not eliminate the contribution of the electrolyte to the total voltage drop of the electrochemical cell; however, the electrolyte characteristics can be evaluated using either current interrupt methods or impedance spectroscopy.

In recent years, geometrically well-defined point and patterned microelectrodes have received increasing attention from the fuel cell community. However, few researchers have exploited the benefits of the resultant constriction of the electrochemical current at the working electrode. In most instances a reference electrode is retained as part of the configuration [(21)(22)(23)(24)(25)(26)]. In contrast to this trend, Fleig and coworkers [(27)(27)(28)(29)(30)(31)] have adopted a point electrode geometry that is explicitly reference-less. For dense, surface-limited electrodes, the assumption that the point geometry has effectively eliminated the contribution of the counter electrode is likely valid. However, the microstructure examined bears little relation to composite electrocatalyst mixtures employed in 'real' fuel cells. Indeed, Pt studies in chapter 8 indicate a substantial difference in the electrochemical behavior between solid and porous electrodes. In 2008, Uda et al. proposed a refinement of the reference-less method [(32)] in which the area of the working electrode is restricted, but the microstructure of interest is retained. In principle, this allows one to take advantage of a measurement geometry that is free of complications due to misalignment of reference electrodes and apply it to a 'realistic' composite electrode. Again, however, it is assumed, without direct validation, that the response of the counter electrode is negligible.

In the present work we carry out a combined computational and experimental study to determine under which conditions the critical assumption of the reference-less geometry - that the counter electrode can be neglected - applies. The model is verified, and the impact of the counter-electrode is discussed in the specific context of electrochemical reactions at the interface between platinum and the solid acid electrolyte CsH2PO4. Viability of this electrolyte for fuel cell applications has been demonstrated [(33)]and, furthermore, for cells fabricated with 25 m thick membranes, it has been shown that electrocatalysis is rate-limiting [(5)]. Hence, study of the Pt-CsH2PO4 interface has both scientific and technological relevance. In the specific implementation of the reference-less geometry here, the electrolyte contribution to the system voltage drop is experimentally determined by A.C. impedance spectroscopy. While this technique provides the added advantage of revealing the

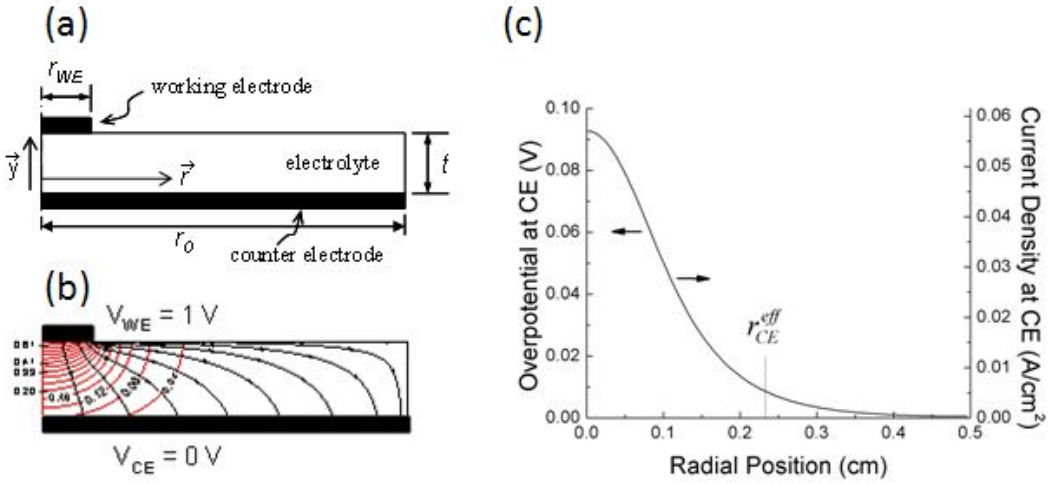


Figure 5.1: (a) Cell geometry in the reference-less configuration; (b) example of calculated equipotential and current lines; and (c) overpotential and current density at the interface between the electrolyte and the counter electrode. Calculations performed for $k$=0.615 $\Omega^{-1}$ cm$^{-2}$, $\sigma$ = 0.021, $t$=0.1 cm, $r_{WE}$= 0.0691 cm, and $r_0$ = 0.5 cm.

occurrence of any multi-step electrode processes, a detailed examination of electrochemical reaction pathways is beyond the scope of the present study.

## 5.2 model description

The geometry of interest, which displays cylindrical symmetry, is shown in figure 5.1(a). An electrolyte disc of thickness $t$ and radius $r_0$ is contacted along the entirety of one of its faces with a counter electrode and the opposing face with a centrally placed microelectrode electrode of radius $r_{WE}$. The voltage at the counter electrode is set at zero, and a fixed nonzero voltage is applied at the working electrode.

The resulting potential distribution in the electrochemical cell, $\phi(r, y)$ is a function of both radial position $r$ and vertical position $y$ and is governed by Laplace's equation, given in cylindrical coordinates as

$$\frac{1}{r}\frac{\partial}{\partial r}\left(r\frac{\partial \phi}{\partial r}\right) + \frac{\partial^2 \phi}{\partial y^2} = 0 \tag{5.1}$$

The (ionic) current density, $j$, through the electrolyte depends on the potential gradient

according to Ohm's law, which, for a cylindrical coordinate system is given as

$$j = \sigma \nabla \phi(r, y) = j_r(r, y)\hat{r} + j_y(r, y)\hat{y} \tag{5.2}$$

$$j_r = \sigma \frac{\partial \phi}{\partial r} \qquad\qquad j_y = \sigma \frac{\partial \phi}{\partial y} \tag{5.3}$$

where $\sigma$ is the ionic conductivity of the electrolyte (taken to be independent of position, $j_r$ and $j_y$ are the current densities in the radial and vertical direction, respectively, while $\hat{r}$ and $\hat{y}$ are the unit vectors in the $r$ and $y$ directions, respectively.

At the electrodes, the finite electrocatalysis kinetics generate a potential drop across each of the electrode — electrolyte interfaces, beyond the potential change induced by electrochemical equilibration between the metal and electrolyte. This potential drop, referred to as the overpotential, $\eta$, in the general case, displays a non-linear dependence on current, as already noted above. At sufficiently small overpotentials, however, the behavior can be approximated as linear, and the interfacial current density $j_\perp$, is proportional to the overpotential according to

$$j_\perp = k\eta = \pm k(\phi^{electrolyte} - \phi_0^{metal}) \tag{5.4}$$

where the proportionality constant, $k$, is the reaction rate constant (inversely proportional to the interfacial area specific resistance and also taken to be independent of position), $\phi^{electrolyte}$ is the potential at the electrolyte side of the interface, and $\phi_0^{metal}$ is the potential at the metal side of the interface, and, where appropriate, additional subscripts WE and CE are used to specify these terms as being those of the working or counter electrode, respectively. (the specification $\pm$ ensures that the overpotentials at the two electrodes are the same sign, with + for the working electrode and - for the counter electrode.) An implicit assumption in this expression is that the electron distribution within the electrolyte does not change within the time scale of the experiment, justifiable for large band-gap electrolytes such as $CsH_2PO_4$ . This boundary condition further relates the overpotential at the electrode to the electrolyte properties. Specifically, considering equations 5.3 and 5.4, one obtains

$$\eta = \frac{j_\perp}{k} = \frac{-\sigma}{k} \left. \frac{\partial \phi}{\partial \hat{y}} \right|_{y=0,t} \tag{5.5}$$

The boundary condition at the remaining electrolyte surfaces, including the exposed upper boundary (*i.e.* that not covered by the working electrode) and the two vertical boundaries at $r$=0 and $r$=$r_0$ are simply that the flux through the boundary is equal to zero. At r=0, the zero flux condition results from the axial symmetry of the electrochemical cell. At the other two boundaries, the zero flux condition is a result of electrical insulation. Along with the transport and Laplace equations, the boundary conditions and the material properties, $\sigma$ and $k$, fully define the potential profile within the electrochemical cell. The solution, $\phi(r, y)$, is obtained here numerically using an in-house program written by Dr. Yong Hao, based on the finite-volume formalism and finite-difference discretization [(34)]. The finite volume approach enables representation of partial differential equations as algebraic equations, whereas the finite difference discretization provides the specific algebraic expression. Here, Laplace's equation (Eq. 5.1) is discretized on an axisymmetric cylindrical coordinate system within the electrolyte. Since both equation (Eq. 5.1) and the boundary conditions (5.4) are linear, the discretization yields a system of linear algebraic equations with the unknowns being the values $\{\phi_i\}$ defined at each grid point. This system of equations is then solved iteratively to yield $\{\phi_i\}$. Because the gradient in the potential is much greater in the vicinity of the working electrode than in that of the counter electrode, the numerical mesh used for the computation was made fine in the vicinity of the electrode interfaces (in the regions close to $r$=0, $r$=$r_{WE}$ and $y$=0, $y$=$t$) and progressively coarsened towards teh center and insulating boundaries. For a given mesh, convergence of $\{\phi_i\}$ was defined to be satisfied when the relative variation of each $\phi_i$ became smaller than a specified value, typically 1E-8, whereas the appropriate mesh resolution was assured by computing $\{\phi_i\}$ for progressively finer meshes until the results became insensitive to higher resolutions. An initial validation of the solution procedure was performed by ensuring that, under several limiting conditions, known analytical or computational results were reproduced: (1) the Newman result for a finite-radius cylindrical electrode in the limit of a semi-infinite electrolyte [(35)]; (2) the conventional parallel plate resistor result in the limit of $r_{WE}$=$r_0$; and (3) the spreading resistance result of Denhoff [(36)] in the limit $r_0 \rightarrow \infty$ and $k$=$\infty$.
An example of a typical computed potential distribution profile is shown in figure 5.1(b) with current distribution normal to the equipotential lines. Several points are noteworthy. First, as implied through the use of a global reaction constant, it is assumed here that the entirety of the interface between the working electrode and electrolyte is electrochemically

active. That is, no attempt is made to simulate the real physical situation in which isolated triple-phase boundaries within this interface are the sites for electrochemical activity. Hence, the simulation yields equipotential lines that vary smoothly in the vicinity of the electrodes. Second, the majority of the flux follows the shortest path from the working electrode to the center of the counter electrode. That is, the current density is at a maximum close at close to $r$=0 and falls rapidly as $r$ approaches $r_0$. Turning to the behavior of the potential, at the working electrode, $\phi_{WE}^{electrolyte}$ varies only slightly with radial position. In contrast, at the counter electrode, because of the concentration of the flux close to $r$=0, the potential $\phi_{CE}^{electrolyte}$ displays a strong dependence on radial position. Indeed, at any given radial position, the ratio between interfacial current density and overpotential is simply the rate constant, as expressed in Eq.(5.4), behavior that is captured in figure 5.1(c).

Given that the electrode overpotentials are not single-valued quantities, it is not immediately obvious how one can compare the relative contributions of these overpotentials to the total voltage drop across the cell. Specifically, the challenge is to define a single-valued effective voltage at the electrolyte side of the interface. The approach taken here is as follows. It is proposed that the interfacial power dissipation, $P$, obtained from an integration of the position dependent quantities must equal the power dissipation obtained from the evaluation of single-valued parameters. Specifically, for the case of the counter electrode positioned at $y$=0, the power computed from a point-wise integration is

$$P = 2\pi \int_0^{r_0} j(r) \cdot \phi(r, y = 0) r dr \tag{5.6}$$

whereas that expected from single-valued parameters is

$$P = I\eta_{CE}^{eff} = \left(2\pi \int_0^{r_0} j(r) \cdot r dr\right) \eta_{CE}^{eff} \tag{5.7}$$

where $I$ is the total current (easily computed as a single value), and $\eta_{CE}^{eff}$ is the effective electrode overpotential. Equating these two definitions of power yields

$$\eta_{CE}^{eff} = \frac{\int_0^{r_0} j(r) \cdot \phi(r, y = 0) r dr}{\left(2\pi \int_0^{r_0} j(r) \cdot r dr\right)} \tag{5.8}$$

A similar expression is readily obtained for the working electrode by performing the integration at y=t. With these overpotentials so defined, the extent of isolation, $\xi$, is

simply defined as the ratio of the overpotential at the working electrode, $\eta_{WE}$, to the total electrode overpotential:

$$\xi = \frac{\eta_{WE}}{\eta_{WE} + \eta_{CE}} \tag{5.9}$$

The closer this value to 1.0, the more effective the asymmetric geometry in providing the desired electrochemical data. For a geometry in which $r_{WE} \leq r_{CE} = r_0$ (with $k_{CE}$=$k_{WE}$) the isolation has a minimum possible value of 0.5.

From the overpotential at the counter electrode, equation 5.8 and the total current, the total interfacial resistance at the counter electrode can be computed:

$$R_{CE} = \frac{\eta_{CE}}{I} \tag{5.10}$$

If it is assumed that the area-specific interfacial resistance, $R^*$, and in particular that of the counter electrode, $R^*_{CE}$, is a fixed material constant (equal to the inverse of the reaction rate constant, $k$), the total interfacial resistance then implies an effective area, and hence effective radius, $r^{eff}_{CE}$, over which the current density at the counter electrode is significant. Specifically,

$$R^*_{CE} = \frac{1}{k} = R_{CE} \cdot \pi (r^{eff}_{CE})^2 \qquad \Rightarrow \qquad r^{eff}_{CE} = \sqrt{\frac{1}{\pi k R_{CE}}} \tag{5.11}$$

the radius value is indicated in figure 1(c) and it is evident that at $r$=$r^{eff}_{CE}$, the overpotential and current density have fallen significantly, to 9.5% of their respective peak values.

## 5.3 Computational Results

While it is possible to evaluate the effective radius of the counter electrode, $r^{eff}_{CE}$, using the numerical procedures described above for any given set of input parameters, or even to evaluate the dependence of $r^{eff}_{CE}$ on a particular parameter with all others fixed, of greatest utility is a high-quality analytical approximation that enables immediate evaluation of $r^{eff}_{CE}$ (and $\xi$) without recourse to such a computation. The first step in establishing such an approximation is the selection of the appropriate parameter space of relevance. It can be readily anticipated that $r^{eff}_{CE}$ will depend on the material parameters, $\sigma$ and $k$, and on the geometric parameter $t$. In contrast, the geometric parameter $r_{WE}$ can be expected to have

a negligible impact on the current and field lines when $r_{WE} < t$, and, similarly, that $r_0$ will have no impact in the limit $r_0 \to \infty$, expectations that are confirmed below. Accordingly, simulations were performed over a range of values of $\sigma$, $k$, $t$, and $r_{WE}$, as specified in Table 5.1, under the constraint that $r_{WE} < t$ and for a fixed, large value of cell radius, $r_0$ (set to 3 cm).

Table 5.1: Range of numerical calculation input parameters used in generating figure 5.2 and the parametric fit expressed in Eq. 5.12. Computations carried out with $r_0$ (=3 cm) $>> r_{CE}^{eff}/t$

| Parameter | Minimum | Maximum | Units |
|---|---|---|---|
| Reaction rate constant, $k$ | 0.01 | 3.162 | $(\Omega\ \mathrm{cm}^2)^{-1}$ |
| Thickness, $t$ (with $t > r_{WE}$) | 0.03 | 1.0 | cm |
| WE radius, $r_{(WE)}$ | 0.005 | 0.05 | cm |
| Conductivity, $\sigma$ | 1E-3 | 1E-1 | $(\Omega\ \mathrm{cm})^{-1}$ |
| Cell radius, $r_0$ | 3.0 | 3.0 | cm |

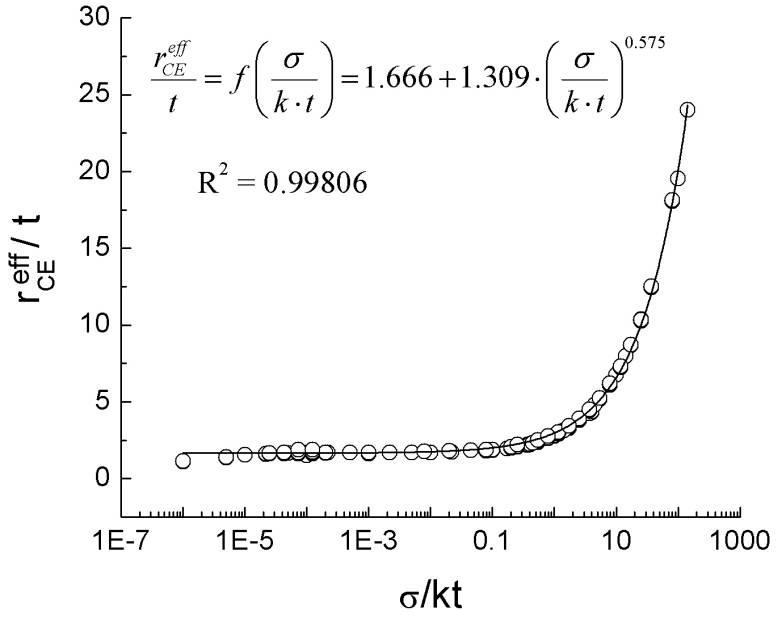


Figure 5.2: Correlation between the dimensionless parameters $r_{CE}^{eff}/t$ and $\sigma/kt$ after with variables ranges defined in table 5.1. Points are the results of the numerical calculations, limited to results for which $r_{CE}^{eff} < 0.85\ r_0$, and the line is the best fit to the inset allometric function.

Each parameter was varied over at least two orders of magnitude. Although the ranges for the material and geometric parameters are selected to represent experimental systems,

no generality is lost as a consequence of the specific ranges selected. Each computation was composed of approximately 15,000 grid points, whose spacing was refined to yield higher resolution in the vicinity of the electrode-electrolyte interfaces, as already noted above. Using 470 computed values of $r_{CE}^{eff}$ which obeyed the additional constraint $r_{CE}^{eff}$¡ 0.85 $r_0$, it was ultimately found that the results, figure 5.2, could be described by the allometric function:

$$\frac{r_{CE}^{eff}}{t} = f\left(\frac{\sigma}{k \cdot t}\right) = 1.666 + 1.309 \cdot \left(\frac{\sigma}{k \cdot t}\right)^{0.575} \tag{5.12}$$

For $\sigma/kt$ values between 1E-6 and 100. As anticipated above, by restricting the geometries to those in which radius of the working electrode is less than the electrolyte thickness, $r_{CE}^{eff}$ is independent of $r_{WE}$.

Embodied in the results presented in figure 5.2 and the expression above is the dependence of $\xi$ on material properties $\sigma$ and $k$ and the geometric parameters $t$ and $r_{WE}$. The explicit relationship is obtained by noting that the total current passing through each of the electrodes is the same,and further more that the reaction rate constants for the two electrodes are the same. Using these equalities and making the reasonable assumption that $r_{WE}^{eff} \approx r_{WE}$, one obtains from Eq. 5.8

$$\xi = \frac{R_{WE}}{R_{WE} + R_{CE}} = \frac{1}{1 + (r_{WE}/r_{CE}^{eff})^2} \tag{5.13}$$

where $r_{CE}^{eff}$ can be directly computed from 5.12. As indicated above, it is to be expected that the solution to the Laplace equation with the given boundary conditions will be independent of cell radius in the limit $r_0 \to \infty$. To identify the conditions under which $r_0$ becomes significant, a series of calculations were performed in which, for a fixed value of $\sigma/k$ (=3.41x10$^{-2}$ cm) the overall cell radius was varied down to a small value (0.1 cm). In figure 5.3, the isolation is plotted as a function of overall cell radius for several specific values of the working electrode radius (specifically $r_{WE}$ = 0.2 mm, 0.4 mm, and 0.691 mm). Beyond the expected observation that greater isolation is achieved for electrodes with smaller contacts, it is apparent that in all three configurations, the isolation is independent of $r_0$ once the overall cell radius reaches a value approximately 20% greater than $r_{CE}^{eff}$, consistent with the criterion used to generate the data set of figure 5.2 (the value of $r_{CE}^{eff}$

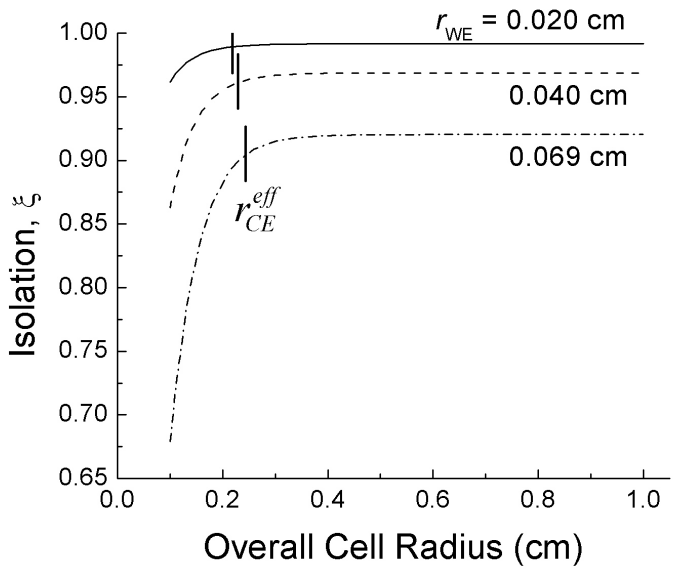


Figure 5.3: Dependence of isolation, $\xi$ on overall cell radius, $r_0$, for three different working electrode radii. Also shown are the $r_{CE}^{eff}$ calculated from equation 5.12. Results were calculated for $k = 0.615\ \Omega^{-1}\text{cm}^{-2}$, $\sigma = 0.021\ \Omega^{-1}\text{cm}^{-1}$, $t$=0.1 cm.

for each of the configurations is indicated directly on each plot). This behavior is consistent with the observation that the majority of the current flows through the central region of the cell and thus increasing the cell radius significantly beyond the calculated effective counter electrode radius has minimal impact on the potential profile. A key implication of this result is that for cells of sufficient radius, imprecision in placement of the working electrode does not impact the measured overpotential at that electrode. Such geometric insensitivity sharply contrasts that of typical reference electrode geometries in which slight misalignments in the placement of electrodes can have a major impact on the measured results [(9), (10)]. By relaxing the requirements of precision placement of electrodes, the reference-less configuration greatly simplifies the experimental fabrication steps.

It is of some value to consider the physical origin of the dependence of isolation on the dimensionless quantity $\sigma/kt$. Referring to equation 5.5, it is apparent that the overpotential $\eta$ is proportional to the local component of the gradient in the potential field along the direction normal to the interface, with the proportionality constant being the ratio of the two material parameters, $\sigma/k$. As a consequence, solutions for $\eta$, and accordingly, the isolation, depend not on the individual values of $\sigma$ and $k$ but rather on the ratio $\sigma/k$. The manner in which $\xi$ depends on this ratio is shown in figure 5.4 for several specific

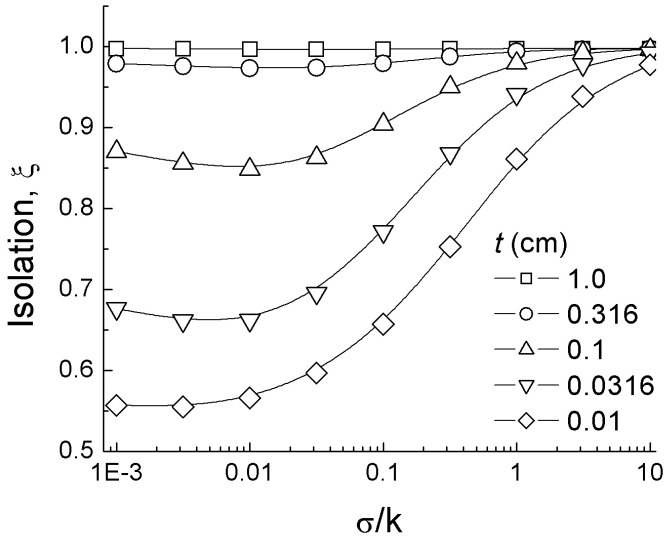


Figure 5.4: Dependence of isolation, $\xi$ on the ratio of intrinsic material properties, $\sigma/k$, for varying cell thicknesses, $r_{WE}$=0.1 cm, and $r_0$= 3 cm. Points represent computed values and solid lines are guides to the eye.

values of cell thickness, $t$, with a fixed working electrode radius, $r_{WE} = 0.1$ cm. Because $\sigma$ and $k$ were varied independently to obtain these data, it is possible to confirm that the resulting value of $\xi$ depends only on the ratio, as anticipated. Furthermore, the figure reveals that at a given $\sigma/k$ value, the isolation increases monotonically with thickness. This can be understood to result from the broadening of the current distribution at the counter electrode, which lowers the overpotential at that interface. Moreover, for a given cell thickness, it is apparent that the isolation reaches limiting values at both extrema in $\sigma/k$. At high $\sigma/k$ values, the electrolyte approaches a state of 'perfect' conductivity, and the isolation therefore approaches a value simply determined by the radii of the two electrodes. at low $\sigma/k$ values, the potential distribution within the electrolyte approaches that expected for perfect (reversible) electrodes, and the isolation approaches a value determined by $r_{WE}$ and $t$. Indeed, as evident from equation 5.12, in this limit, $r_{CE}^{eff}$ is simply $1.667t$, and hence the isolation, via equation 5.13, depends only on the ratio $r_{WE}/t$. Finally, although the origin of the shallow minimum in $\xi$ cannot be readily explained, this feature was confirmed, via extensive computations in this regime, to reflect the real behavior of the system, rather than a computational artifact of mesh resolution or convergence criterion.

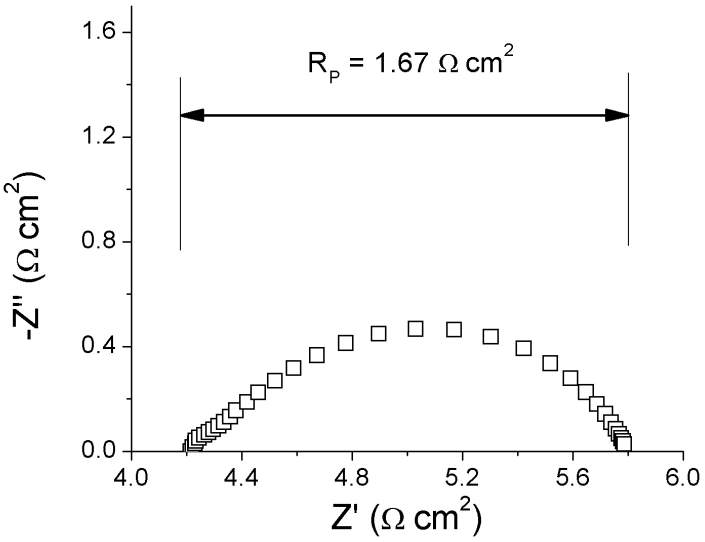


Figure 5.5: ACIS impedance for symmetric cell at 240 °C in humid (0.43 atm $p\mathrm{H_2O}$) hydrogen 5 hours after heating.

## 5.4 Model verification

Beyond cell geometry, two key experimental inputs are required for the evaluation of the potential profile and the extent of isolation of the voltage drop at the working electrode. These are the electrolyte conductivity, $\sigma$, and the inverse of the area specific resistance, $k$. These two terms were determined from an impedance measurement of an electrochemical cell with a simple, symmetric geometry as described in chapter 3. Composite electrodes were prepared from platinum black and $CsH_2PO_4$ combined in a 3:7 weight ratio and mechanically mixed. The tri-layer cell was fabricated by a co-pressing method in which the three powder layers were uniaxially cold-pressed between two 3/4" diameter porous sintered stainless steel disks at 125 MPa for 20 minutes.

As a demonstration of this microelectrode method, the electro-oxidation of hydrogen was probed.A.C. impedance measurements were carried out at uniform 240 °C in humid (0.43 atm $p\mathrm{H_2O}$) hydrogen flowing at 50 sccm.

The impedance spectrum obtained from the symmetrical cell is shown in Figure 5.5 in Nyquist form. It was found that the response could be best fit assuming two processes using an $(\mathrm{R}_{electrolyte})(\mathrm{RQ})(\mathrm{RQ})$ equivalent circuit and the sum of the latter two resistances is used to represent the total interfacial impedance, $\mathrm{R}_P$. From this impedance data, $k$ is

taken to be the inverse of the electrode area specific resistance. The value determined here, 0.615 $\Omega^{-1}$ $cm^{-2}$ is consistent with values measured in chapter 5. Similarly, the value of the electrolyte conductivity ($\sigma$ = 0.0210 $\Omega^{-1}cm^{-1}$), related to the impedance at the high frequency limit, is in excellent agreement with earlier reported values (37).

## 5.5 Experimental studies using the reference-less geometry

For the experimental implementation of the reference-less method, two asymmetric cells of the geometry developed by Uda et al (32)., termed here the microelectrode configuration, were fabricated. Both cells employed a $CsH_2PO_4$ + Pt composite mixture identical to that described above as both the counter electrode material and as the working electrode material, but with the working electrode applied to a limited area as described in Chapter 7. The working electrode areas (determined by optical microscopy after testing) were 1.47 $mm^2$ for the first microelectrode cell and 0.38 $mm^2$ for the second microelectrode cell, the $CsH_2PO_4$ electrolyte thicknesses were 1.2 mm and 7.1 mm respectively.

Electrochemical impedance and polarization measurements were carried out using the same apparatus employed for symmetric cell characterization and under the same experimental conditions. The D.C. polarization curves were collected by cyclic voltammetry (5 mV/s) with a range of ± 300 mV for the thinner cell (Cell 1), and ± 400 mV for the thicker cell (Cell 2). The latter was measured with a larger voltage excursion because the overall resistance is significantly higher.

## 5.6 Results and Discussion

The measured impedance spectra and electrode polarization curves, for both cells, are presented in figures 5.6 and 5.7, respectively. From the impedance data, the resistances due to the electrolyte and the electrodes (sum of the counter and working electrodes) are immediately available, and in both figures the results are corrected for the measured electrolyte resistance for ease of comparison.

Computationally, using the definition established for electrode overpotentials, Eq. 5.8, the voltage drop across the electrolyte is readily obtained and hence so is the electrolyte

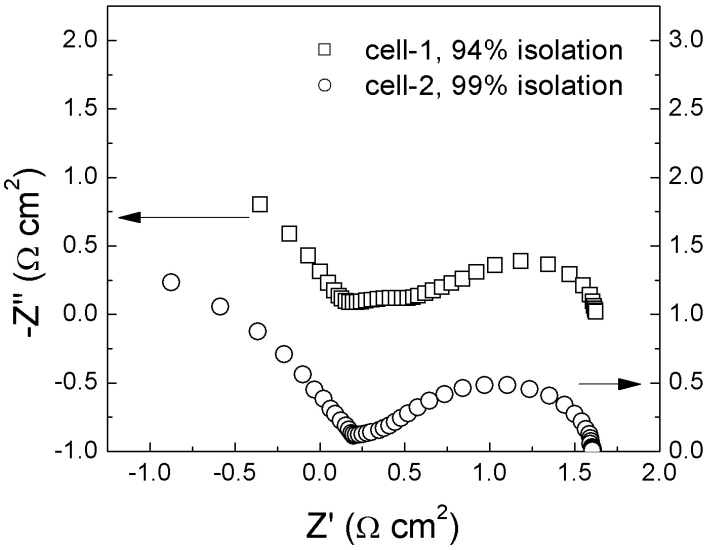


Figure 5.6: ACIS impedance of microelectrode cells at 240 °C in humid (0.43 atm $p\mathrm{H_2O}$) hydrogen 5 hours after heating. Data are corrected for $\mathrm{R}_S$ from fitting and normalized to the area of the working electrode measured by optical microscopy.

contribution to the system resistance, in addition to the resistances associated with each individual electrode. From the value of the potential drop across the electrolyte, it is noted that the strength of the electric field within the electrolyte remains below 3 V/cm, justifying the implicit assumption made in obtaining the electrode overpotential curves (Fig. 5.7) that the electrolyte is ohmic over the voltage range of the experiment. In table 5.2, a comparison is provided between the resistance values obtained from the complete calculation, the analytical prediction, and the experimental measurement in the referenceless geometry. The predicted value in the case of the counter electrode is then computed according to $R_{CE} = 1/(\pi(r_{CE}^{eff})^2 k)$ where the allometric expression (Eq. 5.12) is used to obtain $r_{CE}^{eff}$. In the case of the working electrode, it is simply the result directly implied by the electrode area, $R_{WE} = 1/(\pi(r_{WE})^2 k)$. In the case of the "experimentally" obtained isolation value, here again, the allometric expression is used to predict $r_{CE}^{eff}$ and thereby $R_{CE}$. - and isolation is made independently of a direct physical measurement of $r_{WE}$. That is, so long as the electrolyte thickness is greater than the radius of the working electrode, the isolation is largely insensitive to the exact value of $r_{WE}$, further relaxing the requirements of precision electrode fabrication.

Overall, it is apparent that there is excellent agreement between the three sets of values

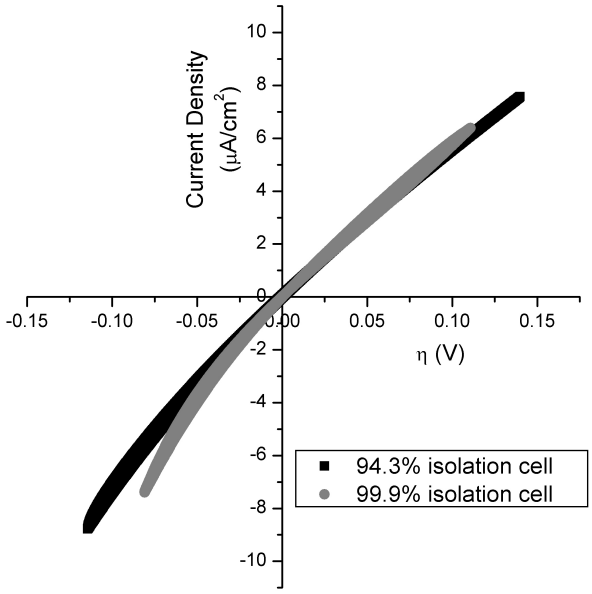


Figure 5.7: IR-corrected polarization curves from the two asymmetric powder composite (Pt:$CsH_2PO_4$ 3:7 by wt) microelectrode cells measured at 240 °C in humid (0.43 atm $pH_2O$) hydrogen. $R_S$ for correction was calculated from ACIS fit, while area for normalization measured by optical microscopy.

Table 5.2: Comparison between computed, predicted, and measured cell resistances for cells of two differing geometries and hence expected isolation values. Cell 1: $t$ = 0.12 cm, $r_{WE}$ = 0.684 m; Cell 2: $t$ = 0.71 cm, $r_{WE}$ = 0.348 mm

| | Cell 1 | | | Cell 2 | | |
|---|---|---|---|---|---|---|
| R (Ω) | Computed* | Predicted | Measured | Computed* | Predicted | Measured |
| $R_S$ | 141.5 | n/a | 142.1 | 626.0 | n/a | 659.3 |
| WE | 110.7 | 110.6 (a) | n/a | 438.0 | 427.9 (a) | n/a |
| CE | 7.3 | 6.8 (b) | n/a | 0.6 | 0.3(b) | n/a |
| $R_P$ | 118 | 117.3 (c) | 11 | 438.6 | 428.2(c) | 425.2 |
| $\xi$ (%) | 93.8 | 94.3(c) | 94.1(d) | 99.9 | 99.9(c) | 99.9(d) |

(*) Directly computed using the definition of overpotential provided in Eq. 8; (a) Estimated based on the area of the working electrode and the assumption of constant current density across the interface between the working electrode and the electrolyte; (b) Predicted based on the analytical allometric expression (Eq. 13); (c) predicted based on comments (a) and (b); (d) Determined based on comment (b), from which the counter-electrode resistance is evaluated, and the experimentally measured value for the total electrode resistance.

presented in table 5.2. The agreement between the computed and predicted electrode resistances (within a fraction of a percent for cell 1, and within 3% for cell 2), as well as between the isolation values, indicates that the allometric function provides a satisfactory representation of the computational results. The agreement between the computed and experimental results, in turn, validates the computational approch.

The IR-corrected polarization curve (Fig. 5.7) reveal important aspects of the electrochemical reactions which will be discussed in chapter 8. They can be used, however, to contextualize the isolation calculation further. At positive bias, the slopes decrease relative to equilibrium (become more resistive), whereas at negative bias, the slopes increase (become less resistive). Additionally at positive bias, the two curves agree very well with each other, while at negative bias, they diverge. These two observations - the asymmetry of IV characteristics and divergence are, in fact, manifestations of the same phenomenon. As proton reduction occurs at the working electrode, hydrogen oxidation, with its lower reaction rate constant, occurs at the counter electrode. With increasingly negative bias, the relative contribution of the working electrode to the sum of the electrode overpotentials decreases, and the extent of isolation decreases relative to the value at zero-bias. Accordingly the data become more and more "polluted" with the contribution of the counter electrode and this effect is greater for the cell with a lower isolation value. This result indicates that an extremely high degree of isolation at zero bias is required if the experiment is to retain a sufficiently high level of isolation over the entire voltage range. Conversely, isolation improves under forward bias as the counter electrode becomes less resistive and the working electrode more. This behavior of isolation with bias is not general, but rather depends on the electrode of interest's kinetics.

Considering only the results at zero-bias, in the case of cell 1, the 94% isolation indicates that attribution of all the non-electrolyte impedance to the working electrode leads to an overestimation of the potential drop at this electrode by  5%. Consequently, an assumption without validation that the electrode overpotential is sufficiently isolated at the working electrode for an apparently attractive geometry can easily lead to an underestimation of the electrochemical activity of an electrode material. Alternatively, if one follows the standard approach of using electrolyte resistance to calculate electrode area from Newman's equation, and then again makes the assumption that the counter electrode resistance ins ngligible, one would overestimate the radius of the working electrode by 23%. With this radius, the

total electrode resistance would be underestimated by 37%. These large under- and overestimates demonstrate the importance of accurately assessing the level of true isolation in a micro- or point electrode geometry.

These cautionary points notwithstanding, it is apparent that even cell 1, with a zero-bias isolation value of 0.94%, has a sufficiently confined working electrode such that the asymmetry of the electrochemical reaction, Eq. 4.4, is revealed. It is noteworthy that the hydrogen oxidation, relevant for fuel cell applications, remains apparently linear over the range of overpotentials that are typically encountered at the anode. The implication is that the rate constant obtained from a symmetric cell measurement is, in the case of $CsH_2PO_4$ -based fuel cells with Pt-based electrodes, applicable for a phenomenological description of anode behavior. More detailed analysis and discussion of this geometry is presented in chapter 8.

## 5.7 Conclusions

It is demonstrated that, as alluded to in the literature, a microelectrode geometry can be utilized to directly probe the electrochemical characteristics of a single electrode without the requirement of a reference electrode. The microelectrode geometry can constrain the electrode potential drops in the system such that the majority of the measured electrochemical impedance is due to the working electrode of interest. A direct correlation between isolation and geometric and material parameters is presented. From the complete numerical computations, the relationship, specifically, the dependence of the effective area of the counter electrode on the dimensionless quantity $\sigma/kt$, is explicitly mapped to a simple functional form. From $r_{CE}^{eff}$ and the assumption that the potential at the small, working electrode does not vary with radial position within $r_{WE}$, the extent of isolation is readily computed. It is further shown that geometries which might intuitively appear to provide sufficient isolation, can lead to gross over- or underestimates of material properties. Additionally, if the extent of isolation changes with bias, as would be generally be expected due to asymmetry of the electrochemical reactions' $j - \eta$ behavior, interpretations of the polarization curves can become increasingly difficult. thus direct determination of the extent of isolation is critical for the accurate determination of electrochemical behavior. With sufficient isolation, the referenceless geometry has the distinct advantage, as shown computationally, of being largely

insensitive to electrode placement. This stands in contrast to the strict requirements for accurate electrode placement in a conventional experiment utilizing a reference electrode. Lastly, the investigation of hydrogen redox kinetics in the platinum-$CsH_2PO_4$ system was used to confirm the computational methodology, but also revealed a kinetic asymmetry that does not fit to either Butler-Volmer or Fickian mass-diffusion characteristics.

# Chapter 6

# Experimental Methods for Asymmetric geometries

With the development of a viable approach to isolating electrode kinetics using a two-electrode geometry, an additional suite of experimental methods and infrastructure was developed.

## 6.1 Porous Asymmetric Geometry with powder composites

The principle advantage of Uda's composite electrode construction, over the dense microelectrodes generally employed in SOFC research, is that it provides a bridge between well-defined mechanistic studies and operational fuel cells by isolating an electrode with identical microstructure to the system of interest.

### 6.1.1 Design and Fabrication

The challenge involved in implementing asymmetric powder geometry was primarily one of maintaining uniform microstructure across a restricted (sub-millimeter) diameter - and of contacting the electrode without occluding gas access. Because of the success of PTFE seals in sealing dual-chamber cells, a PTFE mask was used to restrict the working electrode, as shown in figure 6.1. Electrical contact is made to the working electrode by way of a porous stainless steel mesh (of the same diameter as the $CsH_2PO_4$ -counter electrode half-cell) pressed against the working electrode. In addition to masking the electrode, the PTFE also provides mechanical adhesion between the electrolyte and the steel gas diffusion layer.

The process of fabricating cells with asymmetric powder electrode geometries is picto-

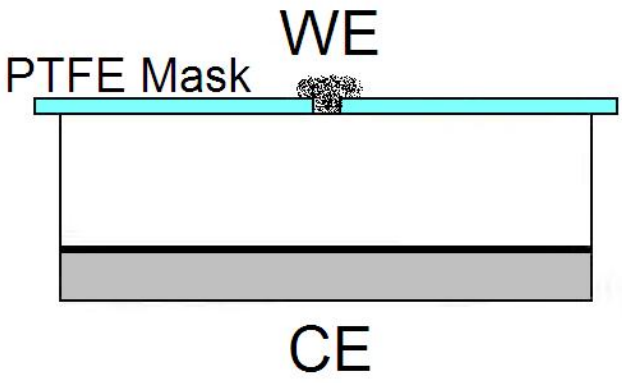


Figure 6.1: Schematic of a PTFE-masked powder composite electrode test cell with a porous counter electrode.

rially detailed in figure 6.2.

### 6.1.2 Test Infrastructure

All previous cell holders (both dual- and single-chamber) and testing equipment described in chapter 4 maintain their utility in studying this Geometry. With porous stainless steel supporting both electrodes, the cell externally appears identical to similarly supported full fuel cells.

### 6.1.3 Advantages of asymmetric powder electrodes

1. Uses same electrode composites as end-use cells.
2. Seals well with dual chamber construction.
3. Can use existing test infrastructure.
4. Can vary axial pressure on electrode-electrolyte interface.

### 6.1.4 Drawbacks of asymmetric powder electrodes

1. Poorly defined interfacial area.
2. Frequency dispersion of electrolyte complicates impedance fitting.
3. Poorly defined microstructure increases difficulty of material comparisons.

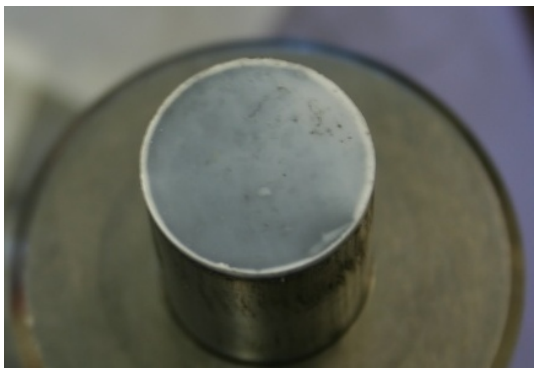

(a) Stainless steel-supported counter electrode + $CsH_2PO_4$ half-cell pressed optically clear.

(b) 1 inch wide PTFE tape with approximately 1 $mm^2$ aperture.

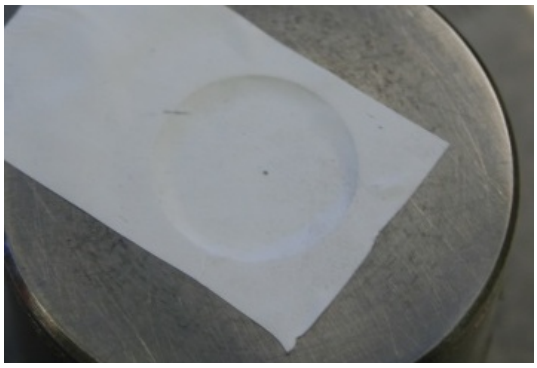

(c) Half-cell in die, covered with PTFE mask.

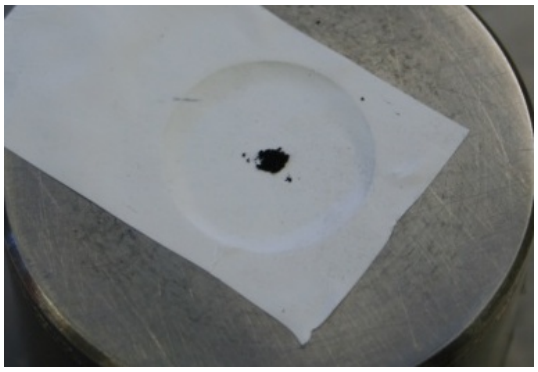

(d) 4 mg of Pt-$CsH_2PO_4$ composite electrode dispersed over mask

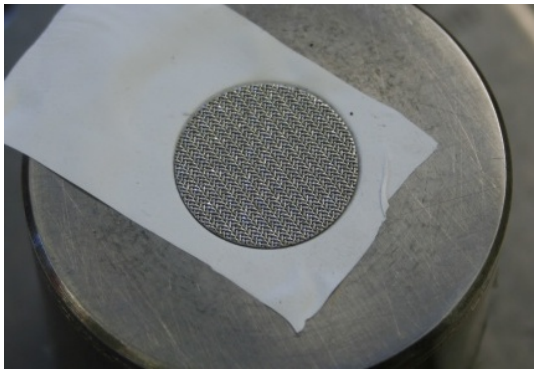

(e) Stainless steel mesh gas diffusion layer placed over working electrode

(f) Complete, pressed assembly. PTFE tape may be excised.

Figure 6.2: Photographs depicting the steps in fabricating asymmetric powder microelectrode test cells.

4. Low isolation.

Of these drawbacks, the most confounding is the last: low isolation. Despite working electrodes with interfacial areas orders of magnitude smaller than the geometric area of the counter electrode, significant contamination of measurements by the counter electrode can greatly skew measurements, invalidating subsequent conclusions. To demonstrate the effects of insufficient isolation, a 260 micron thick $CsH_2PO_4$ cell with a 0.025 $cm^2$ working electrode and a 2.8 $cm^2$ counter electrode was fabricated and tested at 242 °C . The nyquist plot in hydrogen shown in figure 6.3(a) reveals a total resistance of only 30 Ω , corresponding to an isolation of 82%.

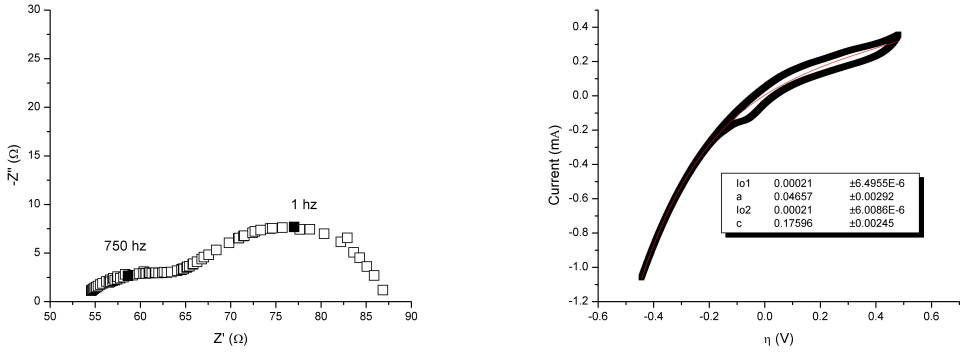


(a) ACIS Nyquist plot of a low-isolation Pt-$CsH_2PO_4$ powder microelectrode cell in humid (0.33 atm $pH_2O$)$H_2$.

(b) IR-corrected CV of a low-isolation Pt-$CsH_2PO_4$ powder microelectrode cell in humid (0.33 atm $pH_2O$)$O_2$. Despite a reasonably good fit ($R^2$=0.991), fit exchange coefficient for cathodic reaction is 0.17.

Figure 6.3: Sample study conducted on an insufficiently isolated powder microelectrode geometry.

The measured the cathodic behavior of the cell by slow rate cyclic voltammetry in figure 6.3(b) is qualitatively correct, but fitting to the Butler-Volmer equation yields an unphysical value for the exchange coefficient. Had we neglected the counter electrode, based on the two orders of magnitude difference in electrode areas, we would be led to a very incorrect conclusion about platinum-$CsH_2PO_4$ cathode behavior.

In fitting an unconstrained Butler-Volmer to the $j - \eta$ behavior of 6.3, the intrinsic exchange coefficient is calculated to be 0.176, far from the range of $\alpha$ = (0.417+/- 0.105) expected from fully symmetric, dual-chamber fuel cell tests in chapter 5. Thus, significant care must be taken to ensure that high-isolation configurations are achieved.

## 6.2 Dense Asymmetric Geometries: Wires

Of the considered working electrode geometries, the wire electrode is closest to that employed by Fleig and others in their studies of SOFCs. While they commonly deposit dense microelectrodes through patterned photolithography ((27)) or by deforming a wire against the electrolyte ((25)), neither option is readily available for use with the $CsH_2PO_4$ electrolyte. Water solubility and a plastic softness at operating temperatures necessitate the development of a novel approach.

### 6.2.1 Design and Fabrication

As shown later in Chapter 10, $CsH_2PO_4$ densifies quite readily at room temperature, so implementation of wire electrodes focused on impregnating the $CsH_2PO_4$ electrolyte with short lengths of wire. Initially, single wire cells were implanted and tested as schematically shown in figure 6.4(a).

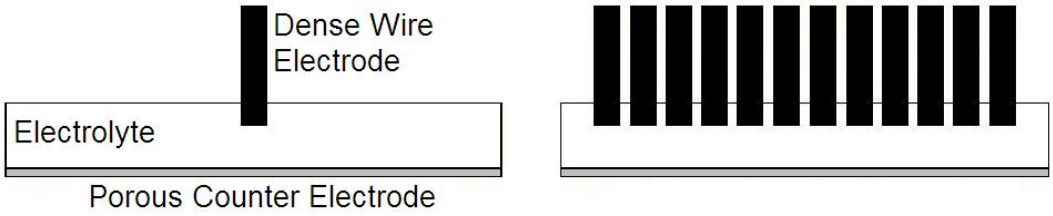


(a) Schematic of a single, extruding, dense wire electrode impregnated in $CsH_2PO_4$ with a porous counter electrode.

(b) Schematic of 12 extruding wire electrodes

Figure 6.4: Schematic of asymmetric wire-electrode assemblies.

This was considered a waste of run-time and real estate, however, so eventually the experimental capability was increased to test up-to 12 working electrodes on a single cell, as in figure 6.4(b)

Fabricating these cells provided an additional challenge. For wires electrodes that were to extrude beyond the electrolyte surface, a sacrificial naphthalene layer was utilized as in figures 6.5(a) and (b).

For flush wire electrodes, the short lengths of wire were simply stood on end and co-pressed into the remaining half-cell - as depicted in figure 6.5(c). The development of alternative fabrication methods was motivated by the desire to obtain well-defined, dense

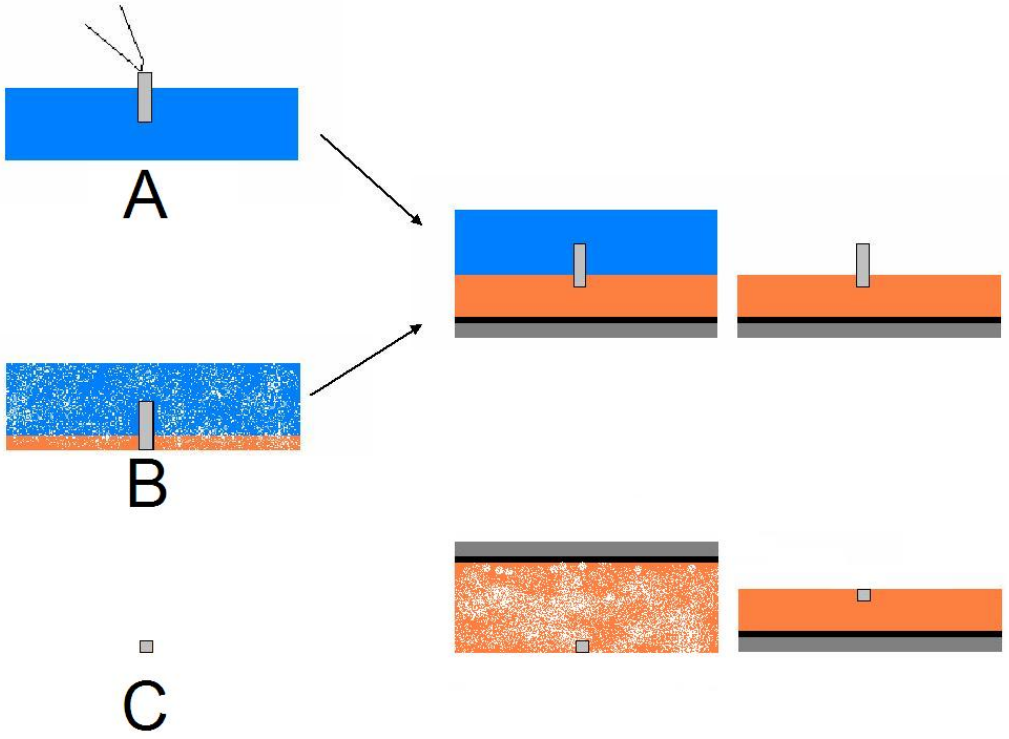


Figure 6.5: Three methods for fabricating wire-electrode test cells. A) A solid naphthalene (blue) disk is impregnated with a heated length of wire, then the remaining half-cell is pressed against the disk, the loose $CsH_2PO_4$ (orange) densifies around the extruding wire and the naphthalene is then sublimated. (B) The wire is stood vertically in loose $CsH_2PO_4$ , backfilled with loose naphthalene, pressed, and then follows (A). (C) A short length of wire is co-pressed with the half-cell.

triple-phase boundaries where the wire electrode contacts the $CsH_2PO_4$ electrolyte. Photographs of a cell made by fabrication method A are shown before the naphthalene is evolved in figure 6.6, and after sublimating in figure 6.7(a).

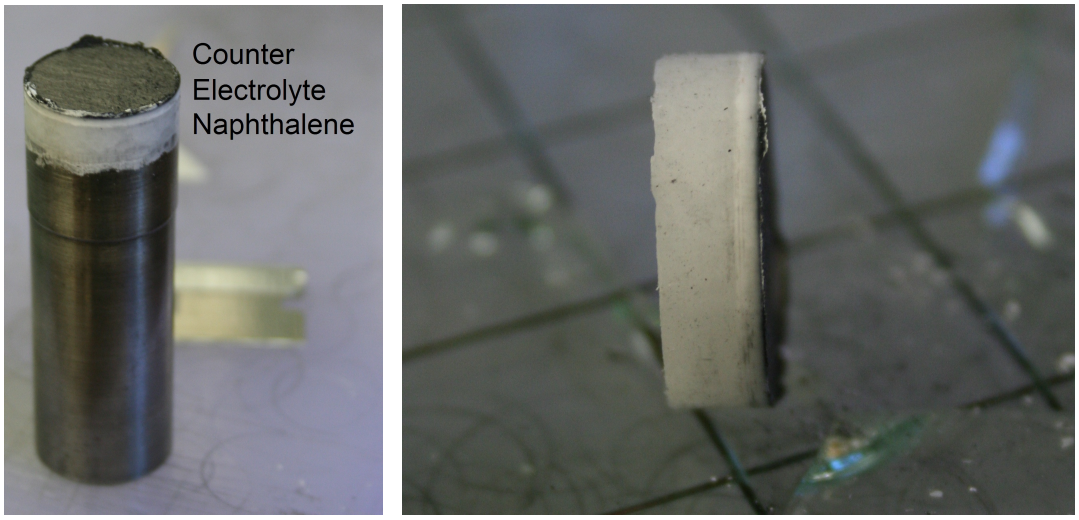


(a) Photograph of extruding wire electrode cell fabrication at second step of the fabrication process A or B depicted in figure 6.5.

(b) Photograph of wire-impregnated-naphthalene — $CsH_2PO_4$ — counter electrode cell before cleaning and sublimation

Figure 6.6: Photographs of a wire-impregnated-naphthalene — $CsH_2PO_4$ — counter electrode cell during fabrication.

After removing the naphthalene by melting most of it off and sublimating the remainder with a heat gun, the wire electrode is free-standing and can be contacted with the working electrode lead. The counter electrode is supported by a silver ring which also acts as a current collector.

The fabrication of a multiplexed wire electrode cell made by fabrication method B is shown in figure 6.8.

Fabrication method C was eventually adopted due to concerns regarding densification during pressing at the naphthalene-$CsH_2PO_4$ -wire interface. While fabrication is simpler, it requires additional care in preparing the wire electrodes. Flush wire electrodes are cut by hand with a razor blade under a stereoscope. Tested diameters of purchased wires ranged from 250 microns to 404 microns. In order to get the electrodes to stand on-end during co-pressing, a cut cylinder height of approximately 100-200 microns was generally attempted. Low magnification SEM micrographs of two electrodes cut from platinum wire are presented

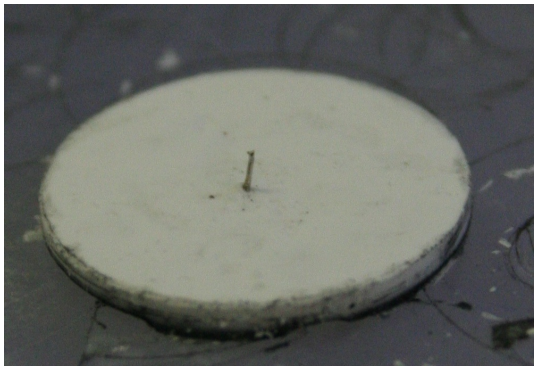

(a) Photograph of single extruding wire electrode cell as fabricated.

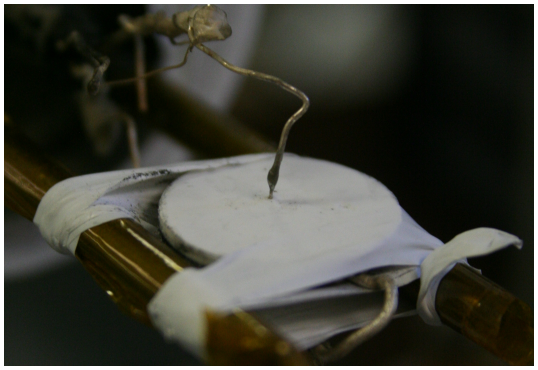

(b) Photograph of single extruding wire electrode cell fitted into symmetric test holder. Contact with working electrode is achieved by contacting lead with silver paint while the counter electrode (below) is contacted with a silver ring.

Figure 6.7: Photographs of an asymmetric wire electrode (single) cell as fabricated and loaded into single chamber cell-holder.

(a) Photograph of multiplexed wire cell at first stage of figure 6.5(b) before backfilling with naphthalene.

(b) Photograph of multiplexed wire cell after densification with naphthalene (and subsequent sublimation thereof), and loading into multiplexing cell holder.

Figure 6.8: Photographs of a multiplexed asymmetric wire electrode cell made by fabrication method B and loaded into multiplexing single chamber cell-holder.

in figure

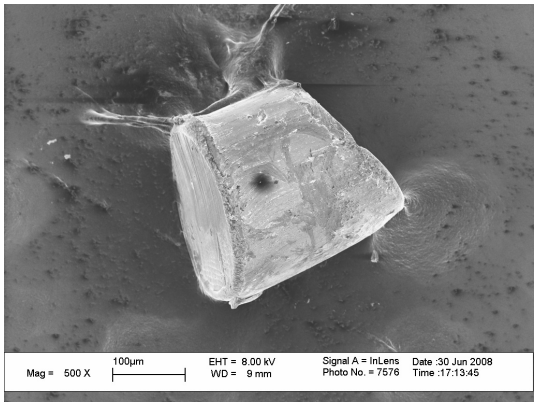


(a) SEM micrograph of a wire electrode cut with a vertically oriented razor blade.

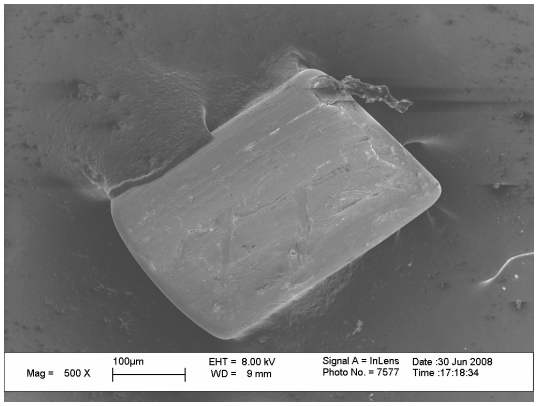


(b) SEM micrograph of a wire electrode cut with a double-ended obtuse angle oriented razor blade. This electrode was then sonicated in water, acetone, and ethanol for 20 minutes each.

Figure 6.9: SEM micrographs of cylinders cut from platinum wire. Angled cuts - as in (b) - are necessary to obtain parallel faces, while the surface roughness seen in (a) can be smoothed with sonication in solvents.

Even this approach, unfortunately, did not always result in high-quality triple-phase interfaces, as seen in figure 6.10 which shows relatively poor densification at the surface as pressed.

To investigate the $CsH_2PO_4$ -wire-gas interface, flush-electrode cells were fabricated and then broken, and the electrode carefully removed. The hollow, left by the electrode was then examined by SEM and shown in figure 6.11.

Given the sintering ability of $CsH_2PO_4$ , however, it was expected that the surface would densify, and the contact with the wire electrode would be come better defined with time at operating temperature. A wire electrode cell was fabricated and maintained at 240 °C in humid (0.38 atm $pH_2O$) hydrogen for 12 hours before cooling to room temperature. The SEM micrograph in figure 6.12 shows that the $CsH_2PO_4$ has, indeed, sintered which not only improved the triple-phase boundary, but also caused the electrolyte surface to recess slightly, relative to the electrode surface. As this moves the triple-phase boundary further away from the location of the cut, it is expected to yield a more representative description of the $CsH_2PO_4$ -wire-gas interface.

To investigate the $CsH_2PO_4$ -wire interface after heating, another cell was fabricated at 4 tons for 15 minutes, heated to 240 °C for 3 hours, cooled, broken, and the electrode was

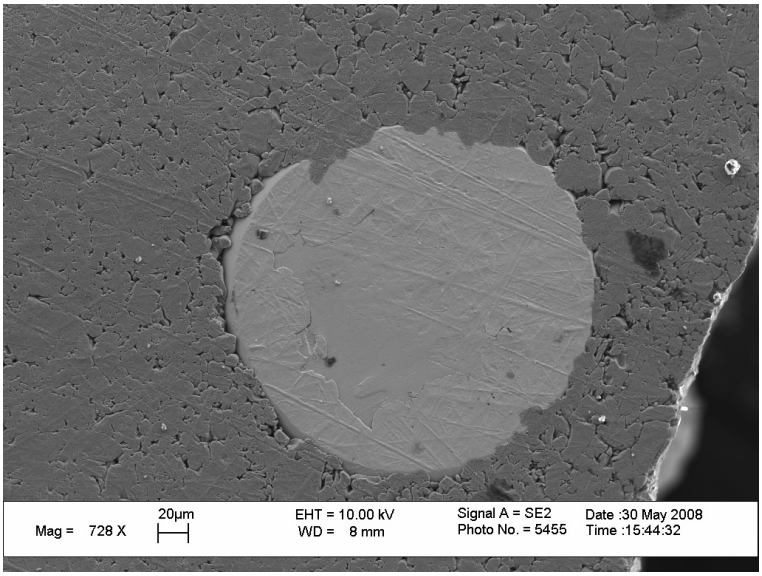


Figure 6.10: Top-down SEM microraph of a flush dense wire electrode cylinder co-pressed into a $CsH_2PO_4$ electrolyte. The cell was pressed at 4 tons for 15 minutes. Significant porosity can be seen at edges

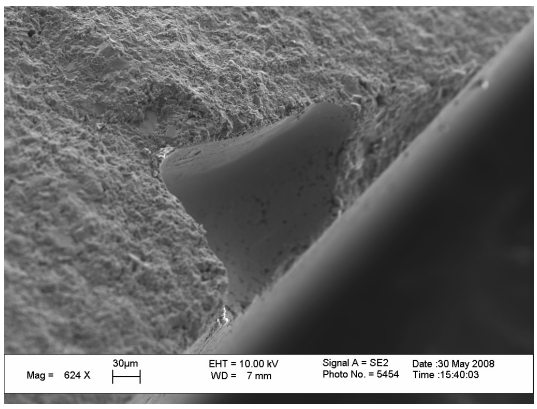


(a) Low magnification SEM of the hollow shows the shape of the wire electrode and that the electrolyte structure seems undamaged by the electrode removal.

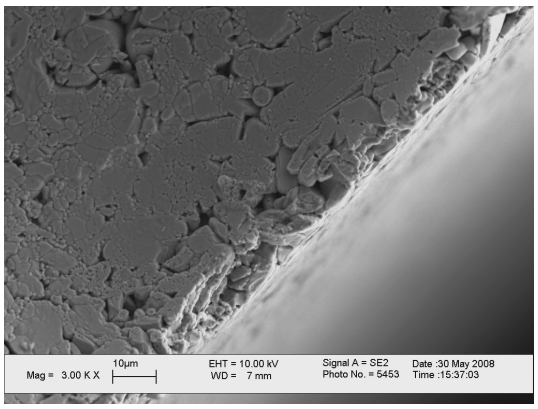


(b) 3kx magnification SEM of the hollow shows gas access to triple-phase boundaries approximately 10 microns deep into the electrolyte.

Figure 6.11: SEM micrographs of the hollow left by an as-pressed wire electrode reveals the poorly densified triple-phase boundary 10 microns into the electrolyte.

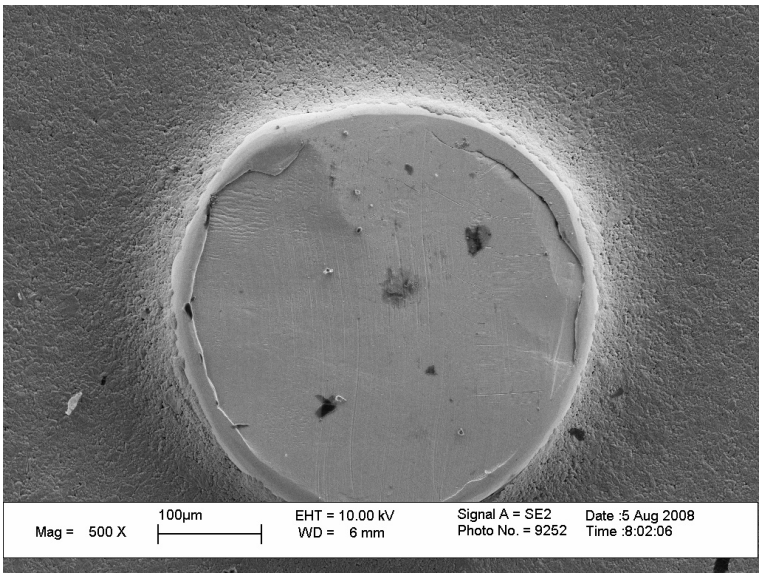


Figure 6.12: Top-down SEM microraph of a flush dense wire electrode cylinder pressed into a $CsH_2PO_4$ electrolyte. The cell was also pressed at 4 tons for 15 minutes, and was then heated to the superprotonic phase for 12 hours. The triple-phase boundary appears to be well-defined.

removed, as in figure 6.11. The hollow micrographs, shown in figure 6.13, reveal a much better-defined interface without apparent gas channels beyond the triple phase boundary.

### 6.2.2 Test Infrastructure: single-chamber

#### 6.2.2.1 Wirebonding

After co-pressing cylindrical wire electrodes into $CsH_2PO_4$ half-cells, electrical contact was achieved through ultrasonic wire-bonding the wire electrode to a secondary pad with a Westbond wirebonder. The wire used for bonding was 25 micron diameter Al99Si1. Early attempts used gold wire because of concerns regarding the thin aluminum wire's stability in high-temperature, oxidizing environments; but subsequent tests showed that the easier to work with Al99Si1 wire maintained integrity over all tested conditions and time. The wire-bonder settings are not included as variations in wire quality require significantly different settings - even within a single spool.

#### 6.2.2.2 Cell Holder

While the flexible single-chamber cell used in Chapter 5 and described in chapter 3 was suitable for single-electrode cells, multiplexing capability necessitated the inclusion of ad-

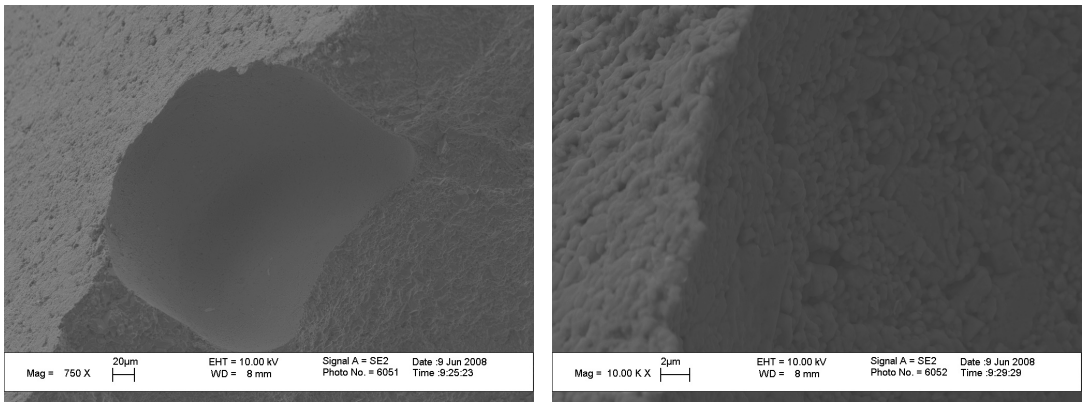


(a) Low magnification SEM of the hollow shows the shape of the wire electrode and that the electrolyte structure seems undamaged by the electrode removal.

(b) 10kx magnification SEM of the hollow shows a dense interface, without apparent gas access.

Figure 6.13: SEM micrographs of the hollow left by a wire electrode in a cell heated to 240°C in humid (0.38 atm $p\mathrm{H_2O}$) hydrogen gas reveals a well-defined interface.

ditional electrical leads into the test chamber. A holder, therefore, was fabricated with 4 swagelok ultratorr ports, each sealing a quad-core 1/4" alumina tube. The holder in question can be seen in the background of figure 6.8. Of the 16 available ports, one was used for a thermocouple, two for the counter electrode, and 12 for contacting working electrodes. The last lead was left unused.

#### 6.2.2.3 Multiplexing

The last lead was omitted because of limitations in switching capability. The HP 3488A switching unit contained 3 modules. Each module could connect any of its 5 leads to any other within the array. This construction was not ideal for the multiplexing application, but was adapted by connecting the electrochemical test equipment to the first lead of each of the 3 modules, leaving 4 leads per module, or 12 total that could be connected to the potentiostat. A photograph of the connection is shown in figure 6.14.

With space for two additional modules, this unit could potentially handle multiplexing for up to 20 electrodes.

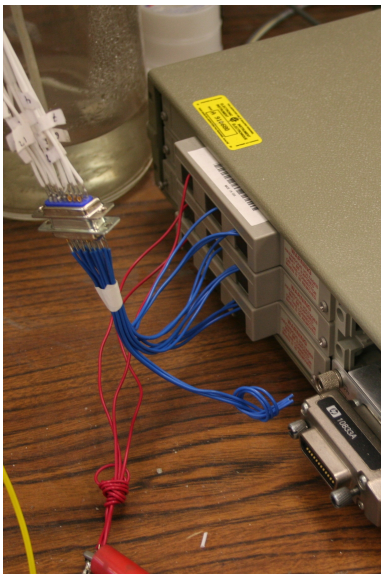

Figure 6.14: Back of HP 3488A switching unit showing connections to the potentiostat (red wire) and connections to the 12 cell leads (blue) which were soldered into a 15 pin connector for easy installation.

#### 6.2.2.4 Test Fixture

Because of the delicacy of the wirebonds, it was necessary to fabricate a secondary fixture that could secure the cell and connect the wirebonding pads to the Cell holder described above. A fixture was designed with a counter bore to secure the cell and provide electrical contact to the counter electrode, while 12 electrically isolated leads were arrayed as contact pads for wire bonding and for connection with the cell holder. Photographs of the fixture with and without a loaded test cell are shown in figure 6.15. The separate fixture was also necessary because wirebonding directly to the cell-holder would have been near-impossible due to clearance issues.

The fixture shown in figure 6.15 went through one last iteration, however. The gold contact pads were replaced with gold-plated quick-release connectors (such as those found in rs-232 connectors), this allows the cell to be installed quickly and as silver paint is only used to contact the counter electrode leads with the plate, there is no danger of contamination or shorting from the silver paint.

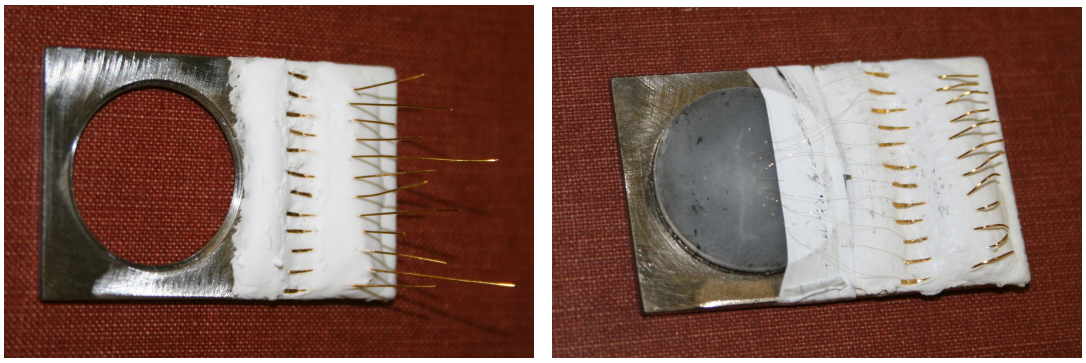

(a) Test fixture with counterbore, counter electrode contact, and 12 leads for working electrodes.

(b) Test fixture with cell loaded and wire-bonded with gold wire.

Figure 6.15: Photographs of multiplexing test fixture with and without a loaded and wire-bonded cell.

### 6.2.3 Test Infrastructure: dual-chamber

While unconventional, several wire electrode tests were conducted in a dual-chamber configuration - the counter electrode as the anode, and the wire as the cathode. This can only be done with an extruding wire of the form fabricated by Methods A or B. To contact the working electrode, the pressure-less holder described in chapter 4 was modified. The cells were still sealed with Viton as described in chapter 4, and the anode still painted with silver to contact the anode-ring, but a teflon-jacketed silver-plated copper wire was sealed into the cathode chamber and contacted the wire of interest.

(a) Modified pressureless holder-half-cell, prior to sealing the top stainless steel ring to the Macor, and contacting the wire electrode. Wire Electrode is contacted with gold wire to prevent reactions with contact lead, a precaution later deemed unnecessary.

(b) Modified pressureless holder, set up for dual-chamber, asymmetric solid electrode cell testing.

Figure 6.16: Photographs of the modified dual-chamber wire electrode test chamber.

### 6.2.4 Advantages of Wire electrodes

1. The commercial availability of electrode materials.
2. Multiple electrodes may be tested on one cell.
3. Electrodes have a known diameter.
4. Electrodes are easily cleaned/annealed.
5. Potential for in-house alloying of new materials exists.
6. There is potential for reuse of electrodes.

### 6.2.5 Drawbacks of Wire electrodes

#### 6.2.5.1 Deformation

Though ideally cylindrical, electrodes cut from wire tend to be deformed by the process as seen in the non-circular cross-section of the electrode in figure 6.17 While this deformation

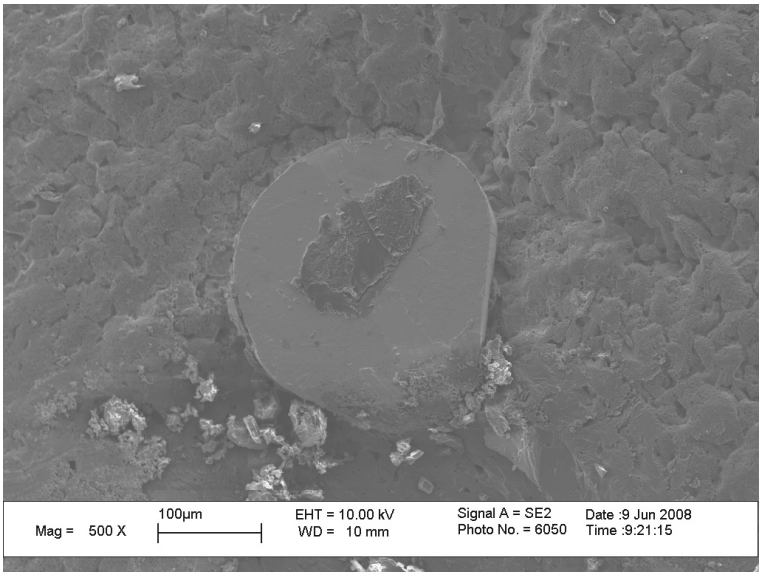


Figure 6.17: SEM Micrograph of a wire electrode (after testing), the central mark is the remnants of the wirebonded Al99Si1. The wire was deformed during fabrication, and the nominally circular cross-section flattened on one side.

introduces error in calculating the triple-phase boundary length it is not entirely uncorrectable, as post-mortem image analysis can calculate true perimeter, and the error would be relatively small, regardless.

#### 6.2.5.2 Depth

A less tractable issue is that of electrode depth. It is not clear that the $CsH_2PO_4$ - wire interface is active in the absence of gas access, but as it is a possibility, it deserves consideration.

As a quick calculation, the interfacial area of a cylinder with one open face is simply $\pi \cdot d^2/4 + \pi \cdot d \cdot h$ for a 0.25 mm diameter, 0.3mm long cylindrical electrode, the calculated area is 0.285 $mm^2$, but for an uncertainty of cylinder depth as little as 100 microns (due to measurement imprecision, non-uniform depth, or electrolyte shrinkage), an error of approximately 25 % is introduced, with little recourse for analytic correction.

#### 6.2.5.3 Pressureless

Lastly, as $CsH_2PO_4$ exhibits plastic behavior in its high-conductivity phase, there is a chance stresses on the electrode - from thermal mismatch, vibration, or the weight of the contact lead - may deform the nearby $CsH_2PO_4$ . Without pressure, there is no way to maintain the microstructural interface.

## 6.3 Dense Asymmetric Geometries: Foil

In order to address the uncertainty in depth inherent in hand-cut wire electrodes, cut foil was considered as an alternative to wire electrodes. Foils share many strengths with wire electrodes, but as they have a defined thickness, interfacial area is controlled. Additionally, the much larger ranges of available diameters allows a higher-confidence fitting when elucidating if a given process is area-specific or length-specific.

### 6.3.1 Design and Fabrication

The fabrication of cells with foil electrodes is nearly identical to that of cells with wire electrodes - the only difference being how you prepare the dense electrode. Whereas wire electrodes were cut from a single length of purchased wire, foil electrodes are cut from a single sheet of purchased foil. As the triple-phase boundary with electrolyte and gas is defined by the perimeter of the electrode, this method has larger uncertainty in triple-phase length. However, a larger range of working electrode radii may be probed.

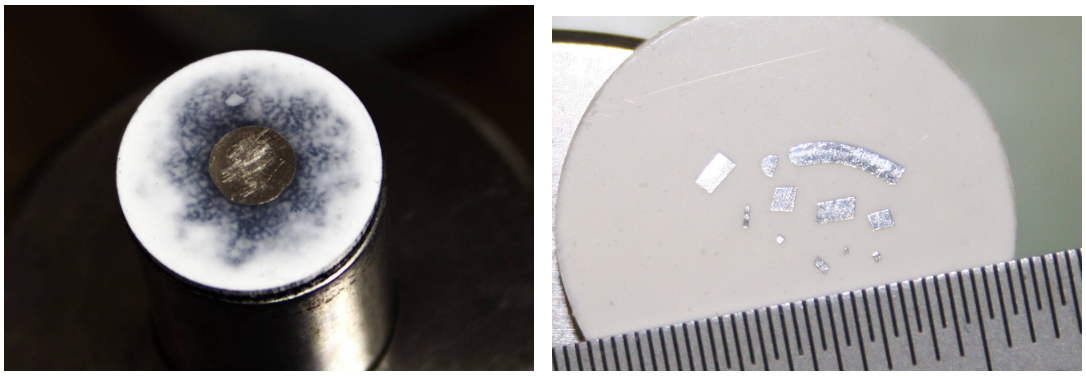

(a) Photograph of single foil electrode densified into $CsH_2PO_4$ . The opacity gradient indicates the density gradient away from the foil, but shows that the electrolyte near the electrode is highly dense.

(b) Photograph of a cell with a variety of foil shapes and sizes pressed into the electrolyte.

Figure 6.18: Photographs of asymmetric geometry foil-electrode cells in single and multiplexed fabrications.

Figure 6.18 shows photographs of the flexibility of foil electrodes as a wide variety of shapes and sizes can be tested in an effort to identify mechanism dependencies.

### 6.3.2 Test Infrastructure

Cut pieces of foil have identical infrastructure requirements with wire electrodes made by fabrication approach C. Foils are easily wirebonded and the same holder and test fixture may be used.

### 6.3.3 Advantages of Foil electrodes

- Foils are commercially available.
- Controlled perimeter through in-house cutting
- Interfacial area is controlled.
- Foils are easily cleaned/annealed.
- Though more difficult than with wire, there is potential for in-house alloying
- Electrodes may be cleaned and reused.

### 6.3.4 Drawbacks of Foil electrodes

- Pressureless
- Potentially non-representative microstructure

## 6.4 Dense Asymmetric Geometries: Inverse geometry

The uncontrolled microstructure of wire and foil electrode-electrolyte interfaces was identified as the greatest weakness of the respective approaches. As the electrodes are only mechanically restrained by the soft electrolyte, the microstructural interface is very sensitive to physical deformation, such as that shown in figure 6.19. This electrode was tested at 240 °C in humid (0.38 atm $p\mathrm{H_2O}$) $\mathrm{H_2}$.

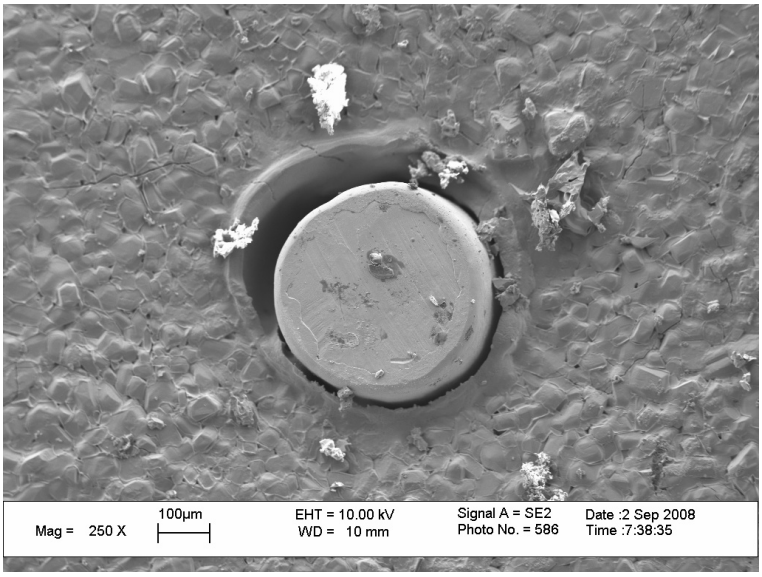


Figure 6.19: SEM Micrograph of a wire electrode showing a strong deformation of the electrode-electrolyte interface during testing.

### 6.4.1 Design and Fabrication

In order to enable external mechanical force to hold the electrolyte against the electrode, a new geometry was conceived and implemented wherein the working electrode is larger than the electrolyte + counter electrode half-cell, as schematically drawn in figure 6.20.

In practice, the inverse geometry is the easiest of the solid-electrode constructions to implement. All that is required is the fabrication of a half-cell ($\mathrm{CsH_2PO_4}$ electrolyte pressed

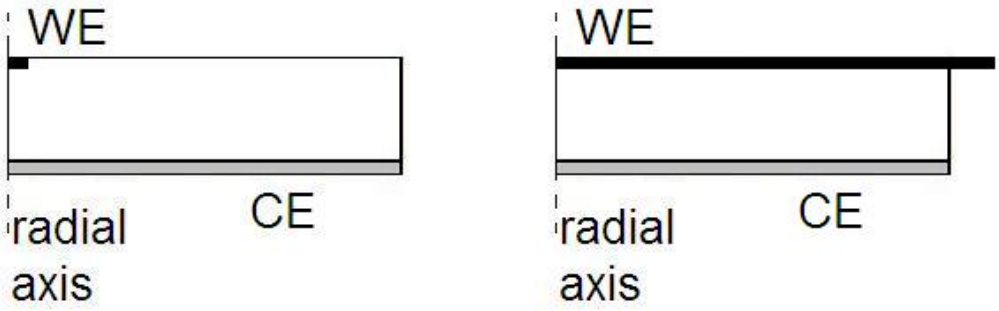


(a) Schematic of wire and foil electrode geometries, where pressure cannot be placed on the interface without blocking gas access or contacting the electrolyte with an unwanted material.

(b) Schematic of inverse geometry, which allows pressure to be placed on the working electrode, maintaining contact with the electrolyte.

Figure 6.20: Schematic of inverse geometry test cell.

against a Toray paper supported electrode, generally Pt:$CsH_2PO_4$ in (3:7 by weight). Uniformly, tested inverse electrodes were purchased metal foils, 25 mm square. This method, however, enables a great deal of flexibility in tested electrodes. For example, a thin layer of electrode material could be deposited onto a flat conductive substrate, then pressed against a half-cell. Even materials with poor electrical conductivity could be tested in this manner as deposited layers can be thin enough to allow limited electron mobility. Triple-phase length can be controlled by varying the half-cell diameter. Additionally, if contamination is sufficiently limited, both half-cells and electrodes can be cleaned and reused with this approach. Lastly electrical connection to the working and counter electrodes under pressure does not require silver paint - and the 4-point leads are connected with small quick-connects - so loading the cell and the fixture are also extremely fast.

### 6.4.2 Test Infrastructure

Because the inverse geometry precludes the testing of multiple electrodes, the simple holder shown in figure 3.7, or similar may be used. To exert reasonable pressures, however, a new test fixture was cobbled together and is shown in figure 6.21 along with a prepped half-cell and an irregularly cut piece of nickel foil. Pressure is exerted through tightening nuts and spring washers on the four 8-32 bolts. Not shown are the top plate and the porous stainless steel disk used as a current collector for the counter electrode.

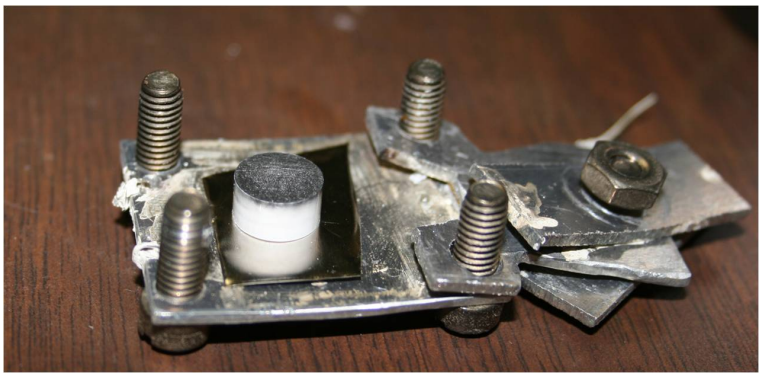

Figure 6.21: Photograph of the "Hanayoridango" inverse electrode holder, showing foil working electrode and 9.3 mm diamter pressed half-cell with Toray paper supported electrode.

### 6.4.3 Advantages of Inverse-Geometry electrodes

- Commercial availability
- Controlled perimeter through controlled perimeter half-cells
- Controlled interfacial area
- Easily cleaned/annealed/reused
- Potential for in-house synthesized electrodes
- Can be tested under pressure

### 6.4.4 Drawbacks of Inverse-Geometry electrodes

- Potentially non-representative microstructure
- Cannot be tested in dual-chamber
- Isolation is not readily calculable, and is lower than that for other dense working electrodes.
- Can only currently test a single electrode at a time.

## 6.5 Conclusions

A great variety of asymmetric geometries have been developed, enabling a flexible approach to characterizing electrodes. Concurrently, the necessary infrastructure was identi-

fied, designed and implemented. In bridging the gap between real-world application fuel cell electrodes and controlled, isolated electrodes suitable for study, kinetic mechanisms of the $CsH_2PO_4$ -electrode system can be representatively treated. Using wire electrodes in conjunction with the developed multiplexing infrastructure allows higher-throughput testing and direct comparisons between material properties. Replacing the wire electrodes with foil, however, allows fine-tuning of double-phase and triple-phase dimensions for the determination of mechanistic dependencies. Lastly, the inverse geometry combines the benefits of apples-to-apples comparisons of wire electrodes with the facile control over interfacial dimensions of foil electrodes, with the additional benefit of pressure-derived stabilization of the electrode-electrolyte interface.

The material flexibility of the inverse geometry is also a great advantage, though far from fully exploited in this work.

While the intrinsic properties of both the electrolyte and of the electrode-electrolyte kinetics confounded standard approaches to characterization, they necessitated the development of a new approaches - ones capable of effectively treating the $CsH_2PO_4$ system, but also potentially capable of broader utility.

# Chapter 7

# Anode Studies

In Chapter 5, the activity of platinum-based anodes was seen to be more than an order of magnitude more facile than cathodes. This observation has several implications of note: firstly, the nature of anode kinetics of the Pt-$CsH_2PO_4$ are nearly inaccessible through standard approaches; and secondly, since the anode is a minority contributor to total operation overpotentials, a non-platinum alternative could be viable even with more sluggish kinetics. In this chapter, the techniques developed and described in chapter 7 are used to characterize platinum anodes both in representative electrode microstructures and in defined microstructures. The defined microstructures are used to compare candidate non-platinum anode materials directly.

## 7.1 Platinum anode studies

### 7.1.1 Powder microstructure

With the methodologies developed in chapters 6 and 7, kinetics become accessible and the step is to verify system fidelity between symmetric electrode geometries and mechanism-elucidating asymmetric geometries. The simplest approach is to compare impedance spectra of the two systems qualitatively, and to compare the activation energies of each.

Asymmetric microelectrodes are expected to evince fidelity to operating fuel cell electrodes based on their nominally identical electrode microstructure and composition. Pursuant to the eventual goal of comparing intrinsic material properties, carbon is excluded from further investigation, restricting studies to electrode-electrolyte-gas systems. Additionally, though the microelectrode cells investigated in chapters 6 and 7 used the same catalyst mixture at both the working electrode and the counter electrode, a straightforward

method of increasing the isolation for a given geometry is to 'worsen' the working electrode effectively - decreasing the area-normalized reaction rate constant by decreasing the platinum loading.

Two binary Pt:$CsH_2PO_4$ electrode composites were synthesized as described in chapter 4. The first was made 3:7 by weight, as investigated in chapters 5 and 7. The second mixture was made at 1:19 by weight of the same component materials. From these binary electrocatalyst mixes, three cells were fabricated and tested.

- A symmetric cell of 30 mg of standard Pt:$CsH_2PO_4$ (3:7 by wt) electrode mix with a 0.4 mm thick $CsH_2PO_4$ electrolyte.
- The first microelectrode cell, using the same Pt:$CsH_2PO_4$ (3:7 by wt) electrode mixture for working and counter electrodes, was prepared as described in chapter 7 with a 1.1 mm thick $CsH_2PO_4$ electrolyte.
- The second microelectrode cell, identical to the first, but using the low-loading Pt:$CsH_2PO_4$ (1:19 by wt) for the working electrode and the standard Pt:$CsH_2PO_4$ (3:7 by wt) for the counter electrode.

All three cells were supported with SS304 GDLs and fabricated with a single, uniaxial cold press at 137 MPa for 5 minutes. The cells were loaded into a symmetric holder and heated at 1 °C /min to 231 °C in humid (0.38 atm $pH_2O$) hydrogen gas flowing at 30 sccm.

Impedance spectra were continuously acquired for all three cells as they were heated to 250 °C and back down at 0.1 °C /min. Impedance plots of the symmetric cell were fit to $R_S(R_{P1}Q)(R_{P2}Q)$ equivalent circuits, while dispersion at high frequency reduces fit confidence for the higher-frequency process. The source of the frequency dispersion is the capacitive interactions between the gas-diffusion layer and the electrolyte [(38)(39)]For clarity, the lower frequency arcs of the microelectrodes are simply fit to an equivalent circuit of the form $R_S(R_PQ_P)$. Representative Nyquist plots and the arrhenius behavior of all three cells are show in figure 7.1 while the activation energies, summarized in table 7.1, show good agreement with fit ohmic activation energies of approximately 40 kJ/mol (though convoluted with the small high-frequency process) and with the low-frequency fits of approximately 30 kJ/mol. Similarly, the zero-bias impedance spectra of the cells' low frequency arcs under different concentrations of hydrogen - from 0.085 atm to 0.66 atm of

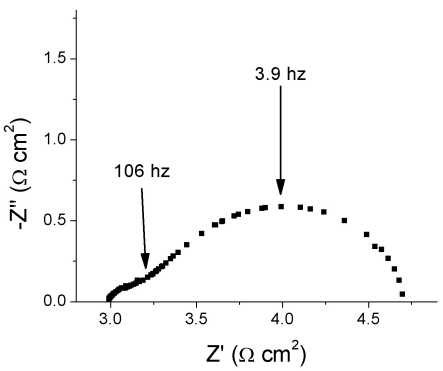


(a) Nyquist plot of symmetric cell with binary (3:7) electrodes.

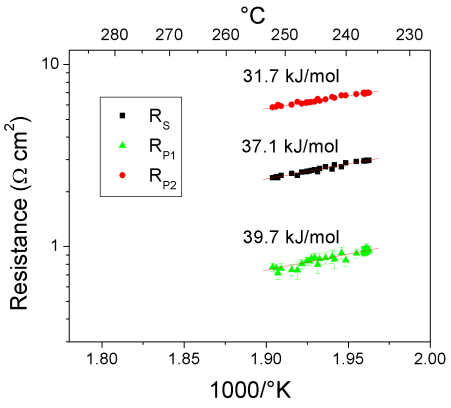


(b) Arrhenius behavior of symmetric cell with binary (3:7) electrodes

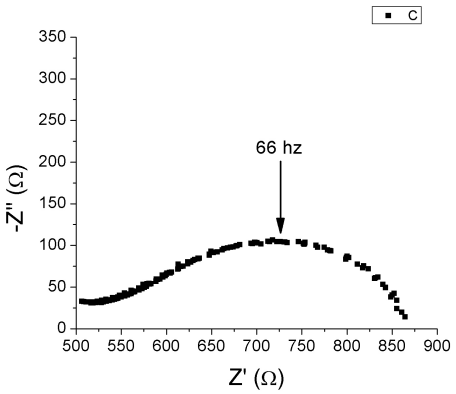


(c) Nyquist plot of microelectrode cell with binary (3:7) electrodes.

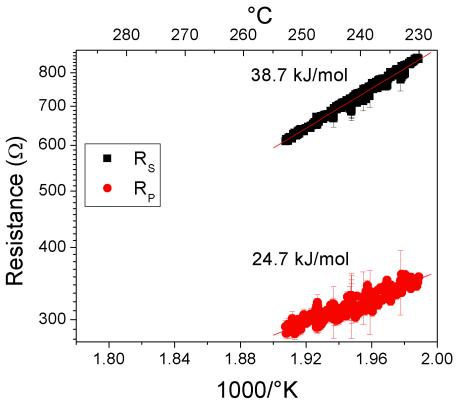


(d) Arrhenius behavior of microelectrode cell with binary (3:7) electrodes

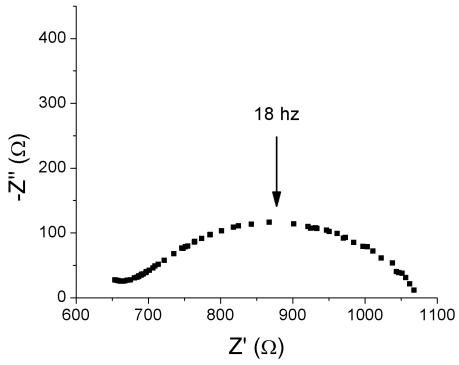


(e) Nyquist plot of microelectrode cell with binary (1:19) WE and binary (3:7) CE.

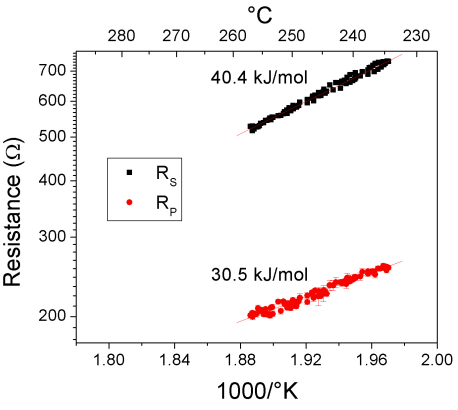


(f) Arrhenius behavior of microelectrode cell with binary (1:19) WE and binary (3:7) CE.

Figure 7.1: Nyquist plots and arrhenius behavior for three binary Pt:$CsH_2PO_4$ electrode cells.

hydrogen - were obtained yielding power-law dependencies as $R_P \propto P^{-n}$ of 0.773, 0.34611, and 0.3234 for the low-frequency arcs of the fully symmetric cell, the 3:7 microelectrode cell and the 1:19 microelectrode cell, respectively.

| Fit Impedance | Symmetric powder | Microelectrode (3:7) | Microelectrode (1:19) |
|---|---|---|---|
| $R_S$ (ohmic) | 37.1 ± 0.5 | 38.7 ± 0.1 | 40.4 ± 0.2 |
| $R_{P1}$ (high freq) | 39.7 ± 4.23 | n/a | n/a |
| $R_{P2}$ (low freq.) | 31.7 ± 0.5 | 24.7 ± 0.4 | 30.5 ± 0.5 |

Table 7.1: Summary of the activation energies (kJ/mol) of the three binary Pt:$CsH_2PO_4$ electrode cells

Characterizing the kinetics of platinum-$CsH_2PO_4$ based electrodes in hydrogen is further complicated by the fact that impedance spectroscopy shows at least two co-limiting processes, which require identification at each steady-state bias with impedance spectroscopy. The overall behavior of these microelectrodes in hydrogen is described by cyclic voltammetry in figure 5.7, though this treatment did not separately treat each contributing process, the exponential increase in current at negative potentials, combined with nearly linear $j-\eta$ behavior at positive potentials qualitatively eludes fitting to standard mechanisms. For a more detailed kinetic treatment, the microelectrode cell with the Pt:$CsH_2PO_4$ (1:19 by wt) composition working electrode was tested at 258 °C at cell biases from -0.3 V to 1.0 V (approximately -70 mV to 700 mV overpotential). The fit resistance of the low-frequency arc is plotted against steady state current in figure 7.2. Qualitatively, the resistance curve is concave upwards and increases monotonically with current, evincing similar characteristics as a process limited by Fickian diffusion. As shown in Appendix B, A rate limiting step of follows the $R(i)$ behavior

$$R = \frac{RT}{nF} ln\left(\frac{1}{i_{lim} - i}\right) \tag{7.1}$$

Which, at a given temperature, is only informed by the number of participating electrons, $n$, and the limiting current $i_{lim}$. Figure 7.2 also shows the fit to equation 7.1, though the calculated $n$ of 0.154 is unphysical, suggesting that while the process is mass-diffusion limited, it cannot be described by 1-D Fickian diffusion.

To investigate the high-frequency arc, a fourth cell was similarly fabricated with Pt:$CsH_2PO_4$ (3:7 by wt) electrodes and tested under identical conditions. Accessing the high-frequency arc requires slow scans of the entire frequency range at each bias. Given the additional time required per scan, scans were conducted at 0 V bias after each biased scan, and figure

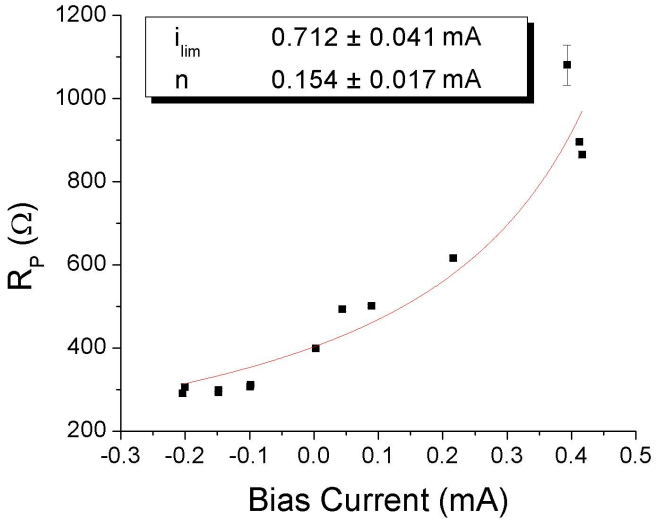


Figure 7.2: Biased ACIS study of Pt:$CsH_2PO_4$ (1:19 by wt) microelectrode in humid (0.42 atm $pH_2O$) hydrogen atmosphere at 258 °C .

7.3, showing a sample nyquist plot and the impedance vs bias results shows that these "touchback" scans were largely reproducible.

The detailed kinetic study of the microelectrode cell by ACIS, however, only serves to confirm that the mechanism describing platinum anode kinetics cannot be well-described by a charge transfer process, nor a 1-D Fickian diffusion process.

Thus, the platinum anode can be characterized - specifically the large, low frequency impedance is seen to be a mass-diffusion limited process with an activation energy of 30 kJ/mol and a power dependence on hydrogen concentration of 0.33. Though the rate determining steps of the platinum anode appear to be mass-diffusion limited in nature, the specific nature remains an open question. The microelectrode construction is seen to represent the kinetics of operating fuel cell electrodes - an expected result given the nominally identical microstructure.

### 7.1.2 Defined microstructures

In the previous section, asymmetric powder microelectrodes were demonstrated to be a powerful tool for identifying the kinetics of platinum anodes. That the construction is capable of isolating kinetics of representative microstructures without the need for a reference electrode is exceptionally powerful. The intrinsic activity of platinum is not, however

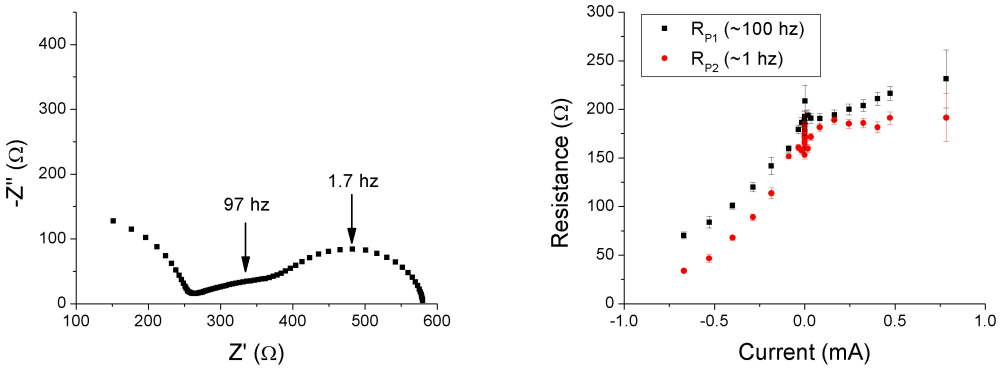


(a) Full frequency impedance scan of Pt:$CsH_2PO_4$ (3:7 by wt) microelectrode cell.

(b) Fit electrode process impedance vs bias.

Figure 7.3: Detailed biased impedance study of a Pt:$CsH_2PO_4$ (3:7 by wt) microelectrode cell in humid (0.38 atm $pH_2O$) hydrogen at 235 °C .

accessible, as the microstructure of microelectrode cells is considered representative but remains uncontrolled. Controlled microstructures are generally obtained through a combination of lithography and deposition to create non-porous electrode-electrolyte interfaces with defined structures, but the mismatch in thermal expansion coefficients - combined with the volume change as $CsH_2PO_4$ transitions to the cubic, superprotonic phase - confounds thin film deposition. Simultaneously, the high-quality patterns generally obtained through photolithography are inaccessible due to the solubility of $CsH_2PO_4$ in water.

While standard approaches to controlled microstructure are made difficult by the idiosyncratic material properties of the $CsH_2PO_4$ electrolyte, similar idiosyncracies enable interesting non-standard approaches: discussed in chapter 7 as the wire electrode and the inverse electrode.

#### 7.1.2.1 Pt wire electrodes

Initially, it is important to discern the fidelity with which dense electrode kinetics mimic porous electrode kinetics.

A platinum wire electrode cell was fabricated by approach C with a 0.25 mm diameter platinum wire working electrode, 30 mg of Pt:$CsH_2PO_4$ (3:7 by wt) supported by a SS304 mesh GDL counter electrode, and 1.2 g of $CsH_2PO_4$ electrolyte. After heat-treating and wirebonding, the cell was loaded into the single-chamber test fixture and heated at 1°C

/min to 236 °C in humid (0.38 atm $pH_2O$) hydrogen. Impedance spectroscopy was used to identify the impedance dependencies under the same varied conditions of the microelectrode in section 8.1.1. Temperature, $pH_2$, and cell bias were varied and impedance spectra were acquired. The results, with a sample nyquist plot showing two processes, are presented in figure 7.4.

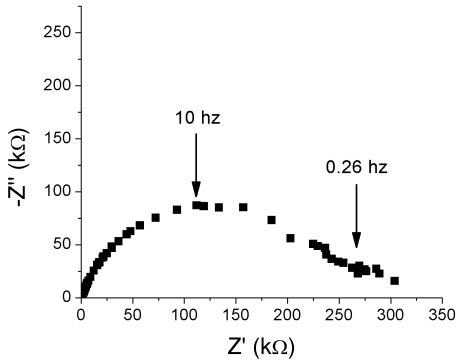


(a) Nyquist plot of Pt wire electrode impedance at 236 °C .

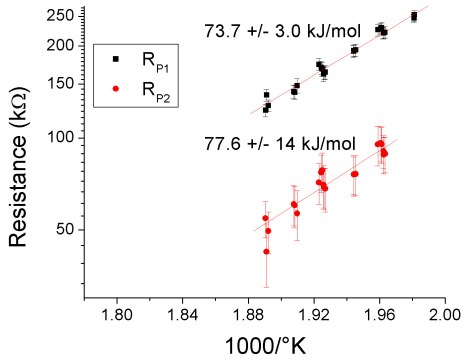


(b) Arrhenius behavior of wire electrode processes.

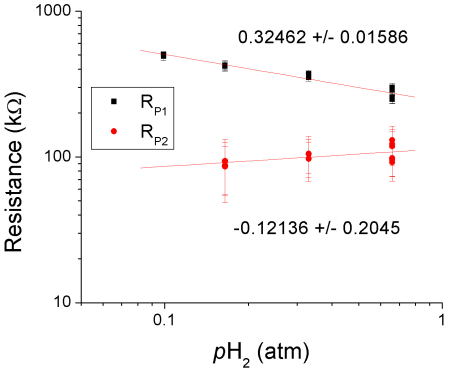


(c) Power law dependence of $R_P$ on $pH_2$.

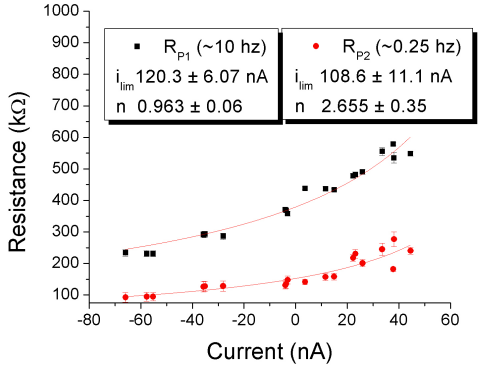


(d) Kinetics of wire studies by biased ACIS, fit to Eq. 7.1

Figure 7.4: Overview of anode studies performed on a Pt wire electrode cell in symmetric, humid (0.42 atm $pH_2O$) hydrogen.

The first indication that wire electrodes probe a different mechanism from the powder electrodes is seen in the shape of the nyquist plot of figure 7.4(a). Though the wire electrode is also co-limited by two processes, the characteristic frequency of high frequency arc is closer to the lower characteristic frequency of powder electrodes, while the lower frequency arc is incomparable to any processes seen in the binary Pt:$CsH_2PO_4$ electrode system.

Additionally, the activation energies are markedly different, approximately 30 kJ/mol for powder electrodes compared to 75 kJ/mol for each of the wire electrode processes. Most significantly, biased kinetic studies reveal that both anode processes are limited by a mass-diffusion step with the high and low frequency processes involving 1 and 2 electrons per step, respectively.

It is clear, then, that while the move towards controlled microstructures may allow an apples-to-apples material comparison, conclusions gleaned from such studies are not necessarily predictive of operating fuel cell kinetics.

Value still exists in identifying intrinsic catalytic activity in such systems, however, as it remains a facile method for screening possible anode materials. Once identified, however, studies on representative microstructures are clearly necessary as mechanisms are shown to be microstructure-dependent for platinum at the least.

To identify such intrinsic activity, the measured impedance of identical electrodes tested under identical conditions are compared. A sample set of 55 electrode resistances, $R_P$ tested at 248 °C in humid (0.38 atm $pH_2O$) hydrogen single chamber environment were compiled. Electrodes were cut from 0.25 mm diameter platinum wire, cleaned by sonicating for 10 minutes each in water, acetone, ethanol, and isopropanol. All cells were fabricated (approach C) with approximately 30 mg of binary Pt:$CsH_2PO_4$ (3:7 by wt) counter electrodes and approximately 1 g of $CsH_2PO_4$ electrolyte. They were heated at 1 °C /min and measured by ACIS at zero-bias. The impedance was fit to R(RQ)(RQ) circuits and the total impedances compiled into figure 7.5.

The calculated mean from the 55 electrodes is 87.3 kΩ with a standard deviation of 47.7 kΩ (or 55% of the mean). Despite the theoretically well-defined microstructure, pt wire electrode resistances are seen to be only weakly reproducible. With large sample sizes, mean values are tractable, but the poor reproducibility implies either poor definition in microstructure or chemical contamination of the electroactive interface. Either possibility reduces confidence that the mean resistance corresponds to the true intrinsic activity of platinum.

#### 7.1.2.2 Pt inverse electrodes

The scatter in platinum electrode impedance shown in figure 7.5 was considered to be likely caused by microstructural variation between electrodes due to the softness of $CsH_2PO_4$ in

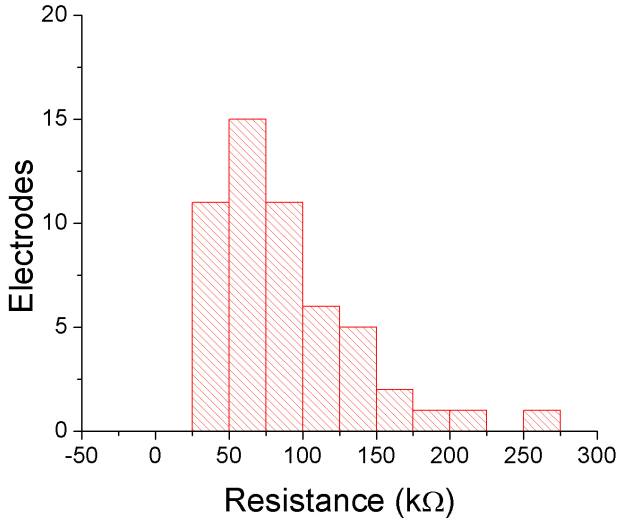


Figure 7.5: Compiled zero-bias $R_P$ results from 55 0.25 mm diameter Pt electrode (Fabrication C) measured at 248 °C in humid (0.38 atm $pH_2O$) hydrogen.

the cubic phase and the lack of external stabilization of the platinum-$CsH_2PO_4$ interface. To stabilize this interface mechanically, the inverse electrode geometry was developed (as described in chapter 6). Because of the chronology of development, only 5 inverse electrode cells were fabricated and tested, each was assembled by pressing a half-cell of approximately 4 mm thick $CsH_2PO_4$ electrolyte half-cells with toray-paper supported Pt:$CsH_2PO_4$ counter electrodes pressed at 143 MPa for 10 minutes. The half-cells were pressed against a 25 mm square piece of platinum foil which had been cleaned by sonication in water, acetone, ethanol, and then isopropanol. Four bolts in the test fixture were tightened to 2 in-lbs of torque each and the cell was heated at 1°C /min in symmetric, humid (0.42 atm $pH_2O$) hydrogen to 250 °C . The elevated initial temperature was selected to hasten interfacial densification of the electrolyte against the platinum foil.

A typical nyquist plot is shown in figure 7.6. The impedances of the five cells, and the characteristic frequency associated with each impedance, is shown in table 7.2.

The high frequency process is shown to be extremely reproducible with a mean of 435.86 Ω with a standard deviation 15% of the mean. The low frequency arc, however, is very irreproducible between cells. While the source of this irreproducibility remains an open question, chemical impurities at the electroactive region is a likely culprit - as the microstructure

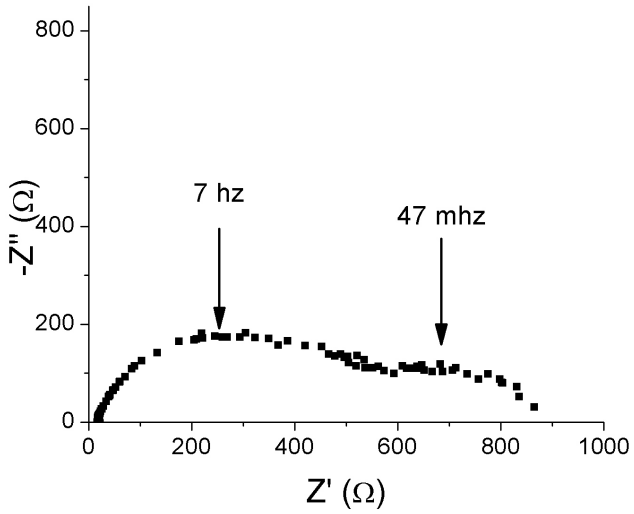


Figure 7.6: Typical nyquist plot of a platinum inverse electrode with 9.3 mm diameter $CsH_2PO_4$ half-cell tested at 250 °C in humid (0.42 atm $pH_2O$) hydrogen.

| Cell number | $R_{P1}$ (Ω ) | $f_{0,1}$ (hz) | $R_{P2}$ (Ω ) | $f_{0,2}$ (hz) |
|---|---|---|---|---|
| 1 | 516.9 | 7.4 | 385.4 | 0.047 |
| 2 | 423.1 | 14.7 | 171.1 | 0.028 |
| 3 | 404.6 | 14.1 | 175.9 | 0.037 |
| 4 | 347.9 | 4.0 | 1019 | 0.076 |
| 5 | 486.8 | 8.0 | 1137 | 0.016 |

Table 7.2: Summary of platinum inverse electrode impedances tested at 250 °C in humid (0.42 atm $pH_2O$) hydrogen

should be mechanically stabilized. While it is beyond the scope of this investigation, sputtering dense films onto flat substrates of glass, or similar, would be an excellent way to control chemical composition.

Mechanistic studies similar to those done for platinum wire electrodes were also undertaken and are presented in figure 7.7.

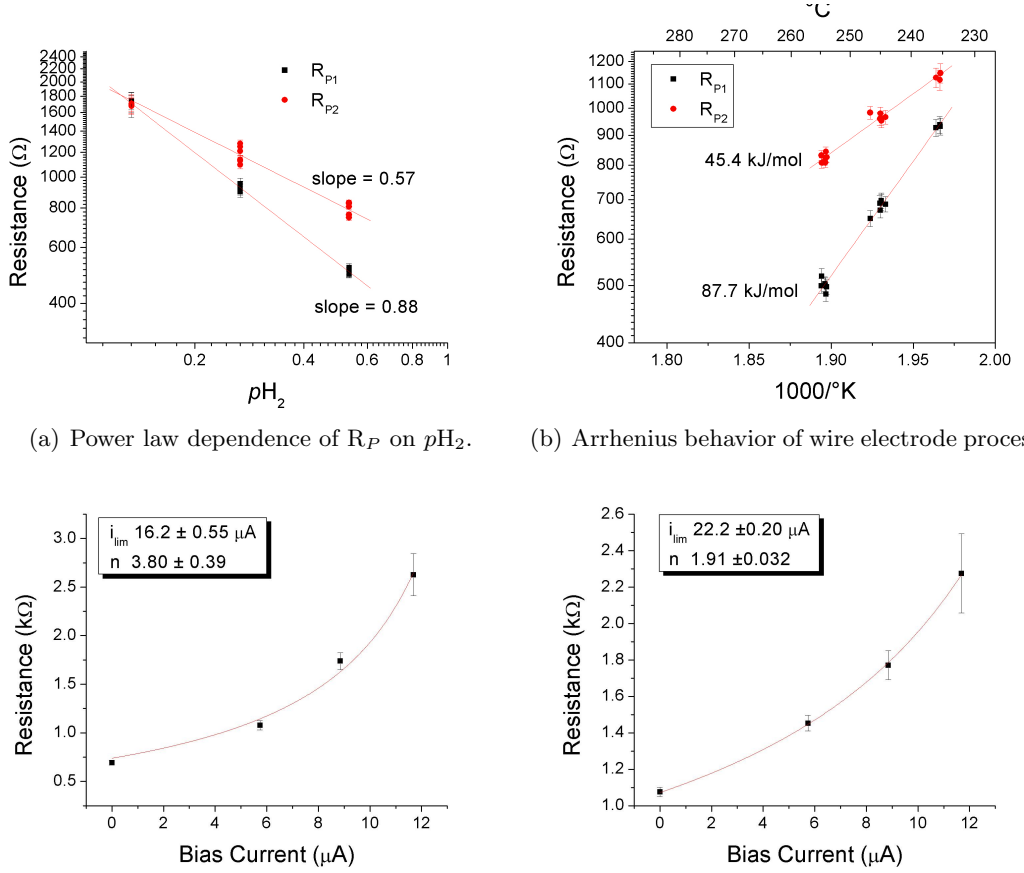


(a) Power law dependence of $R_P$ on $pH_2$.

(b) Arrhenius behavior of wire electrode processes.

(c) Kinetics of $R_{P1}$ studied with biased ACIS, fit to Eq. 7.1.

(d) Kinetics of $R_{P2}$ studied with biased ACIS, fit to Eq. 7.1

Figure 7.7: Sample studies conducted on a platinum inverse electrode at 250 °C in humid (0.42 atm $pH_2O$) hydrogen.

### 7.1.3 Platinum anode conclusions

Direct evaluation of an electrocatalyst is complicated by heterogeneity of activity within a porous electrode. Even were it tenable to normalize current by by triple-phase boundary within such an electrode, macroscale concentration gradients within the electrode would result in nonuniform rates. Investigations in this field traditionally sidestep this obstacle by

macro-scale normalization by cross-sectional area. These normalized activities are informed by extrinsic properties (e.g. triple phase boundary density, concentration gradients, etc.) as well as the intrinsic activity of the investigated material

The lion's share of this research effort has been to transcend the crude, extrinsically-informed metrics of electrode catalytic activity and instead develop the capability to characterize the intrinsic activity of an electrode-electrolyte interface. The high degree of scatter in $R_P$ for identical wire electrodes, as shown in figure 7.5, however, gives excuse to less rigorous treatments, such as "activity" used by PEMFC researchers, or "area-specific resistance" used by SOFC researchers.

The rate-limiting mechanism which informs measured resistance in these systems was shown to be related to 1-dimensional mass-diffusion and fit well to Eq. 7.1 in every case. As such, it is possible that the reaction pathway for these systems involves a two-phase boundary between platinum and $CsH_2PO_4$ - as opposed to a triple-phase boundary between platinum, $CsH_2PO_4$ , and air. Were the double-phase fully active, the measured resistance should scale with the inverse of the double-phase area.

Put another way, the measured resistance, $R \propto d^k$ where $r$ is the diameter of the dense electrode and $k$ is the reaction order. If the full area of the solid electrode - electrolyte interface is active, $k = -2$. If only the triple-phase boundary is active, however, $k = -1$.

Over the course of this research project, a great number of electrodes were tested. By compiling those measured under identical conditions, the sample constricts significantly, but still yields statistically significant results.

Figure 7.8 plots the total electrode resistance from wire electrodes of two diameters (fabricated by approach C) and inverse electrodes of two diameters, measured by zero-bias ACIS at 250 °C in humid (0.38 atm $pH_2O$) hydrogen. Other than the already-discussed scatter of a given system, two significant observations may be made. First, the linear fit reveals a power dependence of -1.02 ($\pm$ .09), showing that the $R_P$ varies with triple-phase length, not double-phase area. Secondly, because the resistance is shown to vary linearly, (in the absence of an offset) this fit allows the calculation of resistance as a function of length at 250 °C .

$$R = \frac{13.6 \pm 1.8}{diameter(mm)} k\Omega \tag{7.2}$$

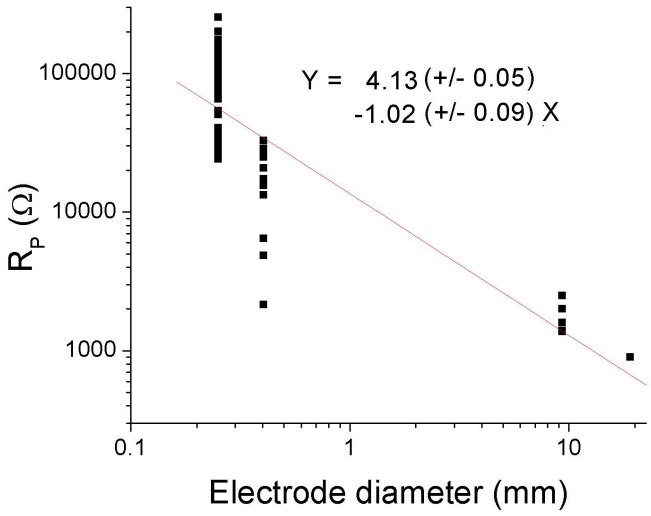


Figure 7.8: Compiled zero-bias $R_P$ results from 93 Pt electrodes (wire by fabrication approach C, and inverse) plotted against electrode diameter in log-log form and shows that $R_P$ scales with the inverse of the triple-phase boundary length.

Identifying the linear dependence electrode diameter does not, of course, preclude the possibility of a somewhat active double-phase boundary. Indeed, the rate limiting steps for these dense platinum electrodes is a form of surface mass diffusion (since gas-phase is only weakly activated). This can be interpreted two ways: either the hydrogen is diffusing on the surface of platinum to the Pt-$CsH_2PO_4$ triple-phase boundary, or hydrogen is diffusing past the triple-phase boundary and accessing a significant area within the Pt-$CsH_2PO_4$ double-phase boundary. The smallest dense electrode tested was 250 microns, as long as this diffusion length is significantly less than 250 microns, the active region can be viewed as a rectangle of width $\delta$ and the length approximated by the interfacial circumference. Stabilizing the microstructure with axial pressure in the inverse electrode geometry is seen to yield a different rate-limiting step from both the wire-electrode geometry and the powder geometry, though the high-frequency co-limiting process is seen to be much more reproducible, the low-frequency process is not. Care in controlling the chemical composition of the participating components is considered a viable solution.

The rate-limiting processes for nano-scale platinum anodes, however, differ from those of micro-scale platinum anodes - suggesting that for nanoparticle platinum, available path lengths are less than $\delta$, meaning the entirety of the nanoparticle (or nanoparticle Pt-

$CsH_2PO_4$ interface) is active for the hydrogen redox reaction. Kinetic studies of microelectrodes yield the most accurate view of operating platinum anode kinetics - namely an approximately constant resistance with bias, do not fit well to any expected kinetic model tested. It is of note, however, that the charge-transfer limited cathode kinetics become faster with bias, the anode kinetics do not - implying that apportioning the operating overpotentials between cathode and anode based on zero-bias impedance in symmetric environments is not entirely appropriate.

Lastly, this investigation of platinum electrodes revealed a potential broad flaw in studies of well-defined electrodes. Namely, that catalysis over electrodes with dense, micron-scale features may differ greatly from those with nano-scale features (as used in operating fuel cells) - or even from similar bulk studies of a different macroscale geometry.

The development and rigorous treatment of microelectrodes, therefore, is an extremely powerful tool for characterizing minority contributors to overall electrode losses.

## 7.2 Non-platinum anode materials

In Chapter 5, anode kinetics are seen to be extremely facile, especially in composite. Put another way, in operating fuel cells there is a significant insensitivity of the total overpotential to anode losses. Schematically, if the total electrode resistance at 200 $mA/cm^2$ of an operating fuel cell is approximately 250 mV, only ≈15 mV are developed at the anode. Correspondingly, a 100% increase in anode resistance would only cause a 6% increase in total overpotential.

In terms of applications, this creates a degree of leeway in the selection of non-platinum catalysts for the hydrogen oxidation reaction - catalysts that are less active than platinum may still find utility based on other properties - notably cost.

Composite powder microstructures, while able to represent operating losses, are unsuitable for candidate material screening, as microstructures vary too much for an apples-to-apples comparison.

Instead, wire electrodes were employed in order to study defined microstructures in an identical environment. Survey candidates were drawn from first-row transition metals and platinum-group elements. Specifically, Co, Ni, Pd, Ag, Pt, and Au were screened. Wires were purchased from Alfa Aesar, cut to approximately 200 micron lengths with parallel

faces, and cleaned by sonicating for 10 minutes each in deionized water, acetone, ethanol, and isopropanol. The counter electrode was 30 mg of Pt:$CsH_2PO_4$ (3:7 by wt), supported by a SS304 mesh GDL, and the electrolyte was 1.1 grams of $CsH_2PO_4$ . The cell was fabricated following approach C, loaded into the multiplexing single-chamber test fixture, and electrically contacted - all as described in chapter 6.

After sealing into single-chamber fixture, the cell was heated at 1 °C /min to 240 °C in humid (0.38 atm $pH_2O$) argon, then hydrogen, flowing at 30 sccm. Cyclic voltammograms were measured for each electrode between -100 mV and +200 mV total cell voltage. The $j - \eta$ characteristics, shown in figure 7.9(a), reveals kinetic similarities for all materials, namely an exponential increase in current at negative potentials and an apparent limiting current at positive potentials. the exception is palladium, whose current appears linear, if not concave-up at positive potentials.

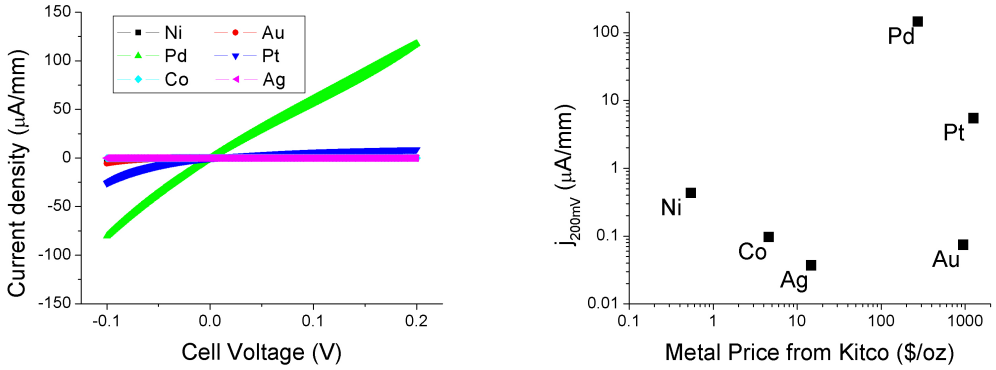


(a) Cyclic voltammograms of candidate materials. (b) Circumference-normalized current density (at 200 mV bias) vs material cost.

Figure 7.9: Survey of candidate anode materials.

Clearly palladium is the most active of the tested wire materials, but to compare the full survey group, the current at 200 mV was taken as a proxy for anode material activity and plotted vs the bullion price in $/oz in figure 7.9(b). From this figure, it is evident platinum is the material with the second highest activity after palladium and before nickel - the three electrodes separated from each other by over an order of magnitude in activity. Additionally, though the current density of the nickel electrode at 200 mV is approximately 10% that of platinum, the cost of nickel is over three orders of magnitude less per oz.

The high activity / cost of nickel and the high overall activity of palladium seen in figure

7.9 motivated additional characterization of these two non-platinum anode candidates.

### 7.2.1 Nickel

Though nickel is a commonly used anode material for solid oxide fuel cells (and in some instances, alkali fuel cells), it is not generally employed as an anode for proton conducting electrolytes. Little, therefore, can be gleaned from literature regarding the kinetics of hydrogen oxidation over nickel.

#### 7.2.1.1 Wire electrode

In investigating nickel as a candidate material, the approach is to first characterize the controlled microstructure geometry (wire and inverse).

Approximately 1 cm lengths of 0.25 mm diameter nickel wire were cut, cleaned and fabricated by approach B with 1.3 g $CsH_2PO_4$ and 35 mg of Pt:$CsH_2PO_4$ (3:7 by wt) counter electrode supported by a SS304 GDL pressed at 137 MPa for 30 minutes. After removing the sacrificial naphthalene, the cell was loaded into the symmetric cell fixture as in figure 6.7, and heated at 1 °C /min to 236 °C in humid (0.38 atm $pH_2O$) hydrogen.

The results from impedance measurements by zero-bias ACIS are shown in figure 7.10. The nyquist plot of figure 7.10(a) presents significant difficulty in analysis while two arcs are evident, the impedance is not well-described by fitting to a R(RQ)(RQ) equivalent circuit. Instead, four RQ tanks are used and for analysis the two high frequency impedances are summed and termed $R_{P1}$, while the two low-frequency impedances are summed and termed $R_{P2}$. The resistance of both are seen to degrade linearly over the first 8 hours of measurement(Fig. 7.10). To identify if the measurement, itself, was responsible for the degradation, the cell was allowed to equilibrate without testing for 30 hours. The impedance increased over that time, showing that the change in resistance was not due to the electrochemical probe. The impedance was considered relatively stable for three measurements (5 hours). The low scan density was caused by the very low characteristic frequencies necessitating impedance scans down to 1 mhz. Arrhenius and $pH_2$ power dependencies were then measured - shown in figure 7.10(c) and (d).

The degree of irreproducibility observed in platinum wire electrodes recommends a statistical treatment of the nickel-$CsH_2PO_4$ system as well. 14 nickel wire electrodes (0.25 mm diameter) were prepared (fabrication B and C) and tested in an identical manner. The

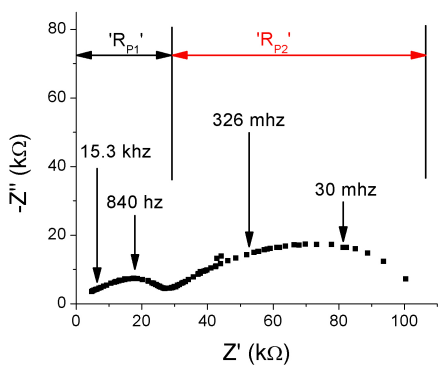


(a) Sample Nyquist plot showing four fit processes, treated as two.

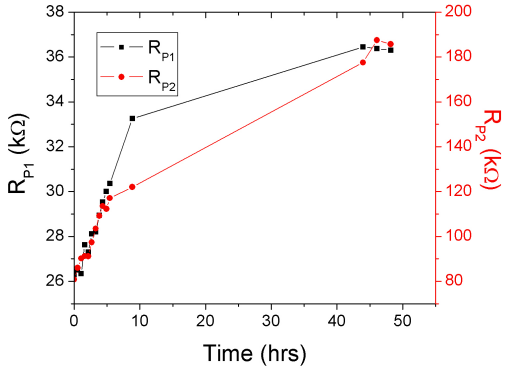


(b) 50 hour longevity scan showing long relaxation time.

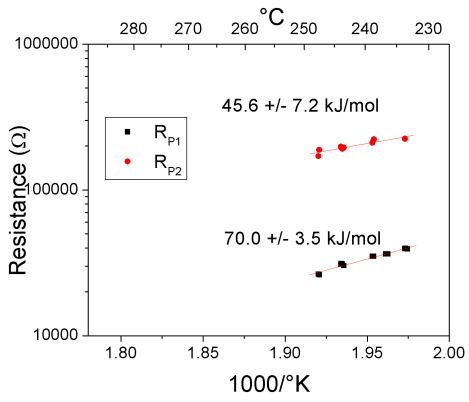


(c) Arrhenius plot measured after stabilization.

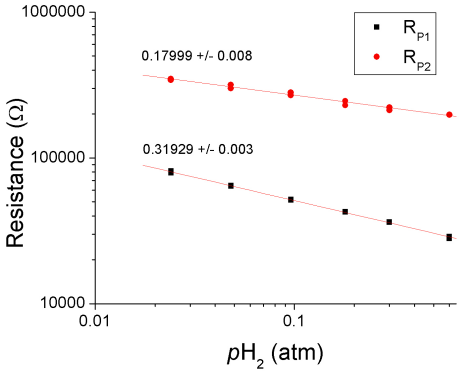


(d) Impedance dependence on gas flow rate at 247 °C .

Figure 7.10: Zero-bias ACIS measurements of a 0.25 mm diameter nickel wire electrode in humid (0.38 atm $pH_2O$) hydrogen.

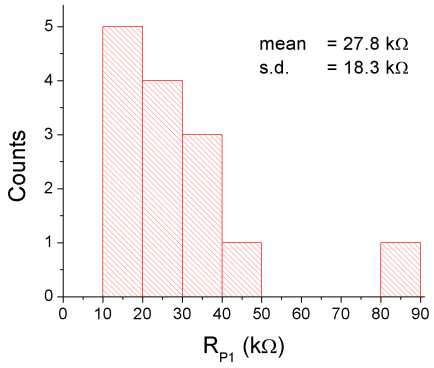


(a) Histogram of $R_{P1}$.

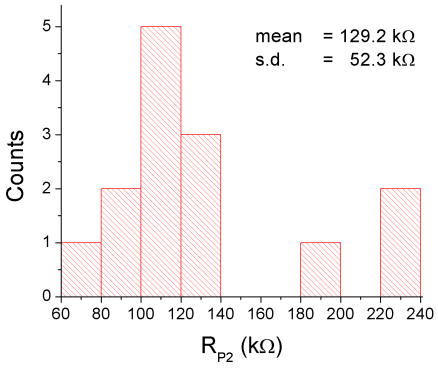


(b) Histogram of $R_{P2}$.

Figure 7.11: Compiled results from 14 0.25 mm diameter nickel wire electrodes measured by zero-bias ACIS at 236 °C in humid (0.38 atm $pH_2O$) .

zero-bias impedances, measured by ACIS at 236 °C show mean $R_P$ values of 27.8 ± 18.3 kΩ for $R_{P1}$ and 129.2 ± 52.3 kΩ for $R_{P2}$ as shown in figure 7.11.

Excluding the three, high-resistance outliers yields a $R_{P1}$ = 25.3 ± 10.5 kΩ and $R_{P2}$ = 105.1 ± 22.5 kΩ for a total, combined $R_P$ of approximately 130 kΩ when measured at 236 °C . This is higher than the zero-bias impedance obtained for platinum wire electrodes (87.3 kΩ from figure 7.5)of the same diameter, but as the platinum results were compiled at 248 °C , they are not directly comparable. Approximating the total platinum wire electrode $R_P$ as a single process with activation energy of 75 kJ/mol allows the estimation of the mean platinum wire electrode zero-bias impedance as 131 kΩ . The large standard deviations from both sets of measurements, however, reduce confidence in authoritative comparisons. At the least, the zero-bias resistances of nickel and platinum wire electrodes are seen to be comparable.

#### 7.2.1.2 Inverse electrode

In addition to wire studies, nickel was also examined by inverse electrodes. 9.3 mm diameter half-cells of 500 mg $CsH_2PO_4$ electrolyte with 10 mg of Pt:$CsH_2PO_4$ (3:7 by wt) supported by toray paper were pressed at 134 MPa for 20 minutes, loaded into the hanayoridango (figure 6.21) sample holder - contacted against nickel foil. The 4 bolts were tightened to 1 in-lb of torque per bolt. The cell was loaded into the single-chamber test fixture and heated at 1 °C /min to 255 °C in humid (0.38 atm $pH_2O$) hydrogen.

Zero-bias impedance measurements reveal nickel inverse electrode kinetics are dominated by a warburg arc at low-frequency, as well as a smaller, high-frequency arc(figure 7.12(a). Accordingly, impedance was fit to a $R_S(R_{P1}Q)W$ equivalent circuit. Arrhenius measurements (figure 7.12(b)) show activation energies which differ from the nickel wire processes - an observation consistent with the differing nyquist plots. Mechanistically, warburg nyquist plots suggest mass-diffusion limited processes and biased impedance scans of the low-frequency arc fit extremely well to a one-electron fickian-diffusion limited process. Though the mechanisms clearly differ, the magnitude of nickel inverse electrode zero-bias impedance is also comparable to that of platinum inverse electrodes. Only two electrodes were tested with total zero-bias impedances of 1.07 kΩ ± 130 kΩ .

Given the high activity of nickel studied with wire and inverse electrodes, several attempts were made to compare nanoparticle nickel catalyst composites to platinum corol-

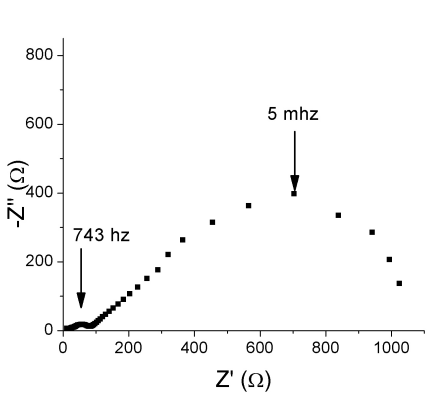


(a) Sample Nyquist plot showing two processes, the lower-frequency of which is the characteristic warburg half-teardrop.

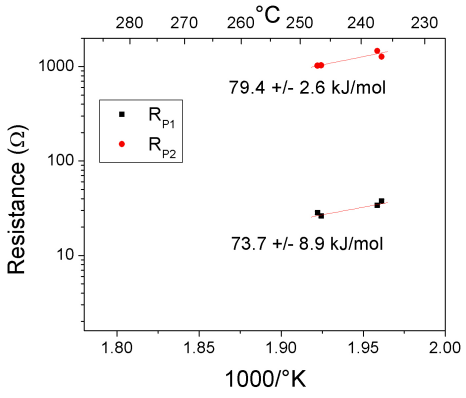


(b) Two-point arrhenius behavior obtained from zero-bias ACIS.

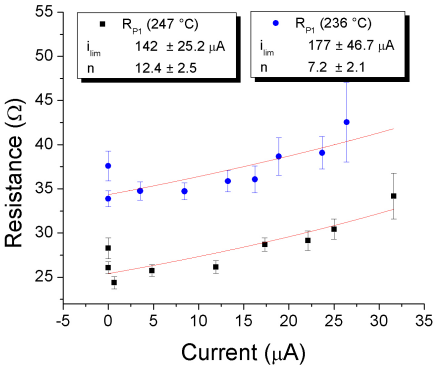


(c) Kinetics of high-frequency electrode process from biased ACIS qualitatively fits to Eq. 7.1, though calculated n value is unphysical

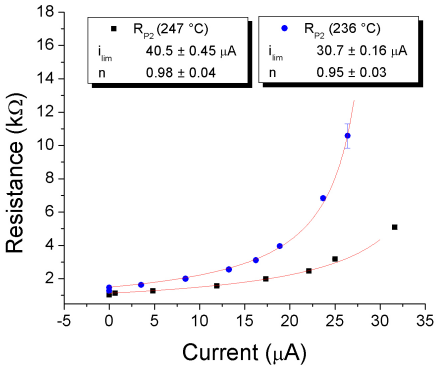


(d) Kinetics of low-frequency electrode process from biased ACIS fits excellently to a 1-D Fickian diffusion step involving one electron.

Figure 7.12: ACIS measurements investigating activation energy and mechanism of a 9.3 mm diameter nickel inverse anode in humid (0.38 atm $pH_2O$) hydrogen.

laries, but the impedances measured from such systems were unrealistically high - greater than the impedance measured from the inverse electrode. For a more detailed description, see Appendix section D.1.

### 7.2.2 Palladium

Palladium is well-studied as a hydrogen conduction membrane [(40)(41)] as such, the high activity seen in figure 7.9 may be legitimately viewed with suspicion. Were the electroactive region for palladium two-dimensional, as opposed to 1-dimensional for the other candidates, the high activity would disappear as the interfacial scale shrank to the nanopowders of operating fuel cell electrodes.

#### 7.2.2.1 Palladium wire electrode

11 wire electrodes were cut from a single length of 0.203 mm diameter palladium wire, cleaned by sonication for 10 minutes each in water, acetone, ethanol, and isopropanol, and then pressed into 1.1 g of $CsH_2PO_4$ electrolyte. The counter electrode was composed of 45 mg of binary Pt:$CsH_2PO_4$ (3:7 by wt). After pressing at 69 MPa for 20 minutes, the cell was loaded into the multiplexing holder, contacts were made to electrodes through wire bonding, the holder was loaded into the multiplexing single-chamber test fixture and the cell was heated at 1 °C /min to 234 °C in humid (0.38 atm $pH_2O$) hydrogen.

Electrode impedance is well-described by a single arc with characteristic frequency approximately 10 khz, as in figure 7.13(a) - enabling high-quality fits to $R_S(R_PQ)$ equivalent circuits. Though the total magnitude of electrode resistance is only weakly reproducible, figure 7.13(b) showing a standard deviation 63 % of mean, the intrinsic thermodynamic properties: activation energy, and $pH_2$ power dependence are extremely reproducible as shown in figures 7.13(d) and (e).

A note on longevity: the measurement of electrode dependence on $pH_2$ shown in figure 7.13(c), took approximately 20 hours - over which, the resistance of the electrode in humid hydrogen (undiluted by argon) increased only 0.03 % per hour. This exceptional stability, combined with a single electrode process, is what made such a high quality treatment of palladium wire electrodes possible.

Since there is only a single limiting process detectable in figure 7.13(a), cyclic voltammograms (iR corrected with the $R_S$ measured from ACIS) may be used to probe the $I - \eta$

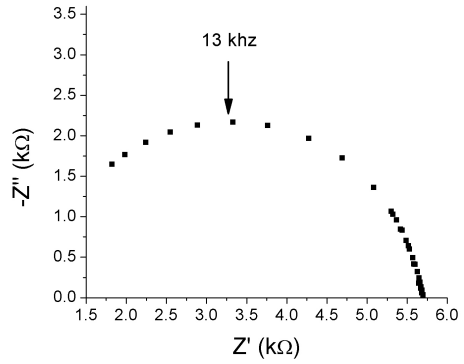


(a) Sample Nyquist plot at 233 °C . in humid hydrogen.

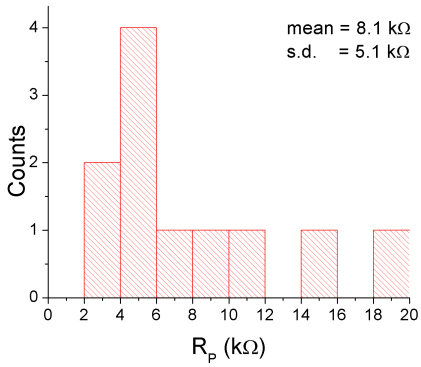


(b) Histogram of compiled zero-bias electrode resistances.

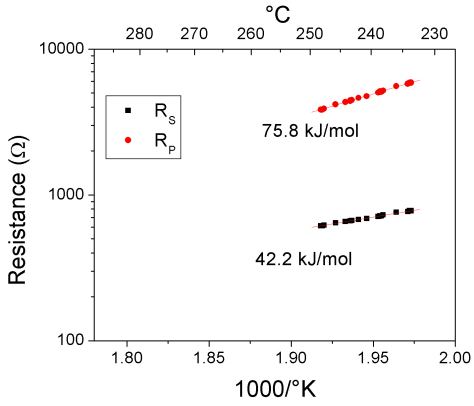


(c) Sample Arrhenius behavior in humid hydrogen. Ohmic activation agrees well with section 5.2.2

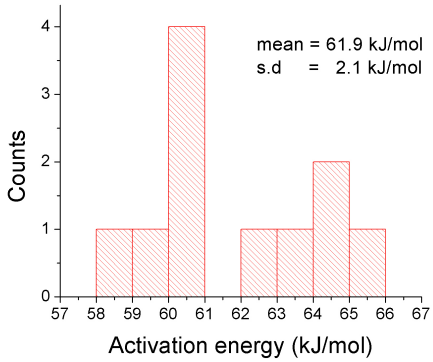


(d) Histogram of compiled activation energies.

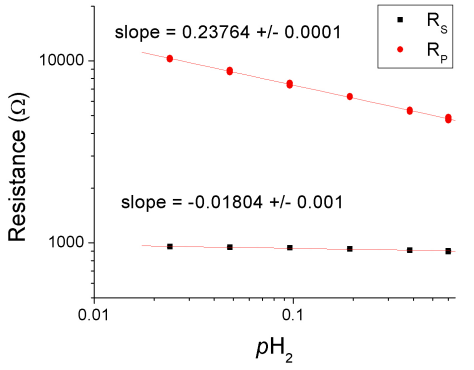


(e) Sample resistance vs $pH_2$ study. Ohmic resistance is independent of $pH_2$.

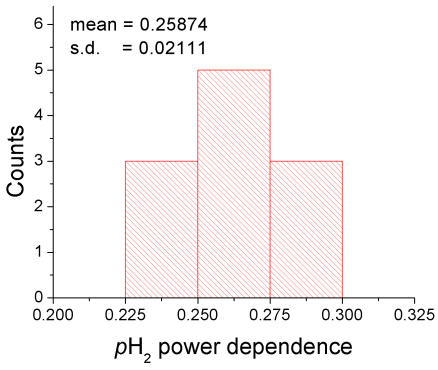


(f) Histogram of compiled power law $pH_2$ dependencies.

Figure 7.13: Representative thermodynamic data and histograms for 0.203 mm diameter palladium wire electrodes tested in humid (0.38 atm $pH_2O$) hydrogen by ACIS.

characteristics of palladium in hydrogen directly.

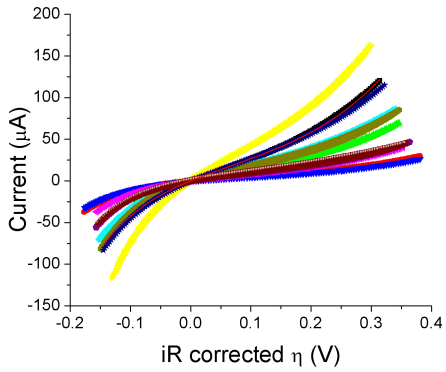


(a) IR-corrected cyclic voltammograms, with excellent fit to Eq. B.28.

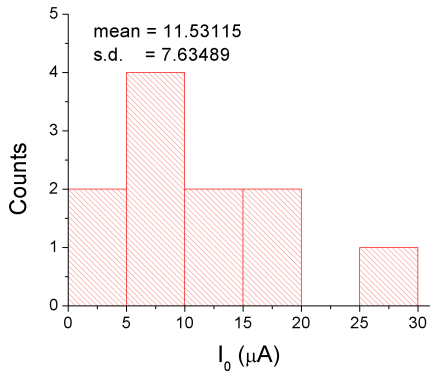


(b) Histogram of compiled exchange current densities, $I_0$, from fitting.

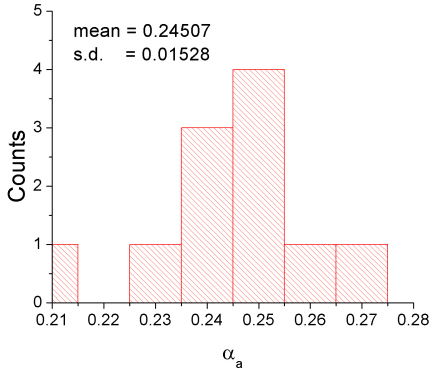


(c) Histogram of compiled $\alpha_a$ from fitting.

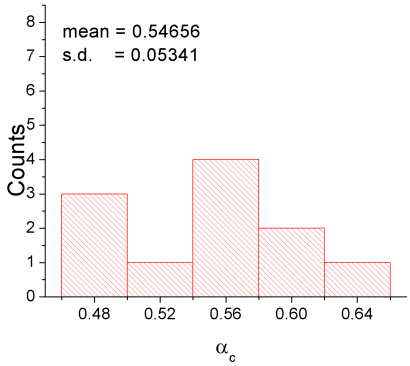


(d) Histogram of compiled $\alpha_c$ from fitting.

Figure 7.14: IR-corrected cyclic voltammograms and histograms of kinetic variables obtained from fitting the CVs to the Butler-volmer expression, Eq. B.28 for 0.203 mm diameter palladium wire electrodes tested in humid (0.38 atm $pH_2O$) hydrogen at 233 °C .

Figure 7.14(a) shows the IR-corrected cyclic voltammograms for all 11 electrodes. The wide dispersion in activity confirms the scatter of zero-bias impedance in Fig. 7.13(b), but each curve fits very well to a Butler-Volmer expression and the compiled kinetic variables from fitting the CV curves (figures 7.14(b)-(d)) are highly reproducible.

From this study, palladium wire electrodes are shown to be limited by a single process. Though the resistance of this process varied greatly between samples, all palladium wire electrodes evinced the same behavior. The single process fit very well to a Butler-Volmer charge transfer reaction with an anodic exchange coefficient of 0.245 ± 0.01, a cathodic exchange coefficient of 0.546 ± 0.05, and a circumference-normalized exchange current den-

sity of 18.1 ± 12 $\mu$A/mm. This exchange current density shows a negative 1/4 power dependence on hydrogen partial pressure and an activation energy of 62 kJ/mol.

That the rate-limiting step for palladium is Tafelian in nature is significant. All other candidate anode materials, including platinum, become more resistive under anodic bias, while palladium would become less resistive.

#### 7.2.2.2 Palladium powder electrode

The zero-bias impedance of a 0.203 mm diameter palladium wire anode is seen, at 5 kΩ , to be almost two orders of magnitude less resistive than 0.25 mm diameter platinum wires under the same conditions. If the low resistance is due to a bulk reaction pathway, however, powder electrodes cannot be expected to evince similarly superior kinetics - as surface kinetics become more prevalent.

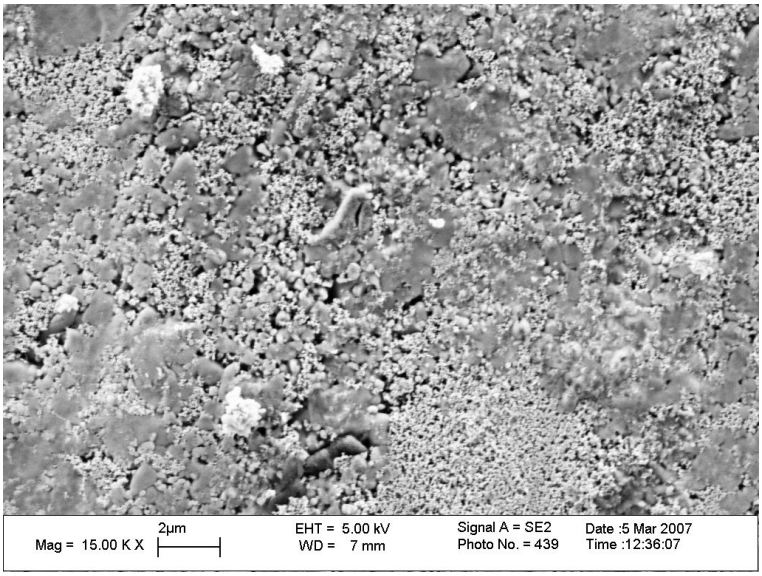


Figure 7.15: SEM micrograph taken at 15 kx magnification of the palladium powder on a $CsH_2PO_4$ electrolyte surface. Feature sizes of the palladium are well below the nominal 1 micron.

Recalling from chapters 4 and 5, the area-specific electrode resistance, $R_P^*$, of the binary Pt:$CsH_2PO_4$ (3:7 by wt) electrocatalyst mixture at 236 °C in humid (0.38 atm $pH_2O$) hydrogen is approximately 1.6 Ω -cm$^2$. To compare palladium to this result as well as possible, a binary mixture of Pd:$CsH_2PO_4$ (3:7 by wt) was fabricated as described in section 4.3. The palladium (Tanaka Kikinzoku,AY-4030) claims a mean particle size from 1.0 - 7.0

$\mu$m with a specific surface area of 9-16 $m^2/g$. The powder was examined by SEM (figure 7.15, however, and particle sizes were observed to be 100 nm or smaller.

A fully symmetric cell was fabricated with electrodes made of 30 mg of Pd:$CsH_2PO_4$ (3:7 by wt) supported by SS304 mesh GDLs. The electrodes were masked with PTFE to an active area of 1.2096 $cm^2$ and co-pressed with 400 mg of $CsH_2PO_4$ at 69 MPa (2 tons) for 5 minutes. The cell was loaded into a low-pressure single-chamber test fixture, and heated at 1 °C /min to 240 °C in humid (0.38 atm $pH_2O$) hydrogen gas flowing at 30 sccm. The zero-bias impedance of the electrodes was measured by ACIS. The Nyquist plot (figure 7.16) shows a great deal of noise, possibly due to the extremely low resistance. Fitting the impedance to a $R_S(R_PQ)$ equivalent circuit obtains an area-specific resistance of approximately 5 m$\Omega$ $cm^2$, and a calculated electrolyte conductivity of 0.014 S/cm. The electrolyte conductivity was analyzed in order to verify that the results were genuine. The area specific resistance of the binary Pd:$CsH_2PO_4$ (3:7 by wt) electrocatalyst mixture was approximately 300 times lower than that of the binary Pt:$CsH_2PO_4$ (3:7 by wt) under identical test conditions. Moreover, the fit resistance is seen to be stable over 22 hours (figure 7.16(b). An unidentified event at 11 hours causes the resistance to spike, but the electrode resistance re-equilibrates over the next 4 hours.

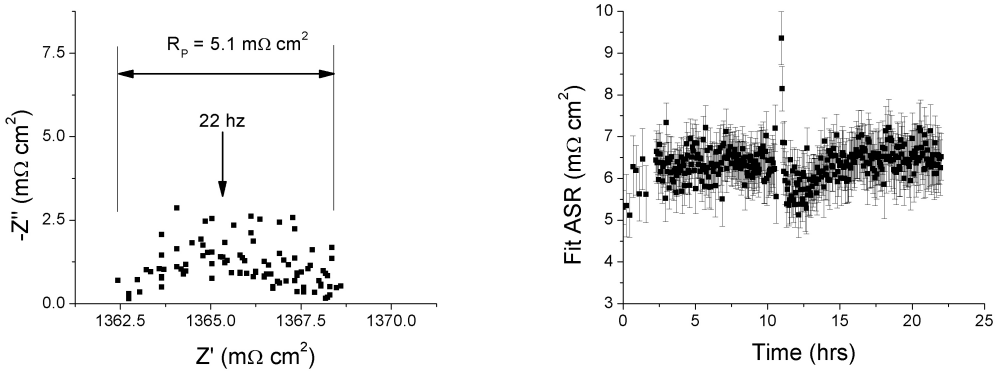


(a) Nyquist plot showing large noise and low resistance.

(b) Fit $R_P$ over 22 hour longevity test.

Figure 7.16: Impedance of Pd:$CsH_2PO_4$ (3:7 by wt) symmetric cell measured at 240 °C in humid (0.38 atm $pH_2O$) hydrogen.

## 7.3 Anode Conclusions

In Chapter 5, the platinum anode was identified as having high activity. That the anode response in operating fuel cells is insignificant compared to the cathode response makes investigation of anode kinetics problematic. The reference-less microelectrode approach was developed to investigate the the mechanism of the hydrogen redox reaction in the platinum-$CsH_2PO_4$ system. Because the anode is co-limited by two processes, the individual behavior of each was probed through ACIS under a range of biases. The rate limiting steps in such systems are not describable through charge transfer kinetics or Fickian mass-diffusion - but behave most similarly to an ohmic element - with a resistance that is insensitive to positive bias. This observation has two significant implications for the study of electrode catalysis in these systems. Firstly, because the anode response is linear with current, it is possible that any IR correction based on direct fitting (as in chapter 5) subtracted both the anode and electrolyte resistances. Secondly, though the zero-bias impedance of the platinum anode is several orders of magnitude lower than the (initial) zero-bias impedance of the platinum cathode, the charge-transfer limited cathode resistance will decrease with current while the anode resistance is unchanged. Put another way, due to differences in mechanism, zero-bias impedance of electrodes in oxygen (to study the cathode) and hydrogen (to study the anode) are not, in themselves, predictive of overpotential apportionment during fuel cell operation.

Additionally, because the anode is a minor contributor to the total overpotential, the opportunity exists for alternative non-platinum catalysts. Even materials with lower intrinsic activity may be viable anode candidates. To access intrinsic material activities, wire electrode geometries were developed and investigated. The mechanisms of electrodes with defined microstructures, however, are seen to differ from the mechanisms of powder composite electrodes, reducing confidence in the capability of defined microstructural electrode studies to predict losses of operating fuel cell electrocatalysts. Though care must therefore be taken in drawing conclusions without verifying mechanisms and activities with representative electrode microstructures, the wire and inverse electrode geometries enable apples-to-apples comparisons of candidate materials.

The methodology of such comparisons was developed and demonstrated by identifying nickel and palladium from a fairly limited candidate set as potential alternative anode

materials. Nickel and platinum, in both wire and inverse electrode geometries, are mass-transport limited and show comparable activity.

Palladium, on the other hand, is demonstrated to be superior to platinum as an anode material. Not only is the zero-bias impedance nearly two orders of magnitude lower in the case of wire electrodes, but the mechanism of hydrogen oxidation with palladium is Tafelian, compared to a mass-diffusion process for platinum. Meaning that, under bias, the overpotentials of palladium anodes will be even lower than the zero-bias impedance suggests.

Though initially the high hydrogen conductivity of palladium was suspected of indicating spuriously high surface activities, an electrocatalyst mixture composed of nanoscale palladium powder, tested in symmetric hydrogen, shows a zero-bias resistance more than two orders of magnitude lower than platinum.

Though only a limited number of anode candidate materials were investigated, a low-cost material with comparable performance to platinum was identified, as well as a lower cost (but still noble) material with significantly higher performance. More important, however, is the methodology developed in this work for analyzing anode materials in both defined microstructures and powder composites. Future investigations can broaden the set of tested materials to include additional elements, alloys, and intermetallics. Depositing oriented films, in conjunction with the inverse electrode geometry, even allows catalysis of controlled crystal faces to be characterized.

# Chapter 8

# Cathode Studies

## 8.1 Introduction

In chapter 5, it was determined that the primary source of electrode overpotentials in operating $CsH_2PO_4$ -electrolyte fuel cells is the cathode. An advantage conferred by the primacy of a single process is that crude experimental methods are able to determine a significant amount of information - namely that platinum-based cathode kinetics can be described by a Butler-Volmer charge transfer reaction with a cathodic exchange coefficient, $\alpha_c = (0.417+/- 0.105)$. In conjunction with a platinum-based anode, effectively all electrode losses will be due to the cathode. The consequence of this is that as an initial screening of non-platinum based cathodes, fabricating a full fuel cell is one method of identifying cathode kinetics. Measurements will still be convolved, of course, with the additional variables such as sealing and catalyst particle size. While quantitative comparisons are therefore not accessible, this approach is valid for qualitative comparisons.

## 8.2 Thermodynamic preview

In identifying potential candidates for a cathode material, an investigator might look into the thermodynamic stability of a variety of materials in an oxygen environment and compile a chart such as figure 8.1, displaying the energetics both of oxidation and reduction of a number of transition and platinum-group elements at 240 °C .

In examining the energetics, however, it is quickly apparent that of the examined elements, only silver and gold are thermodynamically stable in oxygen at this temperature. All other candidate materials, including platinum, should oxidize - and presumably inactivate

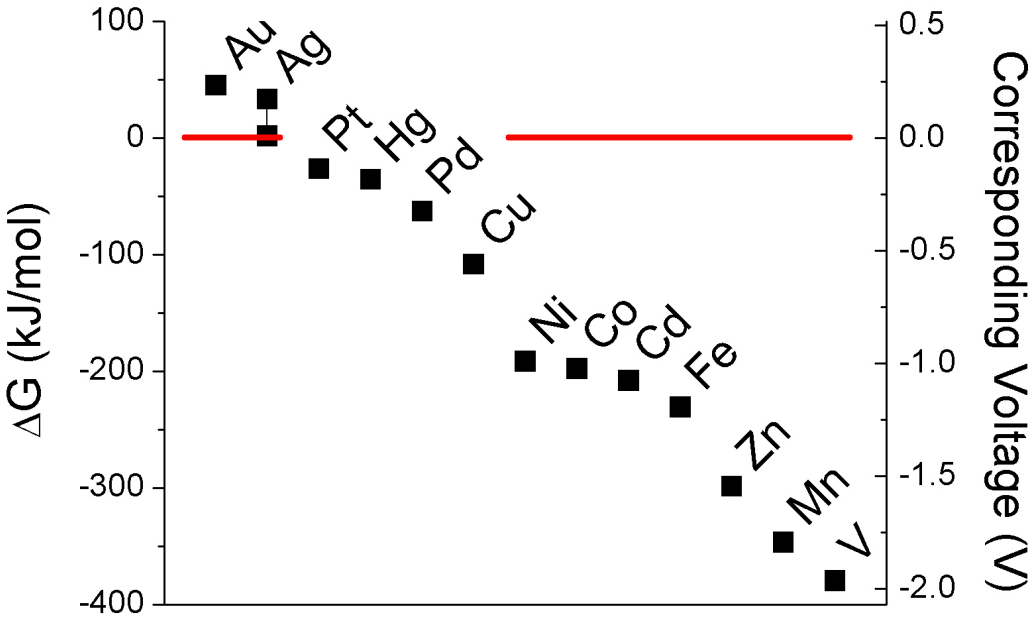


Figure 8.1: Energetics of oxidation for M+ $\frac{1}{2}$ $O_2$ $\rightarrow$ MO. Right axis shows corresponding voltage, related by Faraday's constant.

- in these conditions. However, as the longevity of platinum-electrode fuel cells has been demonstrated [(2)], it is clear that thermodynamic instability, calculated in this manner, is not a disqualifying characteristic. As the electrode potential is modified during current flow, the thermodynamics of oxide formation are correspondingly affected. The implication of this observation is that materials which oxidize at open circuit may still be candidates as cathode materials, since the formation of the oxide may be subsequently reduced during operation. However, the tendency of $CsH_2PO_4$ to react with oxides raises the likelihood that even exposing the metal-$CsH_2PO_4$ interface to oxygen may irrevocably destroy the cell.

With this in mind, investigation was limited to the left-most elements (excluding mercury). This resulted in a basic set of elements including gold, silver, platinum, and palladium. Gold was entirely inactive in every test, however, and will therefore not be discussed.

## 8.3 Platinum

Platinum is the traditional oxygen reduction catalyst. Early studies of platinum through standard approaches confirmed the high activity when compared to alternatives. Because of the difficulties in controlling catalyst dispersion and chamber sealing, as well as the oxidation of nearly all materials at open circuit, confounds the comparison of intrinsic cathode properties.

In chapter 5, the vast majority of platinum electrode losses were attributed to a single process in cathode. In a sense, because the cathode was so much more resistive than the anode, dual-chamber kinetic studies of this system unintentionally isolated the platinum cathode in a straightforward manner, making oxygen studies of asymmetric powder microelectrode cells unnecessary.

Additionally, since the greatest losses are at the cathode, so too are the greatest opportunities for improving catalysis. Pursuant to an apples-to-apples comparison, dense platinum electrodes are investigated in oxygen.

### 8.3.1 Wire

Platinum electrode kinetics in hydrogen were seen to vary between powder electrodes and dense electrodes, suggested by the difference in characteristic frequencies, and verified by

more rigorous kinetic studies. Similar comparisons are necessary before using platinum wire as a baseline to compare to alternative candidates. A 0.25 mm diameter platinum wire cell fabricated by method C (as described in chapter 7) with a 125 MPa uniaxial cold press for 15 minutes, and heat-treated to prevent bubbling (as described in chapter 10). The cell was heated in symmetric humid (0.38 atm $pH_2O$) hydrogen to 236 °C at 1 °C /min. After purging the chamber with humid (0.38 atm $pH_2O$) argon, humid (0.38 atm $pH_2O$) oxygen was flowed over the cell at a linear velocity of 2 cm/s and the impedance scanned from 10 khz to 1 mhz. The impedance is presented in nyquist form in figure 8.2.

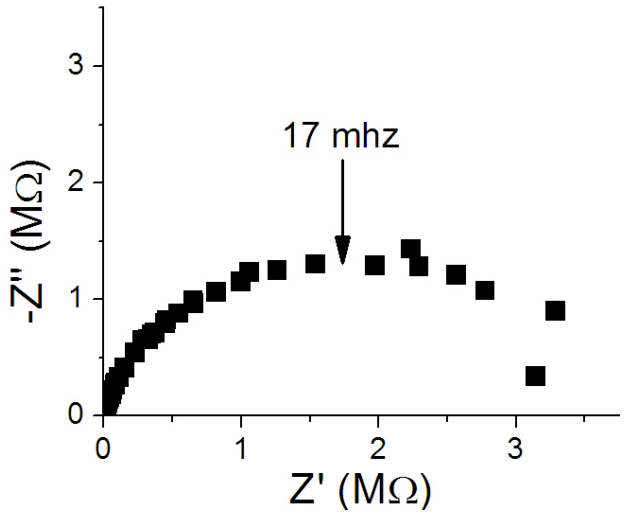


Figure 8.2: Nyquist plot of Pt wire electrode cell tested in symmetric, humid (0.38 atm $pH_2O$) oxygen at 240 °C , showing a single arc with characteristic frequency of 17 mhz.

While the resistance of the platinum wire is expectedly high, the shape is quite similar to nyquist plots of powder electrodes measured in chapter 5, and the single arc's characteristic frequency of 17 mhz agrees well with the characteristic frequencies measured for platinum. This suggests that the mechanisms of composite platinum powder electrodes and dense platinum electrodes is identical.

Fitting the impedance arc yields an ohmic resistance of 621 Ω . The relatively low ohmic resistance, combined with the extremely high resistance of the wire electrode results in the working electrode constituting 99.991 % of the entire cell response. Cyclic voltammetry measurements taken at slow scan-rates ( 10 mV/s) are used as a direct probe of electrode kinetics. GCI was considered unnecessary given the small contributions of the electrolyte

and counter electrode - and errors in estimation of ohmic resistance would have only minor effects on measurements. One such CV scan is shown in figure 8.3.

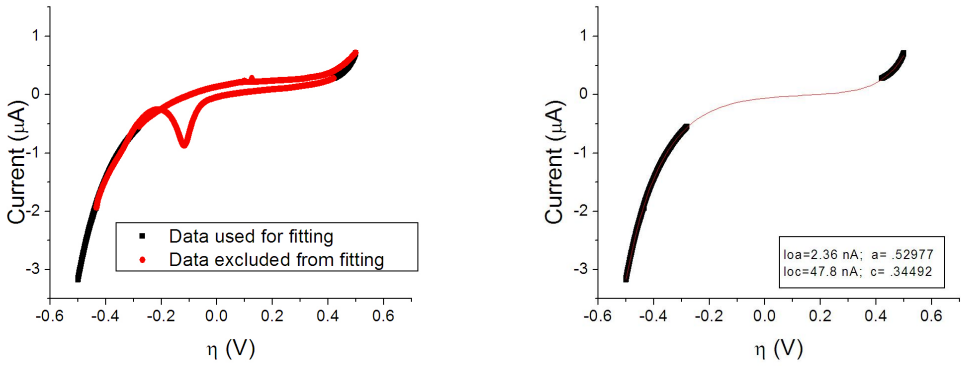


(a) IR-corrected cyclic voltammogram .

(b) Total Fit ASR of Pt cathode vs time.

Figure 8.3: Cyclic voltammograms of Pt wire electrode in symmetric humid (0.38 atm $p\mathrm{H_2O}$) oxygen at 235°C .

Figure 8.3(a) shows the existence of a reduction peak at approximately -0.12 V, corresponding well to the thermodynamic value of -0.13 V predicted in figure 8.1. This again confirms the existence of platinum oxide at ambient cathode conditions, but complicates kinetic treatment, so fitting is restricted to the extremes of the dataset. Additionally, since platinum is tested region is two phases - the metal and the oxide, a standard Butler-Volmer fitting is not applicable. Instead, the two returning arms of the cyclic voltammogram are treated semi-independently and fit to equation 8.1 as shown in figure 8.3(b).

$$I = I_{0,a} e^{\frac{\alpha_a nF}{RT}\eta} - I_{0,c} e^{\frac{-\alpha_c nF}{RT}\eta} \tag{8.1}$$

In this manner, the oxygen reduction kinetics of platinum with $CsH_2PO_4$ can be accurately probed. The water-splitting kinetics of platinum oxide with $CsH_2PO_4$ are also probed, but are not the focus of this work.

| | | | |
|---|---|---|---|
| $I_{0,a}$: | 3.00 nA/mm | $I_{0,c}$: | 60.9 nA/mm |
| $\alpha_a$: | 0.530 | $\alpha_c$: | 0.349 |

Table 8.1: Kinetic parameters of Pt wire cathode obtained by fitting the dataset in figure 8.3 to equation 8.1.

Though the complementary exchange coefficients are inaccessible, if we assume that

they sum to 1 in both cases, the zero-bias impedance can be predicted to be between the values calculated from the kinetics of pure oxide and pure metal, 9.3 MΩ and 0.5 MΩ .

Additionally, the cathodic exchange coefficient measured with platinum wire electrodes is lower than that predicted by the dual-chamber polarization curves in chapter 5, though still within the considerable statistical error.

### 8.3.2 Studying Pt Oxidation with Inverse Geometry

As the inverse geometry was originally developed to stabilize the catalyst-electrolyte interface mechanically, its application in systems that are chemically unstable could be considered limited. However, when used to identify the nature of that instability, it is invaluable to have confidence in mechanical stability so that all other effects may be explicated.

An inverse geometry cell was fabricated as discussed in section 6.4 and employed a 9.3 mm diameter, 0.5 cm thick $CsH_2PO_4$ electrolyte half-cell - supported with Pt:$CsH_2PO_4$ (3:7 by wt.) - held in the test fixture against 25 mm square Pt foil. The cell was then heated in humid (0.38 atm $pH_2O$) hydrogen to 240 °C at 1 °C /min, purged with humid (0.38 atm $pH_2O$) argon followed by humid (0.38 atm $pH_2O$) oxygen, and tested with an Autolab PGSTAT302.

Based on the platinum electrode resistance measured over time in figure 4.20, the electrode degradation in humid oxygen is seen to occur on the order of hours. Given the large reaction time, the rate of oxide formation should be measurable. As a quantitative tool, linear sweep voltammetry (LSV) was employed. LSV differs from CV only in that the voltage is not cycled - but instead has a defined initial voltage and end voltage. This method was employed to enhance confidence that the platinum metal is oxide-free at the beginning of the dwell times between measurements. By beginning from open circuit (0 V vs the platinum counter electrode), and sweeping to -0.35 V, surface oxide may be electrochemically stripped off. It should be noted that setting the voltage to zero will force the working electrode to the same level of oxidation as the counter electrode, and therefore corrupt the experiment. Instead, care was taken to construct the electrochemical method to be potentiostatic during testing, and galvanostatic (0 Amperes) during re-oxidation windows.

Representative LSV curves at different times are shown in figure 8.4(a), while the peaks are integrated and correlated to a total reduction current in figure 8.4 which is seen to increase with the square root of time as in a parabolic rate law.

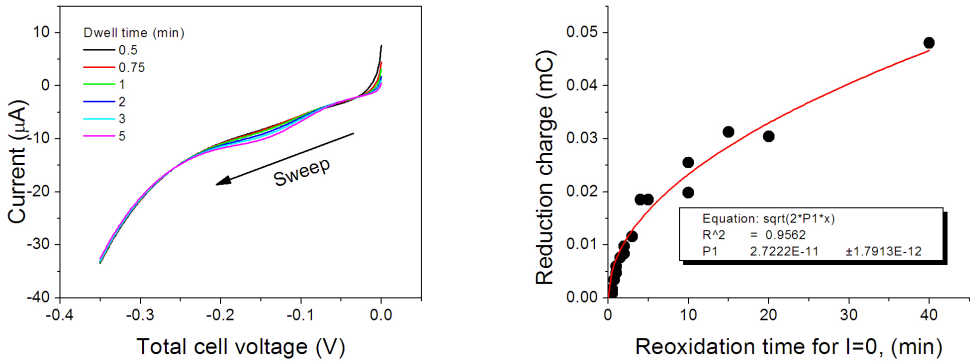


(a) LSV oxide stripping curves conducted with intermediate dwell times ranging from 30 seconds to 5 minutes.

(b) Compiled results from integrating peaks of LSV oxide stripping (with exponential baseline) vs time.

Figure 8.4: Study of platinum oxide formation by timed stripping voltammetry at 10 mV/s. Reduction charge plotted against dwell time reveals a parabolic rate dependence.

$$x^2 = 2k't \tag{8.2}$$

Though quantitative correlation between charge and oxide thickness, $x$, is not expressly determined, for a given cross-sectional area, the thickness and the total reduction charge should vary linearly with each other, resulting in a revised expression

$$Q^2 = 2k"t \tag{8.3}$$

Additionally, the scan can also be fitted to a Butler-Volmer expression to obtain an exchange current density (normalized by half-cell circumference) and exchange coefficient - In this case, 60.7 nA/mm and 0.370, respectively.

### 8.3.3 Platinum conclusions

The activity of the platinum cathode studied by inverse electrode geometry agrees extremely well with that of wire electrodes. Statistical analysis of 27 platinum wire electrodes in oxygen reveals the average cathodic exchange current density to be 54.3 +/- 10.7 nA/mm and the exchange coefficient to be 0.350 +/- 0.053.

Platinum cathode studies using the inverse electrode geometry do not lend themselves to statistical analysis, since only a single electrode may be measured at a time, but of the

three tested, the mean cathodic exchange current density was calculated to be = 69.97 +/- 86.25 nA/mm, and $\alpha_c$ = 0.380 +/- 0.032 showing very good agreement in both exchange current density and exchange coefficients between the two microstructures - in spite of the high scatter in $j_0$ for the inverse electrode geometry.

Additionally, the presence of oxide formation is confirmed, explaining the unsuitability of zero-bias impedance for measuring cathode stability. The rate of oxide formation is found to follow a parabolic law occuring on the order of hours.

The investigation of the platinum cathode is significant not only in characterizing the primary loss mechanism in operating solid acid fuel cells, but also in that it establishes a method by which alternative materials can be tested and directly compared to platinum.

## 8.4 Silver

Silver is an attractive candidate for replacing platinum on the cathode in $CsH_2PO_4$ fuel cells for three primary reasons: firstly, because it is a proven catalyst for the ORR in Alkaline fuel cells (which operate at similar temperatures); secondly, because unlike platinum, it is thermodynamically stable under $CsH_2PO_4$ fuel cell cathode conditions, and lastly because it's significantly more abundant than platinum.

To characterize the ORR, a multiplexed wire cell was fabricated following method C from chapter 6. Working electrodes ~250 microns long were cut from 0.5 mm diameter silver wire, then sonicated for 2 minutes in dilute nitric acid, then 10 minutes each in water, acetone, and isopropanol. 11 electrodes were covered with 1.0 g of $CsH_2PO_4$ and then 30 mg of binary platinum composite supported by stainless steel 304 mesh as the counter electrode. The entire assembly was pressed at 125 MPa for 10 minutes. The cell was secured into the multiplexing holder and contact between holder leads and electrodes was made by wirebonding with 25 micron Al99Si1 wire. After loading into the multiplexing test fixture and sealing in the single-chamber, the chamber was purged with humid (0.38 atm $pH_2O$) argon followed by hydrogen as the cell was heated at 1 °C /min to 239 °C . After purging again with humid argon, oxygen was introduced to the chamber at 30 sccm and the electrodes were analyzed with an Autolab PGSTAT302.

To identify the number of processes involved, the silver electrodes were analyzed with zero-bias impedance spectroscopy - a representative nyquist plot is shown in figure 8.5.

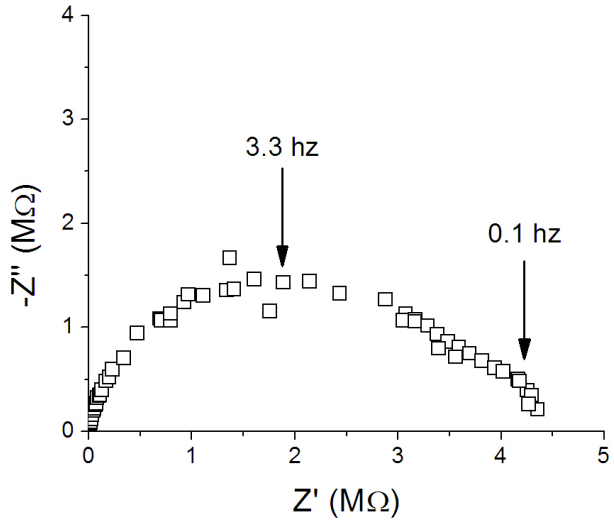


Figure 8.5: Nyquist plot of Ag wire cathode zero-bias impedance from ACIS measured in humid (0.38 atm $p\mathrm{H_2O}$) $\mathrm{O_2}$ at 239 °C

Though a low-frequency arc is detectable, silver cathode kinetics, like platinum cathode kinetics, are dominated by a single process.

To explore the electrochemical landscape of the silver-$\mathrm{CsH_2PO_4}$ system in humid oxygen, one electrode was investigated with cyclic voltammetry from -500 mV to +500 mV at scan rates ranging from 10 mV/s to 100 mV/s. The resulting voltammograms are shown in figure 8.6(a). Two peaks appear close to equilibrium on the return sweep, with positions agreeing well with the reduction of AgO and $\mathrm{Ag_2O}$ respectively. No peak, however, is seen to exist wholly within the cathodic operating range, consistent with expectations.

The kinetic behavior of each of the 11 electrodes was then individually probed with cyclic voltammetry from 0 mV to -300 mV at 10 mV/s and presented in figure 8.6(b). The curves are straightforward, concave down polarization curves, suggesting that silver cathode kinetics are also dominated by a charge-transfer step.

Fitting the cathodic polarizations from the 11 wire electrodes in this cell to a Butler-Volmer expression yields the histograms of exchange coefficients and length-normalized current densities in figure 8.7. Good reproducibility is seen in $j_0$, but high scatter in alpha. Removing the two slight outliers does not significantly reduce the standard deviation. Both outlier electrodes' $j_0$ was between 5.5 and 6.0 nA/mm. The mean measured length-specific current density was 6.1 nA/mm with a standard deviation of 0.57 nA/mm. The mean

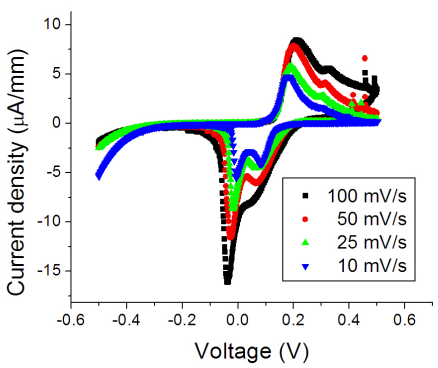


(a) Cyclic voltammogram of a single Ag wire working electrode, measured by CV between -0.5 V and 0.5 V at varying scan speeds. Large redox peaks are detectable.

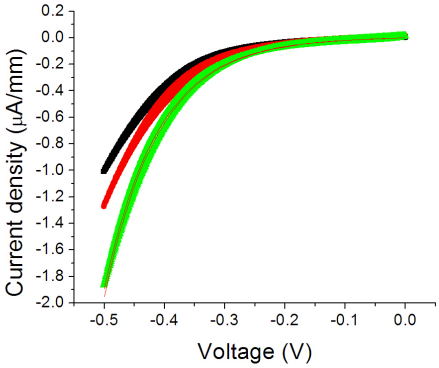


(b) Ag working electrodes measured by cyclic voltammetry between -0.5 V and 0 V (vs Pt counter electrode) at 10 mV/s. No peaks are detected. For clarity, only three measurements are shown.

Figure 8.6: Silver wire electrode cells at 236 °C in symmetric, humid (0.38 atm $p\mathrm{H_2O}$) oxygen tested by CV.

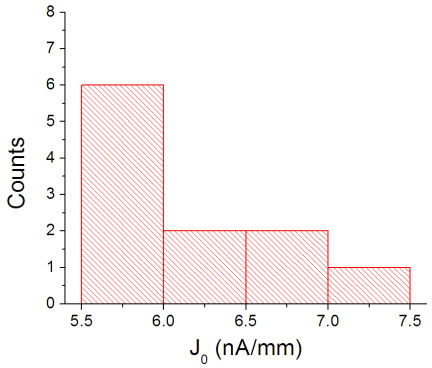


(a) Histogram of fit exchange current densities for Ag wire cathodes.

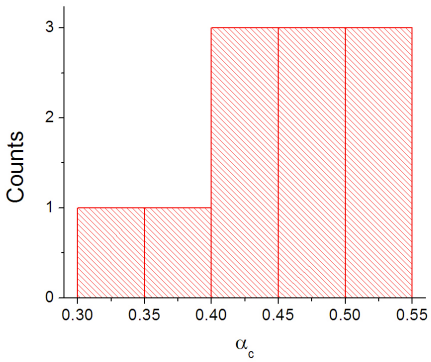


(b) Histogram of fit exchange coefficients for Ag wire cathodes

Figure 8.7: Histograms of silver wire electrode cells at 236 °C in symmetric, humid (0.38 atm $p\mathrm{H_2O}$) oxygen tested by CV and fit to a Butler-Volmer expression.

cathodic exchange coefficient was 0.455 with a standard deviation of 0.063.

## 8.5 Palladium

Palladium is of extremely interesting as a potential cathode material. Through virtue of its high hydrogen conduction, the potential for a change in reaction mechanism from one based on triple-phase boundaries to double-phase boundaries could significantly increase the number of reaction sites. Anode studies in Chapter 7 demonstrated a palladium performance in hydrogen comparable to that of platinum, and as a first test, pure palladium powder (95% purity as used in chapter 7) supported by SS316 GDLs was, by itself, used as both electrode materials for a $CsH_2PO_4$ based fuel cell flowing humid hydrogen on the anode and humid oxygen on the cathode. For comparison, another fuel cell with pure platinum powder electrodes was identically prepared and simple polarization curves with calculated power densities were used to characterize the cells - the results from the two are shown in figure 8.8.

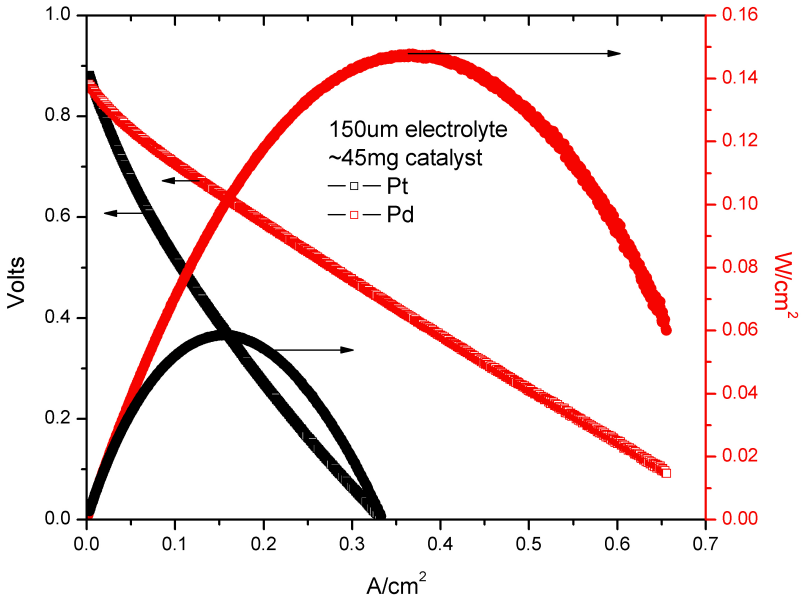


Figure 8.8: Palladium and Platinum electrode (powder) fuel cell polarization curves measured in dual-chamber with humid (0.38 atm $pH_2O$) $H_2$ and $O_2$ at 236 °C

Palladium performed beyond expectations as a cathode. For a non-optimized electrode

microstructure, a palladium-based cell had a peak performance over 2.5 times that of an identically prepared platinum-based cell. Fitting of the form 4.1 also shows an exchange coefficient of 0.6 and an exchange current density of 21 mA/cm$^2$ - approximately an order of magnitude higher than the quaternary platinum composites discussed in chapter 5.

The performance was somewhat short-lived, however. Figure 8.9 shows subsequent polarization scans and reveals a quickly increasing overall cell resistance.

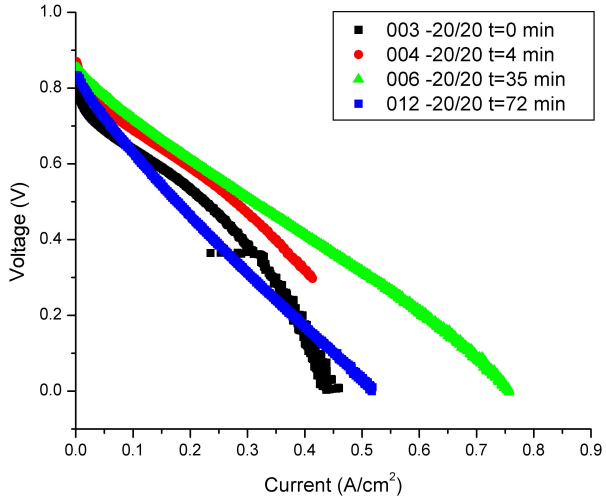


Figure 8.9: Palladium cathode polarization curves taken at different times.

Because of the strong thermodynamic driving force towards the formation of palladium oxide, chemical oxidation was suspected, and a galvanostatic longevity test was performed. Since the electrolyte (Fig. 4.10) and the anode (Fig. 7.16b) are demonstrably stable, the cathode is the likely unstable component. To verify the reversibility and mechanism of the increased resistance, the electrodes were effectively switched by purging both sides with argon and then reversing gas delivery. The results in figure 8.10 show the voltage vs time curves for a 100 mA/cm$^2$ current draw over 12 hours in each environmental configuration.

Evidenced by the return to high voltage - which indicates a low overall resistance - and similar voltage vs time behavior, the instability of the palladium cathode is seen as reversible. The decreased performance is therefore believed to be due to the formation of an electrocatalytically inactive oxide layer. The inactivation of the palladium is initially quite fast, but after the initial drop, seemingly occurs on the order of hours. Because there is no independent current collector in the cathode, it is not clear if active sites are also lost

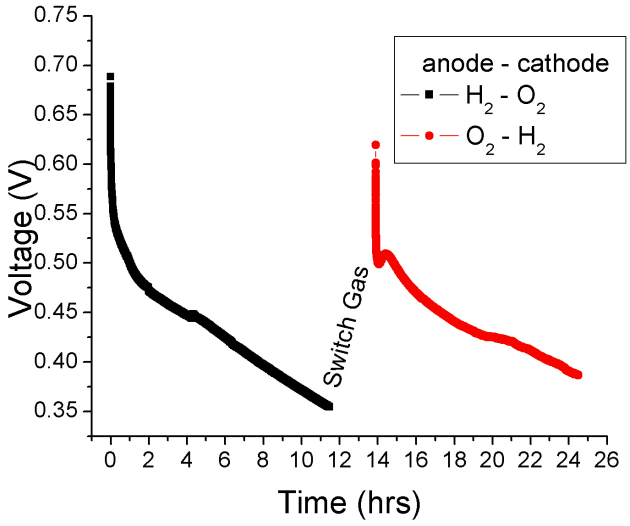


Figure 8.10: Palladium electrode longevity test in fuel cell mode

due to restricted electrical access to the $CsH_2PO_4$ - palladium interface.

To further investigate the palladium cathode, zero-bias symmetric cell measurements of the palladium powder cathode were conducted in humid oxygen atmosphere. The nyquist plot is shown in figure 8.11.

While the nyquist plot is dominated by the single arc, material instability precludes the possibility of in-depth analysis. As a first look at the palladium cathode - and to verify the cathode degradation, impedance plots were fit to an equivalent circuit of the form R(RQ) and the low frequency resistance was plotted vs time in figure 8.12.

As suspected, cathode resistance increases dramatically with time. And unlike the platinum longevity, this degradation occurs in fuel cell mode as well. To mitigate this deactivation, two actions were considered: Either alloy the palladium with a more oxidation-resistant metal or slightly modify the thermodynamic driving force.

### 8.5.1 Alloy

A second approach alloys palladium with a more oxidation-resistant metal. While alloys and their properties constitute an entirely additional field (or two), this was seen as a reasonable approach to both preserve the high cathode performance while introducing some needed stability. Due to the high processing time, only one composition was made and tested.

To guide the alloy composition, the thermodynamics of oxidation of each component were

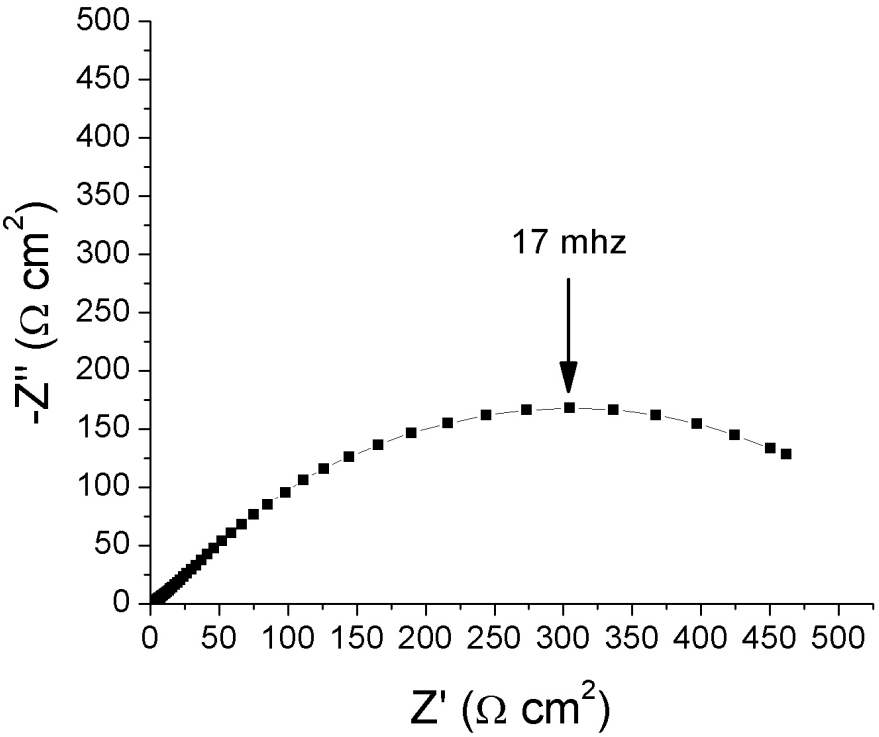


Figure 8.11: Sample nyquist plot of symmetric palladium powder electrodes tested in humid (0.33 atm $p\mathrm{H_2O})\mathrm{O_2}$

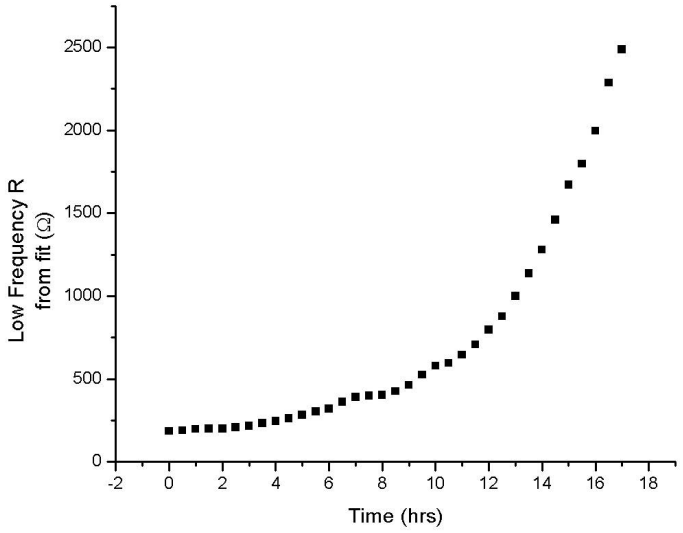


Figure 8.12: Palladium electrode zero-bias ACIS longevity test in symmetric humid (0.33 atm $p\mathrm{H_2O})\mathrm{O_2}$

examined as in figure 8.1. Though stability against oxidation is not explicitly required in an electrode, the composition was chosen so that the average $\Delta G$ of oxidation was equal to zero as in equation 8.4.

$$\Delta G_{a,ox} * (1 - x) + \Delta G_{b,ox} * (1 - x) = 0 \tag{8.4}$$

Silver was selected as the alloying component, and as $\Delta G_{Ag,ox}$ = 1.49 kJ/mol of Ag, and $\Delta G_{Pd,ox}$ = -62.9 kJ/mol Pd, the nominal composition of the alloy was chosen to be 4.5 at. % Pd in Ag. The atomic weight of palladium and silver differ by only a percent.

#### 8.5.1.1 Alloy Synthesis

An ingot was fabricated by arc melting 0.21 grams of palladium and 4.02 grams of silver together in an argon-filled chamber. While silver melts at 962 °C , palladium melts at a much higher 1552 °C . The phase diagram reproduced in figure 8.13 shows only solid solution between the two, easing synthesis. Joe Schramm in Professor William Johnson's lab assisted in the alloying of the ingot. Wires were formed from the alloy ingot by cold-rolling through successively narrower V-grooves until a wire with a square cross-section, 2 mm on a side, was obtained. To analyze the resulting composition, a slice was cut from the center of the wire with a razor blade, sanded, cleaned in isopropanol, then analyzed with energy-dispersive x-ray spectroscopy (EDS) in a LEO SEM at an accelerating voltage of 10 kV. The EDS spectrum was analyzed with INCA software. The micrograph and EDS results are presented in figure 8.14.

The alloy wire composition measured by EDS agrees very well with the nominal composition of 5 at.% palladium in silver.

#### 8.5.1.2 Characterization

A cell was fabricated from the wire after fabrication approach A from Chapter 6 with 1.2 g of $CsH_2PO_4$ electrolyte and a stainless steel GDL-supported Pt/C counter electrode. After densification at 143 MPa for 30 minutes, excess naphthalene was removed at 100 °C in ambient, vented air. The cell was sealed into the dual-chamber pressureless holder with Viton as shown in figure 6.16 and electrodes were contacted to leads with silver paint. The assembly was heated to 238 °C in humid (0.38 atm $pH_2O$) hydrogen, followed by argon at

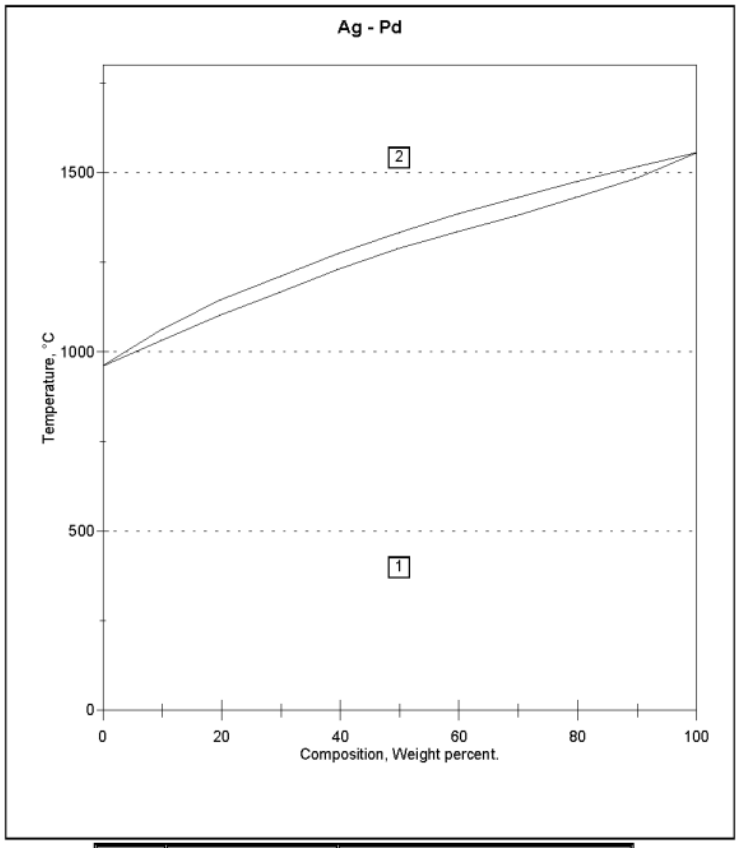


| Box No. | Marked field | Composition or state. |
|---|---|---|
| 1 | Phase field | Solid solution. |
| 2 | Phase field | Liquid |

Figure 8.13: Silver - Palladium phase diagram

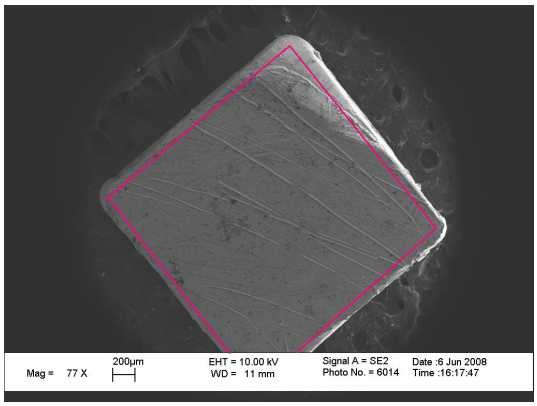


(a) Low magnification SEM micrograph of cross-sectioned alloy wire with indicated region of EDS analysis.

Spectrum processing :
No peaks omitted

Processing option : All elements analyzed (Normalised)
Number of iterations = 1

Standard :
Pd Pd 1-Jun-1999 12:00 AM
Ag Ag 1-Jun-1999 12:00 AM

| Element | App Conc. | Intensity Corrn. | Weight% | Weight% Sigma | Atomic% |
|---|---|---|---|---|---|
| Pd L | 0.02 | 0.9891 | 4.82 | 2.29 | 4.88 |
| Ag L | 0.44 | 1.0005 | 95.18 | 2.29 | 95.12 |
| Totals | | | 100.00 | | |

(b) EDS spectrum taken at 10 kV shows 5 at.% palladium in silver.

Figure 8.14: Cross-sectioned wire seen under low-magnification SEM and compositionally analyzed by EDS.

1 °C /min. After reaching 238 °C , the working and counter electrodes were exposed to humid oxygen and humid hydrogen, respectively. The open circuit voltage was allowed to equilibrate to a low value of 0.8 V before being tested with an Autolab PGSTAT302.

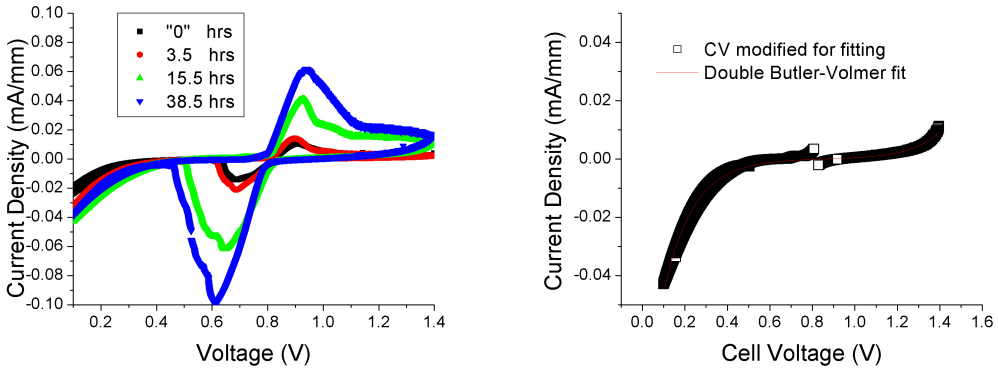


(a) CV scans at different times reveal changing kinetic behavior and increasing reduction charge.

(b) CV scan at 15.5 hours modified for fitting by excluding redox peaks.

Figure 8.15: Cyclic voltammograms of Pd5Ag95 alloy wire electrode in asymmetric, dual-chamber configuration.

Initially, voltage was cycled between 100 mV and 1400 mV at 5 mV/s, scans at 4 different times are shown in figure 8.15(a). To obtain kinetic parameters, peaks were excluded and the remaining dataset fit to a double Butler-Volmer equation. The fit kinetic parameters are shown in figure 8.2.

| $j_{0,a}$: | 130 nA/mm | $j_{0,c}$: | 280 nA/mm |
|---|---|---|---|
| $\alpha_a$: | 0.323 | $\alpha_c$: | 0.318 |

Table 8.2: Kinetic parameters of Pd5Ag95 alloy wire cathode obtained by fitting the dataset in figure 8.15(b) to equation 8.1.

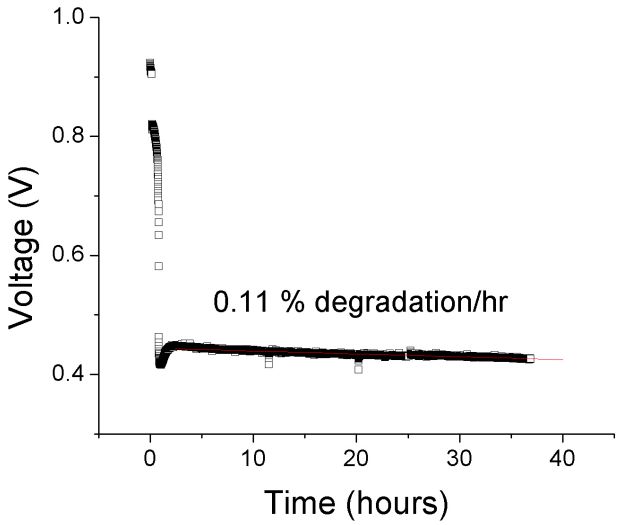


Figure 8.16: Pd5Ag95 alloy wire cell voltage during 35 hour 20 $\mu$A/mm galvanostatic longevity measurement.

To identify if the high performance was sustainable, a current of 20 $\mu$A/mm was drawn for 35 hours. The measured voltage, shown in figure 8.16, is seen to degrade at 0.11% per hour over the tested time.

Thus through alloying palladium and silver, stable performance higher than either constituent element is obtained. Further experimentation is needed in order to verify, however, as the Pd5Ag95 alloy wire is the only one tested that was fabricated in-house and it is possible that interfacial roughness caused an underestimation of electrode perimeter. Another open question presented by figure 8.15(a) is the magnitude of the reduction charge. Integrating the reduction peak area of the scan taken at 38.5 hrs yields a reduction charge of 181 mC. As a back-of-the-envelope calculation, at a cubic lattice constant of 408 pm, 181 mC corresponds to an area of approximately 538 $cm^2$ if the reduced elements are monatomic and bivalent. For an electrode with an interfacial contact of only 0.08 $cm^2$, this strongly suggests that oxidation is occurring in three-dimensions through either the electrode or the electrolyte.

### 8.5.2 Change oxidative driving force

The simplest way to stabilize the palladium cathode is to simply change the oxygen partial pressure. There is a limited range of options, of course, but the $pO_2$ of air is 0.21 and if palladium is stable at these conditions, it would be potentially more suitable for real-world application.

Palladium, like platinum, is thermodynamically unstable even at low $pO_2$, so zero-bias ACIS is definitionally unstable. Linear sweep voltammetry can again be used to quantify oxidation rates as was done with platinum. Because palladium exhibited much lower stability in oxygen than platinum, we investigated not only the oxidation rate, but also its dependence on $pO_2$.

To compare with the platinum stripping experiments, a cell was fabricated in an identical manner, but with a cylinder of cut palladium as the working electrode. 1 gram of $CsH_2PO_4$ was used as the electrolyte and 30 mg of the binary Pt:$CsH_2PO_4$ electrocatalyst composite supported by a stainless steel 304 GDL electrode served as the counter electrode. After pressing, electrodes were contacted with wirebonded 25 micron Al99Si1, and the cell was loaded into the single chamber holder, heated to 240 °C at 1 °C /min in humid (0.38 atm $pH_2O$) hydrogen, then purged with humid argon before commencing testing with an

Autolab PGSTAT 302A.

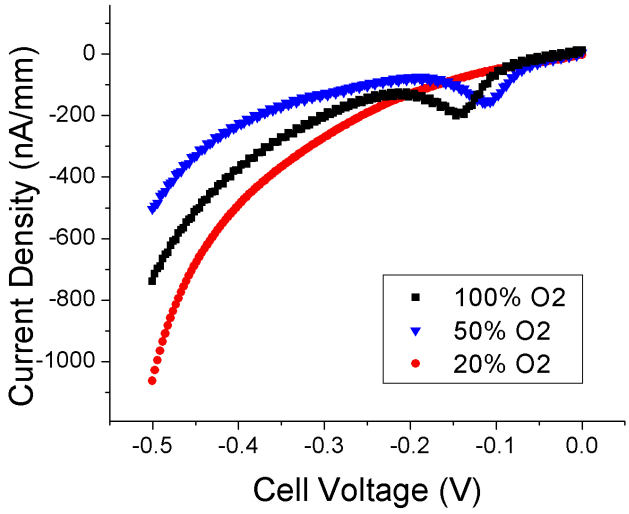


Figure 8.17: LSV measurements following 5 minute dwells, of a palladium wire electrode in various environments.

Linear Sweep Voltammetry (LSV) from 0 V to -0.5 V vs the platinum counter electrode was again used to prove oxidation rates by dwelling at zero current for defined times. LSV scans taken after 300 second zero-current dwells in various concentrations of inlet oxygen (balance argon) are shown in figure 8.17. From pure inlet oxygen to 50% oxygen, a slight shift in peak location to less negative potentials is consistent with thermodynamic intuition. Further dilution of oxygen to 20% however, causes the reduction peak to disappear entirely, and performance is actually seen to improve. Excluding the peaks, the LSV measurements were fit to a Butler-Volmer expression to obtain the values in table 8.3

| Inlet % $O_2$ | $j_0$ (nA/mm) | $\alpha_c$ |
|---|---|---|
| 100 | 29.1 | 0.283 |
| 50 | 15.4 | 0.303 |
| 20 | 33.5 | 0.300 |

Table 8.3: Kinetic parameters of Pd wire cathode in different concentrations of humid (0.38 atm $p H_2O$) $O_2$.

## 8.6 Conclusions

With the methodologies developed in this work, direct comparisons can be made between candidate materials for solid acid fuel cell cathodes. The three pure metals presented in this chapter - platinum, silver, and palladium - all exhibited Tafelian behavior and polarization curves fit well to the Butler-Volmer expression that would be expected for a charge-transfer process and the relevant variables for electrode operating kinetics are presented in table 8.4.

| Material | $j_0$ (nA/mm) | $\alpha_c$ |
|---|---|---|
| Pt | 60.1 | 0.38 |
| Ag | 6.1 | 0.45 |
| Pd | 33.5 | 0.30 |
| Alloy | 280 | 0.32 |

Table 8.4: Summary of tested cathode materials' kinetics measured in humid (0.38 atm $p\mathrm{H_2O}$) oxygen at 240 °C (Pd tested in "air."

Though silver and palladium are shown to be stable cathode materials under certain conditions, platinum shows a higher exchange current density than both. While the Pd5Ag95 alloy shows an exchange current density more than 4 times that of platinum, the results are made less conclusive by two factors: firstly, the cell was tested in dual-chamber mode, so the electrode potential was ill-defined, and secondly, the alloy wire was synthesized in-house. Efforts to smooth the surface were made, but significant surface roughness could account for some of the apparently superior activity. Defined microstructures in symmetric chamber are shown to be excellent predictors of operating mechanism, while simultaneously allowing direct comparisons between candidate materials.

# Chapter 9

# $CsH_2PO_4$

All electrocatalyst studies presented in this thesis were done in conjunction with a $CsH_2PO_4$ electrolyte. As such, to enable and inform the fabrication techniques developed here, a number of studies of $CsH_2PO_4$ itself were undertaken. Of particular interest are mechanical properties, above and below the material's phase transition - as these inform evolving interfaces and fabrication methodologies, respectively.

Additionally, the melting point of $CsH_2PO_4$ is identified as greater than 300 °C , but in practice, cells would fail above 260 °C . This behavior was explained by Uda *et.al.* in 2007 [(42)] as the formation of a partially-dehydrated, liquid phase. Investigation was done into using silica to stabilize the electrolyte in this phase through mechanical effects. There is significant utility in extending the operating range of $CsH_2PO_4$ to 300 °C as many catalysts become very active for alcohol reformation in this regime. [(43)]

### 9.0.1 Sensitivites

As $CsH_2PO_4$ in the superprotonic phase is a stoichiometric proton conductor, the concentration of charge carriers is insensitive to temperature and atmosphere. The one caveat to this is that there only exists a fairly narrow operating window in which the high-conductivity phase of $CsH_2PO_4$ is stable. There was originally some controversy as to whether measured superprotonic properties were genuine, or merely an artifact of dehydration. [(44)(4)]. Haile *et.al.* showed that a sufficiently humid environment was capable of stabilizing the superprotonic phase, and in doing so verified the high protonic conductivity [(33)]. Uda et al further investigated the high temperature - high humidity dehydration behavior [(42)(45)], and revealed an intermediate, partially dehydrated phase - $CsH_{2-2x}PO_{4-x}$. While chemically

stable, however, superprotonic $CsH_2PO_4$ has constant charge carrier density.

## 9.1 Mechanical properties of neat $CsH_2PO_4$

Of these steps involved in fabricating cells based on the $CsH_2PO_4$ electrolyte, the most stressful is the final press, where the gas-diffusion layer may deform and either reduce porosity, delaminate from the electrode mixture, or both. For this reason, a study was undertaken to identify the densification behavior of $CsH_2PO_4$ at room temperature.

### 9.1.1 Densification behavior

The densification behavior of $CsH_2PO_4$ was investigated by uniaxial cold-pressing 200 mg of powder in a nominal 10mm diameter die at various pressures. Density was measured via the Archimedes Method with an in-house built apparatus. Toluene (density: 0.867 g/cm$^3$) was used as the displaced fluid. Densification was calculated as the percentage of theoretical $CsH_2PO_4$ density ($\rho$=3.255 g/cm$^3$), itself calculated from crystallographical data of the monoclinic phase. The results of 1 minute presses and 20 minute presses are shown in figure 9.1.

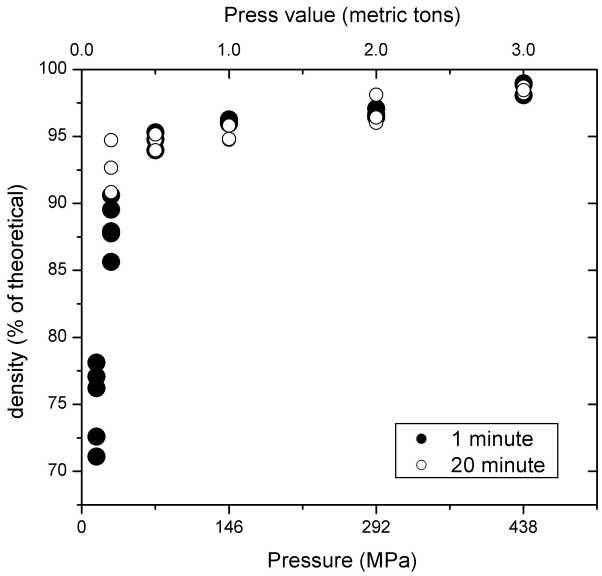


Figure 9.1: $CsH_2PO_4$ density vs pressure for 1 minute and 20 minute presses

Several interesting features are worthy of comment: firstly, $CsH_2PO_4$ is seen to densify

fairly readily, achieving 95% densification at only 73 MPa for 1 minute. Secondly, for pressures exceeding 73 MPa, increased pressing time seems to have little effect on densification. And lastly, at high pressures, 98%-99% density is readily achievable.

### 9.1.2 Sintering Behavior

It is easy to imagine, however, a situation where a fragile electrode or gas-diffusion layer requires low-pressure fabrication. In this situation, it would be desirable to fabricate a Membrane-Electrolyte Assembly with a lower density electrolyte, then heat the cell to the operating temperature to sinter the electrolyte further. Investigation into the high-temperature sintering behavior of $CsH_2PO_4$ is restricted by the relatively low maximum stable temperature, so the sintering conditions were restricted to 16 hours at the approximate operating temperature of 240 °C . Samples were heated and cooled in humid (0.33 atm $pH_2O$) argon at 1 °C /min without any mechanical pressure.

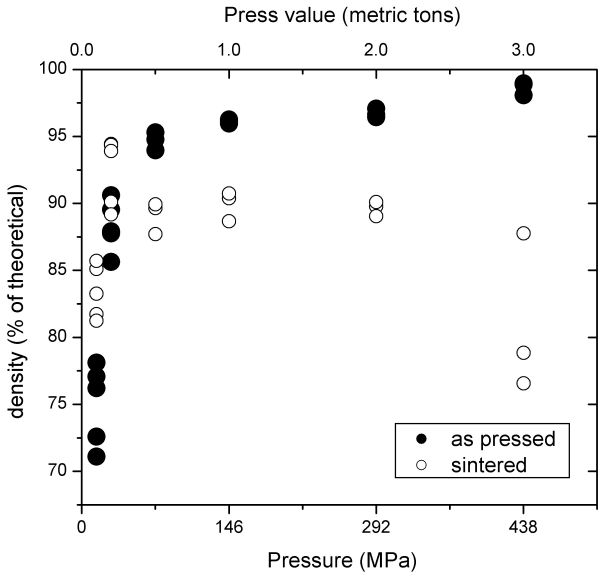


Figure 9.2: $CsH_2PO_4$ density vs initial uniaxial densification pressure before and after pressure-less sintering

While figure 9.2 shows an expected increase in density for pellets with low initial densities - surprisingly, $CsH_2PO_4$ pellets with initial densities above 92.5% actually loses density. Some pellets exhibited the formation of a large internal bubble, as pictured in figure 9.3. Given that the temperature used to probe sintering is the same as would be used for cell operation, this physical change in electrolyte could have significant effects on any subsequent

measurements. Dr. Dane Boysen used NMR to quantify the state of water on $CsH_2PO_4$ at various temperatures and found a significant amount of surface water at grain boundaries (unpublished). If this trapped water were heated without an avenue for dissipation, it could form internal gas pockets. While macroscopic bubbles like the ones shown in figure 9.3 are an extreme example, microscopic pores as well affect the final density.

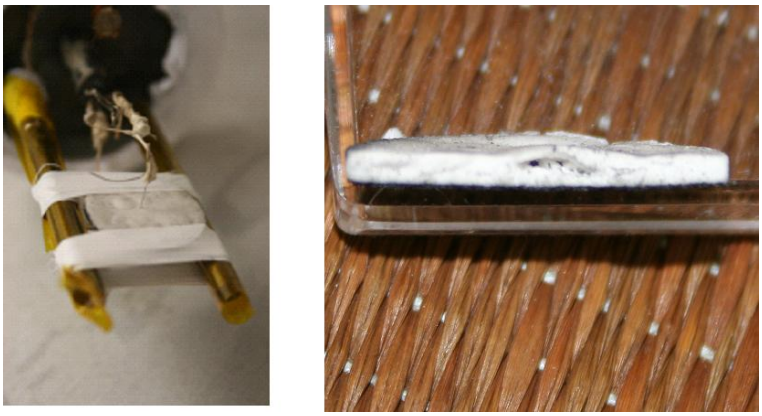

Figure 9.3: $CsH_2PO_4$ Cavity formed by pressure-less sintering of pressed $CsH_2PO_4$

Such pores are considered to be the result of surface water vaporizing on heating without an avenue for dissipation, creating internal gas pockets. To prevent such bubbling, two precautions were taken. Firstly, all $CsH_2PO_4$ electrolyte powder was kept at approximately 120 °C in ambient air to prevent hydration. Secondly, every cell that would be tested without axial pressure was first heated at 1 °C /min to 240 °C in humid (0.38 atm $pH_2O$) argon or hydrogen under pressure. For wire electrode cells made by fabrication method C, the surface was pressed against a cleaned glass slide. For wire electrodes made by fabrication methods A or B, such pretreatment was impossible.

### 9.1.3 Deformation

The mechanical properties of superprotonic $CsH_2PO_4$ was studied by Dr. Jian Wu at Caltech. Using a thermomechanical analyzer, the strain rate of $CsH_2PO_4$ was measured under approximately 0.1 MPa. The results, shown in figure 9.4, reveal plastic deformation (consistent with (3)) with a creep rate of approximately 5E-7 $s^{-1}$.

This superplastic deformation represents a strongly idiosyncratic material property among solid electrolyte fuel cells. While it has potentially challenging implications for device fabrication and longevity, it also presents a potential advantage - specifically in-

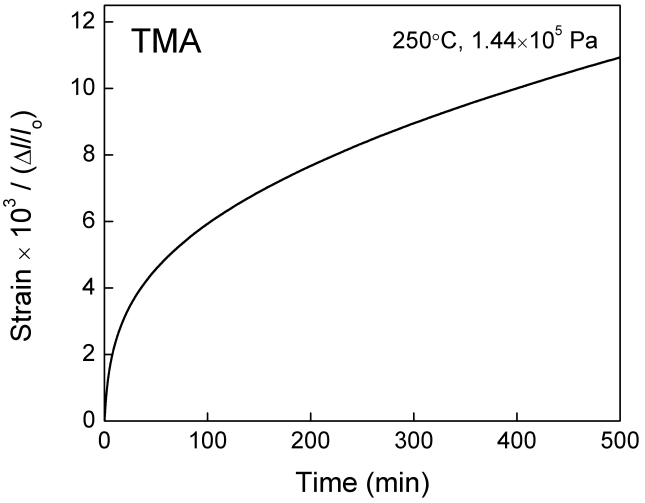


Figure 9.4: Plastic behavior of $CsH_2PO_4$ at 240 °C .

situ densification. To verify that the superplasticity of $CsH_2PO_4$ above the superprotonic transition can be exploited in this manner, a low density pellet was fabricated. To secure pressure, it was sandwiched between two steel-supported glass slides and tightened with 4 8-32 bolts tightened to an initial torque of 2in-lbs each. A detailed calculation can be done to accurately extrapolate force values, but requires values beyond bolt dimensions and torque, and is beyond the scope of this simple experiment. For this, we approximate the initial force as 1 kilonewton - which for a 9.3 mm diameter pellet corresponds to a pressure of 15 MPa. After 19 hours at 240 °C in humid (0.33 atm $pH_2O$)argon, the density increased from 2.58 g/cm$^3$ to 2.88 g/cm$^3$ - or from 79.4% to 88.4% of theoretical density. The torque required to loosen the bolts after testing was lower than could be resolved with the torque wrench, suggesting that the densification was not limited by intrinsic resistance, but rather by the decreasing pressure as the pellet thickness decreased through densification and through transverse strain from compression. This is sufficiently close to the 92% dense value (at which pores are considered isolated) that the validity of in-situ densification is considered verified.

## 9.2 Mechanical properties of $CsH_2PO_4$ on the rocks

$CsH_2PO_4$ -silica composites have been studied by Otomo *et.al.* for the effect that silica inclusions have on the phase transition and conductivity in the low-temperature phase [(46)(47)]. Additional studies have been done of the chemical interactions between $CsH_2PO_4$ and silica [(48)(49)], but given the softness of neat, our interest was primarily in the ability of silica to stabilize the $CsH_2PO_4$ structure.

To compare the composite $CsH_2PO_4$ -silica mixture to pure $CsH_2PO_4$ , a batch was synthesized following the procedure outlined in Chapter 3, section 2. Composites of the form $CsH_2PO_4$ $_{(1-x)}SiO_{2(x)}$ were synthesized for x values ranging from 0.1 to 0.4 by mass. Because the x=0.1 composition behaved similarly to pure $CsH_2PO_4$ (x=0) in solution, while composites with higher silica compositions appeared to form gels as shown in figure 9.5, and due to prioritized time constraints, only $CsH_2PO_4$ +$SiO_2$ (9:1 by weight) mixture was tested.

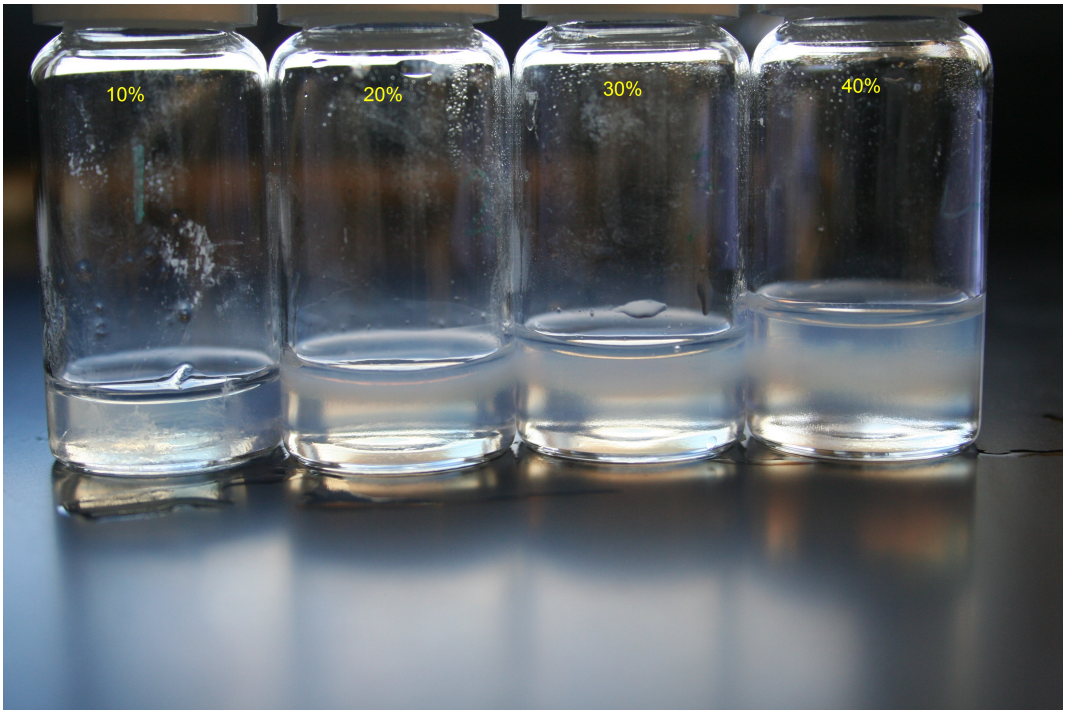


Figure 9.5: Mixtures of colloidal silica in water and dissolved $CsH_2PO_4$ in water at varying dried wt% of silica. While both constituents were suspended or dissolved and therefore very fluid, compositions with silica inclusion higher than 10% formed milky gels.

### 9.2.1 Densificiation and Sintering

To compare the densification behavior between pure $CsH_2PO_4$ and the composite $CsH_2PO_4$ $+SiO_2$ (9:1 by weight), an identical experimental procedure was followed. Pellets were pressed for 1 minute at a variety of pressures, density determined by Archimedes method in toluene, and then pellets were sintered at 240 °C in humid argon. Densities were determined again and the effect of pressing and sintering steps are presented in figure 9.6

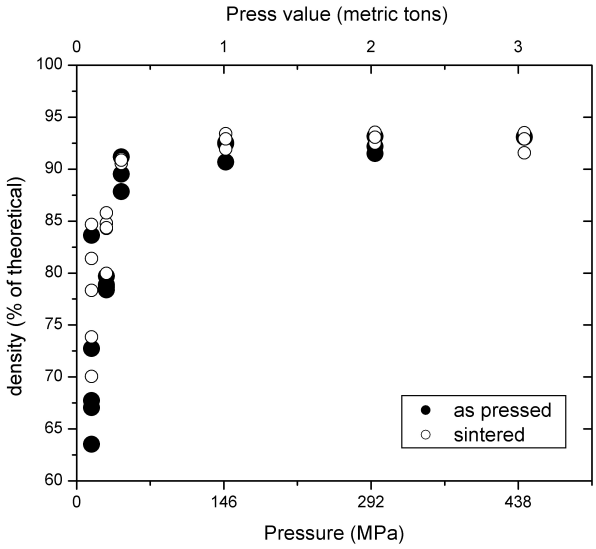


Figure 9.6: $CsH_2PO_4$ $_{(0.9)}SiO_{2(0.1)}$ density vs initial uniaxial densification pressure before and after pressure-less sintering

### 9.2.2 Deformation

The mechanical properties of superprotonic $CsH_2PO_4$ - silica composites were also studied by Dr. Jian Wu at Caltech. Using a thermomechanical analyzer, the strain rate of $CsH_2PO_4$ was measured under approximately 0.1 MPa. The results, shown in figure 9.7, reveal plastic deformation with a creep rate of approximately 1E-7 $s^{-1}$.

## 9.3 Dehydration

### 9.3.1 Neat $CsH_2PO_4$

One additional method of electrolyte processing presented itself when Uda et al reported the liquid, partially dehydrated phase $CsH_{2-2x}PO_{4-x}$. If the dehydration could be re-

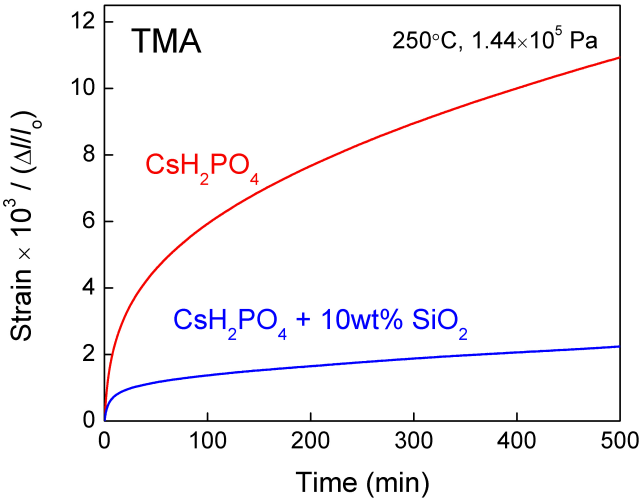


Figure 9.7: Plastic behavior of $CsH_2PO_4$ + 10 wt% silica at 240 °C plotted with the data from figure 9.4 for comparison.

versed, this opens several methods of potential electrolyte processing, from high temperature paint-techniques and injection molding, to sealing performance-damaging cracks that may develop. To investigate the potential for rehydration, ideally high-humidity thermogravimetric analysis could be conducted to ascertain weight loss and recovery. Because the solidified liquid $CsH_{2-2x}PO_{4-x}$ would likely have a low surface-area to volume ratio - and therefore kinetically limit rehydration - thermogravimetric analysis of the rehydration was deemed prohibitively time consuming. Instead, loose $CsH_2PO_4$ powder was lightly pressed and heated in oxygen with 0.33 atm partial pressure of $H_2O$ at 1 °C per minute to 285 °C for 8 hours. The sample was then cooled to room temperature. the results are summarized in table 9.1. the sample is pictured before and after rehydration in figure 9.8 along with corresponding diffraction patterns.

| | |
|---|---|
| Initial Mass: | 590.2 g |
| Final Mass: | 544.1 g |
| % change: | -7.81 % |

Table 9.1: Rehydration of pure $CsH_2PO_4$

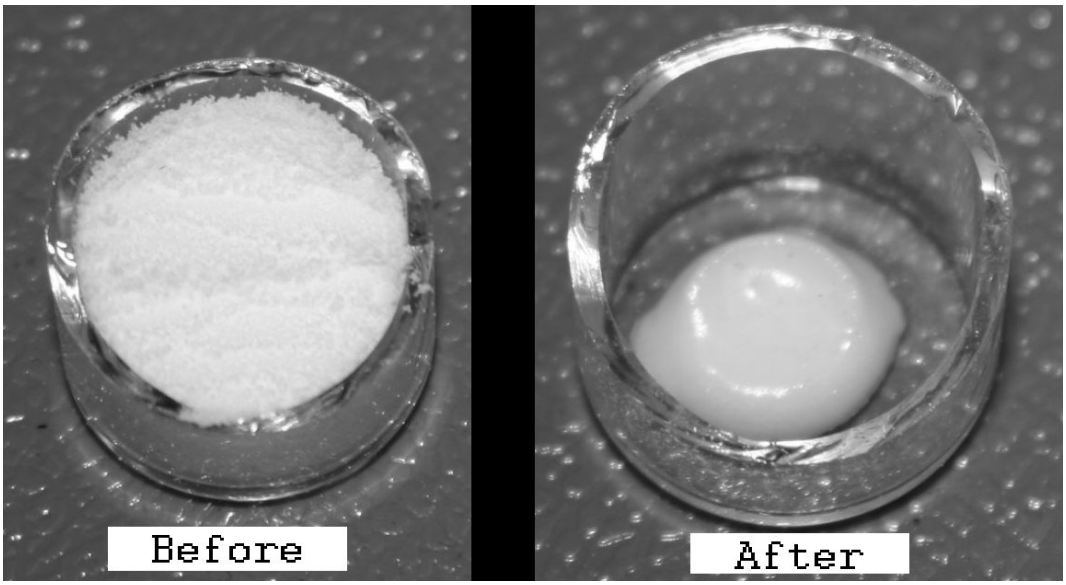


Figure 9.8: Before and after images of loose $CsH_2PO_4$ heated to 285 °C in 0.33 atm $H_2O$, balance $O_2$

### 9.3.2 $CsH_2PO_4$ on the rocks

To examine the effect of silica inclusion on the partial dehydration of $CsH_2PO_4$ , composite powder was tested identically to the pure $CsH_2PO_4$ in section 4.4.1.2. Loose powder was loaded into a silica crucible and heated at 1 °C per minute to 285 °C in 0.33 atm $H_2O$, balance $O_2$. The sample was held for 8 hours at that temperature before being cooled to room temperature at 1 °C per minute. Before and after photographs are shown in figure 9.9 and the gravimetric results are summarized in table 9.2.

| | |
|---|---|
| Initial Mass: | 643.9 mg |
| Final Mass: | 639.2 mg |
| Change: | -0.7 % |

Table 9.2: Rehydration of composite $CsH_2PO_4$ +$SiO_2$ (9:1 by weight)

Visually, the loose powder is almost entirely unaffected, there is a slight shrinkage as the powder seemingly contracted within the crucible, but compared to the dramatic melting of pure $CsH_2PO_4$ seen in figure 9.8, the inclusion of silica is seen to stabilize the structure greatly as well as to allow rehydration of the partially dehydrated product. Phase stability of the composite was verified by XRD before and after partial dehydration, the patterns are shown in figure 9.10

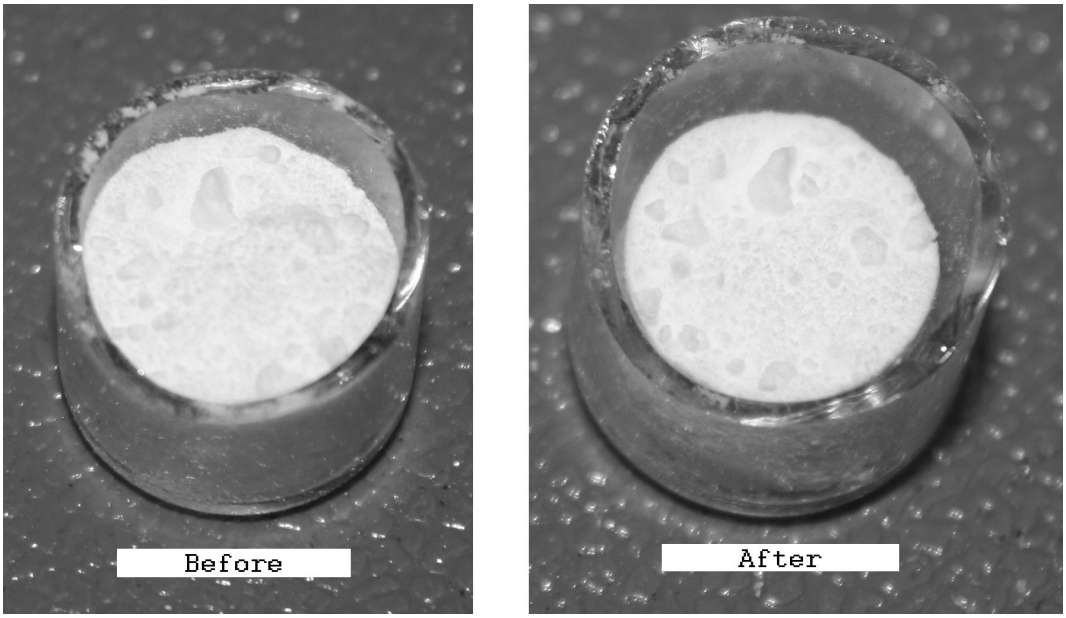


Figure 9.9: Before and after images of loose $CsH_2PO_4$ +$SiO_2$ (9:1 by weight) heated to 285 °C in humid (0.33 atm $pH_2O$)$O_2$

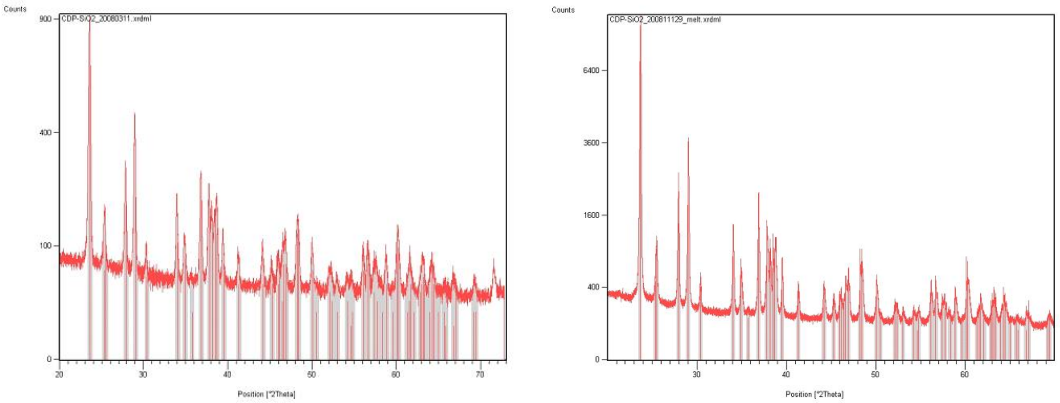


(a) XRD pattern of $CsH_2PO_4$ + 10 wt% silica as synthesized.

(b) XRD pattern of $CsH_2PO_4$ + 10 wt% silica after heating to 285 °C in humid (0.33 atm $pH_2O$)$O_2$ for 8 hours and cooling to room temperature.

Figure 9.10: XRD patterns of $CsH_2PO_4$ + 10 wt% silica powder before and after partial dehydration. Both patterns are compared against peak locations for $CsH_2PO_4$ (ICSD:35-0746) and neither reveals the presence of impurity or dehydrated phases.

## 9.4 Conductivity

Taninouchi et. al ((45)) reported a sharp increase in conductivity of the partially dehydrated $CsH_{2-2x}PO_{4-x}$ phase. However, as this was also associated with a dramatic change in the material state (from solid to liquid), and the stabilizing effect of silica inclusion had just been demonstrated, a simple symmetric test cell was fabricated with 10 wt% silica in $CsH_2PO_4$ as an electrolyte and Toray paper supported Pt/C electrodes, pressed to 94 % dense. The cell, shown in figure 9.11(a) was tested with 4-point ACIS to ascertain if the heightened conductivity remained extant with the stabilized structure. The cell was heated at 1 °C /min in symmetric, 0.42 atm $pH_2O$) hydrogen gas. Electrode and electrolyte resistance were both measured via ACIS, analyzed by fitting to nyquist plots as in figure 9.11(b) and displayed vs temperature in figure 9.12.

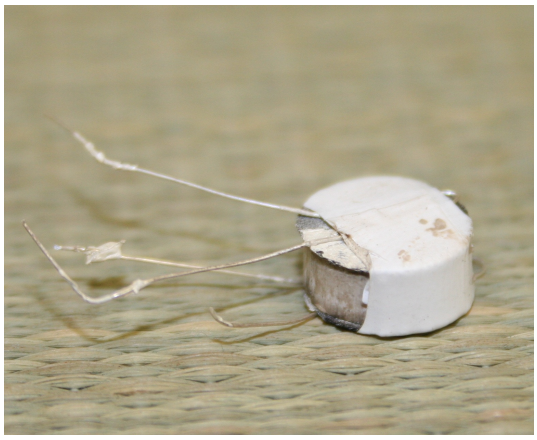

(a) Photograph of $CsH_2PO_4$ -silica composite symmetric cell after testing.

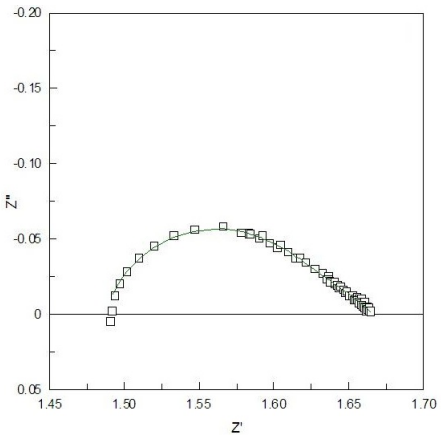


(b) Nyquist plot of $CsH_2PO_4$ + silica composite electrolyte with Toray supported Pt/C electrodes tested at 240 °C in symmetric, humid (0.42 atm $pH_2O$) hydrogen.

Figure 9.11: Composite $CsH_2PO_4$ with 10 wt% electrolyte cell with sample Nyquist plot at 240 °C .

While the electrolyte conductivity presented in figure 9.12 does not increase, contrary to what Taninouchi et al. reported for the partially dehydrated $CsH_{2-2x}PO_{4-x}$ from pure $CsH_2PO_4$ , it also does not decrease dramatically as Taninouchi et al. reported for the fully dehydrated $CsPO_3$ product.

While silica is seen to stabilize not only the structure, but also the conductivity of the electrolyte, the electrodes diverge from arrhenius behavior above 280 °C - corresponding

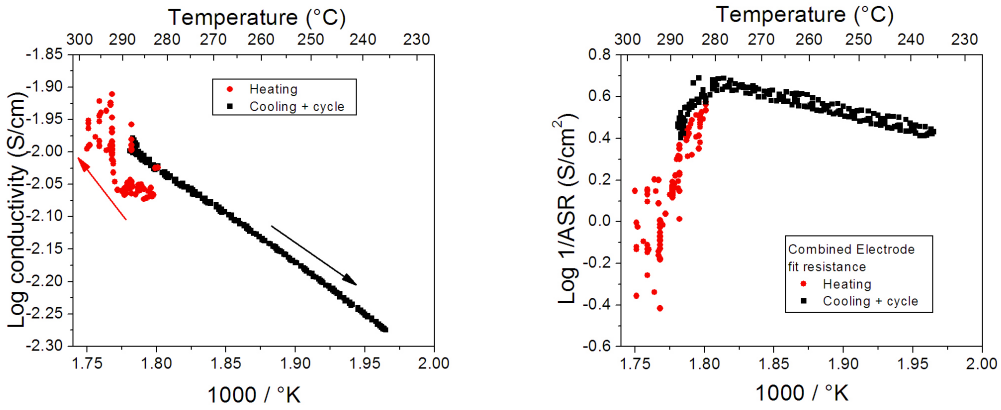


(a) Arrhenius plot of fit electrolyte conductivity. (b) Arrhenius plot of fit electrode conductivity.

Figure 9.12: Fit conductivities of composite $CsH_2PO_4$ + 10 wt% silica electrolyte cell with Toray paper supported Pt/C electrodes, tested up to 300 °C . The electrolyte is noisy but appears stable through the partially-dehydrated regime. The electrode, however, becomes more resistive in the partially-dehydrated regime

to the partially dehydrated $CsH_2PO_4$ regime. Both components' resistances, however, are reversible, suggesting the conductivity of the $CsH_{2-2x}PO_{4-x}$ - electrode interface is intrinsically more resistive than the $CsH_2PO_4$ - electrode interface and becomes limited by an additionl, low frequency process, as seen in the Nyquist plot of cell impedance at 290°C in figure 9.13. The activation energy of the composite electrolyte mixture is seen to be 34.4 kJ/mol below 290 °C , while the activation energy of the summed electrode resistances below 280 °C is observed to be 36.4 kJ/mol.

## 9.5 Conclusions

The mechanical properties of $CsH_2PO_4$ are seen to be unlike those of any other fuel cell electrolyte material. While the ease of densification at low-temperature is a significant advantage, the plasticity of the superprotonic phase allows the mechanical evolution of electrode-electrolyte interfaces away from their as-fabricated microstructures.

Silica inclusion reduces the plastic deformation rate of $CsH_2PO_4$ , but more importantly, is observed to stabilize the partially-dehydrated liquid phase. By preventing this melting, $CsH_2PO_4$ +silica composite electrolytes not only maintain their structure, but also quickly rehydrate into full $CsH_2PO_4$ when cooled. Preliminary probes of this stabilized structure's conductivity were conducted, showing a noisy but monotonic increase in conductivity with

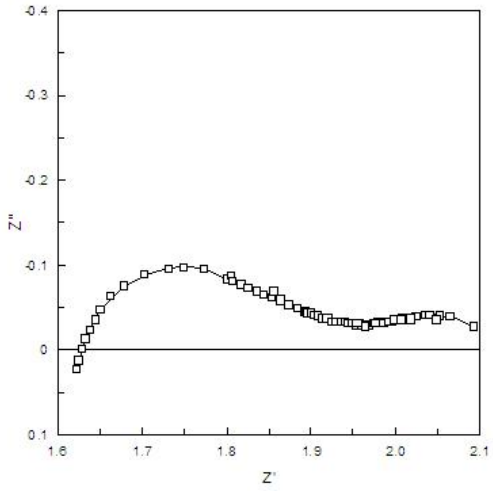


Figure 9.13: Nyquist plot of $CsH_2PO_4$ with 10 wt% silica electrolyte cell and 40 wt% Pt/C electrodes measured at 290 °C in humid (0.42 atm $pH_2O$) hydrogen - above the partial dehydration transition - shows the appearance of an additional low-frequency arc.

heightened temperature up to 300 °C . Electrode resistance above the partially-dehydrated phase transition is seen to decrease, however. While silica inclusion stabilizes the bulk electrolyte, it is likely that the surface reorients as $CsH_2PO_4$ dehydrates. This cannot explain the increased resistance, though, as the low resistance can be recovered upon cooling. More likely, the electrolyte surface kinetics of the partially-dehydrated phase are slower than those of the fully-hydrated phase.

# Chapter 10

# Towards alternative fuels

While the work presented here dealt solely with hydrogen as a reactant gas, due to the low volumetric density of hydrogen gas at standard temperature and pressure, it is a poor fuel for real-world operation. The volumetric density in application is invariably increased by compressing the hydrogen - often to pressures exceeding 400 atm - or also cooling it to -253 °C . More attractive, is the possibility of employing liquid organic fuel, such as ethanol or methanol. The energy densities of a number of liquid fuels are summarized and compared hydrogen (compressed and liquid) in table 10.1. While hydrogen has an expectedly high gravimetric energy density, the volumetric density, even of liquid hydrogen, is a third that of methanol. Additionally, energy must be expended to compress the hydrogen gas.

| Fuel | Gravimetric (MJ/L) | Volumetric (MJ/L |
|---|---|---|
| hydrogen (g 690 atm) | 143 | 4.7 |
| hydrogen (l) | 143 | 5.6 |
| gasoline | 46.9 | 34.6 |
| ethanol | 30 | 24 |
| methanol | 19.7 | 15.6 |

Table 10.1: Summary of gravimetric and volumetric energy densities for several fuels.

Intrinsically, fuel cells are largely fuel-agnostic as they simply convert chemical energy into electrical energy. The kinetics of that conversion, however, are sensitive to reactant identity. A high-activity catalyst for hydrogen oxidation may be quite poor at directly catalyzing the oxidation of methanol. It is for that reason that many methanol cells leverage the extensive body of work done on purely chemical heterogeneous catalysis to reform organics such as methanol into hydrogen and carbon dioxide.

The reformation of organic fuels into hydrogen and carbon dioxide processes are well-

characterized but inevitably result in a finite yield of carbon monoxide. In addition to the issues of fuel cross-over through the polymer electrolyte, the presence of CO in the fuel stream can be a significant issue as carbon monoxide binds strongly to platinum poisons standard PEMFC anodes. Gottesfeld [(50)] reports platinum anode performance impacted at CO concentrations of as little as 5 ppm - meaning that even reformed syngas [(51)] can poison anodes. For solid-oxide electrolyte fuel cells which operate at high temperatures, CO poisoning and fuel cross-over are not issues. At temperatures between 400 °C and 800 °C , however, carbon-containing fuel streams are thermodynamically prone to coking metal catalysts.[(52)(53)]

Solid Acid fuel cells based on $CsH_2PO_4$ electrolytes, on the other hand, have demonstrated high performance with both syngas and when used with an in-line Cu-Zn reformer, with methanol [(54)(55)]. The truly solid electrolyte prevents crossover while the $\approx 250\,^{\circ}C$ operating temperature is low enough to prevent coking.

In this chapter, we explore two possible applications for $CsH_2PO_4$ -based devices in utilizing "dirty" fuel streams contaminated by CO and non-active components. In the first section, we explore the CO tolerance of platinum anodes for $CsH_2PO_4$ based fuel cells. In the second section we demonstrate a stand-alone $CsH_2PO_4$ -based electrochemical pump which may be used to purify reformate streams.

## 10.1 CO tolerance of platinum anodes in $CsH_2PO_4$ electrolyte cells

### 10.1.1 Experimental Methods

To probe the impact of CO on the platinum anode of $CsH_2PO_4$ -based fuel cells throughout the standard anode operating range, as well as at equilibrium, a referenceless point electrode geometry was tested. 30 mg of pt-$CsH_2PO_4$ powder composite in a 3:7 weight ratio was dispersed on a 3/4" porous stainless steel diffusion layer as a counter electrode. For the electrolyte, 1.2 g of pure, in-house synthesized $CsH_2PO_4$ was mechanically dispersed on the counter electrode inside a 3/4" diameter die. Finally, a working electrode was prepared by cutting a 0.3 mm length from 0.404 mm diameter platinum wire (alfa) which was cleaned in dilute nitric acid, followed by acetone and then isopropanol. The working electrode was

loosely embedded in the electrode after fabrication approach C described in chapter 7.

The entire assembly was co-pressed at 4 tons (125 MPA) for 15 minutes. For this geometry and material selection, the calculated counter electrode (Chapter 6) contribution at equilibrium is less than 0.03% of the total electrode resistance, and therefore safely negligible.

The cell was heated at 1 °C /min to 247 °C in a symmetric gas environment composed of a 0.065 atm $H_2$, 0.35 atm $H_2O$, and the balance mixture of CO and Ar achieved by metering Ar and 10% CO in Ar in varying ratios. In this manner, CO concentration was varied between 0 and 59000 ppm. CO in the gas exhaust was confirmed by gas chromatography. Flow rate was maintained at 75 sccm for a linear space velocity of 6.5 cm/min at the sample. The electrochemical properties of the cell were characterized via slow cyclic voltammetry (±200 mV, 10 mV/s) and ACIS (10 mV amplitude, 20 khz - 50 mhz) with an Autolab PGSTAT302 with integrated FRA module.

### 10.1.2 Results and Discussion

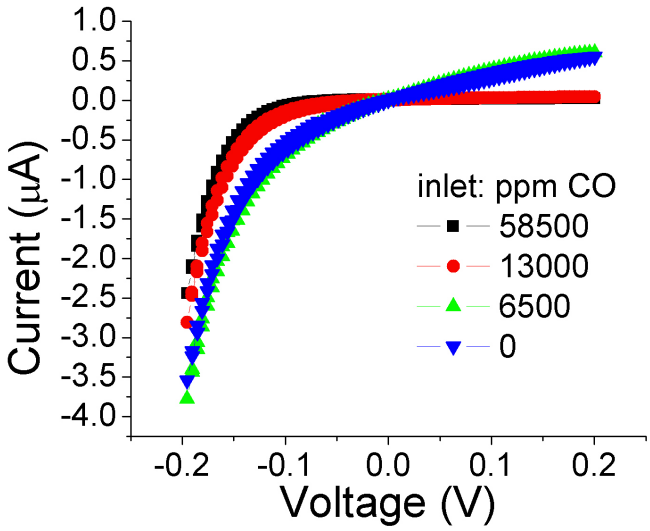


Figure 10.1: Polarization curves for 0, 7000, 14000, and 63000 ppm CO concentrations.

As the impact of CO poisoning is often more pronounced at higher currents than at equilibrium [ref], sample polarization curves were measured at several CO concentrations, shown in figure 10.1. Notably, an improvement in maximum current at +200 mV is observed from 0 ppm to 7000 ppm CO. At every tested CO concentration, current is seen to vary

monotonically with voltage without inflection or anomaly - in qualitative agreement to platinum wire electrode studies in chapter 8. ACIS measurements at equilibrium, therefore, yield high sensitivity proxies to probe the overall impact of CO on anode kinetics. The zero-bias impedance is plotted in nyquist form in figure (a) at varying CO concentrations. To verify reproducibility, CO concentration was cycled twice, first from 0 to 58500 ppm and back to 0 in steps of 6500 ppm, then to 13000 ppm and back to 0 in steps of 2600. At each step, 5 impedance scans were measured and fit to a $R_S(R_{P1}Q)(R_{P2}Q)$. The results for the full scan are shown in figure 10.2(b).

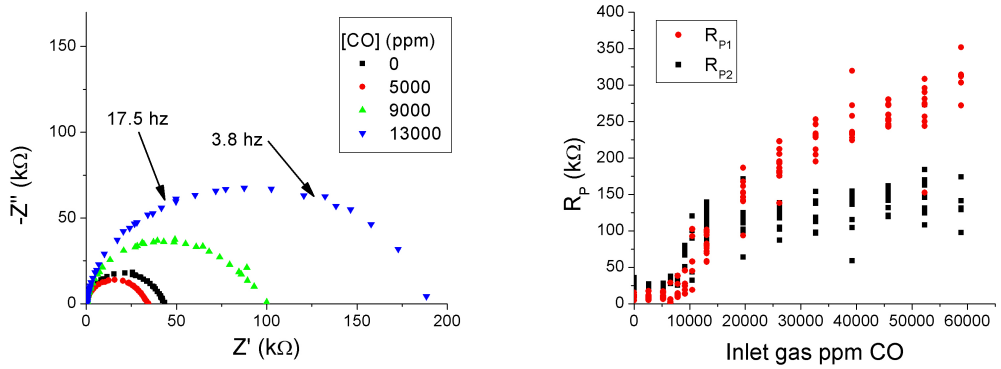


(a) Sample Nyquist plots of zero-bias impedance at several CO concentrations.

(b) $R_{P1}$ $R_{P2}$ plotted vs CO concentration.

Figure 10.2: Sample Nyquist plot and compiled zero-bias resistances for CO concentrations from 0 ppm to 59000 ppm.

The close characteristic frequencies of the two processes are responsible for the high degree of scatter, but both processes appear to be affected similarly by CO concentration, so for clarity, the individual resistances were summed and the total electrode resistance from zero-bias ACIS is plotted against CO concentration in figure 10.3. The slight reduction in electrode resistance up to 7500 ppm inlet CO concentration confirms the improvement observed in the polarization curves (Fig. 10.1).

Beyond 7500 ppm, resistance increases quickly, doubling the initial resistance by 9000 ppm and increasing by an order of magnitude by 45500 ppm.

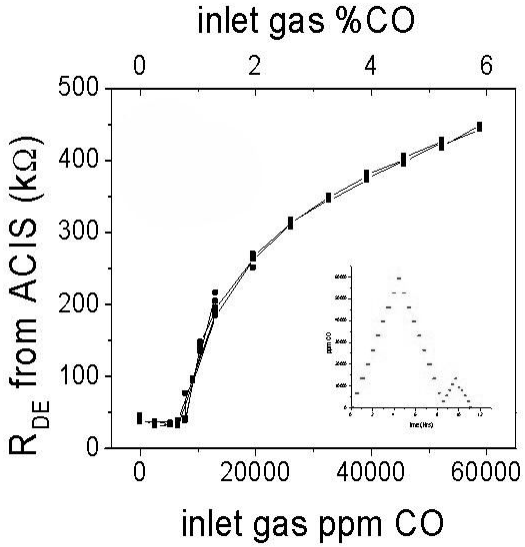


Figure 10.3: Zero-bias resistance of platinum wire electrode vs CO concentration.

### 10.1.3 Conclusions

We have demonstrated that the platinum anodes for $CsH_2PO_4$ -based fuel cells are highly CO-tolerant - up to 7500 ppm. The improvement in anode kinetics is believed to be due to a water-gas-shift slightly increasing the gas-phase hydrogen concentration. This method provides a sensitive probe of anode performance. It should also be noted that for $CsH_2PO_4$ -based fuel cells, platinum cathodes are over 2 orders of magnitude more resistive than platinum anodes [chapter 5], so a reduction in overall operating performance may not be detected until much higher CO concentrations.

## 10.2 Hydrogen Pump

Syngas, as mentioned, contains finite amounts of CO as a consequence of direct, heterogeneous catalysis-based reforming. A common approach to further purify the gas stream is to employ hydrogen separation membranes. Alloys of both palladium-silver and palladium-copper are well-studied membranes for such separation, with high hydrogen conductivity [(56)(57)(58)]. Driving hydrogen diffusion across such a membrane can be done chemically by increasing the pressure of the composite gas such that the partial pressure of hydrogen is greater than the partial pressure of hydrogen on the filtered side.

Instead of chemically driving the reaction, however, fuel cell membranes may be used to drive hydrogen diffusion electrochemically from the reformate mixture to the pure hydrogen side without reliance on a chemical driving force.

### 10.2.1 Experimental methods

In conjunction with $CsH_2PO_4$ electrolytes, however, there is an additional advantage to consider. Dense membranes, if sufficiently facile, could subdue the dehydration of superprotonic $CsH_2PO_4$ by restricting the egress of outgassed water. Initial investigations into dense, hydrogen conducting membranes used Pd77-Ag23 (weight ratio) foils of 20 micron and 40 micron thickness. After several false starts, a method was developed that allowed cells to be reproducibly fabricated. 5/8" diameter circular foils were punched from the foil of interest and placed on top of a 20 mm (0.787 ") diameter die stem as it lay flush within the die. A 3/4" diameter porous stainless steel disk was placed directly over the foil (fig 10.4(a)). By pressing the stainless steel through the die, the foil deforms, binding to the sides of the stainless steel GDL (fig 10.4(b)). This electrode is then wrapped around its circumference with 1/4" PTFE tape, covered in $CsH_2PO_4$ , lightly pressed as a half-cell which is then wrapped again with PTFE tape and finally covered with the other foil-GDL piece. The trilayer structures were pressed at 125 MPA for 10 minutes. In the finished assembly, the $CsH_2PO_4$ (CDP) electrolyte is fully sealed by dense foil and PTFE tape, while the foil electrodes are mechanically supported with excellent electrical contact (fig 10.4(b)). To obtain thin electrolytes (¡100 micron), $CsH_2PO_4$ was mixed with toluene and slurry cast over the foil electrode. The toluene was then allowed to volatilize before continuing with fabrication.

Cells were loaded and tested in the high-pressure dual-chamber holder with the four bolts tightened to 4 in-lbs per bolt of initial torque, then heated in dry hydrogen flowing through both chambers at 1 °C /min. Because no part of the $CsH_2PO_4$ electrolyte was in contact with the chamber environment, the inlet gas was not humidified. Cells were tested by zero-bias ACIS.

### 10.2.2 Results and discussion

ACIS of the foil cell in hydrogen reveals a single arc (Fig. 10.5. Two cells were tested in this manner - one with 20 micron thick foil and the other with 40 micron thick foil. Cell

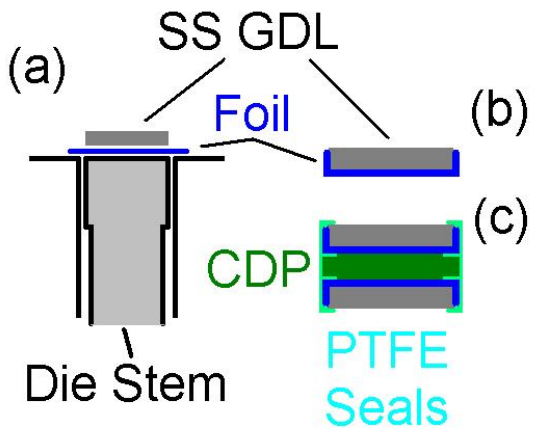


Figure 10.4: Schematic showing approach for achieving gas-tight sealing of $CsH_2PO_4$ (CDP)electrolyte with hydrogen-conducting foil electrodes.

temperature was cycled between 236 °C and 282 °C three times over 140 hours, showing excellent stability. The arrhenius plots of both cells are presented in figure 10.6. For additional comparison, the 40 micron cell resistance was halved and plotted as well, the excellent agreement shows that the electrode resistance scales with thickness in this regime, revealing that Pd77-Ag23 foil is limited by solid-state diffusion with an activation energy of 124 kJ/mol.

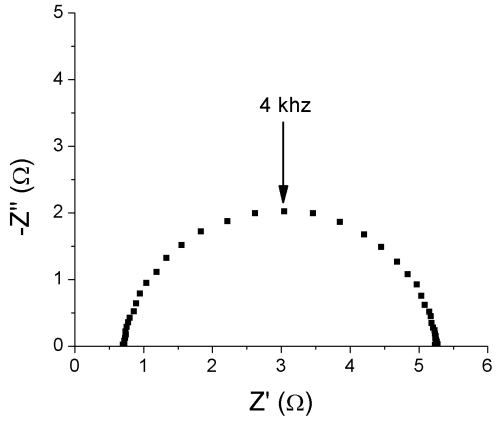


Figure 10.5: Typical Nyquist plot of Pd77-Ag23 foil symmetric cell in dry hydrogen.

Though $R_P$ is several orders of magnitude too high to use as an anode in operating fuel cells, the dense foil construction is seen to be stable in dry environments at zero bias, a useful characteristic for the pure $H_2$ (cathode) side at the least, as it would be both

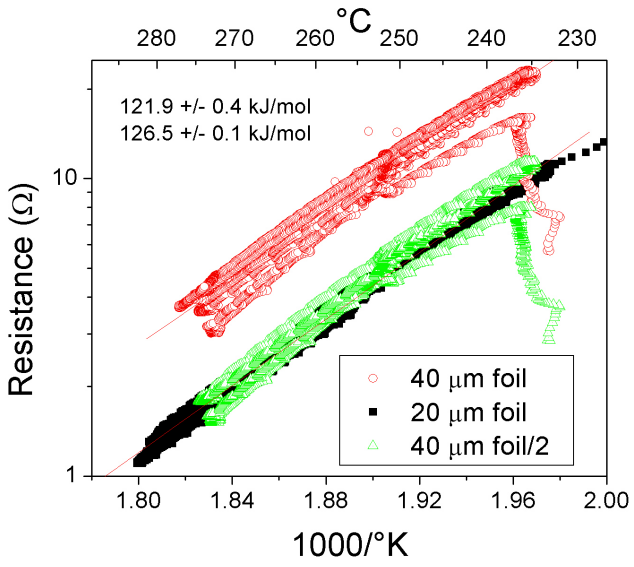


Figure 10.6: Arrhenius behaviour of cells made with 20 and 40 micron Pd77-Ag23 foil tested by zero-bias ACIS in dry hydrogen

technically challenging to humidify the chamber without an additional carrier gas, and would necessitate additional scrubbing of water from the product.

In order to test the foil under bias, two cells were fabricated. The first was made with 40 micron thick Pd77-Ag23 foil bound to stainless steel GDLs as in Fig 10.4(b), though the fabrication approach was slightly different. Instead of pressing a half-cell and sealing that with PTFE tape, the $\approx$ 80 micron $CsH_2PO_4$ electrolyte layer was pressed between two PTFE-wrapped GDL assemblies at 70 MPa And PTFE tape was wrapped around the circumference of the full assembly. The second was fabricated with 27 micron thick Pd60-Cu40 sealed in the manner described earlier (Fig. 10.4).

Cells were again loaded into the high-pressure dual-chamber test fixture under 4 in-lbs of torque per bolt and heated at 1°C /min with both sides exposed to hydrogen. Once at the operating temperature of 255 °C , the inlet to the cathode chamber was shut and cells were tested by galvanostatic potentiometry with intermediate cyclic voltammetry.

The voltage of the Pd77-Ag23 foil cell as a function of time (Fig. 10.7(a)) shows that after an equilibration period of 7 hr, the voltage stabilized at 0.531 V. The highly periodic increases in voltage correspond to times at which I-V curves were collected. Of the total cell voltage, 0.075 V can be attributed to the 75 micron thick electrolyte layer and line/contact resistance. The remainder, 0.456 V, can be attributed to the resistance of the Pd-Ag foil

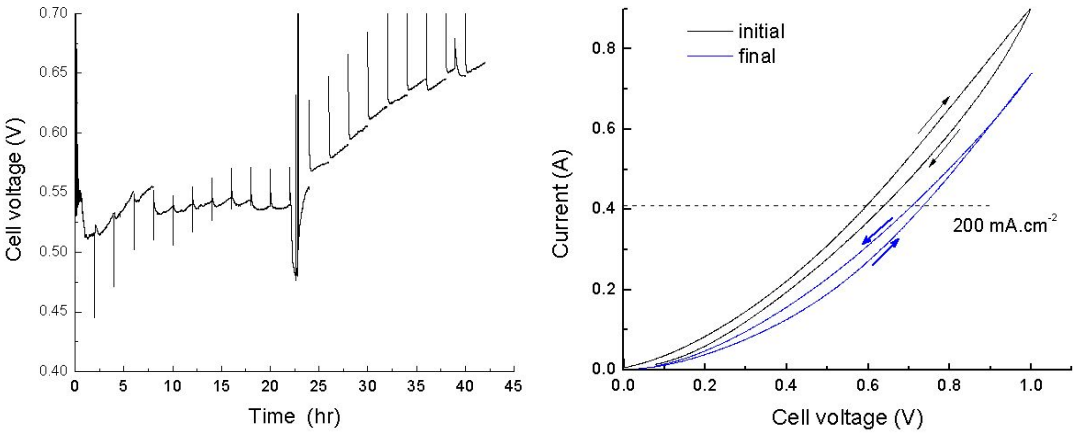


(a) Cell voltage vs time at current load of 200 $mA/cm_2$.

(b) Polarization curves taken before and after testing.

Figure 10.7: Electrochemical behavior of 40 micron Pd77-Ag23 foil hydrogen pump under 200 $mA/cm^2$ current load.

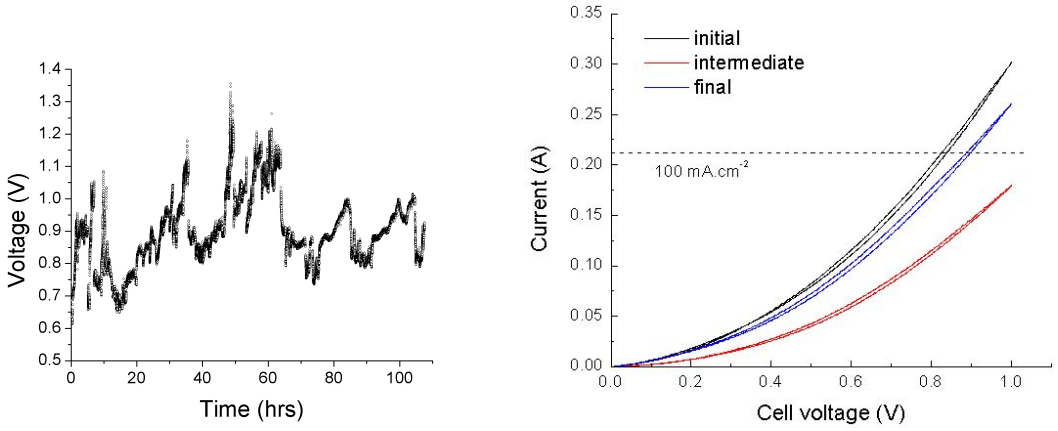


(a) Cell voltage vs time at current load of 100 $mA/cm_2$.

(b) Polarization curves taken before, during, and after testing.

Figure 10.8: Electrochemical behavior of 27 micron Pd60-Cu40 foil hydrogen pump under 100 $mA/cm^2$ current load.

to hydrogen permeation and possibly interfacial resistance at the foil-electrolyte interface. After 22 hours, this cell underwent a catastrophic event that caused a relatively rapid increase in voltage, and for this reason the experiment was turned off after 42 hr. The precise reasons for the failure are unknown, but are attributed to failure of the sealing approach which may have induced catastrophic dehydration of the $CsH_2PO_4$ . The I-V characteristics of this cell decayed with time from the initial to final curves shown in figure 10.7(b). The voltage of the Pd60-Cu40 foil cell as a function of time, figure 10.8(a), showed somewhat greater random fluctuations than that of the first cell and averaged to an overall higher voltage of 0.84 V. While not as obvious, this cell also displayed increases in voltage at the point of I-V curve measurements. Of the total average voltage, 0.06 V can be attributed to the 80 m CsH2PO4 electrolyte layer and line/contact resistance. The remaining voltage drop of 0.78V is far greater than the the non-electrolyte voltage drop of the first cell with half the current density and thinner foils, indicating the poorer performance of Pd-Cu foils. While the behavior of this cell showed greater random fluctuations, overall, the cell displayed a far longer lifetime that Cell1. The greater lifetime is attributed to improvements in the sealing method. The voltage was seen to increase from 40 hours to 60 hours, at which point the bolts were tightened in-situ. The increased pressure lowered the operating voltage approximately 250 mV. The I-V characteristics of this cell decayed with time from the initial to intermediate curves, then improved (though not entirely) after tightening as shown in figure 10.8(b).

### 10.2.3 Hydrogen pump conclusions

Electrochemical pumps based on palladium alloy hydrogen conduction membranes and the $CsH_2PO_4$ electrolyte have been demonstrated. With thin (¡100 micron) $CsH_2PO_4$ electrolytes and 20-40 micron thick alloy foils, such devices are limited in performance by the bulk conductivity of hydrogen through the alloy. Most significantly, dense foil electrodes were able to stabilize the conductivity of the $CsH_2PO_4$ electrolyte without humidifying the feed gasses.

## 10.3 Conclusions

Fuel cells have a great deal of potential for high-efficiency, fuel-flexible, and scalable energy conversion. Potential which has yet to be fully taken advantage of. To maximize utility of fuel cell conversion devices, the fuel is nearly as important as the efficiency. Fuel cells based on solid acid electrolytes, such as $CsH_2PO_4$ , are the lowest-temperature high-performance ones demonstrated. The cross-over impermeable membrane, combined with operating temperature that is near-ideal for alcohol reformation, grant this system undeniable advantages in fuel flexibility. In chapters 7 and 8, a methodology was developed for screening non-platinum electrocatalyst candidates, with preliminary tests identifying high-performing alternatives. In Chapter 9, $CsH_2PO_4$ -based electrolytes were shown to retain high conductivity at approximately 300 °C ; while in this chapter, the resistance of platinum to carbon monoxide poisoning - even at high concentrations - was demonstrated.

Taken together, there exists an excellent opportunity to pursue $CsH_2PO_4$ electrolyte fuel cells using fuels other than hydrogen. The temperature of such cells promotes high-activity of reforming catalysts while lowering the impact of carbon monoxide products - and simultaneously is low enough to prevent carbon coking at the anode. Such cells can be indirect with an in-line reformer, as demonstrated by Uda *etal*. [(55)], or the catalyst screening methodology can be applied to investigating catalysts for direct utilization of alternative fuels.

Whether or not the hydrogen economy is a politically or economically viable future remains unclear - but as the energy demands of humanity continue to increase, so too must our motivation to master nature's energy storage device - the chemical bond. It is the hope of this investigator that the methods developed in this work (and the lessons learned from the failures and successes experienced in its pursuit) will, in the fullness of time, advance humanity's knowledge and capabilities - even if only infinitesimally.

*So long as we live, we will strive.*
*So long as we strive, we will fail.*
*So long as we fail, we will learn.*
*So long as we learn, we will succeed.*

FIN

# Appendix A: Variable definitions

| Symbol | Meaning | Units |
|---|---|---|
| $A$ | Area | $cm^2$ |
| $C$ | Capacitance | F |
| $C_j$ | Concentration of species $j$ | $mol/cm^3$ |
| $E_A$ | Activation energy of a reaction | kJ/mol |
| $F$ | Faraday Constant (charge on one mole of electrons) | C |
| $\Delta G$ | Change in Gibbs Free Energy of a chemical reaction | kJ/mol |
| $\Delta G^0$ | Standard Change in Gibbs Free Energy of a chemical reaction | kJ/mol |
| $GDL$ | Gas Diffusion Layer | |
| $I$ | Current | A |
| $I_{lim}$ | Limiting Current | A |
| $I_0$ | Exchange Current | A |
| $i$ | $\sqrt{-1}$ | |
| $j$ | Current density | $A/cm^2$ |
| $j_0$ | Exchange Current density | A |
| $n$ | Stoichiometric number of electrons involved in an electrode reaction | none |
| $P$ | Pressure | atm |
| $R$ | Rydberg Gas constant | J/mol/°K |
| $R_P$ | Electrode polarization resistance | Ω |
| $R_S$ | Ohmic cell resistance including electrolyte and contact resistance | Ω |
| $R_P^*$ | Area specific Resistance | $\Omega \cdot cm^2$ |
| $R_{MD}$ | Mass-Diffusion resistance of an electrode | Ω |
| $R_{CT}$ | Charge-transfer | Ω |
| $r$ | Radius | cm |
| $r_{WE}$ | Radius of working electrode | cm |
| $r_{CE}$ | Radius of counter electrode | cm |
| $t$ | (a) Electrolyte thickness | cm |
| | (b) Time | s, min, hrs |
| $T$ | Temperature | °C or °K |
| $V$ | Voltage | V |
| $V_0$ | Open circuit Voltage | V |
| $Z$ | Complex impedance | Ω |
| $Z'$ | Real component of impedance | Ω |
| $Z$" | Imaginary component of impedance | Ω |
| $\phi$ | Potential | V |
| $\eta$ | Overpotential ($E$-$E_0$) | V |
| $\eta_{CT}$ | Charge transfer overpotential | V |
| $\alpha$ | Exchange Coefficient | none |

# Appendix B: Derivation of j-$\eta$ characteristics for different Rate Limiting Steps

## B.1 Gas Diffusion is Rate Limiting

For a heterogenous reaction, reactants must first diffuse from the fluid phase to the catalyst surface. As the reaction proceeds at high rates, such as a fuel cell drawing high current, the concentration of reactants at the surface of the catalyst becomes depleted relative to the fluid phase. Note that this treatment is restricted to fluid-phase dynamics - surface adsorption is neglected as well as surface diffusion and charge transfer.

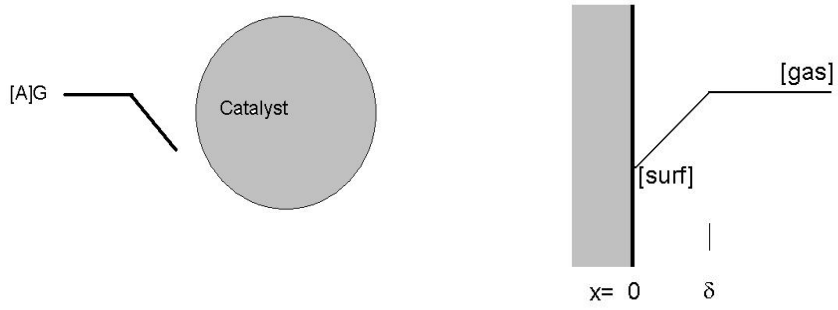


Figure B.1: (a) Schematic of concentration gradient near catalyst and (b) in one dimension

Schematically, the concentration profile is shown in Figure B.1. If the boundary layer is small, relative to the size (and therefore curvature) of the catalyst material, the diffusion path can be depicted in one dimension and solved with Fick's first law of diffusion

$$J = -D\frac{\partial[A]}{\partial x} \tag{B.1}$$

where J is the reactant flux, D is the diffusivity, [A] is the concentration of reactant, A, and x is the distance from the catalyst surface. From conservation of mass, the flux must be constant with distance,

$$\frac{dJ}{dx} = 0 \tag{B.2}$$

Equation B.1 can be differentiated with respect to x, set equal to zero, and then solved with boundary conditions $[A] = [A]_{surface+}\, at\, x = 0$ and $[A] = [A]_{gas}\, at\, x = \delta$, to obtain

$$[A] = [A]_{surface+} + \frac{x}{\delta}([A]_{gas} - [A]_{surface+}) \tag{B.3}$$

Which, plugged into Fick's first law, yields

$$J = -\frac{D}{\delta}([A]_{gas} - [A]_{surface+}) \tag{B.4}$$

If gas diffusion to the electrode surface is the rate limiting step, then at steady state, the flux to the surface equals the rate $\nu$, which can be related to current by Faraday's constant,

$$\nu = \frac{j}{zF} \tag{B.5}$$

, thus we obtain an expression for the current in terms of concentrations

$$j = -\frac{DzF}{\delta}([A]_{gas} - [A]_{surface+}) \tag{B.6}$$

Which can be clarified by defining the limiting current, $j_{lim}$ for the case of maximum gradient - where $[A]_{surface+} = 0$

$$j = j_{lim} = -\frac{DzF}{\delta}[A]_{gas} \tag{B.7}$$

$$\frac{j}{j_{lim}} = 1 - \frac{[A]_{surface+}}{[A]_{gas}} \tag{B.8}$$

What we'd really like is to obtain, however, is a relationship between current and overpotential, $\eta$. So, using the Nernst equation for the transport of reactant R $R_{gas} \longrightarrow R_{surface+}$

$$E = E_0 - \frac{R_c T}{zF} ln(Q) \tag{B.9}$$

where $Q = \frac{[A]_{surface+}}{[A]_{gas}}$ and $E - E_0$ is the definition of overpotential, $\eta$. So,

$$\eta = \frac{R_c T}{zF} ln(\frac{[A]_{surface+}}{[A]_{gas}}) \tag{B.10}$$

$$\frac{[A]_{surface+}}{[A]_{gas}} = e^{\left(\frac{zf}{R_c T}\eta\right)} \tag{B.11}$$

$$\eta = \frac{R_c T}{zF} ln\left(\frac{[A]_{surface+}}{[A]_{gas}}\right) \tag{B.12}$$

Rearranging B.8 and substituting into B.12 gives us a final expression for $\eta(j)$ if transport through the gas-phase is the rate-limiting step.

$$\eta = \frac{RT}{nF} ln\left(1 - \frac{j}{j_{lim}}\right) \tag{B.13}$$

Lastly, we identify the information obtained from equilibrium ACIS measurements. Since fitting to Nyquist plots allows identification of total resistance under DC conditions, that resistance can be used to probe key system characteristics. Recall that ACIS measures $\frac{\Delta V}{\Delta I}$, and for sufficiently small amplitude excursions, $\frac{dV}{dI}$. It is important to keep in mind that expressions derived here are in terms of the current density, j, while ACIS measures un-normalized current.

$$\frac{d\eta}{dI\, x\, Area} = \frac{RT}{nF}\frac{1}{j_{lim} - j} \tag{B.14}$$

$$\left.\frac{d\eta}{dI\, x\, Area}\right|_{\eta, j=0} = ASR = \frac{-R_c T}{zF j_{lim}} \tag{B.15}$$

If we recall that $j_{lim}$ is defined in equation B.7, we can substitute back to obtain

$$ASR = \frac{RT\delta}{D(zF)^2[A]_{gas}} \tag{B.16}$$

## B.2 Surface Diffusion is Rate Limiting

Another form of mass-transport is the diffusion of adsorbed species - be they atoms or molecules - to the reaction zone, in this case the triple phase boundary.

## B.3 Charge Transfer is Rate Limiting

The final electrode step along the half-cell reaction pathway is charge transfer, where the charge carrier is oxidized at the anode and reduced at the cathode. The empirical current-overpotential relationship famously forwarded by Julius Tafel (prior to his suicide in 1918) was an experimental probe of charge-transfer overpotentials. Here, we derive a theoretical justification relationship based on the reaction between oxidized and reduced species

$$O + ze^- \underset{k_-}{\overset{k_+}{\rightleftharpoons}} R \tag{B.17}$$

and use the arrhenius equation to derive rate equations for the forward and backwards steps

$$\nu = c[A]e^{-\frac{E_a}{R_c T}} \tag{B.18}$$

where c is the pre-exponential factor, and $E_a$ is an intrinsic activation energy dependent on catalyst, so that

$$E_{a+} = \Delta G_+ - \alpha z F \varepsilon_i \quad and \quad E_{a-} = \Delta G_- + (1-\alpha) z F \varepsilon_i \tag{B.19}$$

Thus yielding expressions for forward and backward currents, related to $\nu$ as in equation B.13

$$j_+ = zFc_+[R]e^{-\frac{\Delta G_+ - \alpha z F \varepsilon_i}{R_c T}} \quad and \quad j_- = -zFc_-[O]e^{-\frac{\Delta G_- + (1-\alpha) z F \varepsilon_i}{R_c T}} \tag{B.20}$$

it is helpful at this point to introduce the quasi-equilibrium case where no net reaction occurs, in other words, the magnitudes of the forward and reverse currents are equal to each other. this value is termed the exchange current density, $j_0$

$$j_+ = |j_-| = j_0 \tag{B.21}$$

$$j_0 = zFc_+[R]e^{-\frac{\Delta G_+ - \alpha z F \varepsilon_{rev}}{R_c T}} \;=\; zFc_-[O]e^{-\frac{\Delta G_- + (1-\alpha) z F \varepsilon_{rev}}{R_c T}} \tag{B.22}$$

This lets us recast the forward and backwards currents in terms of the exchange current

density and the reversible potential

$$\frac{j_+}{j_0} = e^{\frac{-\Delta G_+ + \alpha z F \varepsilon_i}{R_c T} + \frac{\Delta G_+ - \alpha z F \varepsilon_{rev}}{R_c T}} = e^{\frac{\alpha z F}{R_c T}(\varepsilon_i - \varepsilon_{rev})} \tag{B.23}$$

$$j_+ = j_0 e^{\frac{\alpha z F}{R_c T}\eta} \tag{B.24}$$

And the reverse current can be treated similarly

$$\frac{|}{j_-}|j_0 = e^{\frac{-\Delta G_- - (1-\alpha) z F \varepsilon_i}{R_c T} + \frac{\Delta G_- + (1-\alpha) z F \varepsilon_{rev}}{R_c T}} = e^{-\frac{(1-\alpha) z F}{R_c T}(\varepsilon_i - \varepsilon_{rev})} \tag{B.25}$$

$$|j_-| = j_0 e^{-\frac{(1-\alpha) z F}{R_c T}\eta} \tag{B.26}$$

Finally, the total current density can be expressed as $j = j_+ - |j_-|$ to derive an expression for $j(\eta)$ known as the Butler-Volmer equation after work by John Alfred Valentine Butler (J. A. V. Butler Trans. Faraday Society, 19 729 (1924))and Max Volmer(T. Erdey-Gruz and M. Volmer Z. Phys. Chem. 150 (A) 203-213 (1930))

$$j = j_0 \left( e^{\frac{z F \alpha}{R_c T}\eta} - e^{-\frac{z F (1-\alpha)}{R_c T}\eta} \right) \tag{B.27}$$

The exchange coefficient terms are commonly separated into independent exchange coefficients $\alpha_a$ and $\alpha_c$ to yield

$$j = j_0 \left( e^{\frac{z F \alpha_a}{R_c T}\eta} - e^{-\frac{z F \alpha_c}{R_c T}\eta} \right) \tag{B.28}$$

Because it is impossible to recast the Butler-Volmer equation as $\eta(j)$ with generality, there is utility in examining current-dependent overpotential in two special cases.

### B.3.1 Special case: low $\eta$

Near equilibrium, where $\eta$ and I are both small, the Butler-Volmer equation can be simplified by expanding the exponents with the relation:

$$e^x = \sum_{n=0}^{n} \frac{x^n}{n!} \tag{B.29}$$

Substituting a $1^{st}$ order expansion of B.29 into B.28

$$j = j_0 \left[ (1 + \frac{zF\alpha_a}{R_c T}\eta - (1 - \frac{zF\alpha_c}{R_c T}\eta) \right] \tag{B.30}$$

Simplifies to:

$$j = j_0 \left[ \frac{zF(\alpha_a + \alpha_c)}{R_c T}\eta \right] \tag{B.31}$$

or, refashioned into ohm's law, this is wrong....

$$\eta = j \left[ \frac{R_c T}{zF(\alpha_a + \alpha_c) j_0} \right] \tag{B.32}$$

Thus, the $\frac{\Delta V}{\Delta I}$ measured from ACIS at equilibrium can be used to probe $j_0$

$$ASR = \frac{R_c T}{zF(\alpha_a + \alpha_c) j_0} \tag{B.33}$$

### B.3.2 Special case: high $\eta$

In the event of high overpotentials, however, one term of B.28 comes to dominate. Which one it is depends on the sign of the overpotential. For high $\eta$, the second term approaches 0, leaving the expression as:

$$j = j_0 \left( e^{\frac{zF\alpha_a}{R_c T}\eta} \right) \tag{B.34}$$

Naturally, for large negative overpotentials, the exchange coefficient $\alpha_a$ is replaced with $\alpha_c$. Equation B.34 can be solved for$\eta$ in terms of $j$ to be

$$\eta = \frac{R_c T}{zF\alpha_a} ln \left( \frac{j}{j_0} \right) \tag{B.35}$$

thus, at high overpotentials, the butler-volmer expression for charge-transfer based overpotentials converges to the Tafel equation.

$$\eta = A \times ln \left( \frac{j}{j_0} \right) \qquad where\ A = \frac{R_c T}{zF\alpha_a} \tag{B.36}$$

The tafel plot can also be used to probe $j_0$, as graphing the overpotential as a function of $ln(j)$ converges to a line whose x-axis intercept equals $ln(j_0)$, as shown in figure B.3.2

The drawback to this method of determining $j_0$ is that it requires high-confidence, IR-

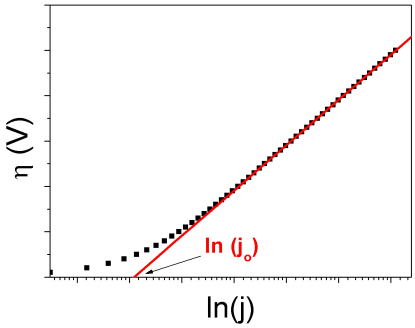


Figure B.2: Theoretical Butler-volmer is shown in black. The red line is a linear fit of the high-current region, extrapolated to $j = j_0$ at zero overpotential

corrected, steady state cyclic voltammograms. Whereas ACIS allows isolation of the charge transfer arc in the frequency regime.

# Appendix C: $CsH_2PO_4$ synthesis

40th most abundant!

## C.1 equipment

- 85% assay Phosphoric Acid (Alfa Aesar #33266)
- Cesium Carbonate 99% (Alfa Aesar # 12887)
- distilled water
- anhydrous methanol
- small beaker
- large beaker
- magnetic stir bar and stirrer
- Butner funnel with seals
- side-ported erlenmeyer flask
- weight ring
- aspirator or similar
- ducted drying oven ( 100 °C

## C.2 bulk $CsH_2PO_4$ synthesis

What follows is a recipe for 14.112 grams of $CsH_2PO_4$ . As with other recipes, quantities can be scaled to accommodate desired yield. Particle size varies widely, but average particle diameter is approximately several microns.

1. wear appropriate safety gear and set up equipment in fume hood
2. place large flask, on stirrer
3. place stir bar in large flask, begin stirring
4. measure 10 grams of cesium carbonate into large flask
5. measure 7.011 grams of 85% assay phosphoric acid into small flask
6. add 5 to 4. reaction is exothermic and evolves carbon dioxide
7. rinse small flask with distilled water, add to 1
8. repeat step 7 until $CsH_2PO_4$ is fully dissolved
9. in a saturated $CsH_2PO_4$ solution, viscous distortions are visible
10. pour anhydrous methanol into solution, inducing precipitation
11. connect aspirator, side-ported erlenmeyer flask, weight ring, butner funnel and seals to create a vacuum filtration system
12. add precipitated mixture into butner funnel
13. filter precipitate
14. wash precipitate in butner funnel with an additional 500 ml of anhydrous methanol.
15. dry precipitate in ducted oven
16. confirm phase purity by X-ray diffraction, referenced to 35-0746

## C.3 fine $CsH_2PO_4$ synthesis

While various approaches are under development for the synthesis of nano-particled $CsH_2PO_4$ , This section merely describes the crude approach used for making fine powdered ( 1 micron)$CsH_2PO_4$ which was used in the synthesis of composite powder electrode materials.

1. dissolve 10 grams of $CsH_2PO_4$ in 8.5 mL of distilled water
2. dissolution is slow near the solubility limit, sonicate the solution and wait ≈20 minutes

3. add solution to disrupted anhydrous methanol bath via a narrow-bore syringe tip (*e.g.* 26G1/2 or an airbrush

4. allow precipitate to settle

5. decant natant precipitate

6. the settled precipitate should be ≈1 micron - if this is sufficient, precipate can be suspended in toluene and then dried

7. alternatively, the natant precipitate can be centrifuged, decanted and suspended in toluene while the procedure is repeated for the settled precipitate from step 4 - this results in finer particles (≈500 nm), but much lower yields

## C.4 Composite $CsH_2PO_4$ -$SiO_2$ synthesis

To make well-mixed $CsH_2PO_4$ -$SiO_2$ composites, 30 wt% silica suspended in water (alfa aesar stock no. 43111), in the desired amount can be added to the $CsH_2PO_4$ solution just prior to precipitation in methanol. While this approach, when used to synthesize Cesium Hydrogen Sulfate ($CsHSO_4$), another solid acid material, provides nucleation sites for precipitation - yielding nano-scale particles - a similar effect is not observed with $CsH_2PO_4$ . Though not quantitatively studied, $CsH_2PO_4$ -$SiO_2$ composites appear to absorb less atmospheric water than pure $CsH_2PO_4$ , remaining friable whereas $CsH_2PO_4$ tends to clump and agglomerate if left at ambient humidity for long periods of time. Theoretical density of the composite $A_{(1-x)}B_x$ (where $x$ is fractional mass) can be calculated as follows

$$\rho_{total} = \frac{\rho_A \rho_B}{(1-x)\rho_B + x\rho_A} \tag{C.1}$$

## C.5 Electrode Material Synthesis

In the course of my research, I, on two occasions found it necessary or advantageous to attempt to synthesize my own electrode powders. Very briefly, the two approaches are described here.

### C.5.1 Nano-nickel

Firstly, promising nickel results in hydrogen motivated the testing of nano-sized nickel. Raney nickel purchased from Alfa Aesar and nano-scale nickel powder provided by Quantum Sphere Inc. were each tested and yielded performances significantly worse than meso-scale nickel powder (Alfa Aesar). To synthesize nano-scale nickel in-house, I followed diSalvo's method ((59)) and dissolved nickel nitrate in ethanol, then precipitated the nickel out using sodium borohydride at room temperature. XRD confirmed pure-phase nickel product, with significant peak broadening confirming the nanometer scale particle size (though Rietveldt refinements were not done).

### C.5.2 Carbon-supported silver

In a similar manner, promising silver results motivated an attempt to disperse silver on carbon - much as platinum is dispersed on vulcan in commercially available composites. The pursued method was crude, however, only mechanically mixing the solid precursors:$Ag_2O$ and acetylene black, then heating in oxygen to 400 °C .

# Bibliography

[1] Hansen J, Sato M, Kharecha P, Beerling D, Berner R, Masson-Delmotte V, Pagani M, Raymo M, Royer D, Zachos J: **Target Atmospheric CO2: Where Should Humanity Aim?** *THE OPEN ATMOSPHERIC SCIENCE JOURNAL* 1998, **2**(1):217–231.

[2] Haile S, Boysen D, Chisholm C, Merle R: **Solid acids as fuel cell electrolytes**. *NATURE* 2001, **410**(6831):910–913.

[3] KIRPICHNIKOVA L, URUSOVSKAYA A, MOZGOVOI V: **SUPERPLASTICITY OF CSHSO4 CRYSTALS IN THE SUPERIONIC PHASE**. *JETP LETTERS* 1995, **62**(8):638–641.

[4] Bronowska W: **Comment on "Does the structural superionic phase transition at 231 degrees C in CsH2PO4 really not exist?" [J. Chem. Phys. 110, 4847 (1999)]**. *JOURNAL OF CHEMICAL PHYSICS* 2001, **114**(1):611–612.

[5] Uda T, Haile S: **Thin-membrane solid-acid fuel cell**. *ELECTROCHEMICAL AND SOLID STATE LETTERS* 2005, **8**(5):A245–A246.

[6] EG&G Technical Services I: *Fuel Cell Handbook (Sixth Edition)*. Morgantown, West Virginia: U.S. Department of Energy 2002.

[7] Vetter K: *Electrochemical kinetics : theoretical and experimental aspects*. New York: Academic Press 1967.

[8] Oldham K, Stevens N: **Uncompensated resistance. 2. The effect of reference electrode nonideality**. *ANALYTICAL CHEMISTRY* 2000, **72**(17):3981–3988.

[9] Rutman J, Riess I: **Placement of reference electrode in solid electrolyte cells**. *ELECTROCHIMICA ACTA* 2007, **52**(20):6073–6083.

[10] Adler S, Henderson B, Wilson M, Taylor D, Richards R: **Reference electrode placement and seals in electrochemical oxygen generators**. *SOLID STATE IONICS* 2000, **134**(1-2):35–42.

[11] NEWMAN J: **OHMIC POTENTIAL MEASURED BY INTERRUPTER TECHNIQUES**. *JOURNAL OF THE ELECTROCHEMICAL SOCIETY* 1970, **117**(4):507–&.

[12] WRUCK W, MACHADO R, CHAPMAN T: **CURRENT INTERRUPTION INSTRUMENTATION AND APPLICATIONS**. *JOURNAL OF THE ELECTROCHEMICAL SOCIETY* 1987, **134**(3):539–546.

[13] Jiang S, Love J, Badwal S: **Electrochemical techniques in studies of solid ionic conductors**. *ELECTRICAL PROPERTIES OF OXIDE MATERIALS* 1997, **125-**:81–132.

[14] Jamnik J, Maier J: **Generalised equivalent circuits for mass and charge transport: chemical capacitance and its implications**. *PHYSICAL CHEMISTRY CHEMICAL PHYSICS* 2001, **3**(9):1668–1678.

[15] Jamnik J, Maier J: **Treatment of the impedance of mixed conductors - Equivalent circuit model and explicit approximate solutions**. *JOURNAL OF THE ELECTROCHEMICAL SOCIETY* 1999, **146**(11):4183–4188.

[16] Lai W, Haile S: **Impedance spectroscopy as a tool for chemical and electrochemical analysis of mixed conductors: A case study of ceria**. *JOURNAL OF THE AMERICAN CERAMIC SOCIETY* 2005, **88**(11):2979–2997.

[17] Jiang S, Ramprakash Y: **H-2 oxidation on Ni/Y-TZP cermet electrodes - a comparison of electrode behaviour by GCI and EIS techniques**. *SOLID STATE IONICS* 1999, **122**(1-4):211–222.

[18] Bard A, Faulkner L: *Electrochemical Methods: Fundamentals and Applications*. New Jersey: John Wiley & Sons 2001.

[19] Christensen P, Hamnett A: *Techniques and Mechanisms in Electrochemistry*. New York: Blackie Academic & Professional 1994.

[20] Fabry P, Kleitz M: **Influence of metal and electrolyte-composition on characteristics of oxygen electrode-reaction on solid oxide electrolyte**. *Journal of Electroanalytical Chemistry* 1974, **57**(2):165–177.

[21] MIZUSAKI J, TAGAWA H, SAITO T, KAMITANI K, YAMAMURA T, HIRANO K, EHARA S, TAKAGI T, HIKITA T, IPPOMMATSU M, NAKAGAWA S, HASHIMOTO K: **PREPARATION OF NICKEL PATTERN ELECTRODES ON YSZ AND THEIR ELECTROCHEMICAL PROPERTIES IN H2-H2O ATMOSPHERES**. *JOURNAL OF THE ELECTROCHEMICAL SOCIETY* 1994, **141**(8):2129–2134.

[22] Bieberle A, Meier L, Gauckler L: **The electrochemistry of Ni pattern anodes used as solid oxide fuel cell model electrodes**. *JOURNAL OF THE ELECTROCHEMICAL SOCIETY* 2001, **148**(6):A646–A656.

[23] Bieberle A, Gauckler L: **Reaction mechanism of Ni pattern anodes for solid oxide fuel cells**. *SOLID STATE IONICS* 2000, **135**(1-4, Sp. Iss. SI):337–345.

[24] Koep E, Mebane D, Das R, Compson C, Liu M: **Characteristic thickness for a dense La0.8Sr0.2MnO3 electrode**. *ELECTROCHEMICAL AND SOLID STATE LETTERS* 2005, **8**(11):A592–A595.

[25] Aaberg R, Tunold R, Mogensen M, Berg R, Odegard R: **Morphological changes at the interface of the nickel-yttria stabilized zirconia point electrode**. *JOURNAL OF THE ELECTROCHEMICAL SOCIETY* 1998, **145**(7):2244–2252.

[26] Bonanos N, Mogensen M: **H-2 oxidation at the interface Ni/Sr0.995Ce0.95Y0.05O2.975**. *SOLID STATE IONICS* 1997, **97**(1-4):483–488.

[27] Fleig J, Baumann FS, Brichzin V, Kim HR, Jamnik J, Cristiani G, Habermeier HU, Maier J: **Thin film microelectrodes in SOFC electrode research**. *FUEL CELLS* 2006, **6**(3-4):284–292.

[28] Brichzin V, Fleig J, Habermeier H, Maier J: **Geometry dependence of cathode polarization in solid oxide fuel cells investigated by defined Sr-doped LaMnO3**

**microelectrodes**. *ELECTROCHEMICAL AND SOLID STATE LETTERS* 2000, **3**(9):403–406.

[29] Brichzin V, Fleig J, Habermeier H, Cristiani G, Maier J: **The geometry dependence of the polarization resistance of Sr-doped LaMnO3 microelectrodes on yttria-stabilized zirconia**. *SOLID STATE IONICS* 2002, **152**(Part A Sp. Iss. SI):499–507.

[30] Baumann F, Fleig J, Konuma M, Starke U, Habermeier H, Maier J: **The Oxygen Reduction Kinetics of Mixed Conducting Electrodes: Model Considerations and Experiments on La0.6Sr0.4Co0.8Fe0.2O3 Microelectrodes**. *Solid Oxide Fuel Cells IX, PV 2005-07* 2005, :1636.

[31] Baumann F, Fleig J, Konuma M, Starke U, Habermeier H, Maier J: **Strong performance improvement of La0.6Sr0.4Co0.8Fe0.2O3-delta SOFC cathodes by electrochemical activation**. *JOURNAL OF THE ELECTROCHEMICAL SOCIETY* 2005, **152**(10):A2074–A2079.

[32] S Katsura TUYA Y Taninouchi: **Measurement of polarization behavior of hydrogen and oxygen electrode in solid acid fuel cell using area-asymmetric cell.** In *JOURNAL OF THE ELECTROCHEMICAL SOCIETY*, Banff, Canada: *Proceedings of the 58th Annual meeting of the International Society of Electrochemistry* 2007.

[33] Boysen D, Uda T, Chisholm C, Haile S: **High-performance solid acid fuel cells through humidity stabilization**. *SCIENCE* 2004, **303**(5654):68–70.

[34] Smith G: *Numerical Solution of Partial Differential Equations: Finite Difference Methods*. London: Oxford University Press 1985.

[35] Newman J: **Resistance for Flow of Current to a Disk**. *Journal of the Electrochemical Society* 1966, **113**:501–502.

[36] Denhoff M: **An accurate calculation of spreading resistance**. *JOURNAL OF PHYSICS D-APPLIED PHYSICS* 2006, **39**(9):1761–1765.

[37] Haile SM, Chisholm CRI, Sasaki K, Boysen DA, Uda T: **Solid acid proton conductors: from laboratory curiosities to fuel cell electrolytes**. *FARADAY DISCUSSIONS* 2007, **134**:17–39.

[38] Fleig J, Maier J: **The impedance of imperfect electrode contacts on solid electrolytes**. *SOLID STATE IONICS* 1996, **85**(1-4):17–24.

[39] Fleig J, Maier J: **Finite element calculations of impedance effects at point contacts**. *ELECTROCHIMICA ACTA* 1996, **41**(7-8):1003–1009.

[40] KAY B, PEDEN C, GOODMAN D: **KINETICS OF HYDROGEN ABSORPTION BY PD(110)**. *PHYSICAL REVIEW B* 1986, **34**(2):817–821.

[41] Grigoriev S, Porembsky V, Fateev V: **Pure hydrogen production by PEM electrolysis for hydrogen energy**. *INTERNATIONAL JOURNAL OF HYDROGEN ENERGY* 2006, **31**(2):171–175.

[42] Taninouchi YK, Uda T, Awakura Y, Ikeda A, Haile SM: **Dehydration behavior of the superprotonic conductor CsH2PO4 at moderate temperatures: 230 to 260 degrees C**. *JOURNAL OF MATERIALS CHEMISTRY* 2007, **17**(30):3182–3189.

[43] A Hightower MSSH W Chueh: **Cerie Supported Rh3Pt2Sn Nanoparticles as Low Temperature Ethanol Steam Reforming Catalysts.** In *JOURNAL OF MATERIALS CHEMISTRY*, Foz Iguacu, Brazil: *Spring Meeting of the International Society of Electrochemistry* 2008.

[44] BARANOV A, KHIZNICHENKO V, SANDLER V, SHUVALOV L: **FREQUENCY DIELECTRIC-DISPERSION IN THE FERROELECTRIC AND SUPERIONIC PHASES OF CSH2PO4**. *FERROELECTRICS* 1988, **81**:1147–1150.

[45] Taninouchi Yk, Uda T, Awakura Y: **Dehydration of CsH2PO4 at temperatures higher than 260 degrees C and the ionic conductivity of liquid product**. *SOLID STATE IONICS* 2008, **178**(31-32):1648–1653.

[46] Otomo J, Ishigooka T, Kitano T, Takahashi H, Nagamoto H: **Phase transition and proton transport characteristics in CsH2PO4/SiO2 composites**. *ELECTROCHIMICA ACTA* 2008, **53**(28):8186–8195.

[47] Otomo J, Minagawa N, Wen C, Eguchi K, Takahashi H: **Protonic conduction of CsH2PO4 and its composite with silica in dry and humid atmospheres**. *SOLID STATE IONICS* 2003, **156**(3):357–369.

[48] Ponomareva VG, Shutova ES: **Electrotransport properties of a high-temperature phase of CsH2PO4 and composite systems with silicon dioxide at different humidities**. *RUSSIAN JOURNAL OF ELECTROCHEMISTRY* 2007, **43**(5):513–520.

[49] Ponomareva VG, Shutova ES: **High-temperature behavior of CsH2PO4 and CsH2PO4-SiO2 composites**. *SOLID STATE IONICS* 2007, **178**(7-10):729–734.

[50] GOTTESFELD S, PAFFORD J: **A NEW APPROACH TO THE PROBLEM OF CARBON-MONOXIDE POISONING IN FUEL-CELLS OPERATING AT LOW-TEMPERATURES**. *JOURNAL OF THE ELECTROCHEMICAL SOCIETY* 1988, **135**(10):2651–2652.

[51] Gellings P, Bouwmeester H: *The CRC Handbook of Solid State Electrochemistry*. New York, New York: CRC Press 1997.

[52] J Sfeir AM J Van herle: **Measurement of polarization behavior of hydrogen and oxygen electrode in solid acid fuel cell using area-asymmetric cell.** In *The CRC Handbook of Solid State Electrochemistry*, European Fuel Cell Forum, Switzerland: *Proc. 3rd European Solid Oxide Fuel Cell Forum (ed. Stevens, P.)* 1998.

[53] T Aida MIHKKY A Abudala: **Measurement of polarization behavior of hydrogen and oxygen electrode in solid acid fuel cell using area-asymmetric cell.** In *The CRC Handbook of Solid State Electrochemistry*, Electrochemical Soc., Pennington: *4th Int. Symp. on Solid Oxide Fuel Cells (ed. Stevens, P.)* 1995.

[54] Haile SM, Uda T, Boysen D, Chisholm CR: **Alcohol fuel cells using CsH2PO4 electrolytes**. *ABSTRACTS OF PAPERS OF THE AMERICAN CHEMICAL SOCIETY* 2006, **231**.

[55] Uda T, Boysen D, Chisholm C, Haile S: **Alcohol fuel cells at optimal temperatures**. *ELECTROCHEMICAL AND SOLID STATE LETTERS* 2006, **9**(6):A261–A264.

[56] Zhang H, Liu D, He M, Xu H, Li W: **Experimental and simulation studies on concentration polarization in H-2 enrichment by highly permeable and selective Pd membranes**. *JOURNAL OF MEMBRANE SCIENCE* 2006, **274**(1-2):83–91.

[57] HOLLECK G, FLANAGAN T: **ELECTROCHEMICAL EXCHANGE CURRENTS OF PALLADIUM AND PALLADIUM ALLOY ELECTRODES AS A FUNCTION OF THEIR HYDROGEN CONTENTS**. *TRANSACTIONS OF THE FARADAY SOCIETY* 1969, **65**(563P):3064–&.

[58] Howard B, Killmeyer R, Rothenberger K, Cugini A, Morreale B, Enick R, Bustamante F: **Hydrogen permeance of palladium-copper alloy membranes over a wide range of temperatures and pressures**. *JOURNAL OF MEMBRANE SCIENCE* 2004, **241**(2):207–218.

[59] Roychowdhury C, Matsumoto F, Zeldovich V, Warren S, Mutolo P, Ballesteros M, Wiesner U, Abruna H, DiSalvo F: **Synthesis, characterization, and electrocatalytic activity of PtBi and PtPb nanoparticles prepared by borohydride reduction in methanol**. *CHEMISTRY OF MATERIALS* 2006, **18**(14):3365–3372.